The role of ligaments in murine osteoarthritic models: markers and mechanics

Thesis submitted in accordance with the requirements of the University of Liverpool for the degree of Doctor in Philosophy by:

Lorenzo Ramos-Mucci.

December 2020

Abstract

Osteoarthritis (OA) is the most common form of arthritis and the leading cause of disability among elderly. It is a multicomponent chronic disease and yet little is known about the role of ligaments in OA. Ligaments are the main mechanical stabilizers of the knee joint, and trauma of the ligament has been closely linked to OA making it a potential target for therapeutics. Cellular, matrix and mechanical pathology of the ligament have not been fully characterised in OA. Furthermore, ligament cellular complexity remains poorly understood, including identification of ligament cell populations and markers in healthy, non-diseased tissue. Understanding the healthy ligament is essential to understand the pathology of diseased OA ligaments.

The goal of this thesis was to characterise and identify markers and mechanical properties in the ligaments in healthy and diseased spontaneous and post-traumatic OA murine models. Histology demonstrated changes in anterior cruciate ligament (ACL) and the medial collateral ligament (MCL) organization and cell morphology between healthy and OA ligaments. In the extracellular matrix (ECM) of diseased ligaments, pathology included proteoglycan and collagen type II (COL2) deposition. ECM pathology coincided with rounded-cell morphology and SOX9 and RUNX2 expression, markers of chondrogenesis, and potentially endochondral ossification. Changes occurred in the early stages of OA, suggesting an important role of ligaments in OA.

Functional changes to the mechanical properties of the ligaments were explored in healthy and diseased OA models. Viscoelastic behaviour demonstrated a decrease in normalised strain rate sensitivity in both the spontaneous and post-traumatic OA ACLs. Furthermore, there was a decrease in stiffness and stress-relaxation in the post-traumatic OA ACL. These findings confirm that ligament ECM composition and viscoelastic properties are closely interrelated. Understanding the underlying pathways driving viscoelastic properties is imperative for OA.

Single-cell RNA-sequencing (scRNA-seq) identified ligament cell populations and gene markers from healthy adult mice knee ligaments. Analysis revealed 20 distinct clusters and nine cell types, from which there were five fibroblast clusters. Most importantly, the smallest fibroblast cluster, included Aggrecan (*Acan*) as well as *Sox9* and *Col2a1* gene markers previously seen in diseased OA ligaments. ACAN-expressing fibroblasts were confirmed in the mid-ligament section of murine cruciate ligaments. The role of this novel fibroblast subpopulation in OA is unknown.

This research introduces a deeper understanding of healthy and OA ligament, including cellular and fibroblast markers, ECM composition and viscoelastic properties, all which indicate that ligaments play a bigger role in OA than previously thought.

Table of Contents

List of Figures

List of Tables

List of Abbreviations

Abbreviations	Full description
AC	Articular cartilage
ACL	Anterior cruciate ligament
ACLT	Anterior cruciate ligament transection
ANOVA	Analysis of variance
ASPN	Asporin
BMP	Bone morphogenic protein
BSA	Bovine serum albumin
COL2	Collagen type II
CSA	Cross-sectional area
DAPI	4′,6-diamidino-2-phenylindole
DMEM	Dulbecco's Modified Eagle Medium
DMM	Destabilisation of the medial meniscus
DNA	Deoxyribonucleic acid
ECM	Extracellular matrix
EDTA	Ethylenediaminetetraacetic acid
E_t	Tangent modulus
FBS	Fetal bovine serum
FGF	Fibroblast growth factor
GAG	Glycosaminoglycan
GDF5	Growth differentiation factor 5
IL	Interleukin
IPA	Ingenuity pathway analysis
kV	Kilovolt
kW	Kilowatt
LCL	Lateral collateral ligament
LF	Lateral femur
LT	Lateral tibia
MCL	Medial collateral ligament
MF	Medial femur
mg	Milligram
MKX	Homeobox protein Mohawk
mL	Milliliter
mm	Millimeter
mM	Millimolar
MMP	Matrix metalloproteinase
MPa	Megapascal
MT	Medial tibia
N	Newtons
OA	Osteoarthritis / osteoarthritic
%/s	Percent per second
PBS	Phosphate-buffered saline

PCA	Principal component analysis
PCL	Posterior cruciate ligament
PMMA	Poly(methyl methacrylate)
PR	Picrosirius red
RB	Red blood
RNA	Ribonucleic acid
RSD	Relative standard deviation
s	Second
SCX	Scleraxis
SLRPs	Small leucine-rich proteoglycans
3D	Three dimensional
TGF	Transforming growth factor
TNMD	Tenomodulin
t-SNE	t-distributed stochastic neighbour embedding
UMAP	Uniform manifold approximation and projection
UMI	Unique molecular identifiers
µA	Microampere
µCT	X-ray microtomography
µL	Microliter
µm	Micrometer

Acknowledgements

First and foremost, thank you to my supervisors, you made this project possible and guided me every step of the way. Thank you to Dr. Blandine Poulet, as your first PhD student I hope I made you proud, thank you for answering all my little questions and introducing me to single-cell RNA-seq. I would also like to express my gratitude to Prof. Eithne Comerford, your guidance, knowledge and connections were fundamental in this project and thank you for motivating me in my writing. Last, but not least, thank you to Prof. Ahmed Elsheikh, your questions opened my way of thinking and helped me think as an engineer. To all of you I am extremely thankful.

I would also like to thank everyone involved in this research; many parts of this work were a result of collaborations. Thank you to Dr. Craig Keenan, you showed me the ropes in histology and much more. Thank you to Mr. Ashkan Eliasy, your help in the biomechanics lab and analysis was above and beyond. Thank you to Dr. Luca Lenzi, your help with scRNA-seq analysis was instrumental. I would also like to express my gratitude to many colleagues behind the scenes who helped me along the way, mainly Prof. George Bou-Gharios, Prof. Rob Van'T Hof, Dr. Kazuhiro Yamamoto, Dr. Margaret Hughes, Dr. Amy Horwell, Dr. Yalda Ashraf Kharaz, Dr Ioannis Kanakis, Dr. Katie Lee and everyone from the Musculoskeletal Biology Department and the Biomedical Services Unit.

I would also like to express the deepest gratitude to my wife, Bárbara Simões to whom I dedicate this thesis. A very special hug to my family and friends from all over the world who supported me. Many thanks to my family in Massachusetts, my parents, my sister, and my brother, Kerry and Luca, my family in Ecuador and my family in Italy, especially my *nonna*. I must also say thanks to the Liverpool crew: Ifi, Michele, Adrien, Dani, Marc, Lee, Conor, Adam, Euan, Mattia, Shah, Roberto, Juliette, Wasu, Francesa, Steph, Lina, Misso, Sergio, the PGR society, the footy group and many others. I am forever grateful.

Lastly, I would also like to thank the Institute of Ageing and Chronic Disease at the University of Liverpool, thank you for funding my research and believing in ligaments!

Chapter 1:
General Introduction

1.1 The human knee joint and ligament function

The human tibiofemoral knee joint is a complex hinge joint made up of soft and hard connective tissues including bones, cartilage, menisci, ligaments, tendons, muscles and the joint capsule, each with their own function necessary for movement [1]. The knee is the largest joint in the human body, connecting the thigh bone (femur) and shin bone (tibia) [1]. The bones are maintained in place and stabilised by four main ligaments: the anterior cruciate ligament (ACL), the posterior cruciate ligament (PCL), the medial collateral ligament (MCL) and the lateral collateral ligament (LCL) (Figure 1.1A) [2]. In the knee joint, the ends of the bone are made up of articular cartilage which create a smooth protective surface [1]. Within the femorotibial joint, crescent-shaped menisci (lateral and medial) are found (Figure 1.1B). Menisci are fibrocartilaginous and act as shock absorber and stabilisers [3, 4] and are attached to the tibial surface by meniscotibial ligaments (Figure 1.2) [2]. In addition, the entire knee joint is surrounded by a joint capsule (Figure 1.1B) lined by a synovial membrane and filled with synovial fluid, which reduces friction and acts as a transport medium [4, 5]. Lastly, tendons link bone to muscle, providing further stability necessary for knee movement and gait [1]. These tissues are highly interconnected and together makeup the knee joint organ [6].

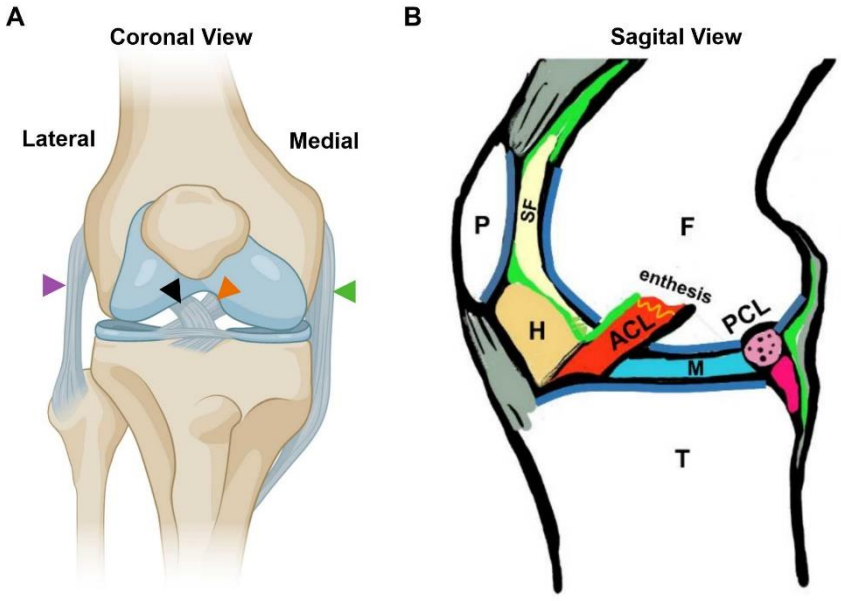

Figure 1.1 Anatomy of the human knee joint. (A) Human knee joint are stabilised by four major ligaments, mainly the anterior (black arrow) and posterior cruciate ligaments (orange arrow) and the medial (green arrow) and lateral collateral ligaments (purple arrow). (B) Schematic of a sagittal cross-section of the knee joint organ showing the femur (F), tibia (T), patellar (P), synovial fluid (SF), Hoffa's fat pad (H), anterior cruciate ligament (ACL), meniscus (M), posterior cruciate ligament (PCL) and synovial membrane (green). Figure B was taken from Schulze-Tanzil et al. [4].

Ligaments have a unique biomechanical function in the knee joint being necessary for normal knee motion and homeostasis [2]. They are made up of dense connective tissue linking one bone to another, providing mechanical support and ensuring knee stability [2]. The ACL connects the lateral condyle of the femur to the medial side of the tibial intercondylar area (Figure 1.2A-B) [7] providing restraining force to anterior tibial displacement, preventing hyperextension [8, 9]. The PCL connects the posterior lateral aspect of the intercondylar area of the tibia to the medial condyle of the femur (Figure 1.2A-B), limiting posterior tibial displacement [10]. The cruciate ligaments are intra-articular and extra-synovial in humans [7]. The collateral ligaments are extra-articular but also guide knee stability. The MCL runs along the medial side of the knee (Figure 1.1A), providing static restraint to valgus stress (outward stress) [11]. Similarly, the LCL on the lateral side of the knee (Figure 1.1A) provides static restraint to varus stress (inward stress) [12].

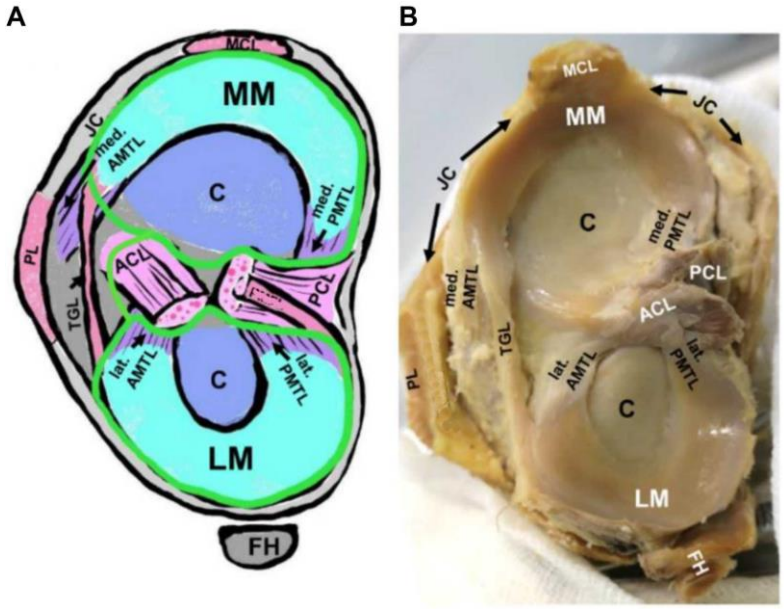

Figure 1.2 Anatomy of the human knee joint ligaments. (A) Axial schematic of the human knee joint and the intraarticular meniscotibial ligaments: cartilage (C), anterior cruciate ligament (ACL), posterior cruciate ligament (PCL), medial collateral ligament (MCL), medial meniscus (MM), lateral meniscus (LM), anterior and posterior meniscotibial ligament (AMTL and PMTL), patellar ligament (PL), fibular head (FH), transverse genicular ligament (TGL) and joint capsule (JC). (B) Axial gross anatomy of the human knee joint and intraarticular ligaments. Figure taken from Schulze-Tanzil et al. [4].

1.2 Murine knee joint and murine models

The anatomy of the murine knee joint is similar to that of the human knee joint [13]. The gross anatomy of the ACL, PCL, MCL and LCL orientation, location and insertion sites in the murine

knee joint is analogous to that of the human [13], suggesting similar functions to the human knee joint. However, the major difference is in the small size of the murine knee joint, as well as differences in the gait (quadruped) and mechanical distribution of the weight bearing forces [14]. These differences result in alterations of the mechanical function of the ligaments: the ACL of the murine models is the strongest knee joint ligament [13], however in humans, studies have shown that the PCL has higher tensile strength than the ACL [15]. Microanatomical structures of the murine ligaments are also similar to the human ligaments, including a fibrocartilaginous layer near the enthesis, aligned fibre structure, capillaries and an epiligament layer [13]. There is currently no literature on whether the murine cruciate ligaments are extra-synovial, however they are extra-synovial in the canine quadrupedal knee joint [16]. Other anatomical differences in the murine knee joints include thinner articular cartilage, which lack transitional and superficial cartilage layers compared to human articular cartilage [17]. The distinction in mechanical forces and cartilage thickness are important to consider in development of translational research.

However, murine models still offer valuable advantages for testing, including the ability to assess disease progression at multiple time points, therapeutic interventions with a rapid outcome assessment and the ability to replicate consistent and repeatable injuries not possible in human research. Furthermore, several murine models show evidence of similar disease pathology to humans such as the murine STR/ort spontaneous osteoarthritis (OA) model [18], which offer a comparable model for the study of human knee ligament biology and translational medicine.

1.3 Ligament structure and composition

Each ligament has a distinct role and composition to match its mechanical function [19, 20], however they share a similar underlying matrix organisation [2]. Ligaments are composed of dense collagenous fibres aligned in parallel, which give them high tensile strength and facilitate their mechanical function [2, 21, 22]. These fibres are made up predominantly of extracellular material and dispersed fibroblasts [23]. The composition of the ligament ECM is two-thirds water and one-third dry weight [2, 23]. The dry content is primarily collagen, which makes up about 75% of the composition [23]. Collagen type I is the main collagen type in all ligaments, making up over 85% of all collagen content, being slightly less than that found in tendons (~95%) [2, 23]. The other collagen types present in ligament are types III, V, VI, XI, and XIV [2, 24]. The exact amounts and arrangement will depend on the ligament [19, 20]. For example, in adult rabbits both cruciate ligaments are composed of 12% collagen type III from the total collagen content [25],

but in the adult rabbit MCLs only 5% of the total collagen is collagen type III [26]. For comparison in human ACLs, approximately 11-14% of total collagen content is collagen type III [27], much higher than the amount of collagen type III found in tendons [20].

The rest of the ligament ECM consists of smaller component such as proteoglycans, elastin, and glycolipids, each important in maintaining ligament function [2, 28]. Two groups of proteoglycans have been demonstrated in ligaments and tendons, mainly small leucine-rich proteoglycans (SLRPs) such as decorin, biglycan, fibromodulin, and lumican, and modular proteoglycans such as aggrecan (ACAN) and versican [29]. Modular proteoglycans such as ACAN improve water retention and enhance resistance to high compressive and tensile forces and are found mainly in the fibrocartilaginous enthesis region [30]. SLRPs, interact with the ECM and growth factors, and consequently play a crucial role in collagen fibrillogenesis during development [29]. Elastin contributes to mechanical properties of the ligament as it enhances resistance to transverse and shear loading [28]. A high amount of elastin (9.86% dry weight) has been reported in canine cruciate ligaments [31]. In contrast, in human MCLs elastin content is estimated at about 5% dry weight [28]. Furthermore, elastin and glycosaminoglycans (GAGs) (a component of proteoglycans), were more prominent in the canine ACL than in the MCL and tendons [20], highlighting important compositional differences between each ligament and tendon.

Ligaments have structured subcomponents with a high degree of organisation which make up part of a complex hierarchical structure (Figure 1.3). At the core of the ligament structure are the collagen molecules composed of three left-handed helical alpha chains (Figure 1.3) [21, 32]. These collagen molecules are first synthesised in the form of procollagen and are modified in the ECM to form collagen microfibrils. Collagen microfibrils and elastin fibres are surrounded by a proteoglycan-water matrix, and the microfibrils are then further arranged through crosslinking into fibrils, fibres, fascicles and eventually the ligament/tendon unit (Figure 1.3) [2, 23]. Each fascicle is surrounded by connective tissue called the endoligament, and the entire ligament unit is enveloped by a more vascular connective tissue layer called the epiligament (Figure 1.3) [33]. This hierarchical structure and the intermolecular crosslinking between subunits is integral for the mechanical ability of the ligament [2].

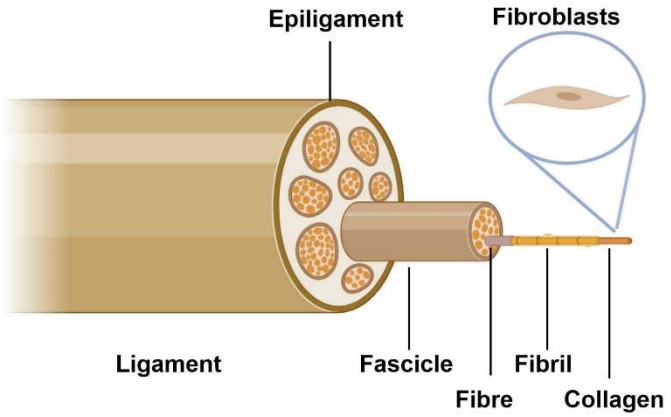

Figure 1.3 Ligament hierarchical structure. Knee ligaments are composed of dense connective tissue with a complex hierarchical structure made up of fascicles, fibres, fibrils, and collagen. The main cell types, fibroblasts, are dispersed in the ligament matrix and in the outer vascular epiligament layer. Figure based on diagram from kastelic et al. [34].

The vasculature of ligaments provides essential nutrients and sensory information in an otherwise avascular fibrous connective tissue [35, 36]. The outer epiligament layer (Figure 1.3) is highly vascular, and in the human ACL its blood supply arrives from the middle genicular artery [33]. Human cruciate ligaments are also surrounded by a synovial fold from which blood vessels also penetrate the ligament and connect to the intraligamentous vascular network [35]. Vascularisation is particularly important after ligament trauma, and in fact a lack of vascular response has been associated with the poor healing potential of the ACL [37].

Innervation of the interfascicular area of the ligament facilitates the joint and limb's proprioceptive functions [38]. Sensory neurons include myelinated and unmyelinated nerves with articular nerve endings including free nerve endings for nociception, and mechanoreceptors such as Pacinian corpuscles, Golgi tendon organs, and Ruffini endings [38]. In the knee joint, these nerve endings can activate muscle reflexes to prevent joint distraction, reduce stress on the ligament and reduce build-up of force [39]. Some mechanoreceptors, such as the Pacinian corpuscles and the Golgi tendon organs are not found in the MCL, but are found in the ACL and LCL of rabbits [40]. In addition, mechanoreceptors are present in greater numbers in the ACL and PCL compared to the MCL and the patellar tendon [40]. The PCL in particular plays a major role in the sensory function of the knee joint [41].

In summary, ligaments are composed of a highly dense but organised ECM with a hierarchical structure, which consists of a collagen molecular core which are bundled into fibre, fibrils and fascicles interspersed with proteoglycans, elastin and a vascular and nerve network [2]. In addition, ligament composition varies slightly among each ligaments due to its specific function [20]. This complex ECM structure and composition is maintained by the native ligament fibroblasts called ligamentocytes [2]. Several studies have tried to identify these cells by studying their cellular origin and markers during development which are outlined in Section 1.4.

1.4 Ligament development and cellular markers

The complex architectural framework of the ligament is synthesised and maintained by the connective-tissue cell family [42]. In ligaments, this includes mainly a type of fibroblast, called ligamentocytes [2], which are not well characterised. Ligamentocytes are found in the fascicles, the endoligament and the epiligament, and are highly organised and aligned to the thick fibres of collagen [25, 43]. Ligamentocytes communicate with neighbouring cells via gap junctions [44] and potentially also via prominent cytoplasmic extensions [2]. Other cell types found in ligaments include the fibrocartilaginous cells in the attachment sites, known as the enthesis [43]. These attachment sites are composed of a partially mineralised region, and chondrocyte-like cells with round cell morphology [45]. Ligament-derived stem cells have also been identified in intra-articular ligaments [46].

Ligamentocyte-specific markers have yet to be identified as currently most ligament markers are ligament/tendon-specific. Both tissues are structurally and biochemically similar [25], but as mentioned previously, tendons and ligaments are unique in their composition [20] and transcriptome which is highly heterogeneous [47]. Cell specific markers involved in development of tendon and ligament tissues have been identified as scleraxis (SCX) and homeobox protein mohawk (MKX) [48, 49]. SCX, a helix-loop-helix transcription factor, is present in the $SCX^{+}/SOX9^{+}$ chondroprogenitor cells at E10.5 which differentiate into ligamentocytes and tenocytes, making SCX the earliest known ligament/tendon cell marker [49]. Furthermore, SCX regulates tenocyte differentiation from mesenchymal stem cells and characteristic gene expression including collagen type I, decorin, fibromodulin and tenomodulin (TNMD) [50]. *Scx* deletion in mice had a varying effect on force-transmitting tendons, ranging from tendon atrophy to ECM disorganisation [51]. Interestingly, *Scx* deletion had no effect on ligament development and function [51].

MKX, a homeobox protein transcription factor, has also been associated with ligament and tendon development and is further maintained in mature ligament cells [48, 52]. MKX can also drive mesenchymal stem cells towards tenocyte differentiation *in vitro* [53], and is present in regions of tendon progenitor cells during embryonic development, but at a later stage than SCX [48]. *Mkx* null mice have underdeveloped tendons in the form of thinning collagen fibrils and deficient collagen type I and TNMD production [52]. *Mkx* deletion had no effect on cruciate ligament development and effects on other ligaments' development and composition were not reported [48, 52]. These differences in development between ligament and tendon tissues suggest a divergent cell lineage.

Growth differentiation factor 5 (GDF5), part of the bone morphogenic protein (BMP) family, is a marker for all synovial joint progenitor cells, prior to SCX expression [54]. All the joint tissue cell types from bone, cartilage and ligament are derived from a GDF5-expressing lineage [54] and GDF5 is maintained in cruciate ligament and meniscal cells throughout development [55]. Synovial joint development involves a continuous influx of cells, and GDF5-expressing cells are thought to regulate lineage divergence and differentiation [55]. *Gdf5* null mice resulted in a lack of intra-articular ligaments (both cruciate ligaments), menisci and thin patellar tendons and collateral ligaments [56].

The full extent of how these markers regulate ligament development and regeneration is unclear. Recent studies have uncovered a complex array of markers which interact with each other, including early growth response factor and TNMD, which have both been directly linked to SCX and MKX expression [51, 57]. More importantly, many of these markers are involved in regulating ECM synthesis. As previously mentioned, SCX regulates collagen type I and proteoglycan expression in tendons [50], MKX also regulates collagen type I production [52] and similarly GDF5 also plays a role with upregulating collagen type I and III and matrix metalloproteinase (MMP)-13 amongst others [58]. These development markers are important for progenitor differentiation and ECM synthesis, and therefore could also be involved in disease pathologies that affect cellular differentiation or the ECM composition in ligaments.

Overall, early development markers have been found such as SCX and MKX which drive ligament and tendon development [48]. These markers and their associated pathways are poorly understood, particularly in mature ligaments, in part, because of the heterogeneity of each individual ligament and tendon [47].

1.5 Ligament mechanics

As previously mentioned, ligament ECM composition and structure is fundamental for tissue function and mechanical properties [2]. Ligaments have to be both flexible and strong in resisting tensile loads in order to support the musculoskeletal system. The mechanical behaviour of ligaments is viscoelastic, meaning it exhibits both viscous and elastic behaviour when undergoing deformation [59]. Viscous materials display resistance to strain linearly with time when a stress is applied, whereas elastic materials stretch and return to their original state in a non-time dependant manner [59]. This behaviour, best represented in a stress-strain curve, shows an exponential increase in force (stress) as the material elongates (strain) and can be divided into three regions: the toe-region, linear-region, and failure-region (see Figure 1.4) [2, 60]. The toe-region demonstrates non-linear and viscoelastic behaviour: non-linear due to "crimped" collagen fibrils [2, 60] and viscoelastic due to collagen interaction with ECM structural proteins [60, 61]. In the toe-region, collagen fibrils undergo "un-crimping" of their wavy structure (termed "fibrillar crimps"), resulting in a non-linear low stiffness behaviour [60]. The linear-region represents stiffer viscoelastic behaviour, due to the collagen fibril molecules stretching and the sliding of collagen triple helices [62]. Typically, the physiological relevant range of ligament mechanics falls within the toe-region, with the linear-region being the upper physiological limits of ligament mechanics [60, 62]. The failure-region is beyond the elastic limits of the ligament, resulting in disruption of the crosslinking of the collagen fibres and irreversible deformation [62].

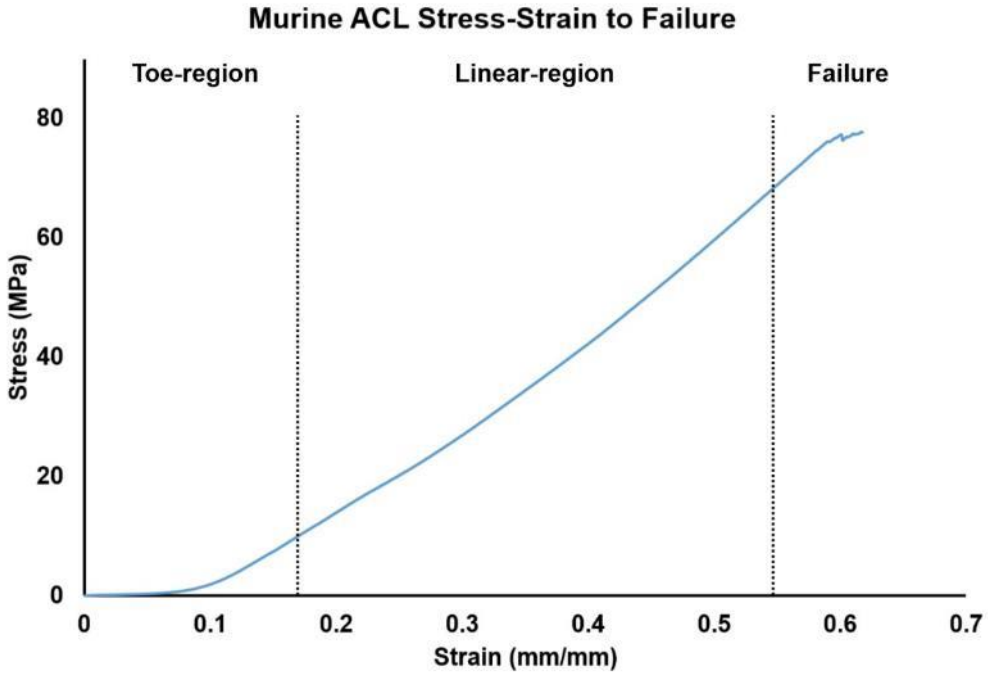

Figure 1.4 Stress-strain curve of the murine anterior cruciate ligament (ACL). Viscoelastic stress-strain showing the non-linear (toe-region), linear and failure regions. The toe-region demonstrates non-linear viscoelastic behaviour and the linear region represents a stiffer viscoelastic region which can return back to its original state if the tissue does not pass the failure point. In the plastic failure region, there is permanent tissue failure, resulting in irreversible damage to the tissue structure. The ultimate load at failure, also known as maximum load, is considered a material property of tissue strength. Based on a diagram from Robi et al. [63].

Viscoelasticity is a time-dependant anelastic behaviour, where the response to a stimulus is delayed due to a loss in energy in the material [64]. The viscoelastic properties of ligament include strain rate sensitivity [59], stress-relaxation [59], creep [65], and hysteresis [66]. Strain rate sensitivity is where the stress-strain curve of ligaments is dependent on the rate at which strain is applied (known as strain rate) (see Figure 1.5A). In ligaments higher strain rates typically result in a stiffer (higher stress) response [59, 61]. Although the mechanisms of strain rate sensitivity are not fully understood, it has been proposed that at slow strain rates fibrils straighten before collagen fibrils start to glide and in faster strain rates fibrils start directly with intra-fibrillar gliding [67]. It has also been theorised that strain rate sensitivity is due to the viscous components of the ligament proteoglycan-rich matrix, where viscosity increases with strain rate [68]. This has been confirmed in mouse tendons, where fascicle without decorin had reduced strain rate sensitivity, but mutations in collagen type I did not affect the tendon strain rate sensitivity [69]. These findings may indicate the strain rate sensitivity is an important viscoelastic property likely affected by the ECM composition and in particular the proteoglycan content.

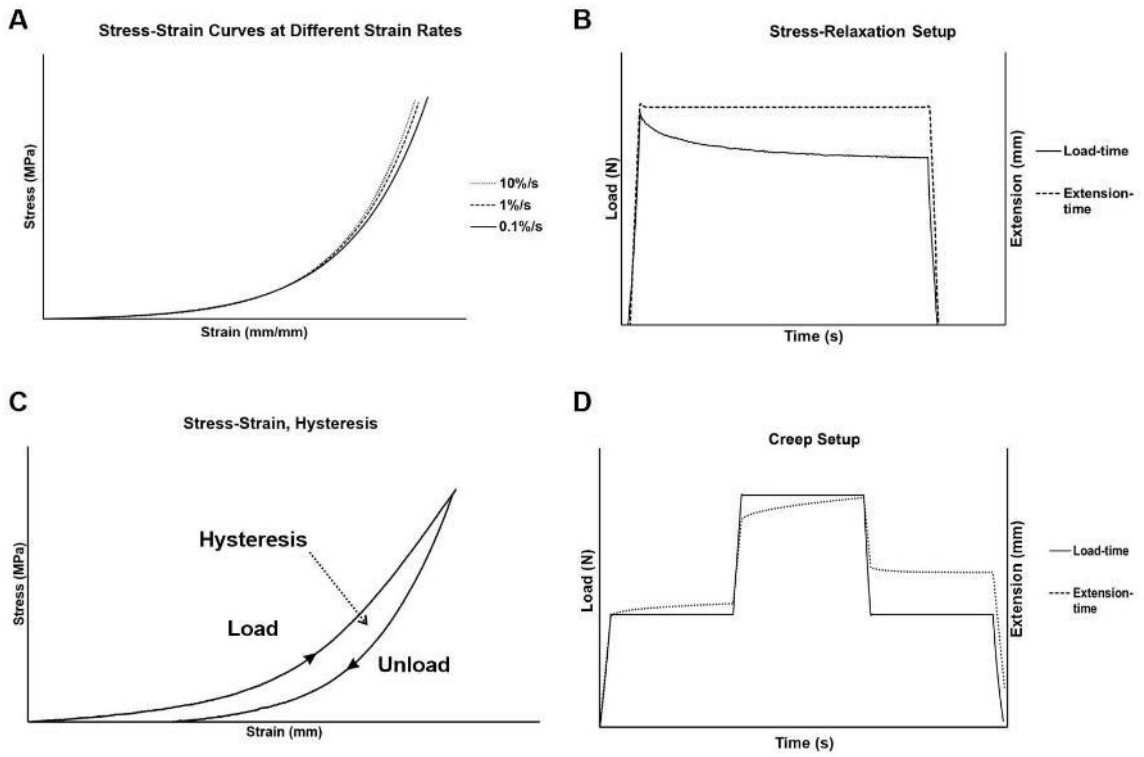

Figure 1.5 Viscoelastic properties of ligaments. These include strain rate sensitivity (A), stress-relaxation (B), hysteresis (C), and creep (D). (A) Strain-rate sensitivity demonstrates different stress-strain curves dependant on the strain rate [59]. (B) Stress-relaxation is the relaxation of the stress over time (load-time), under a constant strain (extension-time) [59]. (C) Hysteresis, the area between the load and unload cycle, represents energy dissipated during loading-unloading [66]. (D) Similar to stress-relaxation, creep is another viscoelastic property, where ligament extension can increase over time (extension-time), under a constant load (load-time). Creep image was adapted from Thornton et al. [70].

Stress-relaxation of a viscoelastic material, such as a ligament, is the ability to reduce stress over time under a constant strain [59] (see Figure 1.5B). Stress-relaxation behaviour is attributable to ligament viscous material response and microstructure reorganising to reduce the overall stress [2]. Studies have shown that no changes in fibre realignment were found during stress-relaxation of rat tendon [71], therefore collagen structure is likely not responsible for stress-relaxation. Stress-relaxation is also strain dependent, and in the rabbit MCL the rate of relaxation decreased with increasing strain [72], which would suggest that stress-relaxation is a viscous material property. Stress-relaxation behaviour is in part controlled by proteoglycan composition as stress-relaxation behaviour was found to be compromised in decorin-deficient mice tendons [73]. This finding was also confirmed in human MCLs which showed an increase in stress-relaxation after chondroitinase treatment which removes GAGs present in proteoglycans from the ligament ECM [74]. Hence, stress-relaxation is likely an important indicator of ligament proteoglycan composition.

Similarly, creep, measures the ability of ligaments to increase their elongation (strain) over time under a constant force [2] (see Figure 1.5D). The mechanisms of creep behaviour include collagen fibre recruitment, as has been shown in rabbit MCLs during creep [75], which would suggest an involvement of the collagen structure. In addition, creep was found to be strain dependent in another study examining rabbit MCLs, similar to stress-relaxation [72], which would again suggest viscous behaviour. Further evidence found that an increase in hydration resulted in an increase in creep elongation [70]. In addition, partial GAG (a major component of all proteoglycans) depletion was also shown to decrease the creep rate in canine cruciate ligaments [61]. Therefore, creep is an important ligament viscoelastic property that can give insight not only on collagen fibre recruitment, but also hydration and GAG content.

Hysteresis, another viscoelastic property, represents the amount of energy dissipated during the loading and unloading cycle of stress-strain [66] in a material and can be measured by the difference between the loading and unloading stress-strain curves [64] (see Figure 1.5C). Although the exact mechanisms affecting hysteresis in ligaments are unknown, it has been theorised that the viscous energy loss during hysteresis occurs due to rearrangement of the inter-fibrillar ECM, such as proteoglycans [76]. In ligaments, hysteresis was shown to decrease significantly in the first preconditioning cycles, but not after the first 10 preconditioning cycles [66]. In addition, hysteresis in ligaments was shown to change with different strain rates [66]. Unlike some of the other viscoelastic properties, hysteresis was shown not to change in human MCLs with a reduction in decorin content [77], hence the role of proteoglycans has not been yet clearly defined in hysteresis. Importantly, freezing of ligament samples did result in significant differences in hysteresis compared to non-frozen ligaments, but only in the first few load-unload cycles [78], therefore preconditioning and storage conditions are important for when considering studies examining ligament mechanical properties.

In summary ligament viscoelastic behaviour is mainly attributed to collagen structure and interaction with ECM structural proteins [60, 61] such as the proteoglycans, decorin and biglycan [79, 80], which are necessary for viscoelastic properties including strain rate sensitivity [69] and stress-relaxation [73]. Therefore alterations in viscoelastic properties could be an effective indicator of early disease pathologies such as OA where ECM structure and compositional changes have been reported [6].

1.6 Osteoarthritis (OA)

OA is the most common form of arthritis and the leading cause of disability among the elderly affecting millions of people worldwide [81]. An estimated 18% of women and 10% of men worldwide over 60 years of age have evidence of radiographic OA [82]. In the United Kingdom, incidence of OA in any joint was about 8.6/1000 overall, with a higher prevalence in women [83]. The risk factors for OA include ageing, obesity, exercise, genetic predisposition, trauma, mechanical factors and gender [6]. Knee joint OA is of particular importance as it is the most prevalent type of OA [84] and its incidence is expected to increase due to obesity and trauma [84]. Furthermore, currently there is a lack of successful treatments for knee OA, most therapies target symptoms or late stage knee replacement surgery [85]. There is a need to better understand the pathology during knee OA to create better treatments that address disease progression.

Knee joint OA has been labelled as a 'whole-joint' or organ disease due to the wide range of intra-articular tissues that are affected with this pathology [6] (Figure 1.6). In OA articular cartilage, an imbalance between anabolic and catabolic activity result in ECM degradation, inhibition of new ECM formation and consequent cartilage degradation [86-88]. In the affected periarticular bone, there is an increase in bone remodelling, thickening of the subchondral plate and bone attrition and cyst formation due to endochondral ossification [88-90]. The synovium has also shown significant pathological changes in OA, even before cartilage degeneration, including infiltration of macrophages, lining hyperplasia and fibrosis, and production of pro-inflammatory cytokines [91]. These catabolic and proinflammatory mediators then in turn affect adjacent cartilage by promoting ECM degradation [92]. Lastly, the meniscal degeneration in the form of meniscal tears and weakening of the structural properties is believed to be a cause [93] and consequence of OA. Aetiology and risk factors of OA are numerous, however some pathological changes in OA have been attributed to fractures, including intra-articular fractures in the cartilage [86] and microfractures in the subchondral bone [94], and also mechanical instability, such as meniscal tears [93] and ligament injuries [95].

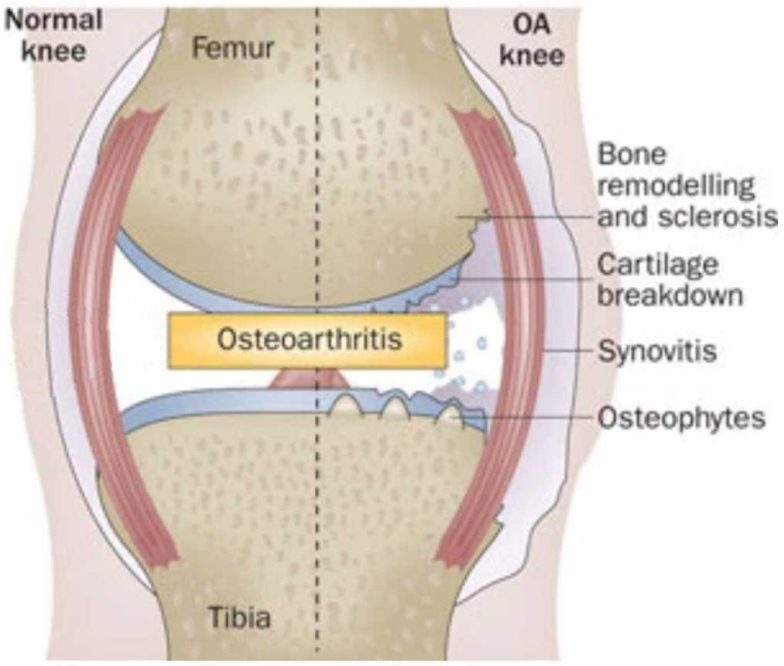

Figure 1.6 Pathological changes in the osteoarthritic (OA) knee joint organ. Pathology includes cartilage degeneration, bone remodelling, subchondral bone thickening, osteophyte formation, synovial inflammation, meniscal and ligament degeneration [6]. All knee joint tissues are affected, suggesting that OA is a disease of the joint as an organ. Image adapted from Wluka et al. [96].

1.7 The link between ligament trauma and knee osteoarthritis

Ligament injury is a major risk for knee joint OA development. Of all ligament injuries in the human knee joint, ACL tears are the most common [97] with a higher incidence of injury occurring in females compared to males [98]. Following diagnosis of an ACL injury, an average of 50% of patients developed OA in the 10 to 20 years following injury [99]. A high incidence, 51%, of radiographic knee OA was also found in female soccer players, 12 years after ACL injury [100]. In a study of patients with symptomatic knee OA that had knee joint magnetic resonance imaging, 22.8% had evidence of complete ACL rupture and most could not recall any trauma that would explain their knee injury [101].

Ligament injury and OA development has also been observed in animal models which could provide further insight into post-traumatic knee OA [102]. The most common model used to examine OA in animals are surgically induced models. ACL transection (ACLT) is the earliest model, which was developed in large animals such as dogs (Pond-Nuki model) [103] and resulted in cartilage degradation, osteophyte formation and meniscal fibrillation [103, 104]. Similarly,

post-traumatic OA following ACLT has also been shown in mice, leading to severe joint instability and the marked features of OA including cartilage degeneration and osteophyte formation, as well as increase in MMP13 and COLX [105, 106]. The destabilisation of the medial meniscus (DMM) most usually performed in rodents is another common model for knee joint OA induction in which the medial meniscotibial ligament is transected [107]. These studies postulate a direct link between ACL injury and OA. It remains unclear if OA development could precede ACL injury and whether the ACL is an active contributor to the pathogenesis of knee OA [6].

1.7.1 Joint organ injury response and ligament pathology

Studies on post-traumatic OA demonstrate an intricate whole joint organ response, which could reveal pathways and potential crosstalk between neighbouring tissues that drive OA progression.

Whole joint response post-ligament trauma include an inflammatory response marked by proteoglycan deposition [108] and MMP upregulation [109, 110]. An increase of proteoglycan levels has been reported in the human knee joint synovial fluid following ACL or meniscal rupture in the initial 3-4 weeks after rupture which remained elevated for up to four years [108]. A change in proteoglycan composition was also observed in the healing MCL of rabbits, most notably a decrease in decorin content and an increase in biglycan [111]. Changes in proteoglycan composition, particularly decorin and biglycan, have been shown to change ligament mechanical function [79, 80] as previously mentioned (Section 1.5).

MMPs are involved in the inflammation and proliferation phase of ligament healing to promote matrix turnover [112]. In pigs, after ACLT, MMP-1, MMP-13 and ADAMTS-4 expression were upregulated in the transected ligament [109]. ADAMTS-4 is another matrix degrading enzyme which is also expressed in cartilage in the early stages post-ligament injury driven by pro-inflammatory markers [113]. Wright et al. tested the role of MMP-12 in MCL wound healing with MMP-12 deficient mice [110]. Following MCL transection, MMP-12 deficient mice had delayed MCL repair resulting in lower recruitment of macrophages, and lower ultimate force and stiffness at earlier time points but not at later time points [110]. This would suggest that MMP-12 plays a role in MCL post-trauma particularly at early stages by influencing the inflammatory response. MMPs were also involved in the early stages of spontaneous OA and ligament degeneration [114], which will be discussed in Section 1.8. These findings would further suggest similarities in the pathways affected during spontaneous and post-traumatic OA.

Whilst there have been many studies showing the consequential increase of proteoglycans, growth factors and MMPs in cartilage post injury, very few have studied the direct interaction of ligament with other tissues and this remains the biggest question in the role of ligament pathology in conditions such as OA. A recent study by Chinzei et al. has given insight into the crosstalk between ACL remnants and chondrocytes obtained from OA patients [115]. Periostin, an ECM protein expressed in many tissues, was highly expressed in torn ACLs along with MMP-13 and ADAMTS-4 [115]. Additionally, in a co-culture *in vitro* system, ACL remnants had an effect on the expression of anabolic and catabolic genes in chondrocytes [115]. Furthermore, transforming growth factor (TGF)-β1 treatment had no effect on periostin expression, meanwhile interleukin (IL)-1β inhibited periostin expression [115]. Hence ACL remnants can have a direct effect on chondrocyte matrix turnover. This research opens the gates for further studies on direct ACL crosstalk with cartilage and other surrounding tissue.

The direct involvement of the ligament post-traumatic injury and in secondary OA remains poorly understood, though there is clear proteoglycan deposition [108] and MMP upregulation [109, 110] occurring in the synovial fluid following ligament injury. New research on ligament crosstalk revealed that ligament remnants might play a bigger role than previously expected [115]. Future research should focus on ligament crosstalk as well as similarities and differences between post-traumatic and age-related spontaneous OA.

1.8 OA and ligament pathology

1.8.1 Ligament pathology in early stages of spontaneous OA

Several studies have suggested that age-related ligament degeneration precedes cartilage degeneration in the early stages of spontaneous OA [114, 116]. One of the first studies in this area, studied the effects of collagen remodelling of the ACL in the STR/ort mouse model [114]. The STR/ort mouse strain is a well-recognised model for spontaneous OA [18], with similarities to human OA, including cartilage lesions, bone sclerosis, osteophyte formation and the presence of MMPs and aggrecanase [117, 118]. Collagen remodelling in the STR/ort ACLs was found to be present before macroscopic and radiological signs of knee joint OA, and the collagen remodelling was associated with higher levels of MMP-2, a metalloproteinase involved in matrix remodelling [114]. This study was the first to suggest that pathological and degenerative changes can occur in the ACL prior to OA signs in other articular tissues.

Early cruciate ligament degeneration was further studied in the early stages of OA in the Dunkin Hartley guinea pig spontaneous OA model compared to the normal Bristol strain 2 [116]. This OA model consistently develops cartilage degeneration in the medial tibial plateau at nine months, and other OA symptoms including calcification of the collateral ligaments at 22 months [119, 120]. Quasnichka et al. measured an increase collagen turnover in the ACLs (particularly MMP-2) which preceded both bone and cartilage pathology [116, 121]. In both of the STR/ort murine model and Dunkin Hartley guinea pig model, ligament collagen remodelling and ligament mechanical function was affected in age-related early stages of OA development.

Naturally occurring ACL degeneration has been observed in canine breeds with a high risk of cruciate ligament rupture [122] leading to eventual OA development [123]. Similar to the murine and guinea pig spontaneous OA models [114, 116] higher pro-MMP2, immature cross-links, total GAGs and water content were found in ruptured cruciate ligaments compared to intact ligaments [122]. Following these studies, ultrastructural differences in the cruciate ligaments from high and low- risk canine models were also analysed [124, 125]. Canine breeds with high risk of ligament rupture had significantly smaller collagen fibrils [124] and intercondylar notch spaces [125] compared to those from low-risk breeds. Knee laxity is believed to contribute to smaller intercondylar notch spaces [125], resulting in impinged areas of the ACL, which had elevated levels of MMP-2 and sulphated GAGs [124]. Additionally, fibrocartilaginous markers were present in ligament and tendon enthesis and these markers had higher expression in the canine breeds with a low risk of ligament rupture [124] mirroring similar findings to that seen in the spontaneous guinea pigs [116] and mice [114]. This could suggest that the fibrocartilaginous markers have a protective effect on canine ligament rupture.

Similar findings of ligament degeneration have also been observed in human knee joints. Hasegawa et al. analysed 120 human ACL and cartilage samples obtained from post-mortem tissue banks [126]. ACLs and cartilage from these joints were histologically scored for inflammation, chondroid metaplasia, cystic changes, collagen fibre orientation, and mucoid degeneration [126]. Ligament degeneration correlated with cartilage lesions and ageing and furthermore in a certain subset of patients ACL degradation preceded cartilage lesions [126]. Ligament degeneration was associated with ligament sheath (synovial membrane) inflammation, including hyperplasia, inflammatory cell infiltration and synovial stroma formation [126]. Furthermore, ECM disorganisation in the ACL occurred before synovial inflammation in some young donors without any history of knee trauma, and mucoid degeneration was highly prevalent in all ACLs [126]. Several studies have found similar results of degeneration in the PCL [127,

128]. These results support the findings from the animal models and suggest that age-related degeneration of the ACL can occur in the early stages of OA prior to articular cartilage changes but its contribution to the pathogenesis of knee OA is unknown.

1.8.2 Ligament pathology in the late stages of OA

Several studies have revealed several underlying cellular and extracellular changes occurring in the ligaments in the late stages of OA [129, 130]. In many of these studies the origin of OA (post-traumatic or spontaneous) is unclear, however these studies present clues of potential mechanisms driving ligament degeneration and OA pathology.

Hasegawa et al. characterised the cellular and ECM changes in human ACLs at all stages of OA development [129]. Ligament total cell density was greatly reduced in the ACL of aging donors but increased in the degenerated ACLs of donors with severe cartilage degeneration and OA [129]. This finding was due to perivascular accumulation of cells and cell aggregates in sites of degeneration [129]. The perivascular cells had a 'fibroblast-like' phenotype and had hematopoietic markers suggesting recruitment of bone marrow-derived fibrocytes [129]. The other cell aggregates had a 'chondrocyte-like' phenotype and expressed SCX (tendon or ligament marker), SOX9 (a major transcription factor in chondrogenesis) and RUNX2 (a regulator of chondrocyte hypertrophy) [129]. Moreover, there was increased MMP expression (MMP1, MMP3, and MMP13) in the degenerated OA ACLs originating from the chondrocyte-like cells as well as COL2 and collagen type III, and X production [129]. All of these markers increased with OA severity suggesting abnormal differentiation of resident ACL cells was driving irregular ECM production during OA. The presence of SCX and SOX9 was also confirmed in the ACL and PCL of OA patients in a separate study by Kumagai et al. [131].

MKX, another transcription factor with specificity for tendons and ligaments as previously described (Section 1.4) is also involved in OA progression [130]. Nakahara et al. analysed ACLs from OA patients greater than 60 years-old with a mild to severe grade of knee joint cartilage scoring and found that the presence of MKX-positive cells were significantly reduced in areas of collagen fibre degeneration [130]. ACL fibroblasts *in vitro* showed that IL-1β suppressed MKX expression and reduced collagen type I alpha 1 and tenascin-XB (an ECM glycoprotein which regulates collagen fibrillogenesis) expression and upregulated SOX9 expression [130]. These findings offer a potential mechanism for MKX suppression, driven in part by pro-inflammatory cytokines such as IL-1β.

BMPs, members of the TGF-β family of growth factors, are also involved in ligament degeneration and OA progression [132]. Ruschke et al. found significantly reduced levels of BMP-2 target genes ID1 and SMAD6 in fibroblasts isolated from the ACL of OA patients compared to non-OA fibroblasts, suggesting that OA might modify BMP-2 signalling pathways [132]. In addition, in the ACLs of patients undergoing knee replacement surgery there were a high percentage of calcium deposits in 64.4% of all ACL samples, however calcification was not correlated to ACL degeneration [132]. Though BMP-2 signalling is affected in OA ligaments, the role of BMP-2 signalling in calcium deposition and OA remains unclear.

Other cellular changes reported in the cruciate ligaments of OA patients include loss of innervation [128]. Neurofilaments were absent in 40% of ACLs taken from OA patients undergoing knee replacement surgery [128]. In addition, nociceptive (pain) sensors in the ACL decreased significantly in OA patients and also following injury [133]. However, effects on innervation can vary based on the ligament; another study found no changes in neurofilaments in PCLs from OA patients compared to healthy ligaments obtained post-mortem from patients with no history of joint disease [134]. Loss of innervation in the PCL has been reported including 65% of neurovascular bundle degeneration in the PCL from OA patients undergoing knee replacement surgery [135]. Another study showed that nociceptive (pain) sensory innervation remained constant in the PCL of OA patients, even during loss of overall innervation [136]. Loss of innervation can occur concurrently with OA progression, however its contribution to joint disease progression and the driving forces in this deficiency should be explored further.

In summary, cellular changes in the ACL in the late stages of OA included an increase in ‘chondrocyte-like’ cells [129], reduction of MKX-positive cells [130], reduction of BMP2-signalling [132] and reduction of neurofilaments [128]. Hence pathological changes in the ACLs in the late stages of OA are associated with changes in the fibroblast cell population. The cause of these cellular changes remains unknown as well as if these cellular changes actively contribute to disease progression.

1.8.3 Ligament mechanics associated with OA

Impaired mechanical properties of ligaments in the spontaneous OA animal models has been confirmed [114, 116]. In the spontaneous OA STR/ort mice knee joints, the ACLs had a lower ultimate load at failure than healthy control mice populations (CBA mice) in the early stages of OA [114]. In the spontaneous OA Dunkin Hartley guinea pig model, there were no significant

differences in the ultimate load at failure of the ACL compared to non-OA populations (Bristol Strain-2) [116]. However at physiologically-relevant loads, critical deformation of the ACL, a measure of laxity, was significantly greater than the non-OA controls before evidence of cartilage degeneration [116]. A study on mechanics of the ACL of dog breeds found a slightly weaker ultimate load to failure and significantly greater knee joint laxity in dogs at a high-risk of ligament rupture compared to breeds with lower-risk of ligament rupture [137]. These spontaneous OA animal models demonstrated early changes in the ligament mechanical properties occurring before cartilage degeneration and suggest that ACL mechanical properties may be important for spontaneous knee joint OA pathology.

Knee ligament and joint mechanics in humans also change during OA progression. Hagena et al., compared ACLs and PCLs taken from patients undergoing knee replacement surgery due to OA, rheumatoid arthritis and 'healthy' non-OA and non-rheumatoid arthritis patients [138]. A decrease in stiffness and ultimate load at failure was found in the OA ACLs and PCLs, along with an increase in viscoelastic stress-relaxation [138]. This decrease in stiffness and ultimate load is similar to the mechanical functions of ACLs seen in the spontaneous OA animal models, and similarly suggests that these mechanical properties are compromised during OA progression.

Changes in the mechanical properties of ligaments during OA varies in other knee ligaments [139, 140]. Varus and valgus laxity, indicators of MCL and LCL laxity, measured *in vivo* with a dynamometer did not change in OA patients compared to healthy non-diseased knee joints [139]. However, some studies have found an increase in the stiffness of MCL and LCL, measured *in situ* in cadaveric knee joints from OA patients compared to non-OA cadaveric knee joints [140]. These findings indicates that changes in ligament stiffness during OA can occur in extra-articular ligaments and not only in the ACLs [138].

In summary, ligament mechanical tensile strength and viscoelastic properties are altered during OA progression [114, 138]. However, many of the viscoelastic properties mentioned previously (strain rate sensitivity, creep and hysteresis) (Section 1.5) have been largely unreported in OA ligaments. In addition, understanding the underlying driving factors affecting these mechanical changes and potential mechanotransduction pathways remain relatively unknown. For further understanding, both ECM composition and mechanical properties and their relationship must be fully determined in healthy and OA ligaments.

1.8.4 Structural and signalling proteins involved in ligament function and secondary OA

Genetically modified animal models give insight into specific ECM markers and signalling proteins and their role in ligament function and consequent OA development. Murine joints of targeted collagen V-null mice had a phenotype similar to Ehlers-Danlos syndrome, characterised by joint hypermobility and premature OA formation [141]. Histological sections demonstrated cartilage degeneration in the lateral tibia of one-month-old mice from this model and later stages produced inflammation and osteophyte formation [141]. Additionally, irregular collagen fibril alignment in one-month-old mice resulted in fewer and larger collagen fibrils in the ACL midsubstance [141]. Mechanical properties of the ACLs in these mice also demonstrated significant decrease in elastic stiffness and modulus [141]. This study highlights the importance of collagen V in fibrillogenesis and of hypermobility as an initiator of OA.

SLRPs, such as biglycan and fibromodulin, are also important in collagen fibrillogenesis of ligaments and tendon [142]. Biglycan and fibromodulin double knockout mice had tendons with smaller collagen fibrils and decreased elastic stiffness, tendon ossification and resulted in premature OA in the knee joint [142]. Meanwhile, fibromodulin-null mice also had greater incidence of OA development which manifested in the form of ligament degeneration preceding cartilage degeneration [143]. Ligament cell morphology in the fibromodulin-null mice was also altered and the cells became more ‘chondrocyte-like’ and less fibroblastic, expressing high levels of lumican, another SLRP [143]. No collagen fibril abnormalities were noted within the cartilage at the same time as the ligament changes, indicating a distinct role of fibromodulin in ligament homeostasis.

The role of matricellular signalling protein NOV, also known as CCN3, was studied in NOV deficient mice [144]. NOV is normally expressed near the femoral enthesis of the collateral ligaments, as well as in the articular cartilage, menisci and synovial lining [144]. Deficiency of NOV resulted in OA-like pathology including joint abnormalities such as meniscal calcification, osteophyte formation in the lateral tibia, and articular cartilage degeneration [144]. Ligament degeneration was also noted, including complete degeneration of both cruciate ligaments and abnormal proteoglycan staining (safranin-O) possibly indicating fibrocartilage-like changes near the insertion sites and also in the synovium and collateral ligaments [144]. Since NOV is present in many tissues, it is likely a key signalling protein for the whole knee joint homeostasis, not specifically in the ligaments.

Other signalling molecules important in ligament function include hormones [82] and free radicals [145]. Hormones have been studied in OA development, due to the high prevalence of OA in the female population [82, 146] and the presence of oestrogen and progesterone receptors in the human ACL stroma [147]. Warden et al. tested the role of oestrogen and its receptors (ERα and ERβ) in the ACL and MCL of rats and mice [148]. In rats, oral gavage of ethynylestradiol, a synthetic oestrogen treatment, had no effect on the viscoelastic or tensile properties of the MCL or ACL [148]. Similar results were seen in the ERβ null mice which had no effect on the viscoelastic of tensile properties of the MCL or ACL [148]. These findings agreed with a similar study on knee ligaments of sheep where after 6 months of oestrogen administration, there was no difference in the mechanical strength of the ACLs [149]. Therefore, while gender may play a role in risk of ligament injury and OA in humans, it may not be due to oestrogen.

Nitric oxide, a free radical and gaseous signalling molecule, has also been associated to OA due to its role as a mediator of inflammation that can activate MMPs [150]. In normal canine ACL explants, higher nitric oxide production was found than the other collateral ligaments, likely to be due to the greater number of inducible-nitric oxide-synthase expressing cells [145]. Additionally after an inflammatory stimulus (composed of IL-1, tumor necrosis factor and lipopolysaccharides) nitric oxide production also increased in these canine cruciate ligaments which in turn activated MMP production [145]. This increase in nitric oxide production was not seen in the MCL or other ligaments [145]. It is suggested that nitric oxide production could play an important role in the ACL, particularly during inflammation leading to degeneration. The protective properties of nitric oxide on OA development have been noted in cartilage [151], but not in ligaments.

Understanding the role of ECM structural and signalling proteins, along with other signalling molecules such as oestrogen and nitric oxide and their relationship to ligament fibroblasts is integral to understanding ligament pathology. It is possible that these same pathways are involved in OA pathology. The differences and similarities in these pathways in secondary versus spontaneous OA could highlight important disease targets.

1.9 Hypothesis and aims

To comprehend the broader role of ligaments in OA development we must first characterise ligament composition and function in diseased and healthy knee joints. This thesis will address the hypothesis that cellular, ECM composition and mechanical properties are compromised in the early and late stages of OA in the cruciate knee joint ligaments of murine spontaneous and post-

traumatic OA models. This compromised cellular and ECM composition will be evaluated in cellular morphology, structural organisation and presence of ECM and cellular markers. Changes in mechanical function will be evaluated in the ligament viscoelastic properties. Characterising these histopathological and mechanical properties will give insight into the microenvironments in which ligament fibroblasts are exposed to during OA and furthermore changes in the early stages of OA could reveal potential disease driving factors. In addition, using murine models, this thesis will address OA aetiological differences through comparison between post-traumatic and spontaneous OA models. Similarities and differences in the cellular markers, ECM composition and mechanical properties were analysed in multiple murine OA models.

Our histopathological characterisation of ligament cellular and ECM markers was limited to specific markers and a currently incomplete understanding of ligament markers. To address this, this thesis explored the hypothesis that the ligament cellular makeup and fibroblast heterogeneity is more complex than has been previously demonstrated. For this hypothesis, the final goal was to identify specific fibroblast subpopulations and their potential roles in murine knee ligaments using unbiased high-resolution transcriptomics.

To summarise, the overarching goal of this thesis was to characterise the healthy and OA ligament markers and mechanics. With this goal in mind, the specific aims and objective of this study were the following:

- Determine changes in cellular and extracellular markers occurring in knee ligaments and surrounding tissues during the early and late stages of OA development in post-traumatic and spontaneous OA murine models.
- Characterise the viscoelastic and material mechanical properties of the ACL in the early stages of OA progression in post-traumatic and spontaneous OA murine models.
- Identify the cellular makeup, fibroblast subpopulations and their relevant markers in healthy murine knee ligaments using exploratory single-cell RNA-sequencing.

Chapter 2:
Pathological Changes in Ligament and Meniscal Tissues in Murine Spontaneous and Post-Traumatic Osteoarthritis

2.1 Introduction

In this chapter we looked at murine spontaneous and post-traumatic OA models to further explore meniscal and knee ligament pathology during early and late stages of OA development. The spontaneous OA murine model analysed was the STR/ort mouse strain [152], and the post-traumatic OA models included a destabilisation of the medial meniscus (DMM) mouse model [107] and a non-invasive mechanical trauma model [153]. In addition, we also characterised knee OA progression in a novel spontaneous OA murine model: the CD1 mouse strain [154].

2.1.1 Spontaneous OA murine models

In spontaneous OA models, OA develops as a natural part of the ageing process, classified as primary or idiopathic OA [102]. OA in these mice models mimic non-traumatic OA in humans, thought to be a result of aging, wear and tear and other risk factors [102]. The STR/ort mouse is known to exhibit early-onset spontaneous OA with high incidence and severity, and reproduces features of human knee OA such as proteoglycan loss, cartilage fibrillation, osteophyte formation and subchondral bone thickening [152, 155-159]. Meniscal and collateral ligament changes have been briefly reported in STR/ort mice, including ossification in the medial meniscus [152] and a positive association between MCL calcification and OA development [160]. In STR/ort cruciate ligaments, collagen remodelling and lower mechanical strength have been reported [114].

A new spontaneous OA mouse model (CD1) has recently been reported [154]. These mice develop OA-like symptoms at 1 year of age which include cartilage erosion of the medial femoral condyle, subchondral bone damage, osteophyte formation and meniscal degeneration [154]. There is currently no literature about changes to knee ligament pathology in the CD1 mice knee joint, and no description of pathological changes in early stages of OA development.

2.1.2 Post-traumatic OA murine models

Post-traumatic OA models offer a diverse aetiology of OA development in comparison to spontaneous OA models [161]. The induction of OA is well described in the murine DMM post-traumatic model, induced by surgical transection of the meniscotibial ligament and resulting in moderate-to-severe lesions mainly in the medial compartment by 8 weeks post-trauma [162, 163]. A more novel post-traumatic OA model is the non-invasive mechanical trauma model which

results in a lesion in the femoral condyle and OA development within 6 weeks post-trauma [153]. To date, pathological changes in meniscus and knee joint ligaments are poorly described in these models of OA.

2.1.3 Hypothesis and aims

Past studies have shown changes in ligament function in the early stages of OA in mice [114] and changes in cellular phenotype in the late stages of OA in humans[129]. In this study, we hypothesized that changes in cellular phenotype and ECM occur in the ligament in the early stages of OA. To address this, the overall aim was to identify matrix and cellular pathological changes and biomarkers in knee ligaments and surrounding tissue during OA development. Each of these aims will be assessed in individual murine models of post-traumatic and spontaneous OA.

Aim 1: Our first aim was to explore changes in knee ligament and meniscal tissue organisation and cell morphology during OA disease progression. To do so, we used histological staining techniques such as toluidine blue to look at fibre organisation, alignment, hyperplasia, cell morphology and general proteoglycan deposition. Picrosirius red (PR) staining was also used to determine collagen birefringence and fibre organisation. All these staining techniques were compared at different stages of OA disease progression.

Aim 2: Our second aim was to further expose potential underlying mechanisms driving pathological changes using specific OA and tissue biomarkers. This was achieved using immunohistochemistry for specific cellular and matrix biomarkers of chondrogenesis (COL2, transcription factor SOX9), hypertrophy (transcription factor RUNX2), and ligament proteoglycan (asporin).

Aim 3: Our third aim was to confirm if pathological changes to ligament and menisci could also be detected in a novel OA model. For this aim, we used a new spontaneous OA model (CD1 mice) and analysed ligament and meniscal pathology using histological staining, immunohistochemistry and micro-computed tomography (μCT) imaging. μCT imaging was used to quantify tissue mineralisation of the joint space during disease development.

Aim 4: OA pathology is diverse and can originate in different ways, hence our final aim was to determine if diverse OA models affected meniscal and knee ligament pathologies differently or similarly. To do so, we compared histopathological results from murine OA models of spontaneous and post-traumatic OA.

2.2 Materials and Methods

2.2.1 *In vivo* study design and tissue collection

Murine OA models used in this study included an established spontaneous OA model (STR/ort), a novel spontaneous OA model (CD1), a non-invasive post-traumatic OA model (joint loading) and a surgically induced post-traumatic OA model (DMM) (see Table 2.1). All mice were kept in polypropylene cages, subjected to 12-hour light/dark cycles, at 21±2˚C and fed standard diet ad libitum. All procedures complied with Animals (Scientific Procedures) Act 1986 and local ethics committee.

Table 2.1 Murine spontaneous and post-traumatic OA models used in Chapter 2. This included two spontaneous OA models (STR/ort and CD1) and two post-traumatic OA models (DMM and non-invasive-loading). Murine strain, gender, age, and control group are detailed.

Type of OA	Murine strain, gender	Age (#)	Control (#)
Spontaneous OA	STR/ort, male	26-week-old (n=7) 40-week-old (n=14)	26-week-old CBA (n=6) 40-week-old CBA (n=6)
	CD1, male	24-week-old CD1 (n=10)	12-week-old CD1 (n=10)
Post-traumatic OA	DMM, C57CBA male	18-week-old (n=12)	18-week-old contralateral (n=12)
	Non-invasive loading, C57BL/6J male	14-week-old (n=11)	14-week-old C57BL/6J (n=8)

2.2.1.1 STR/ort and CBA mice

Male STR/ort mouse samples were provided by Professor Pitsillides at the Royal Veterinary College, London, UK. Two time-points of STR/ort mouse tissues were collected: 26-week-old (n=7) and 40-week-old (n=14) (Table 2.1). As this is a spontaneous OA model, a wider variation in OA severity was expected. This age range gave the full extent of OA development encompassing a range of severity grades of disease (OARSI score range from grades 2 to 6) [152, 155-159]. For toluidine blue, PR and immunohistochemical staining analysis, STR/ort samples were categorised based on OARSI cartilage grade and compared to aged-matched healthy male CBA mice (Charles River, UK; n=6 per group) (for OARSI scoring see Section 2.2.5).

2.2.1.2 DMM mice

DMM mice knee joints were provided by Professor Bou-Gharios from the University of Liverpool. Surgical destabilisation of the medial meniscus was performed on the right knee joint in 10 week-old male C57CBA F1 mice (Charles River, UK; n=12) (Table 2.1) as described previously by Glasson et al. [107]. Anaesthesia was induced by injection of 10 μL/g of Hypnorm®/Hypnovel® (at a ratio of 1:1–4 parts water), the right knee joint cavity was accessed via a medial incision. The meniscotibial ligament was transected, resulting in the release of the medial meniscus from its tibial attachment. After transection, the skin was sutured and mice were immediately transferred to a heated post-operative recovery room. After surgery, mice received buprenorphine hydrochloride (Vetergesic; Alstoe Animal Health, York, UK) subcutaneously post-surgery and monitored daily to ensure good health. DMM knee joints were analysed at 8 weeks post-surgery and compared to the contralateral knee joint (left leg) of the same mice (n=12) (Table 2.1). Procedures were approved by the local ethics committee (project license: 709047).

2.2.1.3 Non-invasive mechanical loading mice

Samples from mice following non-invasive mechanical loading mice were provided by Dr. Poulet (University of Liverpool). The right knee joint of eight-week-old C57BL/6J mice (Charles River, UK) (Table 2.1) were loaded repetitively as described previously [153], using a regime that induces progressive AC lesions. Axial compressive loads were applied by a servo-hydraulic materials testing machine (Model HC10, Dartec, UK) via custom-made cups that hold knee and ankle joints flexed and the tibia vertically. The loading pattern consisted of a trapezoidal wave, with peak 9N loads for 0.05 seconds, rise and fall times 0.025 seconds each and baseline hold time of 9.9 seconds at 2N. Forty cycles were applied in each loading episode, and six loading episodes over a period of two weeks were applied. Knee joints were collected at 4 weeks after the last loading episode (n=11), to determine short-term histopathological changes following OA initiation. C57BL/6J male mice at 14 weeks of age were used as age-matched controls (n=4 per group). Procedures were approved by the local ethics committee (project license: P267B91C3).

2.2.1.4 CD1 mice

Male CD1 outbred mice were purchased from Charles River, UK and then housed in the specific pathogen free biological services unit at the University of Liverpool, UK. These mice have been recently shown to develop spontaneous OA after 24-weeks of age [154]. For comparison, a younger (12-week-old) group was compared to an older (24-week-old) group (Table 2.1). Young male 12-week-old CD1 mice were euthanized upon arrival (12-week-old group, n=10) and the remaining were aged for 12 more weeks (24-week-old group, n=10).

2.2.2 Murine tissue preparation

At the time points mentioned above, mice were killed by cervical dislocation for immediate tissue collection. Firstly, skin was removed and hindlimbs were detached near the hip joint. Muscles surrounding the knee joint and femur and tibia were carefully trimmed and removed. Knee joints were fixed in neutral buffered formalin for 24 hours, washed in water and stored in 70% ethanol. CD1 mouse knee joints were then scanned for µCT to evaluate joint mineralisation (see Section 2.2.5). For histological examination, STR/ort, non-invasive mechanical loading and CD1 mouse knee joints were decalcified with 10% formic acid (Sigma) for 1-2 weeks. DMM mouse knee joints were decalcified with 10% ethylenediaminetetraacetic acid (EDTA) (pH 7.4) (Sigma) for 3 weeks. After decalcification, all samples were washed, dehydrated and processed for wax embedding. Knee joint samples were paraffin embedded coronally and sequentially sectioned at 6µm across the entire joint.

2.2.3 Histological staining

2.2.3.1 Toluidine Blue

Toluidine blue was used to assess pathophysiological changes in menisci and knee joint ligaments and for OARSI cartilage scoring in the CD1 mice knee joints (see Section 2.2.5). Protocol for Toluidine blue staining is similar to protocols previously published [153, 164, 165]. For the straining, a quarter of the sectioned histology slides across the joint were stained with toluidine blue at regular intervals (every fourth slide, about 100 µm). Slides were dewaxed and hydrated with xylene (5 min, x2), 100% ethanol, 90% ethanol, 70% ethanol, and distilled water (3 min each ethanol and water wash). Slides were then pre-conditioned with sodium acetate buffer (0.1M, pH 5.6) for 1 minute and stained with toluidine blue (0.1% toluidine blue in 0.1M solution of acetate

buffer, pH 5.6) for 15 minutes. After two washes with distilled water, slides were counterstained with 0.2% fast green for 5 seconds. Slides were washed with distilled water, and then dehydrated with acetone (x2, 10 seconds) and xylene (x2, 3 minutes) before being mounted with DPX (Sigma). Slides were imaged with a standard brightfield microscope (Nikon Eclipse Ci).

2.2.3.2 PR staining

PR staining can be used to evaluate collagen content and birefringence [166, 167]. Paraffin sections were dewaxed and hydrated with xylene (x2), 100% ethanol, 90% ethanol, 70% ethanol, and distilled water. Sections were stained in Weigert's haematoxylin (Stock A: 1% w/v hematoxylin in 95% ethanol, Stock B: 1.16% w/v ferric chloride in 1% v/v hydrochloric acid in distilled water, 1:1 ratio of stock A and stock B) for 8 minutes. Slides were washed with running water for 10 minutes. Following washing, slides were stained with PR (0.1% w/v sirius red in saturated aqueous picric acid, both from Sigma) for one hour and then washed with 0.5% v/v glacial acetic acid in distilled water for 3 minutes (x2), and dehydrated in 100% ethanol (x3) and xylene. Slides were then mounted in DPX (Sigma). Slides were imaged with a standard microscope with a polarised light analyser and an adjustable polariser (Olympus BX60), and images taken with brightfield for analysis of red collagen staining and with polarised light for analysis of collagen birefringence.

2.2.4 Immunohistochemistry

Immunohistochemistry was performed to localise expression of COL2, SOX9, RUNX2 and asporin (ASPN) (see Table 2.2), based on our published protocol [165]. COL2, SOX9 and RUNX2 markers were chosen to explore chondrogenesis and hypertrophy. As previously mentioned, these markers have been briefly described in human OA ACLs near 'chondrocyte-like' cells [129, 168, 169]. Furthermore, SLRP ASPN was chosen as it is a known inhibitor of chondrogenesis in cartilage and in OA [170], and a known ligament and tendon proteoglycan [171]. RUNX2 and ASPN immunostaining protocol could not be validated in the DMM knee joints, neither were expressed in any part of the DMM knee joints. This is likely due to differences in the histological tissue preparation of the DMM knee joints (EDTA) (see Section 2.2.2).

Histology slides were dewaxed and rehydrated with two washes of xylene (5 minutes each), followed by washes of 100% ethanol, 90% ethanol, 70% ethanol and distilled water (3 minutes each). PAP pen (Thermo) barrier was quickly drawn around each individual section.

For COL2 immunostaining, sections were preconditioned with 0.2M hydrochloric acid for 15 minutes at 37°C and then antigen retrieval was applied with pepsin (3mg/mL in 0.02M hydrochloric acid) for 45 min at 37°C. No antigen retrieval steps were performed for SOX9, RUNX2 and ASPN. All slides were then washed with PBS-T (PBS with 0.1% Tween, Sigma) and blocked for endogenous peroxidase with 0.3% hydrogen peroxide (Sigma) for 15 min at 37°C. Next, slides were washed with PBS-T and blocked for endogenous Avidin/Biotin binding with an Avidin/Biotin Blocking Kit (Vector Labs, SP2001).

Non-specific binding sites were blocked for 1 hour at room temperature with serum block of either mouse-on-mouse (MoM) blocking reagent (Vector Labs) (for mouse primary antibodies) or 10% goat serum (Vector Labs) in PBS-BSA for rabbit primary antibodies (see Table 2.2). Primary antibodies were incubated overnight at 4°C and included COL2 (1/100), SOX9 (1/1000), RUNX2 (1/1000), and ASPN (1/400). Negative controls included a mouse IgG (2µg/mL, Sigma) or rabbit IgG (1µg/mL, Vector Labs). All antibodies were diluted in PBS. Following washing (PBS-T), biotinylated secondary antibody (Vector Labs) was applied for 1 hour (see Table 2.2) and then washed again with PBS-T. Vectastain (Vector Labs) was then applied for 30 min and washed with PBS. Stains were developed with DAB Substrate Kit (Preoxidase) (Vector Labs), dehydrated and mounted with DPX mounting medium (Sigma).

Table 2.2 List of antibodies analysed with immunohistostaining. Antibody description and the corresponding antigen retrieval, serum block and secondary antibody used.

Primary Antibody (dilution)	Antigen Retrieval	Serum Block	Secondary Antibody
COL2 (1:100), Mouse monoclonal, (Thermo, MA5-12789)	Pepsin (Sigma, 10108057001)	MoM Block (Vector Labs, BMK-2202)	Anti-Mouse IgG (Vector Labs, BMK-2202)
SOX9 (1:1000), Rabbit polyclonal, (Millipore, AB5535)	No	10% goat serum in PBS-BSA (Vector Labs, S-1000)	Anti-Rabbit IgG (Vector Labs, BA-1000)
RUNX2 (1:1000), Rabbit polyclonal, (Abcam, ab23981)			
Asporin (1:400), Rabbit polyclonal, (Abcam, ab58741)			

2.2.5 OARSI scoring of cartilage degradation in CD1 mouse knee joints

CD1 mouse knee joints were graded using the OARSI cartilage scoring system [17]. Briefly, the scoring system is the following: grade 0 for normal articular cartilage, grade 1 for lesions in the superficial zone, grade 2 for lesions in the intermediate zone, grade 3 for lesions down to the tidemark and up to 20% of articular cartilage loss, grade 4 for 20-50% of articular cartilage loss, grade 5 for 50-80% of articular cartilage loss, and grade 6 for greater than 80% of articular cartilage loss and bone exposure [17]. Toluidine blue stained sections of the entire knee joint were scored for cartilage lesion severity in each knee compartment: medial tibia (MT), medial femur (MF), lateral tibia (LT) and lateral femur (LF). Using these calculations, the average mean and maximum lesion scores was calculated for each compartment and for the whole knee joint of each mouse. Summed scores of all the compartments were also calculated from the mean and maximum scores.

Statistical analysis was completed using GraphPad Prism (version 6, USA). The data was tested for normality using the Shapiro-Wilk normality test. Both 24-week-old and 12-week-old OARSI maximum and mean score did not pass normality (p-value = 0.0002). Hence an unpaired non-parametric Mann-Whitney test was used to compare the two separate 12-week-old and 24-week-old groups for the maximum and mean OARSI scores.

2.2.6 Micro computed tomography (μCT) for joint space mineralisation of CD1 knee joints

Cadaveric knee joints of the CD1 mice were analysed with micro computed tomography (μCT) to quantify joint space mineralisation which has been shown to increase with OA progression [165]. Knee joints of CD1 mice were scanned with a 4.5μm isotropic voxel size (50kV, 200μA respectively, 0.5mm Aluminium filter; 0.6° rotation angle, no frame averaging) using a Skyscan 1172 μCT scanner (Skyscan, Belgium). Hand-drawn regions of interests of the joint space including menisci (lateral and medial) and other mineralised tissues that were not part of the tibial or femoral bones. These regions of interests were analysed using 3D algorithms in CTAn (Skyscan, Belgium) (Figure 2.1) to provide the mineralised tissue volume (measured as Bone Volume on CTAn). Statistical analysis of mineralised volume comparing the different groups was first tested for normality using the Shapiro-Wilk normality test (GraphPad Prism). Joint mineralisation data for 24-week-old CD1 mice did not pass the normality test (p-value = 0.0005). Hence, an unpaired non-parametric Mann-Whitney test was used to compare the 12-week-old

CD1 mice from the 24-week-old CD1 mice. Three-dimensional models of the menisci were created using CTVox from the region of interest selected for mineralised tissue volume analysis (Skyscan, Belgium).

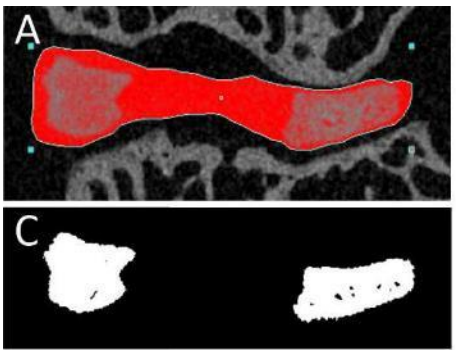

B

CT-Analyzer (CTAn) software task list for joint space analysis	
Thresholding	Global (50 to 250)
Despeckle	Remove white speckles in 3D space
	Volume less than 40 voxels
Despeckle	Remove black speckles in 3D space
	Volume less than 20 voxels
ROI shrink-wrap	Shrink-wrap in 3D space
	Stretch over holes diameter 12 voxels
3D analysis	Basic values

Figure 2.1 Micro computed tomography (µCT) analysis for measuring murine knee joint space mineralisation. (A) Region of interest around the menisci (red) was manually drawn from coronal µCT images. (B) A task list was optimized for processing and quantification of the region of interest. (C) The resulting menisci region of interest after thresholding was quantified. Image taken from Ramos-Mucci et al [165].

2.3 Results

2.3.1 Spontaneous OA STR/ort murine model

In the spontaneous OA STR/ort murine model, knee ligament and meniscal pathology were assessed to identify specific changes occurring during OA progression. Histopathological analysis included toluidine blue and PR staining to visualise cellular and ECM changes, as well as immunostaining to analyse specific marker pathological changes in the ACL, MCL and medial menisci. The collateral ligaments and menisci were analysed as they have been previously reported in the STR/ort mice to exhibit calcification [152] particularly in the medial compartment which is most affected in the STR/ort model [117]. The ACL was also analysed for pathological changes as it has been previously reported to show lower ultimate strength in the STR/ort model compared to healthy CBA [114]. STR/ort knee ligament and menisci were categorised by OARSI scoring of the cartilage degeneration, and compared to healthy aged-matched CBA controls, an OA-resistant mouse strain.

2.3.1.1 STR/ort mice anterior cruciate ligament (ACL) pathology

2.3.1.1.1 Toluidine blue staining

Toluidine blue staining in healthy CBA knee joints showed an organised ACL structure with aligned spindle-like cells and some dark-blue staining in the dense collagenous matrix of the ACL (Figure 2.2A). Rounded-cell morphology in the CBA ACLs was sparse and only apparent in the fibrocartilaginous tibial attachment region (Figure 2.2A, yellow arrow). Toluidine blue staining expanded as OA grade in the STR/ort mouse knee joints increased. In ACLs of STR/ort OA grade 2 mice, toluidine blue staining was present in the mid-ligament matrix and in the tibial attachment site or enthesis (Figure 2.2B, red arrows). In OA grade 4 STR/ort knee joints, toluidine blue staining encompassed the entire ACL and loss of fibre alignment and organisation was apparent (Figure 2.2C). Additionally, ACL fibroblasts had a rounded phenotype potentially indicating hypertrophy (Figure 2.2C, yellow arrows). Lastly, in OA grade 6, toluidine blue staining covered most of the ACL and hypertrophic-rounded cells were present near the tibial attachment site extending towards the ACL (Figure 2.2D, yellow arrows). STR/ort ACLs showed changes in fibroblast phenotype, fibre organisation and potentially matrix changes marked by toluidine blue straining which could indicate proteoglycan deposition.

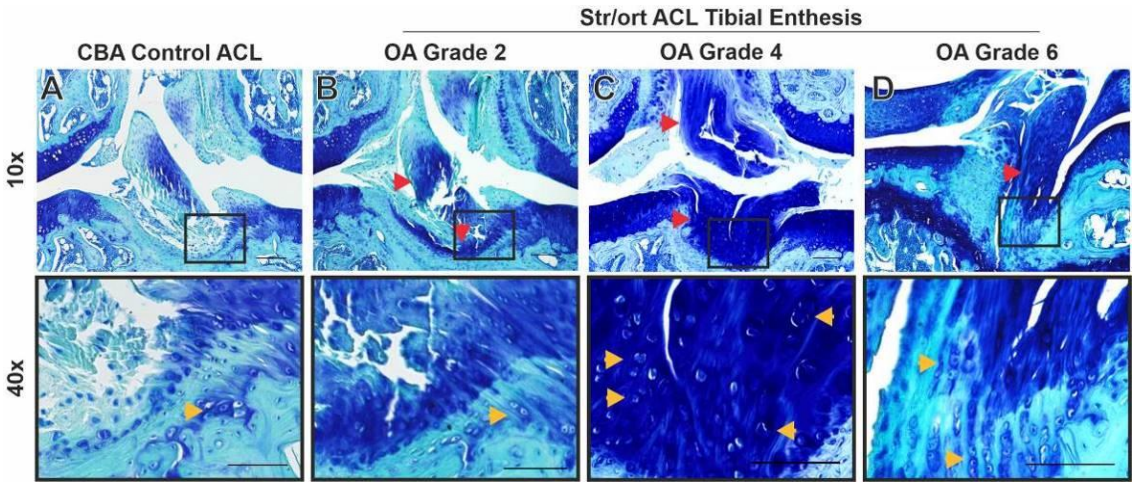

Figure 2.2 Histological staining of the anterior cruciate ligament (ACL) in STR/ort knee joints using toluidine blue. Representative images of: (A) Aged-matched CBA knee joints showed an organised ACL matrix and toluidine blue staining in the mid-ligament region. Rounded-cell morphology was only found in the fibrocartilaginous tibial enthesis region (yellow arrow). (B) OA grade 2 STR/ort ACL had toluidine blue staining at the tibial enthesis and the mid-ligament region (red arrows). (C) OA grade 4 STR/ort ACL had total toluidine blue staining in all regions of the ACL (red arrows) and evidence of rounded-cell morphology throughout the ACL (yellow arrows). (D) OA grade 6 STR/ort ACL demonstrated toluidine blue staining in the mid-ligament region (red arrow) and 'rounded' cell morphology near the tibial enthesis (yellow arrows). Scale bar is 100 µm (10x) and 50 µm (40x).

2.3.1.1.2 PR staining

PR staining was used to analyse collagen content and birefringence of the ACLs in STR/ort mice. Brightfield microscopy confirmed an organised structure and light red collagen staining in the CBA ACL (Figure 2.3A), additionally spindle-cell shaped fibroblast morphology was confirmed in the mid-ligament region of the ACL (Figure 2.3A, green arrow). In OA grade 2 STR/ort knee joints, ACL structure was similar, with some red collagen stain aggregation surrounding spindle-shaped fibroblasts in the ACL (Figure 2.3B, green arrow) and red collagen staining in the outer epiligament regions of the ACL. As OA grade increased, ACL fibre alignment changed and red collagen stain was evident in areas with rounded-cell morphology in the mid-ligament region of the ACL (Figure 2.3C, yellow arrows).

Polarised light microscopy revealed green birefringence in the mid-section of the ACL, indicative of thin fibres, and red-yellow birefringence at the outer epiligament areas, indicative of thicker collagen fibres (Figure 2.3A, blue arrow). In STR/ort ACLs red birefringence was apparent in the outer epiligament regions of the ACL in OA grade 2 (Figure 2.3B) and extended to the mid-ligament region at OA grade 4 (Figure 2.3C). Changes in collagen birefringence suggest thicker collagen fibrils in STR/ort ACLs, potentially indicative of coarser and closely packed collagens such as collagen type I.

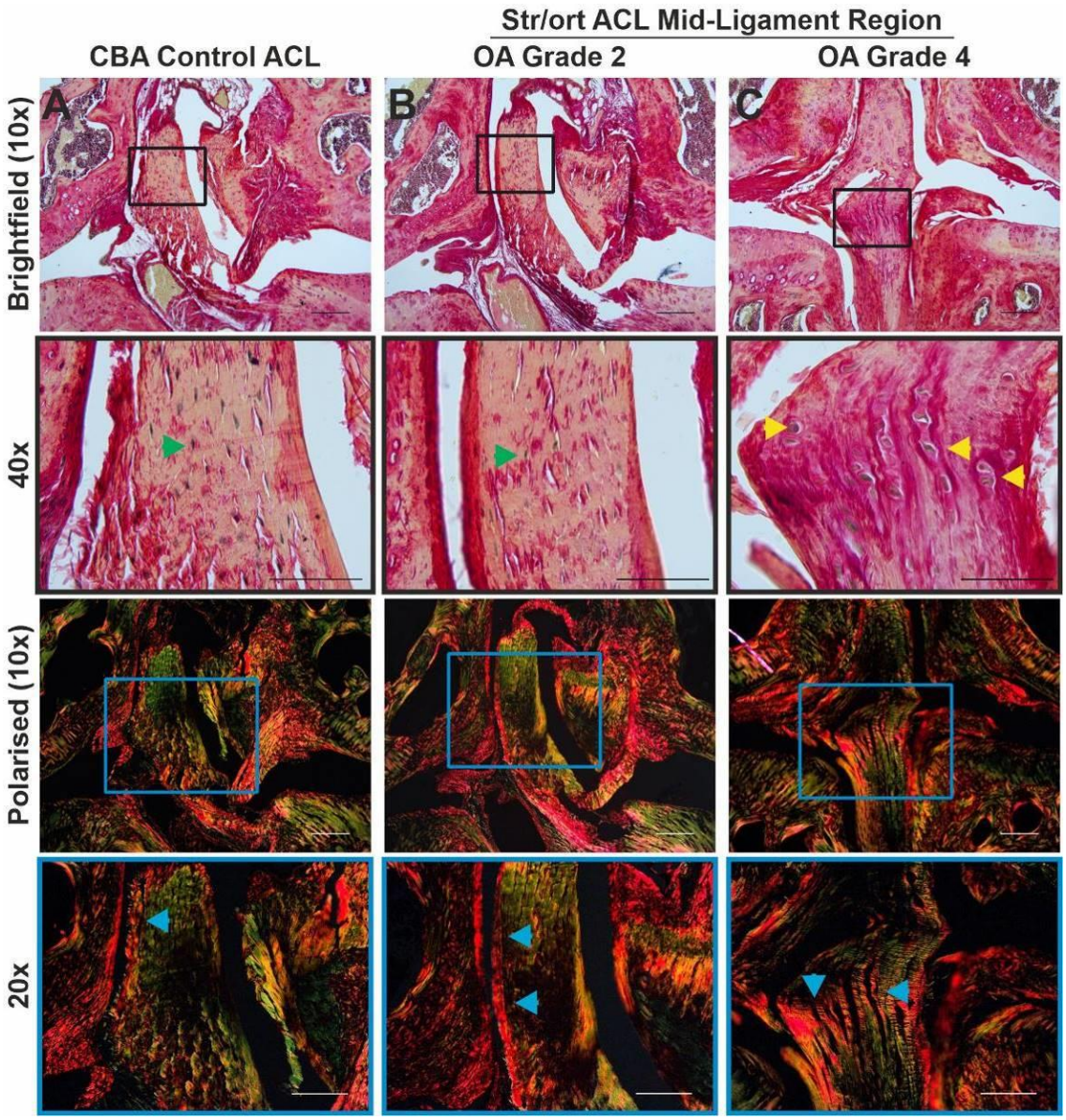

Figure 2.3 Histological staining of the anterior cruciate ligaments (ACL) in STR/ort knee joints using picrosirius red. Representative images of: (A) Aged-matched CBA knee joints had an organised ACL with light red collagen staining and spindle-shaped fibroblasts (brightfield, green arrow). Polarised light showed mainly green birefringence throughout the ACL with some red birefringence in the upper epiligament layer (polarised light, blue arrow). (B) OA grade 2 STR/ort ACL had sparse dark red collagen staining in the mid-ligament region and spindle-shaped fibroblasts (brightfield, green arrow). Red birefringence was found in the outer epiligament region of the ACL (polarised light, blue arrows). (C) OA grade 4 STR/ort knee joints had disorganised ACL fibre alignment and rounded-cell morphology in the mid-ligament region (yellow arrows). The mid-ligament region of the ACL also had dark red collagen staining (brightfield) and red birefringence (polarised light, blue arrows). Scale bar is 100 µm (brightfield and polarised light) and 50 µm (20x, 40x).

2.3.1.1.3 Immunostaining

Immunostaining confirmed changes in the ACL ECM and cellular markers in the OA STR/ort knee joint. We analysed immunostaining of COL2 expression in the ECM, SOX9 and RUNX2 cellular markers, and SLRP marker ASPN. As previously mentioned, these markers were chosen to analyse cartilage-related markers due to the rounded-cell morphology seen in the toluidine blue and PR staining.

Aged-matched CBA mice knee joints demonstrated COL2 expression in a thin layer of the fibrocartilaginous ACL-tibial enthesis region, as well as sparse SOX9, RUNX2 and ASPN expression at the ACL-tibial enthesis (Figure 2.4A, black arrows). Furthermore, in the ACL mid-ligament region of CBA knee joint, COL2, RUNX2 and ASPN were not expressed but some SOX9 expression was evident within spindle-shaped ACL fibroblasts (Figure 2.5A, green arrows).

In the diseased OA grade 2 STR/ort ACL-tibia enthesis, COL2 expression was evident in the insertion sites in similar locations to the toluidine blue staining (Figure 2.4B, black arrow). The ACL-enthesis also showed SOX9, RUNX2 and ASPN expression which extended from the enthesis to within the ACL (Figure 2.4B, black arrows). Looking further at the mid-ligament region of the OA grade 2 STR/ort ACL, showed no COL2, SOX9 and ASPN staining, and only sparse RUNX2 staining near the outer epiligament layer of the ACL (Figure 2.5B, green arrow).

In more severe OA grade 4 STR/ort mice knee joints, the ACL had COL2 deposition surrounding rounded-like cells near the ACL tibial enthesis (Figure 2.4C, COL2, black arrows) and at the ACL mid-ligament region (Figure 2.5C, COL2, black arrows). These changes also aligned with SOX9 and RUNX2 expression which manifested in the ‘rounded’ ligament cells throughout the ligament, and also ASPN expression which was mainly found in the mid-ligament region but not near the tibial enthesis (Figure 2.4C, Figure 2.5C). Overall, STR/ort OA ACLs showed COL2, SOX9 RUNX2 and ASPN expression particularly present in cells with rounded-cell morphology.

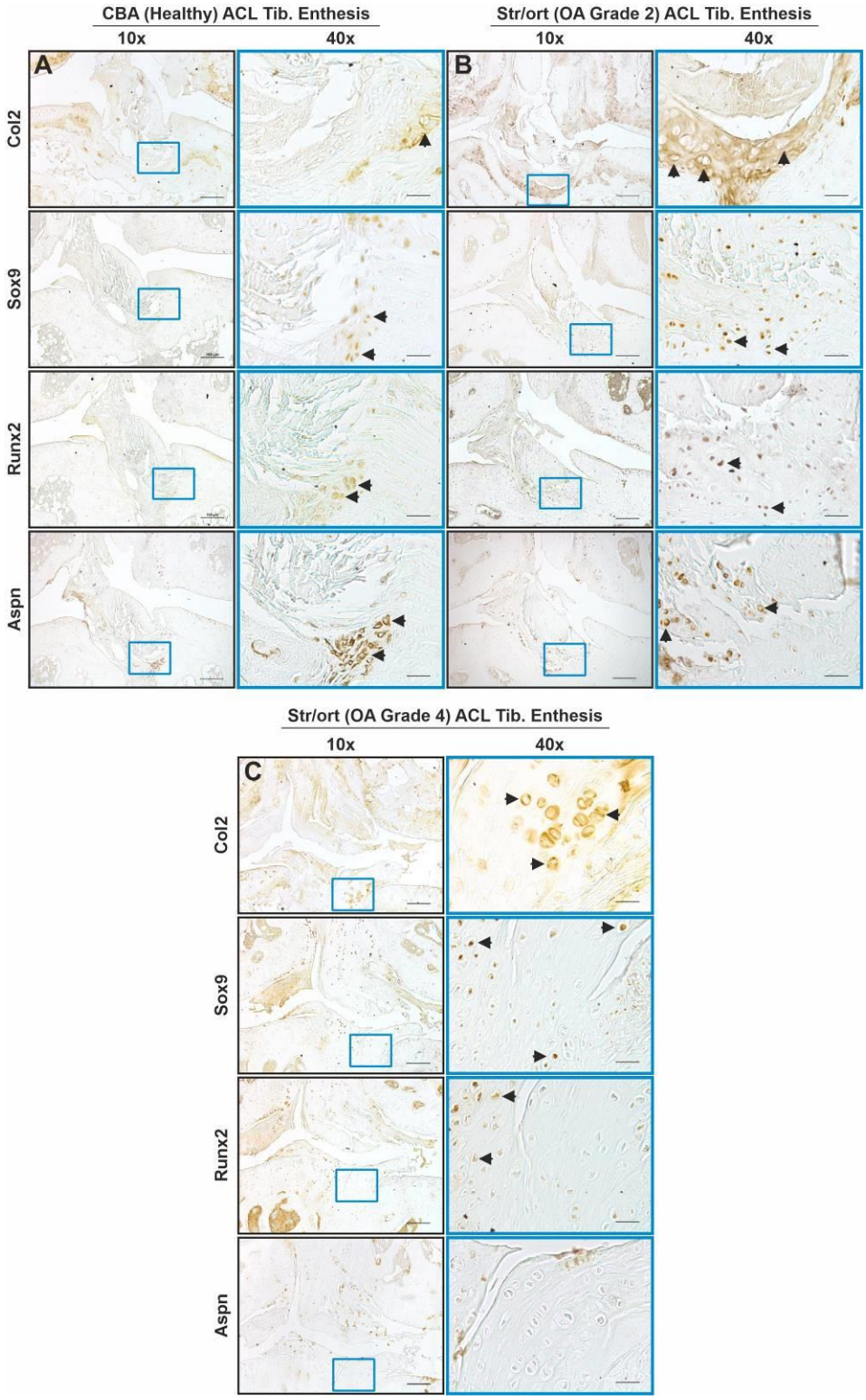

Figure 2.4 Immunostaining of the anterior cruciate ligament (ACL) tibial enthesis in STR/ort knee joints of collagen type II (COL2), SOX9, RUNX2 and ASPN expression. Representative images of: (A) Aged-matched CBA ACL tibial enthesis showed COL2, SOX9, RUNX2 and ASPN expression near the fibrocartilaginous tibial enthesis. (B) OA grade 2 STR/ort ACL showed COL2 deposition in the tibial enthesis, as well as SOX9, RUNX2 and ASPN expression. (C) OA grade 4 STR/ort ACL also had COL2 deposition, and SOX9 and RUNX2 expression near the tibial enthesis particularly in cells with rounded-cell morphology. Scale bar is 100 µm (10x) and 25 µm (40x).

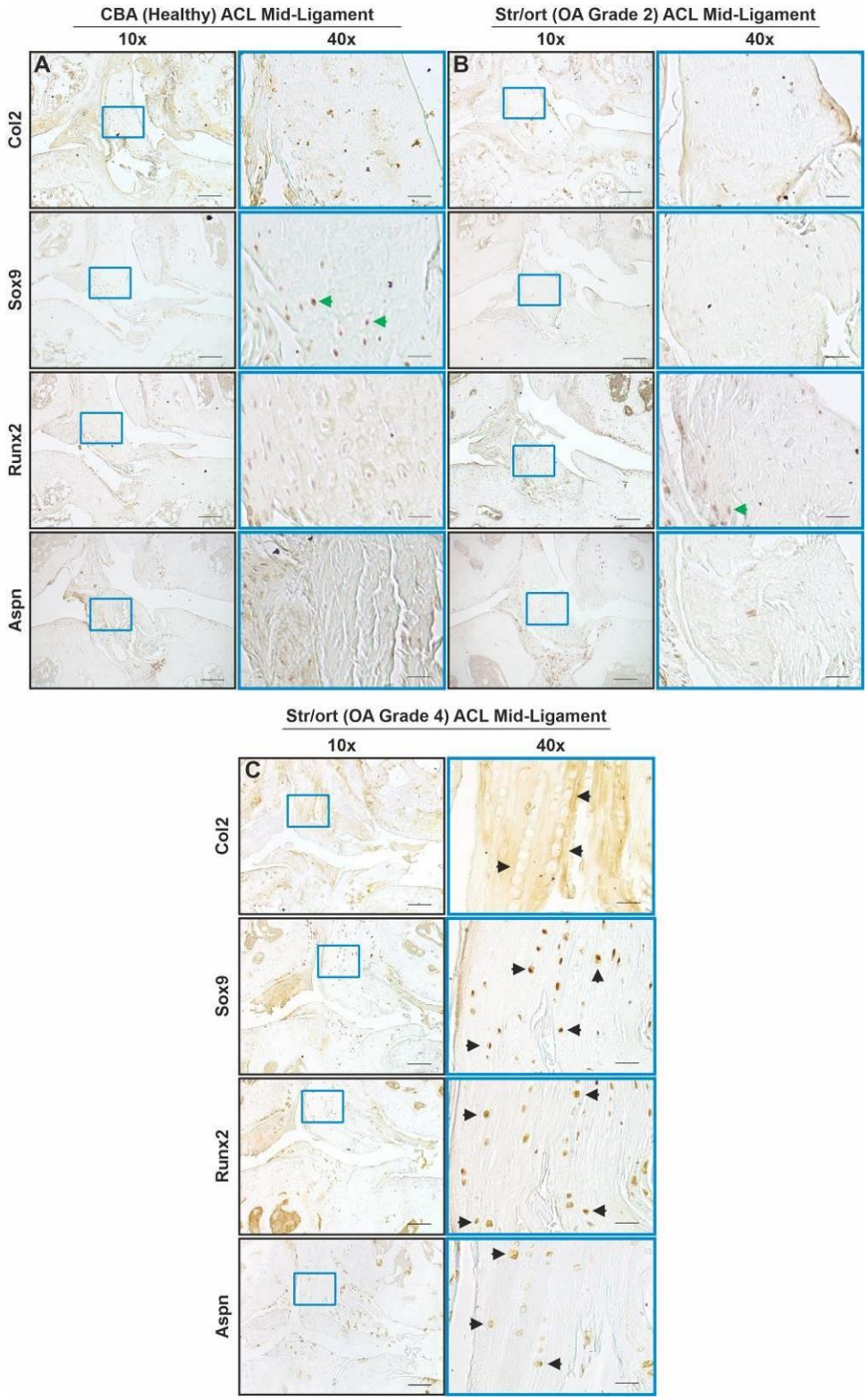

Figure 2.5 Immunostaining of the anterior cruciate ligament (ACL) mid-ligament region in STR/ort knee joints of collagen type II (COL2), SOX9, RUNX2 and ASPN expression. Representative images of: (A) Aged-matched CBA ACL mid-ligament region showed no COL2, RUNX2 and ASPN expression, and sparse SOX9 expression in spindle-like cells (green arrows). (B) OA grade 2 STR/ort ACL mid-ligament showed no COL2, SOX9 and ASPN expression, and some RUNX2 expression. (C) OA grade 4 STR/ort ACL mid-ligament region showed COL2 deposition, and SOX9, RUNX2 and ASPN expression in rounded-like cells (black arrows). Scale bar is 100 µm (10x) and 25 µm (40x).

2.3.1.2 STR/ort mice medial collateral ligament (MCL) pathology

2.3.1.2.1 Toluidine blue staining

Toluidine blue staining of the MCL in STR/ort knee joints was analysed and compared to healthy CBA knee joint. Toluidine blue staining of the CBA aged-matched control knee joint MCLs showed an organised femur-enthesis with ordered toluidine blue staining and rounded-cell morphology at the fibrocartilage zone (Figure 2.6A, yellow arrows), and a mid-ligament region with organised fibre alignment and spindle-shaped fibroblasts with little toluidine staining (Figure 2.6A, green arrow). In STR/ort knee joints with OA grade 2 the MCL had similar fibrocartilage region however fibre organisation near the femoral enthesis was disrupted and hypocellular (Figure 2.6B, green cross). In the MCL mid-ligament region of the OA grade 2 STR/ort knee joints, there were a small number of rounded and potentially hypertrophic cells encircled by toluidine blue staining (Figure 2.6B, yellow arrows). In OA grade 4 STR/ort knee joints, the MCL had toluidine blue staining (red arrows) and rounded-cell morphology (yellow arrows) near the femoral enthesis which extended throughout the MCL mid-ligament region (Figure 2.6C). In severe OA grade 6 STR/ort MCL, there was a clear increase in rounded-cell morphology (yellow arrows), hyperplasia, abnormal tissue formation, loss of fibre alignment and organisation, and evidence of endochondral ossification and mineralisation throughout the MCL (Figure 2.6D).

2.3.1.2.2 PR staining

PR staining analysed collagen birefringence in healthy CBA and OA STR/ort knee joint MCLs. CBA mice knee joints demonstrated MCLs with red staining and rounded-cell morphology (yellow arrows) near the femoral enthesis and at the fibrocartilaginous region, and spindle-shaped cells in the mid-ligament region of the MCL (Figure 2.7A). Polarised light verified green birefringence throughout the entire MCL, with some red-yellow birefringence, indicating thicker fibres, near the femoral enthesis (Figure 2.7A). OA grade 2 STR/ort knee joint MCLs were similar to the healthy CBA MCL, with red staining and red birefringence near the femoral enthesis region and green birefringence throughout the rest of the MCL (Figure 2.7B). In OA grade 4 STR/ort knee joints, red collagen staining and rounded-cell morphology (yellow arrows) increased in all regions of the MCL (Figure 2.7B). Polarised light confirmed changes in the collagen structure, showing red birefringence throughout the entire MCL, including near the femoral enthesis and in the mid-ligament region near the meniscal attachment (Figure 2.7B, blue arrows). This finding indicated thicker collagen fibres in the STR/ort OA grade 4 MCL.

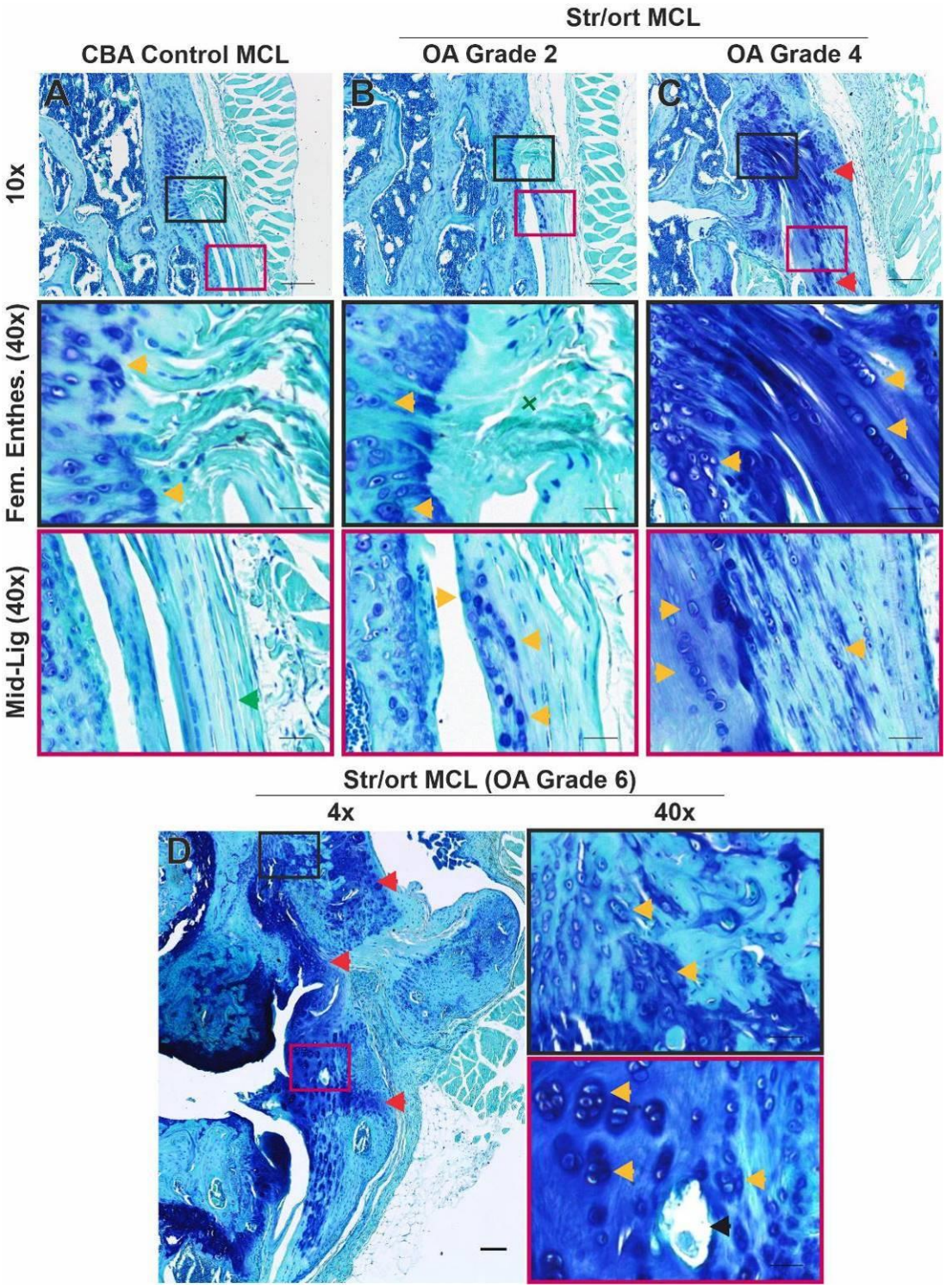

Figure 2.6 Histological staining of the medial collateral ligament (MCL) in STR/ort knee joints using toluidine blue. Representative images of: (A) Aged-matched CBA knee joints showed an organised MCL fibre structure with spindle-shaped fibroblasts (green arrow) and toluidine blue staining in the fibrocartilaginous region (yellow arrows). (B) In OA grade 2 St/ort knee joints, MCL fibre misalignment was evident and toluidine blue staining appeared in the mid-ligament region surrounding cells with a rounded morphology (yellow arrows). (C) In OA grade 4 STR/ort knee joints, toluidine blue staining (red arrows) and rounded-cell morphology (yellow arrows) was present throughout the MCL. (D) In severe OA grade 6 STR/ort knee joints, abnormal MCL structure included complete loss of fibre alignment, hyperplasia and evidence of mineralisation (black arrow). Scale bar is 100 µm (4x, 10x) and 25 µm (40x).

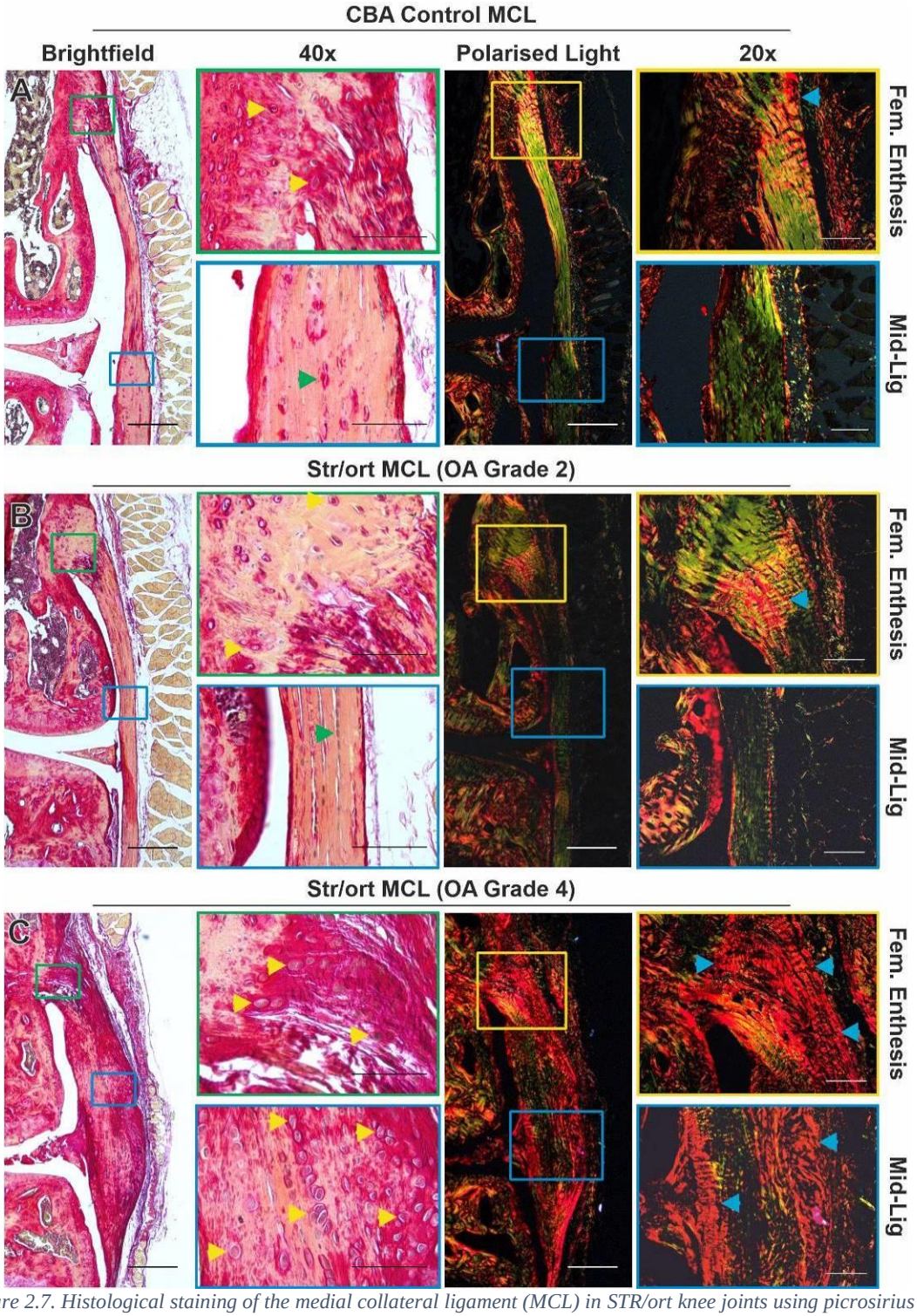

Figure 2.7. Histological staining of the medial collateral ligament (MCL) in STR/ort knee joints using picrosirius red. Representative images of: (A) Aged-matched healthy CBA MCLs showed light-red collagen staining, rounded-cell morphology (yellow arrows) at the fibrocartilage zone, and spindle-shaped cells (green arrow) in the mid-ligament region. Polarised light showed green birefringence throughout the MCL with yellow-red birefringence near the femoral enthesis (blue arrow). (B) OA grade 2 STR/ort MCL was similar, with yellow-red birefringence near the femoral enthesis (blue arrow) and green birefringence in the mid-ligament region. (C) In OA grade 4 STR/ort knee joints, dark red collagen staining was found throughout the MCL and corresponded with rounded-cell morphology (yellow arrows) and red birefringence (blue arrows) near the femur attachment site and in the outer epiligament layers of the MCL mid-ligament region. Scale bar is 200 µm (4x) and 50 µm (20x, 40x).

2.3.1.2.3 Immunostaining

Immunostaining of healthy CBA and OA STR/ort knee joint MCLs showed differences in matrix composition and cell marker expression. CBA MCLs had an organised COL2 expression (black arrow) at the fibrocartilage region of the MCL-femoral enthesis (Figure 2.8A). None of the markers (COL2, SOX9, RUNX2 or ASPN) were expressed in the mid-ligament region of the MCL in CBA mice (Figure 2.8A). In STR/ort knee joints with OA grade 2, COL2 aggregation at the MCL-femoral enthesis was also found in the fibrocartilaginous region, as well as some SOX9, RUNX2 and ASPN expression with extended from the femoral enthesis (black arrows) (Figure 2.8B). In the mid-ligament region of the MCL, there was some SOX9 and RUNX2 expression in the outer epiligament layer. In OA grade 5 STR/ort knee joints, there was further expression of COL2, SOX9, RUNX2, and ASPN markers throughout the MCL (Figure 2.8C). This included expression of all markers near the MCL-femoral enthesis (black arrows) and ASPN expression in the outer epiligament layer near the enthesis (red arrow) (Figure 2.8C). Furthermore, there was COL2 deposition in the mid-ligament region near areas with rounded-cell morphology (black arrows) as well as SOX9, RUNX2 and ASPN expression particularly in similar rounded-cell types (black arrows) (Figure 2.8C).

2.3.1.3 STR/ort mice medial meniscal pathology

2.3.1.3.1 Toluidine blue staining

The menisci of healthy CBA and OA STR/ort knee joints were also evaluated for pathological changes. In healthy CBA knee joints, toluidine blue staining delineated the expected ossified (O), hyaline cartilage (H) and fibrous region (F, red region) of the meniscus with rounded-shaped cells (yellow arrows) near the fibrous region (Figure 2.9A). The severity of pathological changes in the medial meniscus of STR/ort mice increased with AC degradation severity (Figure 2.9B-D). In OA grade 2 knee joints, there was an increase in the area of the fibrous region (Figure 2.9B, red region) which further increased with disease progression (Figure 2.9C-D). In OA grade 4 and 5, this fibrous region showed toluidine blue staining, rounded chondrocyte-like cells (yellow arrows) and formation of bone marrow cavities (black arrows) near the joint capsule (Figure 2.9C-D). Overall, toluidine blue staining demonstrated irregular hyperplasia, toluidine blue staining and changes in cell phenotype in the medial menisci of STR/ort mice.

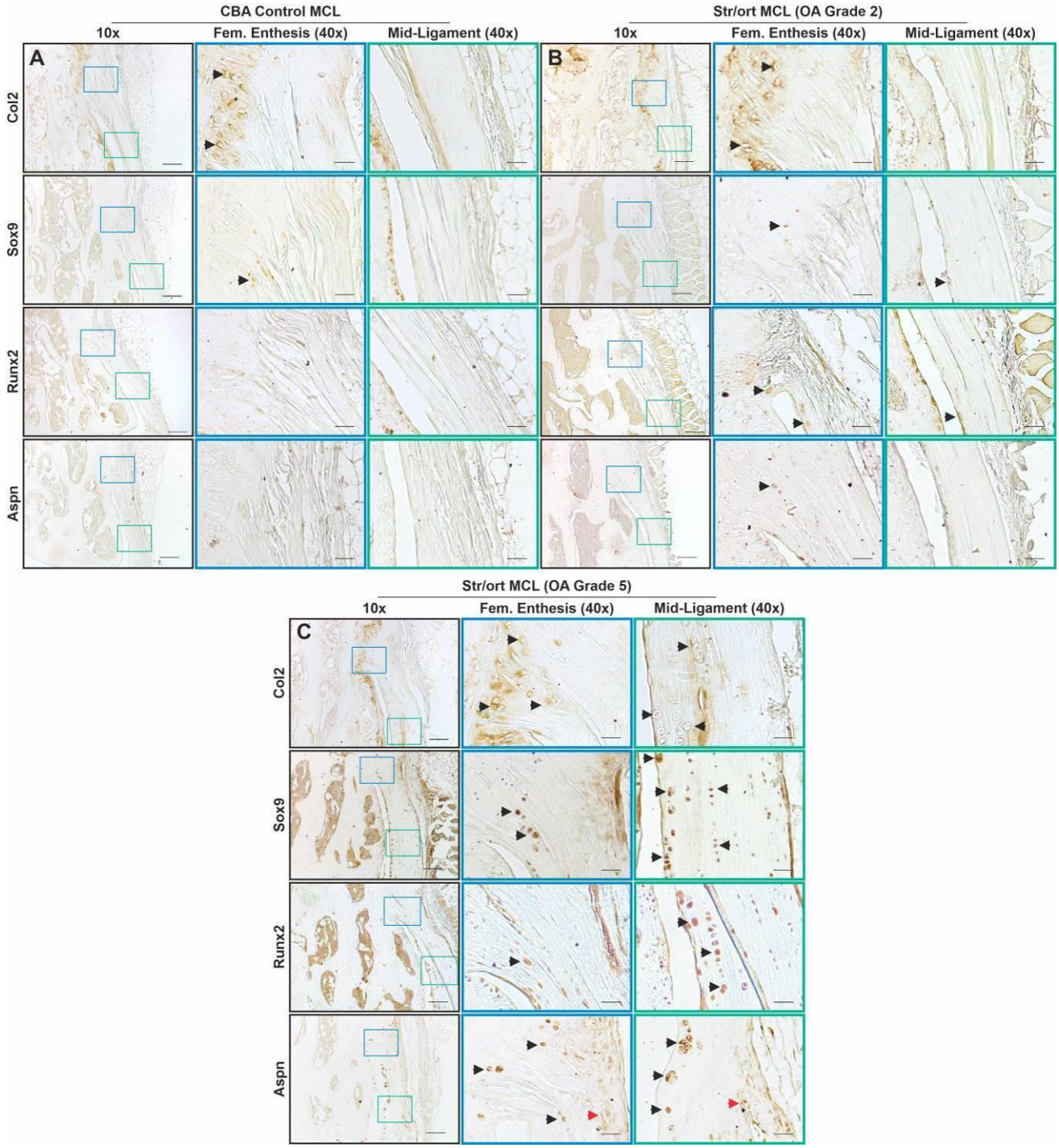

Figure 2.8 Immunostaining of the medial collateral ligament (MCL) in STR/ort knee joints of collagen type II (COL2), SOX9, RUNX2 and ASPN expression. Representative images of: (A) Aged-matched CBA knee joints had an MCL-femoral enthesis with ordered COL2 staining in the fibrocartilaginous region, and no marker expression in the MCL mid-ligament region. (B) OA grade 2 STR/ort MCLs had increased COL2 expression in the fibrocartilaginous femoral enthesis (black arrows) and minor SOX9, RUNX2 and ASPN expression near the femoral enthesis and no marker expression in the MCL mid-ligament region. (C) In OA grade 5 STR/ort knee joints, COL2 expression was evident in the MCL femoral enthesis and in the mid-ligament region near areas with rounded-cell morphology (black arrows). Rounded-cells (black arrows) also corresponded with expression of SOX9, RUNX2 and ASPN. Scale is 100 µm (10x) and 25 µm (40x).

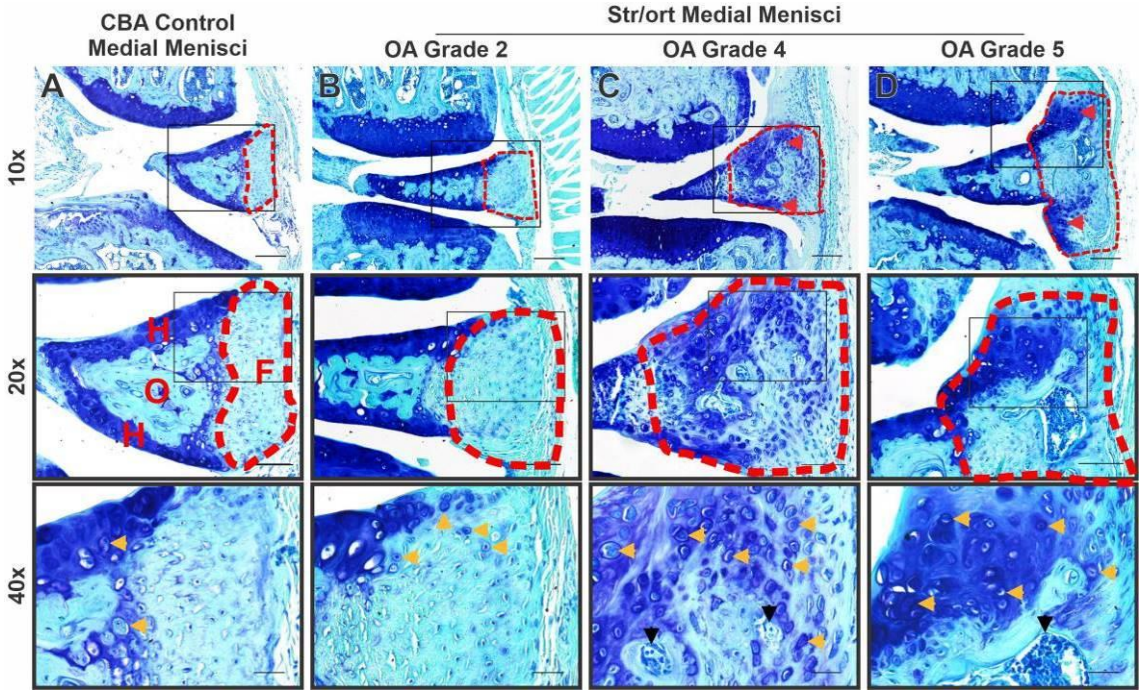

Figure 2.9 Histological staining of the medial menisci in STR/ort knee joints using toluidine blue. Representative images of: (A) Aged-matched CBA knee joints had healthy medial menisci with hyaline cartilage layers (H), ossified central core (O) and an outer fibrous region (F, red region). (B) OA grade 2 STR/ort medial menisci had a slightly enlarged fibrous region (red zone) with rounded-cell morphology (yellow arrows) in the outer fibrous regions. (C) OA grade 4 STR/ort medial menisci had even larger fibrous regions (red zone) with toluidine blue staining and rounded-cell morphology (yellow arrows) and possible bone formation (black arrows) in the fibrous region. (D) In severe OA grade 5 STR/ort knee joints, ossification was more evident (black arrow) and toluidine blue staining and rounded-cell morphology expanded to upper and lower areas of the fibrous region (yellow arrows). Scale is 100 µm (10x), 50 µm (20x) and 25 µm (40x).

2.3.1.3.2 Immunostaining

Immunostaining of the healthy CBA and OA STR/ort medial menisci revealed several markers present in areas of hyperplasia. Healthy CBA medial menisci showed COL2 delineating the hyaline cartilage region of the murine menisci along with some ASPN expression near the fibrous capsular attachment (green arrows) (Figure 2.10A). In OA grade 2 STR/ort knee joints, the fibrous region of the capsular attachment expanded however there were no changes in the staining of COL2, SOX9 and ASPN (Figure 2.10B). In OA grade 5 STR/ort knee joints, meniscal hyperplasia was fully underway in the meniscal fibrous region and COL2 expression (black arrows) was present in the outer expanding meniscal attachment site surrounding areas of bone formation (red arrows) along with rounded-cell morphology with SOX9 and ASPN expression (black arrows) (Figure 2.10C).

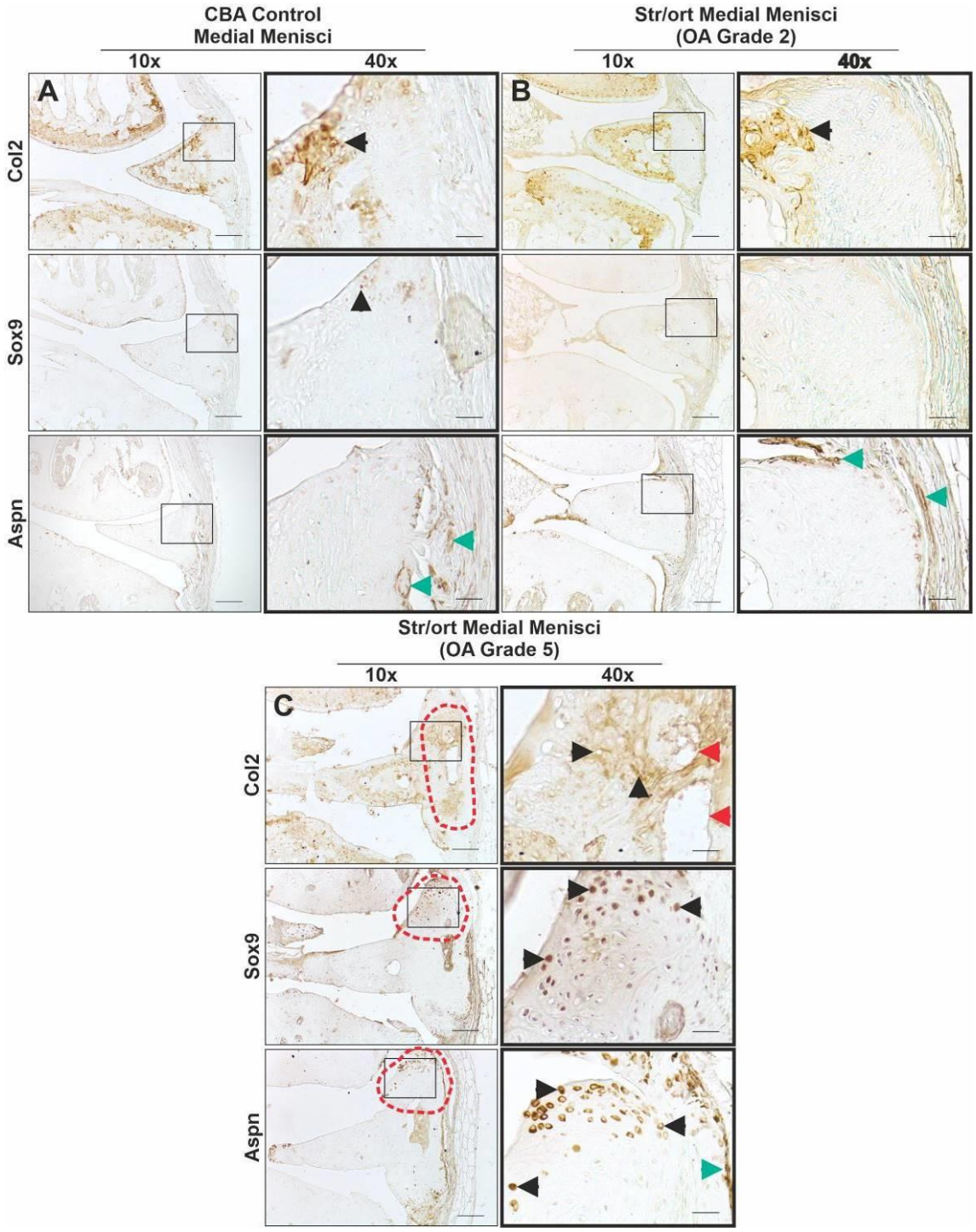

Figure 2.10 Immunostaining of the medial menisci in STR/ort knee joints of collagen type II (COL2), SOX9, and ASPN. Representative images of: (A) Aged-matched CBA knee joints had medial menisci with COL2 staining in the inner meniscal hyaline cartilage region and sparse SOX9 expression (black arrow) within cells in the upper fibrous region, and ASPN expression (green arrows) in the outer joint capsule region. (B) OA grade 2 STR/ort medial menisci had an expanded fibrous region but no evidence of COL2 and SOX9 staining, and only some ASPN staining (green arrows) in the same outer joint capsule region. (C) OA grade 5 STR/ort knee joints had medial menisci with ossification in the fibrous region (red arrows) showed COL2 deposition (black arrows) and SOX9 and ASPN expression (black arrows) in the expanding upper and lower fibrous attachment regions (red region). Scale is 100 µm (10x) and 25 µm (40x).

2.3.1.4 Summary of the STR/ort knee joint OA pathology

Overall, in the STR/ort mice knee joints the ACL, MCL and medial menisci all showed structural changes and rounded-cell morphology in affected areas which seemed to increase with OA progression. More specifically, in the STR/ort ACL there were ECM matrix changes in the tibial enthesis and the mid-ligament region which included COL2 deposition and coincided with cellular changes including rounded-cell morphology with SOX9, RUNX2 and ASPN expression. The MCL in the OA STR/ort knee joints showed similar pathology including hyperplasia and fibre disorganisation and potential bone formation and rounded-cell morphology in the mid-ligament region. Lastly, in the medial menisci of the STR/ort knee joints, hyperplasia and bone formation was notable in the fibrous region of the menisci, also containing COL2 deposition and rounded-cell morphology. These findings demonstrate that STR/ort knee ligament and menisci pathology was marked by structural COL2 changes potentially driven by cellular changes associated with chondrogenesis and hypertrophy.

2.3.2 Post-traumatic OA surgical destabilisation of the medial menisci (DMM) murine model

In the post-traumatic OA model following DMM surgery in the C57CBA murine knee joint, pathological changes in the ACL, MCL and menisci were also determined using histological staining (with toluidine blue, PR staining) and immunostaining for markers of OA. DMM mice were categorised based on the OARSI OA cartilage score, which ranged from OA grade 2 to 6 (mean OARSI score was 3.4 ±0.3), with OA predominant in the medial compartment as expected [107]. As previously mentioned, meniscal and ligament pathological changes in the DMM model have largely not been described. DMM post-traumatic joints were compared to the non-operated contralateral knee joints.

2.3.2.1 DMM mice anterior cruciate ligament (ACL) pathology

2.3.2.1.1 Toluidine blue staining

Toluidine blue staining of the ACL in contralateral knee joints of C57CBA mice showed an organised ACL ECM, with the presence of toluidine blue staining in the fibrocartilaginous region of the tibial enthesis near cells with rounded morphology (yellow arrows) (Figure 2.11A). In the DMM knee joints with OA grade 4, pathological changes in the ACL included ECM disorganisation, fibre misalignment, toluidine blue staining near the tibial attachment site (red arrow) and numerous rounded hypertrophic-like cells (yellow arrows) extending from the ACL-tibial enthesis to the ligament (Figure 2.11B). In severe OA grade 6, the ACL had toluidine blue staining at the fibrocartilaginous region (yellow arrows) and no cellular or fibre alignment within the ligament, no toluidine blue staining and abnormal tissue formation including potential inflammation and blood vessel formation (black arrows) (Figure 2.11C). Toluidine blue staining demonstrated severe pathological changes in the ECM and cellular phenotype in the ACL of the DMM knee joint.

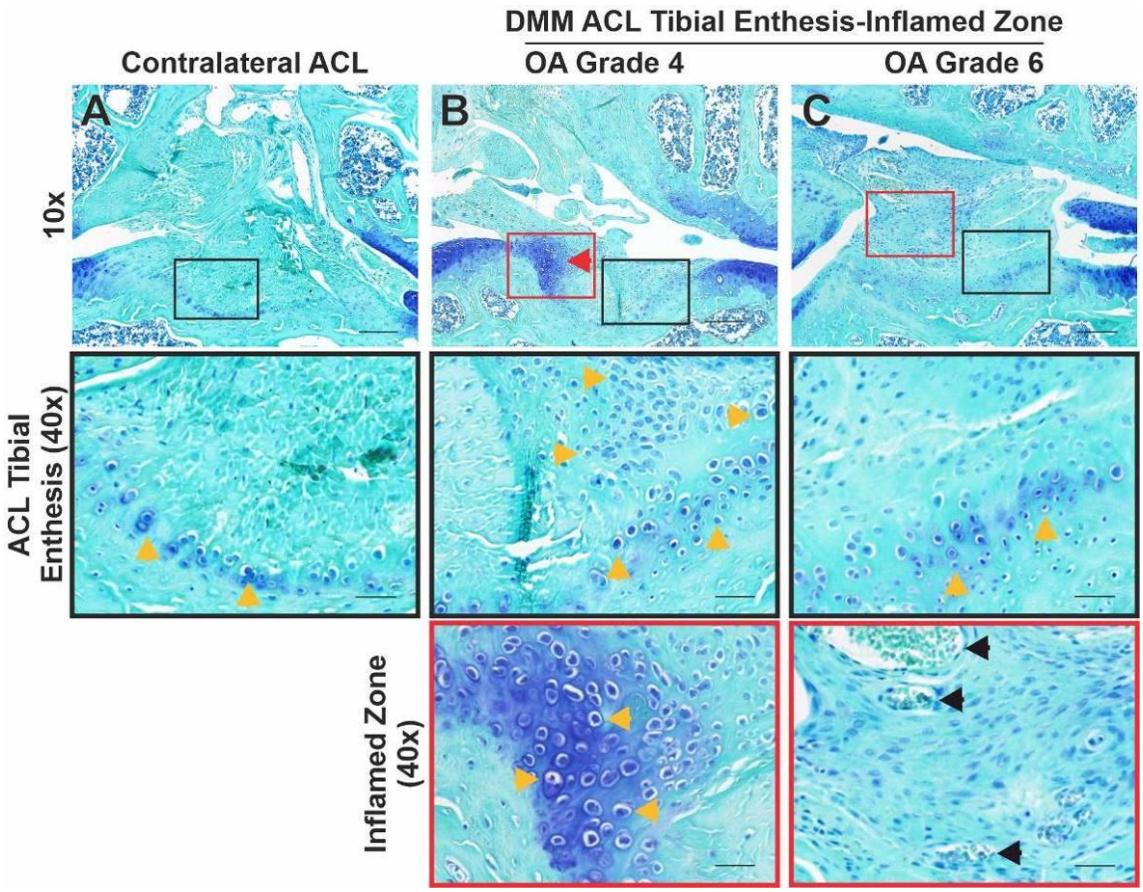

Figure 2.11 Histological staining of the anterior cruciate ligament (ACL) in DMM and contralateral knee joints using toluidine blue. Representative images of: (A) Contralateral (non-operated) knee joint had an ACL with an organised ECM structure and toluidine blue staining in the fibrocartilaginous tibial enthesis region (yellow arrows). (B) OA grade 4 DMM knee joint ACL was disorganised, showed no fibre alignment and had toluidine blue staining near the attachment site (red arrow) and rounded-cell morphology (yellow arrows). (C) OA grade 6 DMM knee joint ACL showed severe misalignment and signs of inflammation including potential blood vessel formation (black arrows). Scale is 100 µm (10x) and 25 µm (40x).

2.3.2.1.2 PR staining

PR staining of the DMM knee joint ACL confirmed changes in the collagen matrix content and organisation. The ACL from the contralateral knee joints had red collagen stain and rounded-cell morphology (yellow arrows) at the fibrocartilaginous region of the tibial enthesis (Figure 2.12A). Polarised light, used to visualise collagen birefringence, in the contralateral knee joints showed green and orange birefringence (blue arrow) near the ACL tibial enthesis (Figure 2.12A). DMM OA grade 4 and 6 knee joints showed widespread red collagen staining throughout the ACL, as well as evidence of rounded cell morphology (yellow arrows) which extended from the fibrocartilaginous region to the mid-ligament region (Figure 2.12B-C). Polarised light in the ACL of the DMM knee joint verified extensive red birefringence (Figure 2.12B-C,). In OA grade 4

knee joints, green birefringence was present above the orange fibrocartilaginous region of the ACL (blue arrow) and orange birefringence was evident in inflamed ligament regions (blue arrow) (Figure 2.12B). In DMM OA grade 6 knee joints, the ACL had red birefringence from the tibial attachment site to the mid-ligament region (Figure 2.12C). Red birefringence would suggest thicker collagen fibres were prominent in the ACL of the OA grade 6 DMM knee joint.

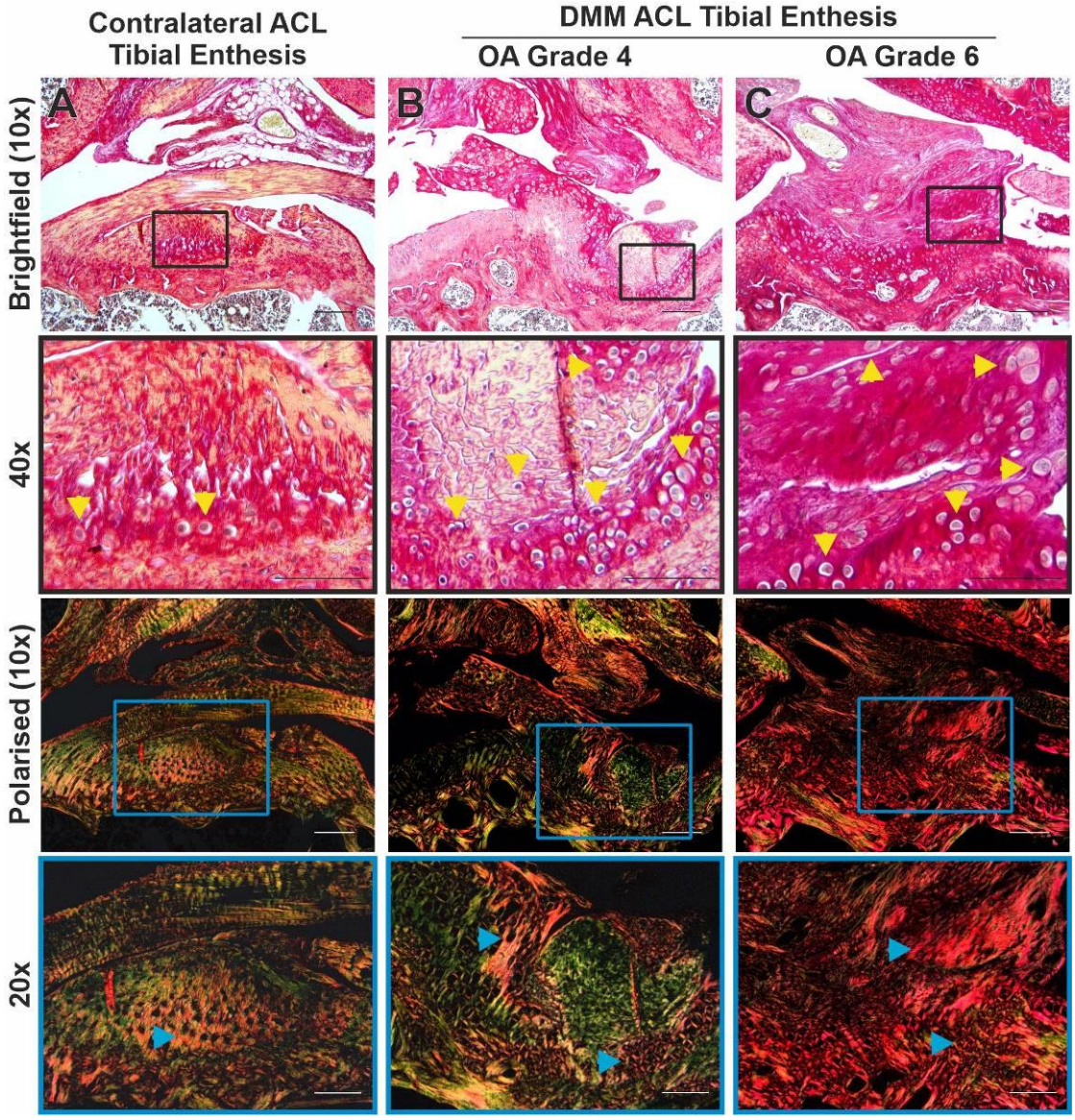

Figure 2.12 Histological staining of the anterior cruciate ligament (ACL) in DMM knee joints using picrosirius red. Representative images of: (A) Non-operated contralateral knee joint ACLs had red collagen staining near the fibrocartilaginous region with rounded cell morphology (yellow arrows). Polarised light showed green and orange birefringence (blue arrow) near the tibial enthesis. (B) The OA grade 4 DMM knee joint ACL had rounded-cell morphology (yellow arrows) in the fibrocartilaginous region and within the ACL. Orange birefringence (blue arrow) was found in the fibrocartilaginous zone and in inflamed regions of the ACL. (C) In OA grade 6 DMM knee joints, rounded-cell morphology (yellow arrows) extended from the ACL tibial enthesis to the mid-ligament and coincided with dark red collagen staining. Polarised light showed red birefringence (blue arrows) extended throughout the ACL, from the tibial enthesis to the mid-ligament region. Scale is 100 µm (10x) and 50 µm (20x, 40x).

2.3.2.1.3 Immunostaining

Immunostaining was used to compare COL2 staining and SOX9 expression in the DMM and contralateral knee joint ACLs. Contralateral knee joints had ACL with COL2 and SOX9 expression (black arrows) in a thin and organised fibrocartilaginous region (Figure 2.13A). In DMM mice with OA grade 4 and 6, the fibrocartilaginous region of the ACL had expanded COL2 expression near regions with rounded-cell morphology (black arrows), along with abundant SOX9 expression (black arrows) which extended from the ACL tibial enthesis to the mid-ligament (Figure 2.13B-C). SOX9 expression correlated with areas of rounded-cell morphology noted with toluidine blue and PR staining. Immunostaining confirmed changes in the fibrocartilaginous region of the DMM knee joint ACL which included COL2 deposition, and SOX9 expression cellular markers extending throughout the ACL.

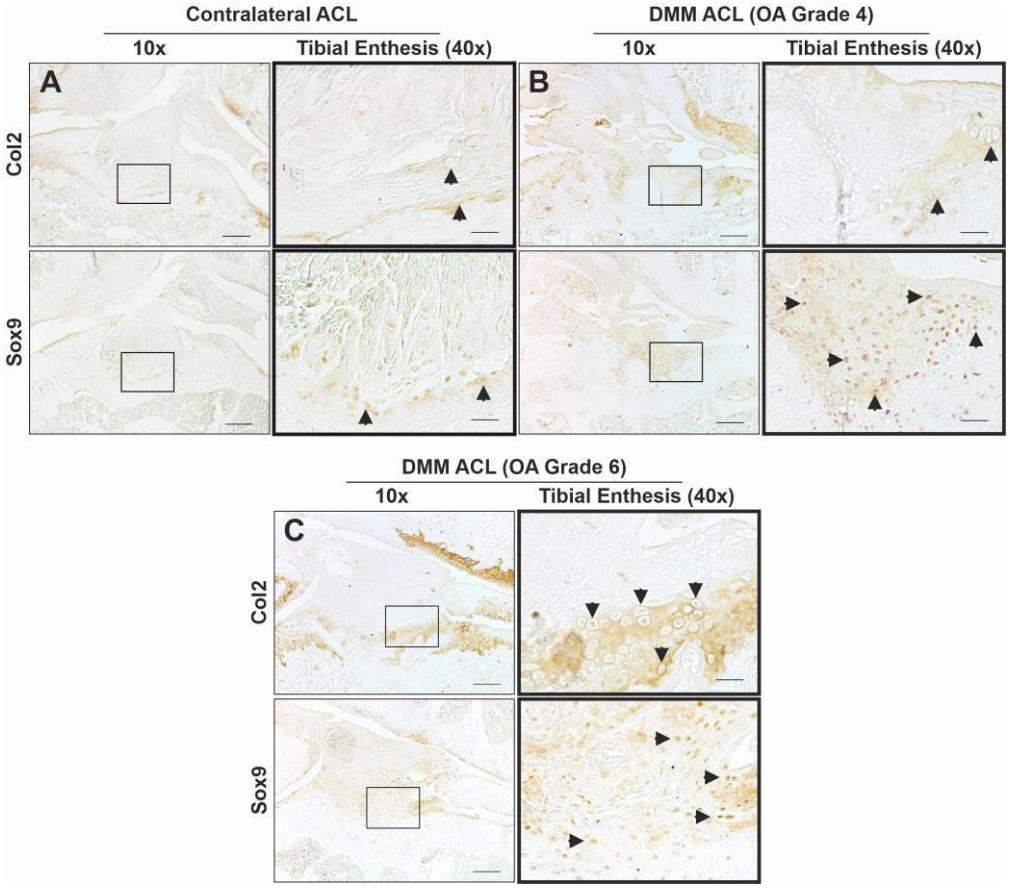

Figure 2.13 Immunostaining of the anterior cruciate ligament (ACL) tibial enthesis in DMM knee joints of collagen type II (COL2) and SOX9 expression. Representative images of: (A) Contralateral (non-operated) knee joint ACL showed minor COL2 and SOX9 staining (black arrows) in the fibrocartilaginous region of the ACL tibial enthesis. (B) OA grade 4 DMM knee joint ACL had COL2 deposition near the ACL tibial enthesis and extensive SOX9 expression in all ligament cells (black arrows). (C) OA grade 6 DMM knee joints had severe ACL deformation with an increased fibrocartilaginous region at the tibial enthesis with COL2 deposition and extensive SOX9 expression throughout the ACL (black arrows). Scale is 100 µm (10x) and 25 µm (40x).

2.3.2.2 DMM mice medial collateral ligament (MCL) pathology

2.3.2.2.1 Toluidine blue staining

Toluidine blue staining in contralateral knee joints showed an organised MCL with toluidine blue staining at the fibrocartilaginous region (yellow arrows) and tide mark (black arrow) of the MCL femoral enthesis. The MCL mid-ligament region of the contralateral knee joint, had aligned fibres and spindle-shaped fibroblasts (purple arrow) (Figure 2.14A). Knee joints from DMM mice with OA grade 4 had MCLs with faint toluidine blue staining at the MCL femoral enthesis (yellow arrows), and structural changes including a fibrous region (red region) parallel and adjacent to the MCL with evidence of toluidine blue staining (yellow arrow) (Figure 2.14B). In the DMM OA grade 6 knee joint there were severe structural changes to the MCL, including a lack of collagen fibre alignment, ECM disorganisation, hyperplasia, and potential formation of bone cavities (red region and red arrows) (Figure 2.14C). Despite evidence of hyperplasia and structural changes in the DMM knee joint MCL there was no toluidine blue staining within the MCL ECM.

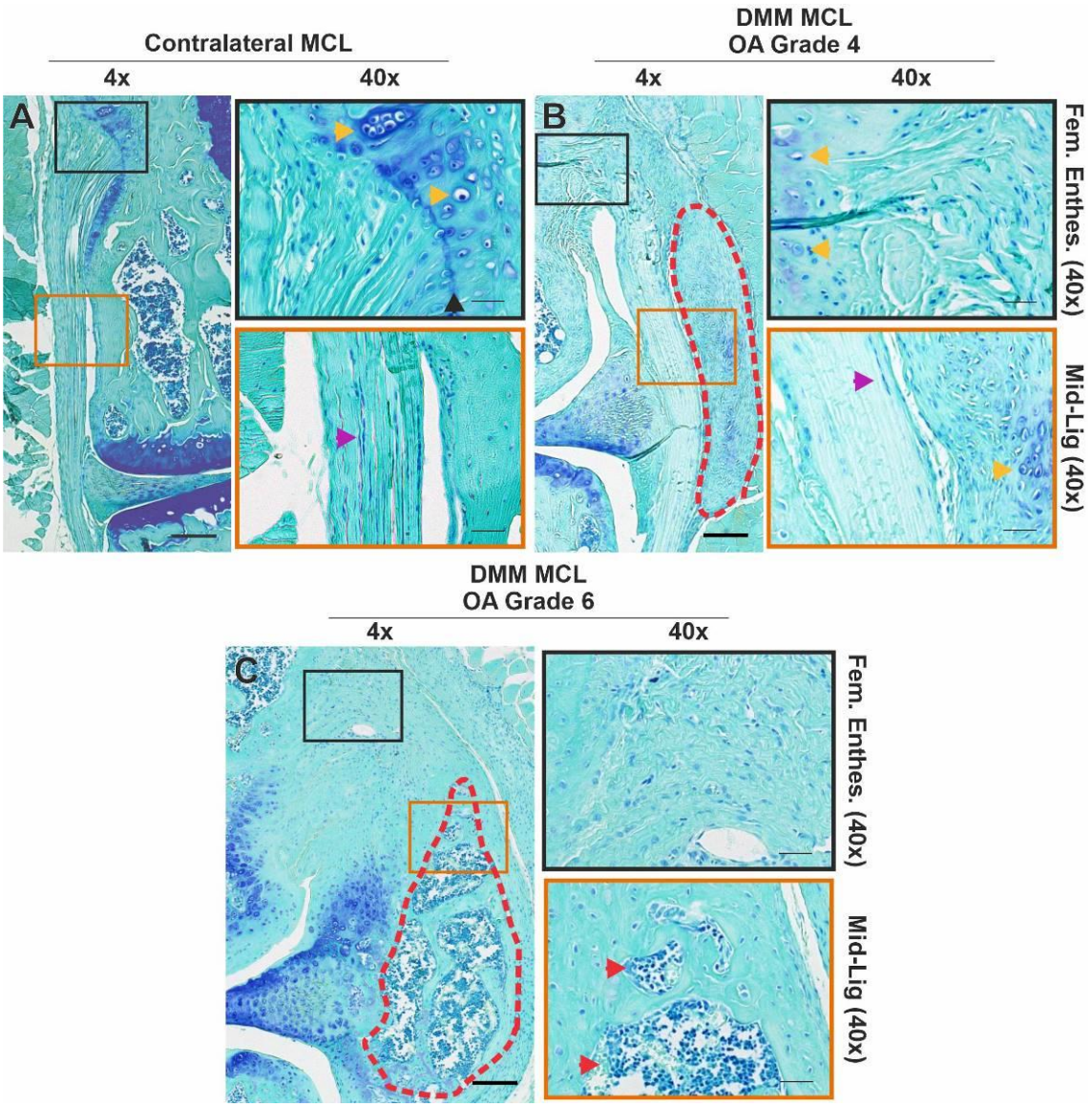

Figure 2.14 Histological staining of the medial collateral ligament (MCL) in DMM knee joints using toluidine blue. Representative images of: (A) Non-operated contralateral knee joint MCL showed toluidine blue staining near the fibrocartilaginous region (yellow arrows) and a tide mark (black arrow). The mid-ligament region of the contralateral knee joint MCL showed fibre alignment and an organised structure with no toluidine blue staining. (B) OA grade 4 DMM knee joint MCL showed a similar MCL structure, however near the femoral enthesis there was a fibrous disorganised region (red region) which extended parallel with the MCL. (C) OA grade 6 DMM knee joint MCL showed evident hyperplasia and no fibre alignment, no toluidine blue staining, and evidence of bone formation in the mid-ligament region (red region, red arrows), near the medial menisci. Scale is 100 µm (4x) and 25 µm (40x).

2.3.2.2.2 PR staining

PR staining was used to analyse collagen birefringence in the DMM and contralateral knee joint MCLs. Contralateral knee joints demonstrated an organised MCL structure with light-red collagen staining (Figure 2.15A). Polarised light showed green collagen birefringence throughout the

contralateral knee joint MCL with yellow birefringence (blue arrows) near the MCL femoral attachment site and a thin layer in the epiligament of the mid-ligament region (Figure 2.15A). In OA grade 4 DMM knee joints, the MCL had light-red collagen staining throughout the ligament, with dark-red staining in the outer fibrous region (yellow region) parallel to the MCL (Figure 2.15B). Polarised light showed yellow-orange birefringence near the MCL femoral enthesis (blue arrow) in the abnormal fibrous region and in the epiligament layer of the mid-ligament region (Figure 2.15B). The OA grade 6 DMM knee joint MCL seemed to converge with the growing medial meniscus and surrounding mineralisation which resulted in an MCL region with abundant red collagen staining, with lack of collagen fibre alignment and clear hyperplasia (Figure 2.15C). Polarised light showed red birefringence (blue arrows) in the MCL from OA grade 6 DMM knee joints (Figure 2.15C). PR staining revealed red collagen birefringence in the DMM knee joint MCL, which would indicate thicker collagen fibre organisation in the diseased MCL.

2.3.2.2.3 Immunostaining

Immunostaining of the MCL from contralateral and DMM murine knee joints revealed changes in COL2 deposition and SOX9 expression. The contralateral MCL showed a thin layer of COL2 staining (black arrows) at the fibrocartilaginous region of the femoral enthesis along with scarce SOX9 staining (black arrows) also at the femoral enthesis and in spindle-shaped fibroblasts in the mid-ligament region (green arrow) (Figure 2.16A). MCL from OA grade 4 DMM knee joints showed similar COL2 staining at the MCL femoral enthesis and no COL2 and SOX9 staining in MCL mid-ligament region except in the outer fibrous region (black arrows) (Figure 2.16B). The MCL from OA grade 6 DMM knee joints, showed further COL2 and SOX9 staining (black arrows) at the femoral enthesis and throughout the MCL including near areas of potential bone formation (red arrows) (Figure 2.16C). Changes in COL2 matrix composition and SOX9 cellular staining was evident in the MCL of diseased DMM knee joints.

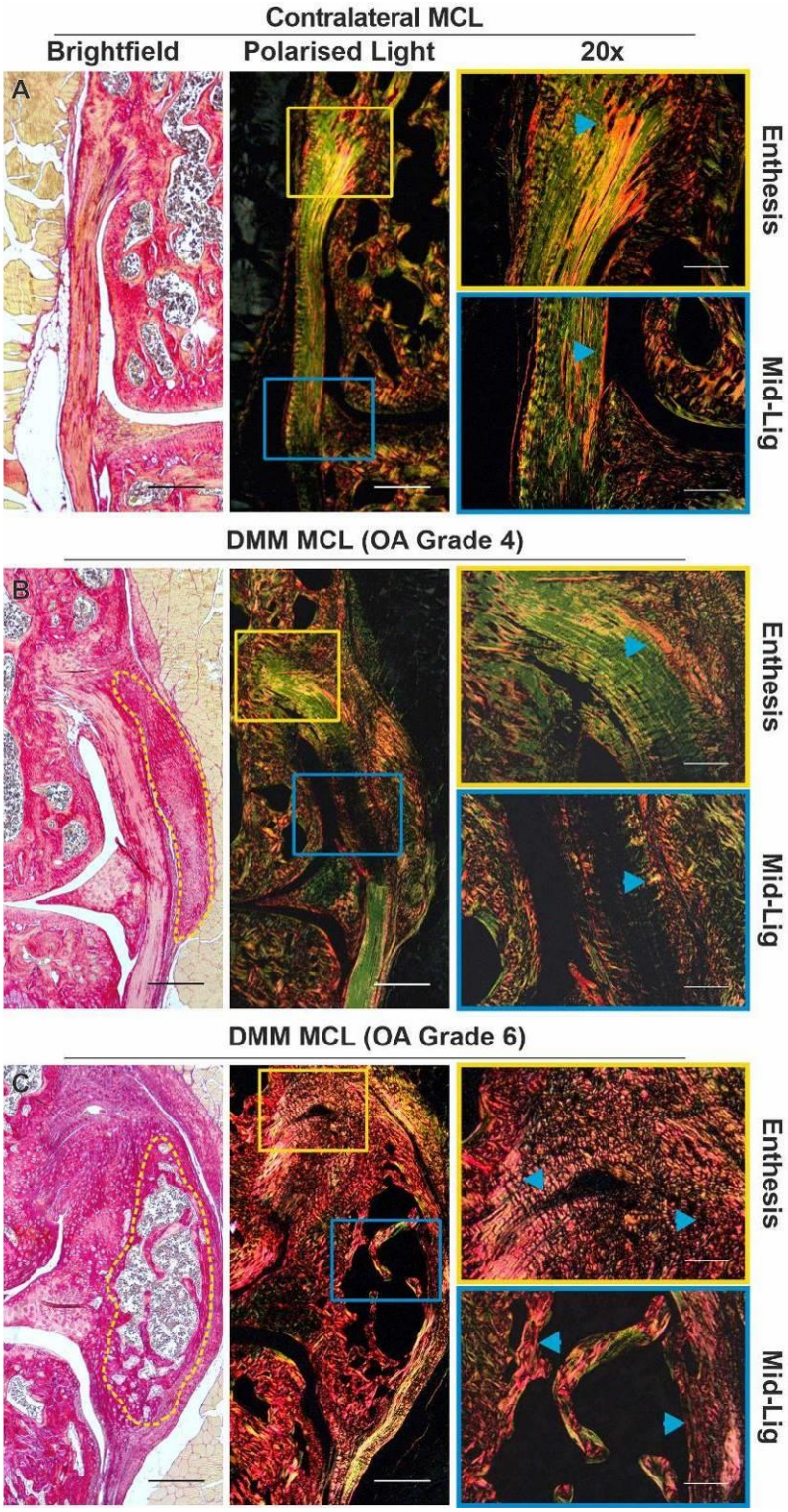

Figure 2.15 Histological staining of the medial collateral ligament (MCL) in DMM knee joints using picrosirius red. Representative images of: (A) Non-operated contralateral knee joint MCL had mainly green birefringence and yellow birefringence (blue arrows) only near the femoral attachment site and epiligament layer of the mid-ligament region. (B) OA grade 4 DMM knee joint MCL showed yellow-orange birefringence (blue arrows) near the attachment site in the adjacent fibrous region (yellow region) and in the epiligament layer of the mid-ligament region of the MCL. (C) OA grade 6 DMM knee joint MCL had red birefringence (blue arrows) in all regions of the MCL, suggesting thicker collagen fibre formation. Scale is 200 µm (4x) and 25 µm (40x).

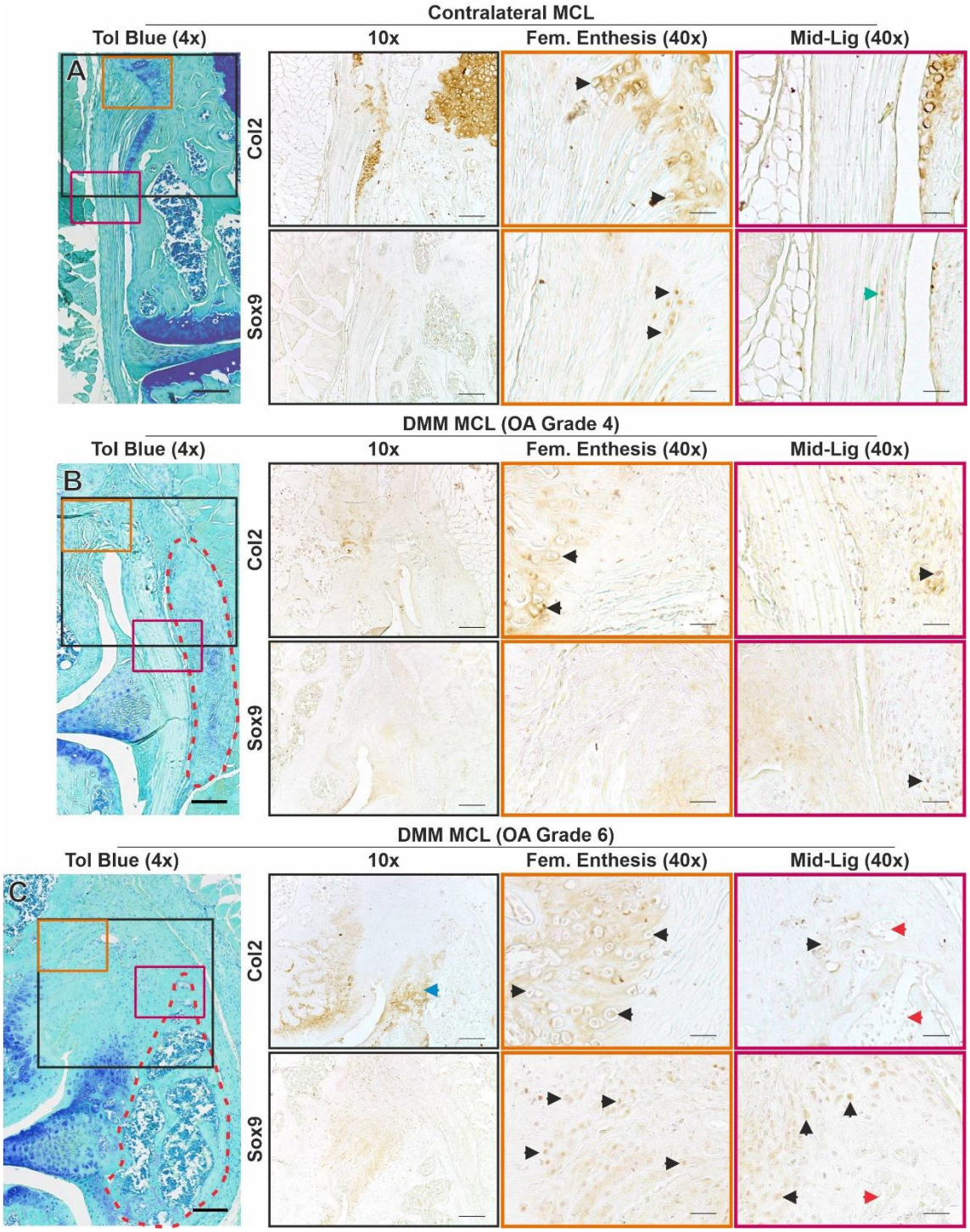

Figure 2.16 Immunostaining of the medial collateral ligament (MCL) in DMM knee joints of collagen type II (COL2) and SOX9 staining. Representative images of: (A) Non-operated contralateral knee joint MCL had COL2 staining and sparse SOX9 expression at the fibrocartilaginous layer of the femoral enthesis and some SOX9 expression in spindle-shaped fibroblasts (green arrow) in the mid-ligament region of the MCL. (B) OA grade 4 DMM knee joint MCL had COL2 staining at the femoral enthesis (black arrows), but no SOX9 or COL2 staining in other parts of the ligament, except in the outer fibrous region (black arrows). (C) In OA grade 6 DMM knee joints, the MCL showed a thicker fibrocartilaginous layer with COL2 deposition near the femoral enthesis and extensive SOX9 staining throughout the MCL (black arrows). COL2 and SOX9 staining was also found in the mid-ligament region (black arrows) near areas of potential bone formation (red arrows). Scale is 100 µm (4x, 10x) and 25 µm (40x).

2.3.2.3 DMM mice medial meniscal pathology

2.3.2.3.1 Toluidine blue staining

Toluidine blue staining of the menisci of the non-operated contralateral knee joint showed medial menisci within normal limits which included toluidine blue staining in the hyaline cartilage portion of the menisci and a clear separation between the meniscal fibrous region (red region) and the capsular attachment and collateral ligament (Figure 2.17A). In OA grade 4 DMM knee joints, the fibrous region of the medial menisci (red region) seemed to converge with the MCL and capsular attachment and showed hyperplasia and abnormal tissue growth including bone formation (black arrows), along with rounded or hypertrophic cells expanding from the hyaline cartilage of the medial menisci (yellow arrows) (Figure 2.17B). OA grade 6 DMM knee joints, showed even more pronounced changes in the medial menisci including hyperplasia and bone formation (black arrows) accompanied by toluidine blue staining (red arrow) and rounded-cell morphology (yellow arrows) (Figure 2.17C). In the inner meniscal tip also demonstrated abnormal tissue growth and toluidine blue staining (Figure 2.17C).

2.3.2.3.2 Immunostaining

The localisation of COL2 and SOX9 expression were determined with immunostaining of the contralateral and DMM knee joint medial menisci. Contralateral medial menisci had COL2 staining near the fibrous region and SOX9 staining in the outer menisci regions (black arrows) (Figure 2.18A). In OA grade 4 DMM knee joints, COL2 outlined the hyaline region of the medial menisci and COL2 and SOX9 could also be found in the upper area of the fibrous region particularly near cells with a rounded morphology (black arrows) (Figure 2.18B). OA grade 6 DMM knee joints had medial menisci with COL2 and SOX9 staining emerging in the upper and lower expanding fibrous region surrounding areas of mineralisation (black arrows) (Figure 2.18C). Similar to the ACL and MCL, in the medial menisci of the DMM knee joints, COL2 and SOX9 expression was found in areas of hyperplasia and surrounding regions of mineralisation.

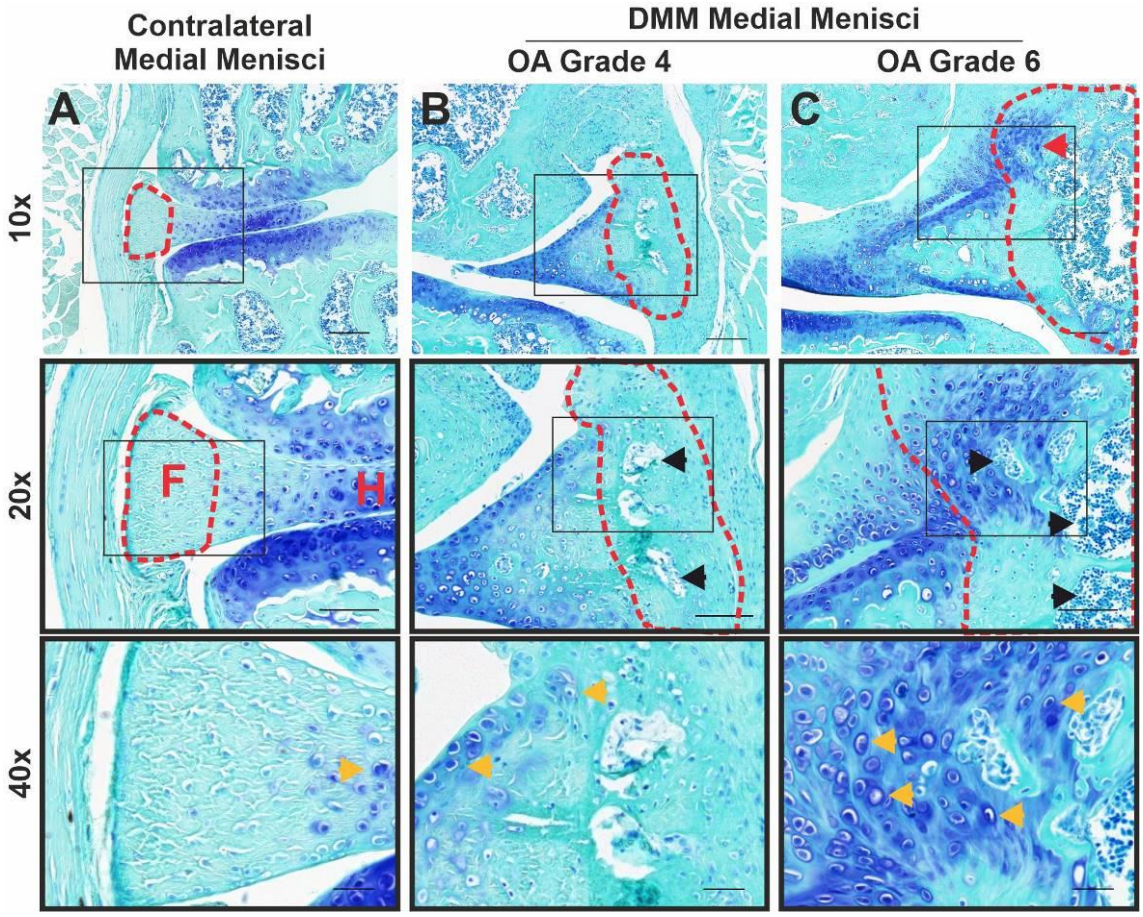

Figure 2.17 Histological staining of the medial menisci in DMM knee joints using toluidine blue. Representative images of: (A) Non-operated contralateral knee joint medial menisci showed toluidine blue staining in the inner hyaline cartilage regions and a small outer fibrous region (red region) separate from the collateral ligament. (B) OA grade 4 DMM knee joints had medial menisci with enlarged fibrous region (red region) which fused with the capsular collateral ligament and had evidence of mineralisation (black arrows) and rounded-cell morphology and toluidine blue staining in the upper fibrous regions (yellow arrows). (C) OA grade 6 DMM knee joints had medial menisci with toluidine blue staining (red arrow) in the outer fibrous regions (red region) and clear evidence of bone formation (black arrows) and rounded-cell morphology (yellow arrows). Scale is 100 µm (10x), 50 µm (20x) and 25 µm (40x).

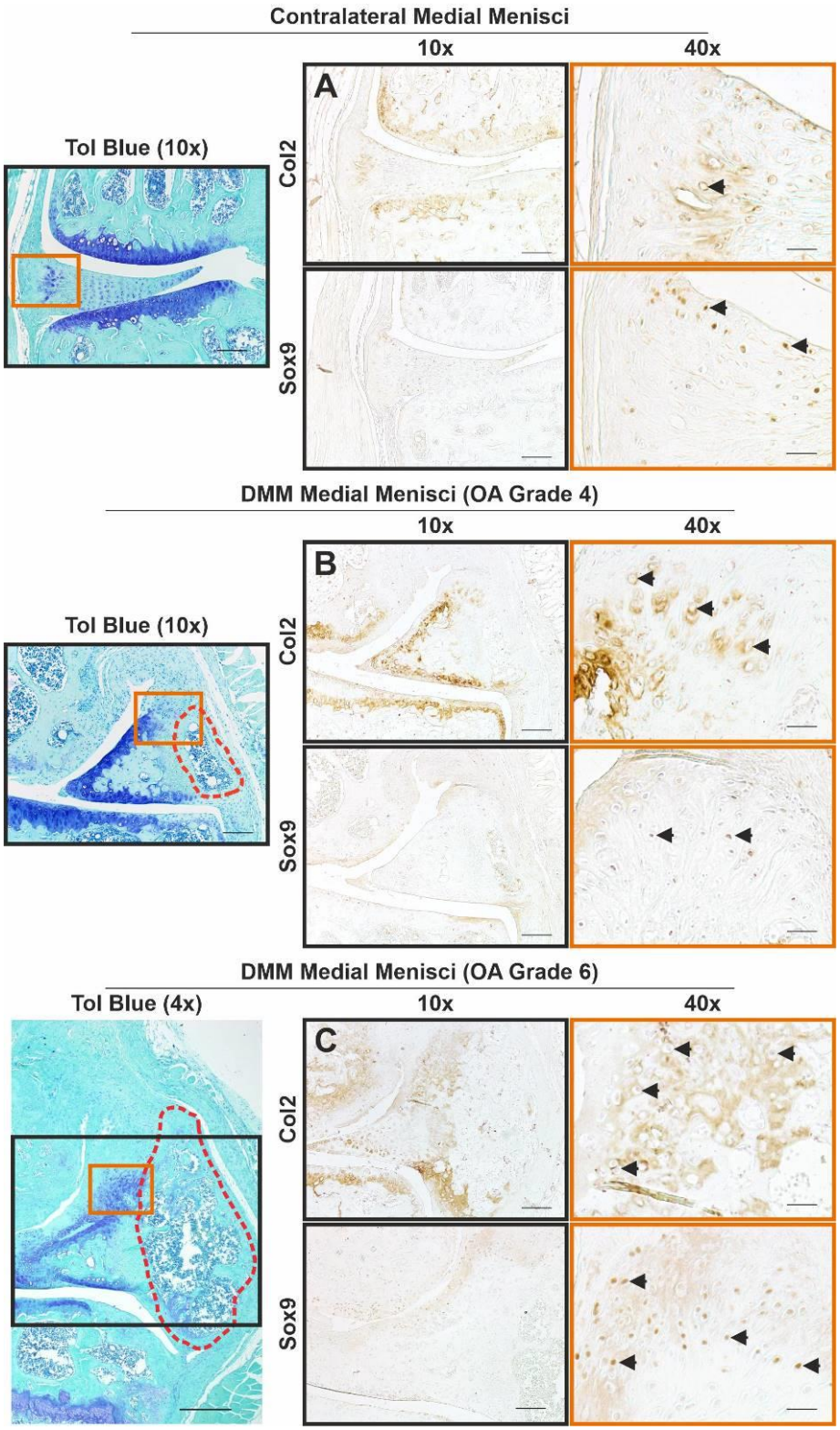

Figure 2.18 Immunostaining of the medial menisci in DMM knee joints of collagen type II (COL2) and SOX9 staining. Representative images of: (A) Non-operated contralateral knee joints had medial menisci with COL2 staining in the fibrous region and SOX9 staining in the hyaline cartilage areas (black arrows). (B) OA grade 4 DMM knee joints had medial menisci with abnormal COL2 and SOX9 staining in the outer fibrous regions near cells with rounded morphology (black arrows). (C) OA grade 6 DMM knee joints had medial menisci with COL2 an SOX9 staining in the upper and lower fibrous regions. Scale is 200 µm (4x), 100 µm (10x), 25 µm (40x).

2.3.2.4 Summary of the DMM knee joint OA pathology

The post-traumatic OA DMM knee joint demonstrated ECM and cellular changes in the ACL, MCL and medial menisci which corresponded with post-traumatic OA disease progression. In the ACL of DMM knee joints at OA grade 4 and 6, there was severe collagen fibre misalignment, ECM disorganisation, and evidence of inflamed or abnormal tissue growth with red collagen birefringence suggesting thicker collagen fibres. The MCL of OA DMM knee joints showed severe pathology including abnormal fibrous tissue parallel to the MCL, bone formation and red collagen birefringence. Ossification extended from the MCL to the fibrous region of the medial menisci in the OA DMM knee joints. Immunostaining showed COL2 deposition and SOX9 expression particularly in the fibrocartilaginous zone of the ACL tibial enthesis, in the MCL femoral enthesis, and in the fibrous region of the medial menisci including near areas of bone formation. This abnormal tissue growth indicated atypical COL2 matrix composition potentially driven by SOX9 expressing cells, indicating chondrogenesis.

2.3.3 Post-traumatic OA non-invasive mechanical loading murine model

Non-invasive mechanical loading of C57BL/6J knee joints allows for examination of OA development in which articular cartilage lesions in the lateral femur are induced and slowly progress over time [153]. OA progression in the C57BL/6J loaded knee joints was previously confirmed and included increased mineralisation compared to healthy non-loaded C57BL/6J knee joints [165]. Loaded knee joints were analysed four weeks post-trauma. Changes in the ACL and lateral menisci have been previously reported in CBA mice following non-invasive mechanical loading and briefly included meniscal ossification and ACL pathological changes [153]. Our aim was to describe these changes in more detail in the C57BL/6J loaded knee joints.

2.3.3.1 Non-invasive mechanically loaded mice anterior cruciate ligament (ACL) pathology

2.3.3.1.1 Toluidine blue staining

Toluidine blue staining of the non-loaded knee joints showed healthy ACLs with collagen fibre alignment and some toluidine blue staining in the mid-ligament region which had mainly spindle-shaped fibroblasts (purple arrow) and a thin layer of toluidine blue staining at the tibial enthesis in the fibrocartilaginous zone (yellow arrows) (Figure 2.19A). Loaded knee joints following four weeks post-trauma, still retained collagen fibre alignment with increased intensity in toluidine blue staining in the mid-ligament region and tibial enthesis (red arrows) (Figure 2.19B). Furthermore, in the loaded knee joints, the ACL mid-ligament region and the fibrocartilaginous enthesis region showed increased rounded cell morphology (yellow arrows) (Figure 2.19B).

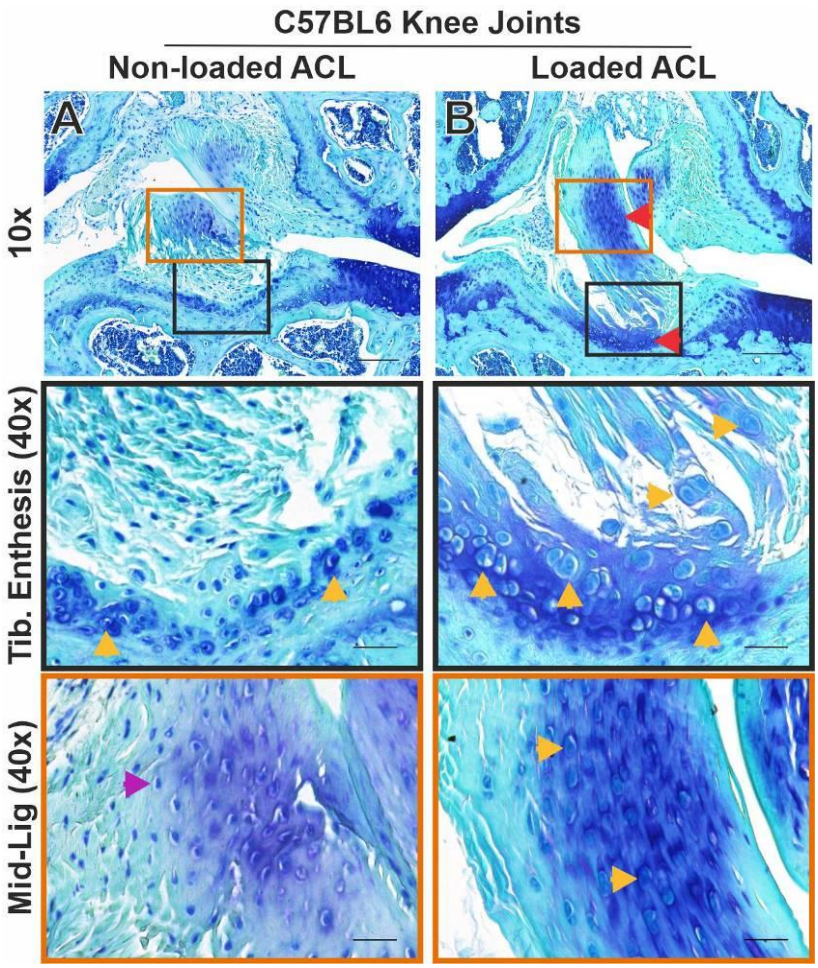

Figure 2.19 Histological staining of the anterior cruciate ligament (ACL) in non-invasive mechanical loading knee joints using toluidine blue stain. Representative images of: (A) Healthy non-loaded knee joints showed an organised ACL with some toluidine blue staining including a thin layer at the tibial enthesis (yellow arrows) and spindle-shaped cells in the mid-ligament region (purple arrow). (B) In loaded knee joints four weeks post-trauma, toluidine blue staining was prominent throughout the ACL in the mid-ligament region and in the tibial enthesis where it surrounded cells with rounded-cell morphology (yellow arrows). Scale is 100 µm (10x) and 25 µm (40x).

2.3.3.1.2 PR staining

PR staining was used to analyse collagen content and birefringence in the non-invasive mechanically loaded OA knee joints and the non-loaded healthy knee joints. The non-loaded knee joints had ACLs with light red collagen staining in brightfield and spindle-shaped cells in the mid-ligament region (green arrows) (Figure 2.20A). Polarised light showed predominantly green-yellow birefringence in the non-loaded knee joint ACL (Figure 2.20A). The loaded knee joint had an ACL with red collagen staining in the mid-ligament region near areas with rounded-cell morphology (yellow arrows) (Figure 2.20B). Green birefringence was also present in the ACL of loaded knee joints along with red birefringence in the outer epiligament regions and near the tibial

attachment sites (blue arrows) (Figure 2.20B). Red birefringence in the loaded knee joint ACL was suggestive of thicker collagen composition.

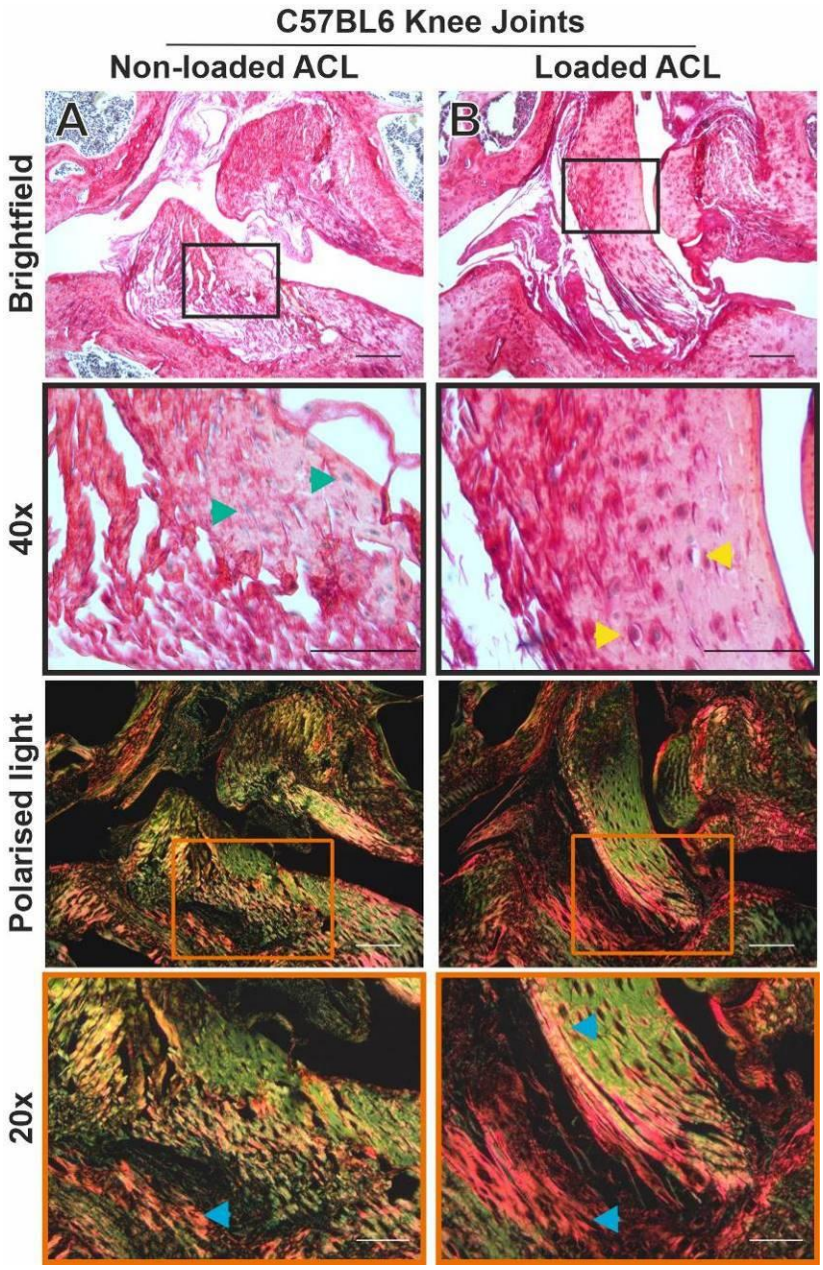

Figure 2.20 Histological staining of the anterior cruciate ligament (ACL) in non-invasive mechanically loaded knee joints using picrosirius red stain. Representative images of: (A) Non-loaded knee joint had ACLs with mainly light red collagen staining (brightfield) and green-yellow birefringence throughout the ACL and orange birefringence near the tibial enthesis (blue arrow). (B) Loaded knee joints four weeks post-trauma had an ACL with red collagen staining and rounded cell morphology (yellow arrows) and red birefringence near the tibial attachment site and the epiligament layer. Scale is 100 µm (10x) and 50 µm (20x, 40x).

2.3.3.1.3 Immunostaining

Non-loaded healthy knee joint had an organised ACL tibial enthesis with a small layer of COL2 staining, sparse SOX9 and RUNX2 staining as expected in the fibrocartilaginous region, and ASPN expression that spread from the tibial enthesis into the ACL (black arrows) (Figure 2.21A). The mid-ligament region of the healthy non-loaded knee joints displayed no COL2, SOX9 and RUNX2 staining, and sparse ASPN expression (Figure 2.22A). In the OA knee joints that underwent non-invasive mechanical loading, the ACL had COL2 deposition near the tibial enthesis, as well as SOX9, RUNX2 and ASPN expression which extended from the fibrocartilaginous region further into the ACL (black arrows) (Figure 2.21B). Furthermore, ASPN expression was also highly expressed in the fibrous tissue adjacent to the ACL (red arrow) (Figure 2.21B). In the mid-ligament region of the ACL of the loaded knee joints, COL2, SOX9 and ASPN expression were highly expressed (black arrows), including pericellular expression of ASPN in the mid-ligament fibroblasts (Figure 2.22B). The mid-ligament region and the tibial enthesis region of COL2 deposition was similar to the areas of increased toluidine blue staining (Figure 2.19B). Immunostaining of the OA loaded knee joints confirmed changes in the ECM of the ACL and fibroblasts markers in the tibial enthesis and the mid-ligament region.

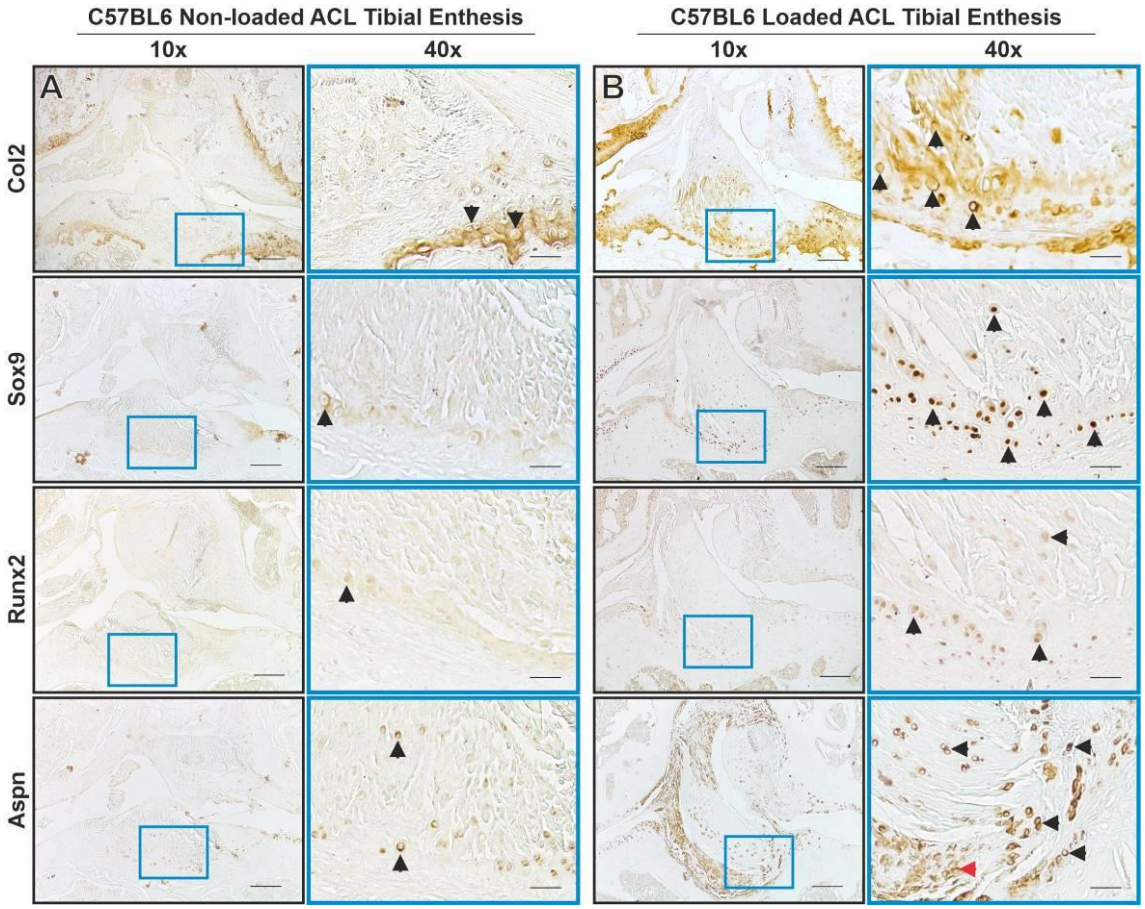

Figure 2.21 Immunostaining of the anterior cruciate ligament (ACL) tibial enthesis in non-invasive mechanically loaded knee joints of collagen type II (COL2), SOX9, RUNX2 and ASPN expression. Representative images of: (A) Healthy non-loaded knee joints showed ACLs with COL2 staining in the fibrocartilagenous region and sparse SOX9, RUNX2 and ASPN staining. (B) Loaded OA knee joints had ACLs with COL2 depostion and high SOX9 and ASPN expression and faint RUNX2 expression in the tibial enthesis. Scale is 100 µm (10x) and 25 µm (40x).

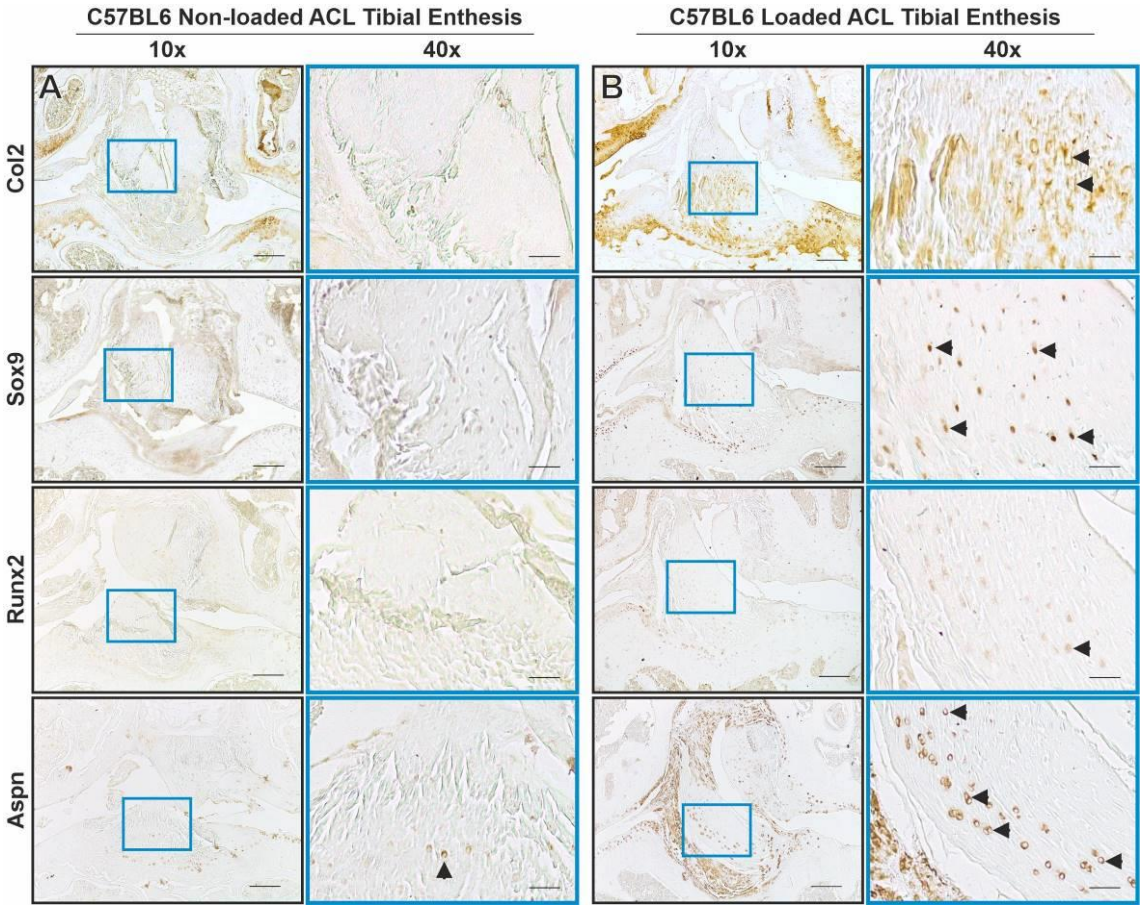

Figure 2.22 Immunostaining of the anterior cruciate ligament (ACL) mid-ligament region in non-invasive mechanically loaded knee joints of collagen type II (COL2), SOX9, RUNX2 and ASPN expression. Representative images of: (A) Healthy non-loaded knee joints had no COL2, SOX9 and RUNX2 staining in the mid-ligament region of the ACL and sparse ASPN staining. (B) OA loaded knee joints had ACLs with COL2 depostion and high SOX9 and ASPN expression throughout the mid-ligament region, and faint RUNX2 expression (black arrows). Scale is 100 µm (10x) and 25 µm (40x).

2.3.3.2 Non-invasive mechanically loaded medial collateral ligament (MCL) pathology

In the non-invasive mechanically loaded knee joint, OA cartilage degradation occurs mainly in the lateral compartment. However, the medial collateral ligament (MCL) was analysed to observe changes in the whole knee joint organ being a major stabiliser of the knee joint and the most injured ligament in the knee joint [172].

2.3.3.2.1 Toluidine blue staining

Toluidine blue staining of the non-loaded knee joint showed MCLs with an organised structure and alignment of the collagen fibres, spindle-shaped cells in the mid-ligament region (purple

arrow), and a delineated toluidine blue stain at the femur attachment site near the fibrocartilaginous zone (black arrow) (Figure 2.23A). Loaded knee joints four weeks post-trauma had MCLs with loss of the toluidine blue tide mark at the femoral enthesis and toluidine blue staining extending from the attachment site further into the MCL, and rounded cell morphology near the femoral enthesis (yellow arrows) (Figure 2.23B). Toluidine blue staining at the MCL femoral enthesis of the OA loaded knee joint could indicate potential proteoglycan deposition.

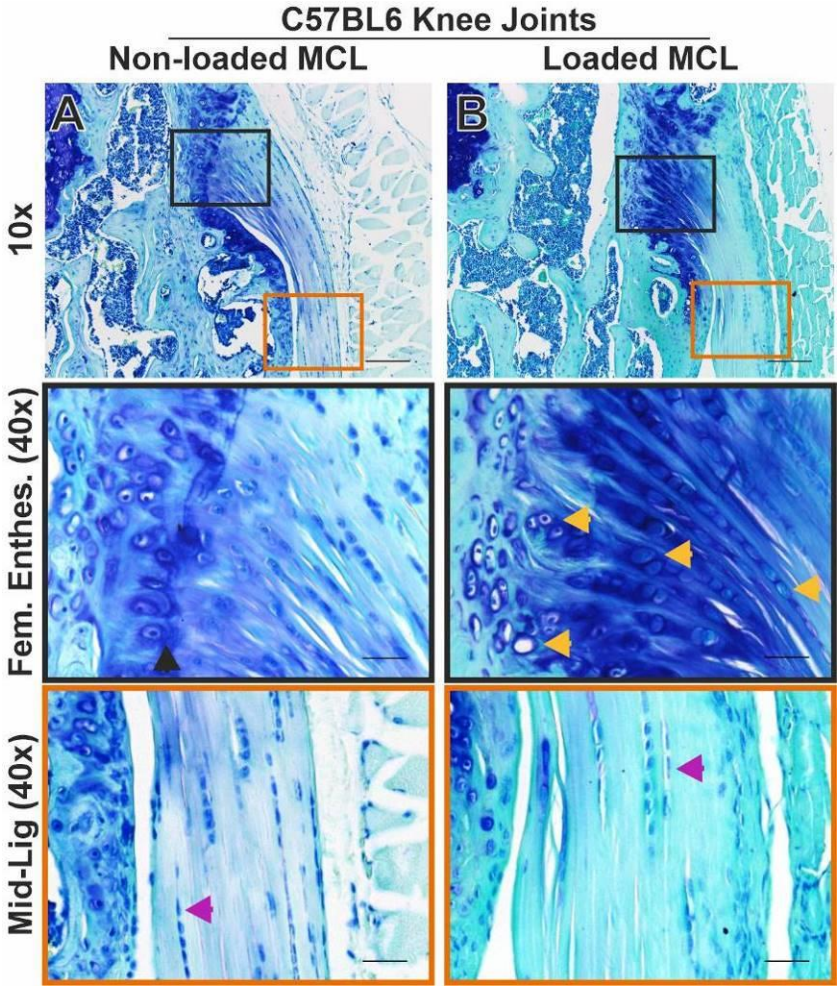

Figure 2.23 Histological staining of the medial collateral ligament (MCL) in non-invasive mechanically loaded knee joints. Representative images of: (A) Non-loaded healthy knee joints had MCLs with clear fibre and cell alignment and toluidine blue staining which delineated the fibrocartilage zone (black arrow), and spindle-shaped cells in the mid-ligament region (purple arrow). (B) OA loaded knee joints had MCLs with toluidine blue staining extending from the femoral attachment site near cells with rounded morphology (yellow arrows). Scale is 100 µm (10x) and 25 µm (40x).

2.3.3.2.2 PR staining

PR staining of the non-invasive loaded knee joint gave further evidence of collagen composition and birefringence. Healthy non-loaded knee joints had an organised MCL structure with light red collagen staining with rounded cell morphology in the fibrocartilaginous zone (yellow arrows) and spindle-shaped fibroblast in the mid-ligament region (green arrow) (Figure 2.24A). Polarised light of the non-loaded knee joints confirmed structured green birefringence by the enthesis and in the mid-ligament region and orange birefringence in the fibrocartilaginous zone (blue arrow) (Figure 2.24A). Four weeks following non-invasive mechanical loading of the knee joint, murine MCLs showed evidence of hyperplasia and increased red collagen staining at the femoral enthesis (yellow arrow) and in the outer epiligament layer in the mid-ligament region of the MCL (Figure 2.24B). Polarised light of these OA knee joints confirmed red birefringence near the MCL femoral attachment site and the outer epiligament layers in the mid-ligament region (blue arrows) (Figure 2.24B), which would suggest thicker collagen formation at both the MCL femoral enthesis and in the MCL mid-ligament region.

2.3.3.2.3 Immunostaining

Immunostaining was used to analyse specific OA markers in the loaded and non-loaded knee joints. Non-loaded knee joints had structured COL2 staining at the MCL femoral enthesis fibrocartilaginous zone, with sparse SOX9 and RUNX2 expression, and ASPN expression at the enthesis (black arrows) (Figure 2.25A). The mid-ligament region of the MCL in the non-loaded healthy knee joints showed no staining of COL2, SOX9, RUNX2 and ASPN (Figure 2.25A). The loaded knee joints post-trauma showed COL2 encroaching from the MCL femoral enthesis and reaching the mid-ligament region (Figure 2.25B). Cellular expression of SOX9 and RUNX2, as well as pericellular expression of ASPN was increased in the MCL femoral enthesis (black arrows) (Figure 2.25B). Furthermore, there was SOX9 and ASPN expression in the mid-ligament region of the MCL (black arrows) (Figure 2.25B). Immunostaining at the MCL femoral enthesis in the OA loaded knee joints confirmed changes in the COL2 matrix composition and expression of SOX9 and RUNX2 suggest chondrogenesis and hypertrophy.

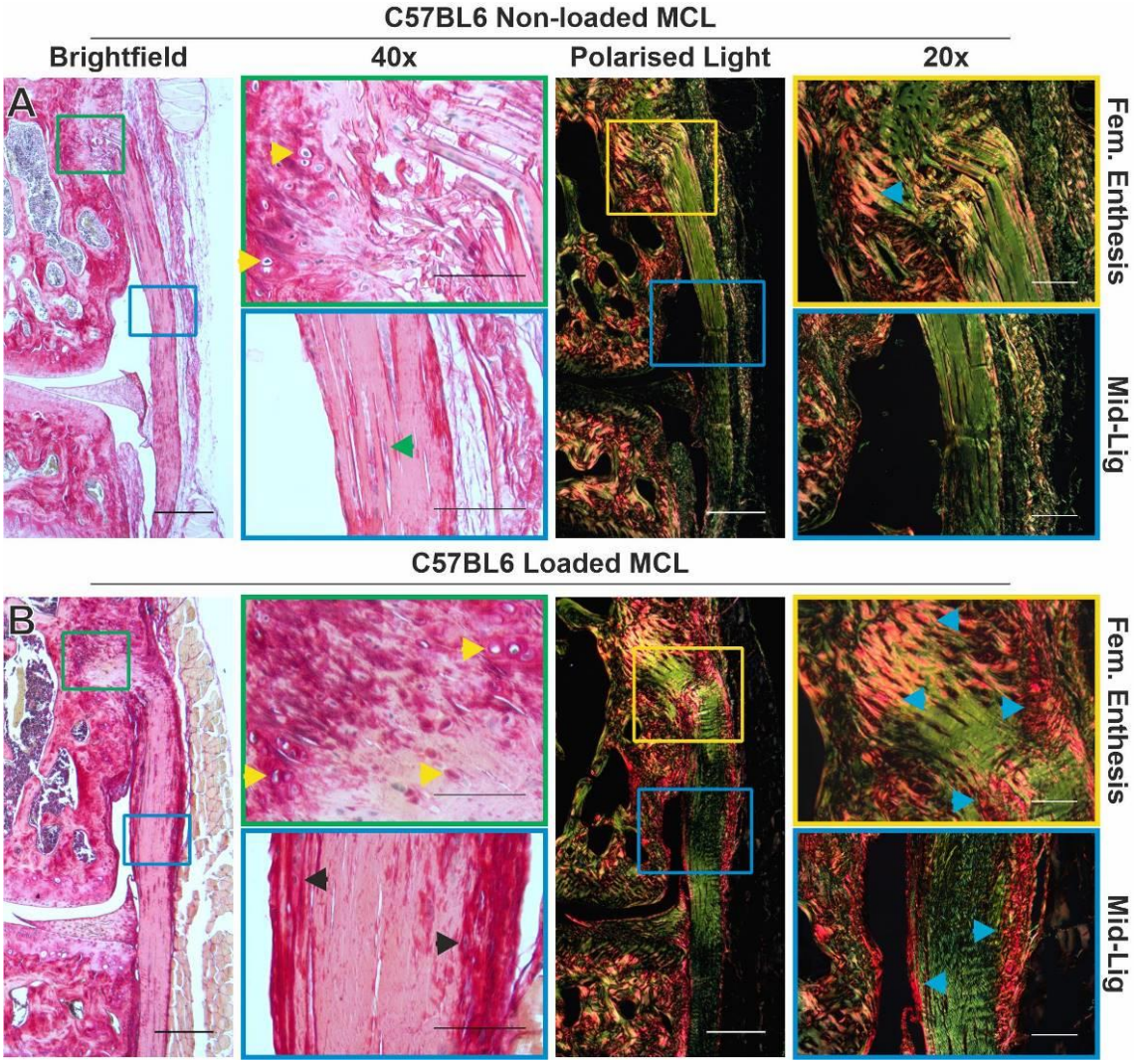

Figure 2.24 Histological staining of the medial collateral ligament (MCL) in non-invasive mechanically loaded knee joints using picrosirius red. Representative images of: (A) Healthy non-loaded knee joint showed light red staining in the MCL, with dark red staining at the fibrocartilaginous zone of the femoral enthesis (yellow arrows). Polarised light showed green birefringence throughout the MCL and orange birefringence near the femoral enthesis. (B) OA loaded knee joint showed hyperplasia near the femoral attachment site with dark red staining (yellow arrows). Polarised light showed red birefringence near the femoral enthesis and in the outer zone of the mid-ligament region in areas of hyperplasia (blue arrows). Scale is 200 µm (4x) and 50 µm (20x, 40x).

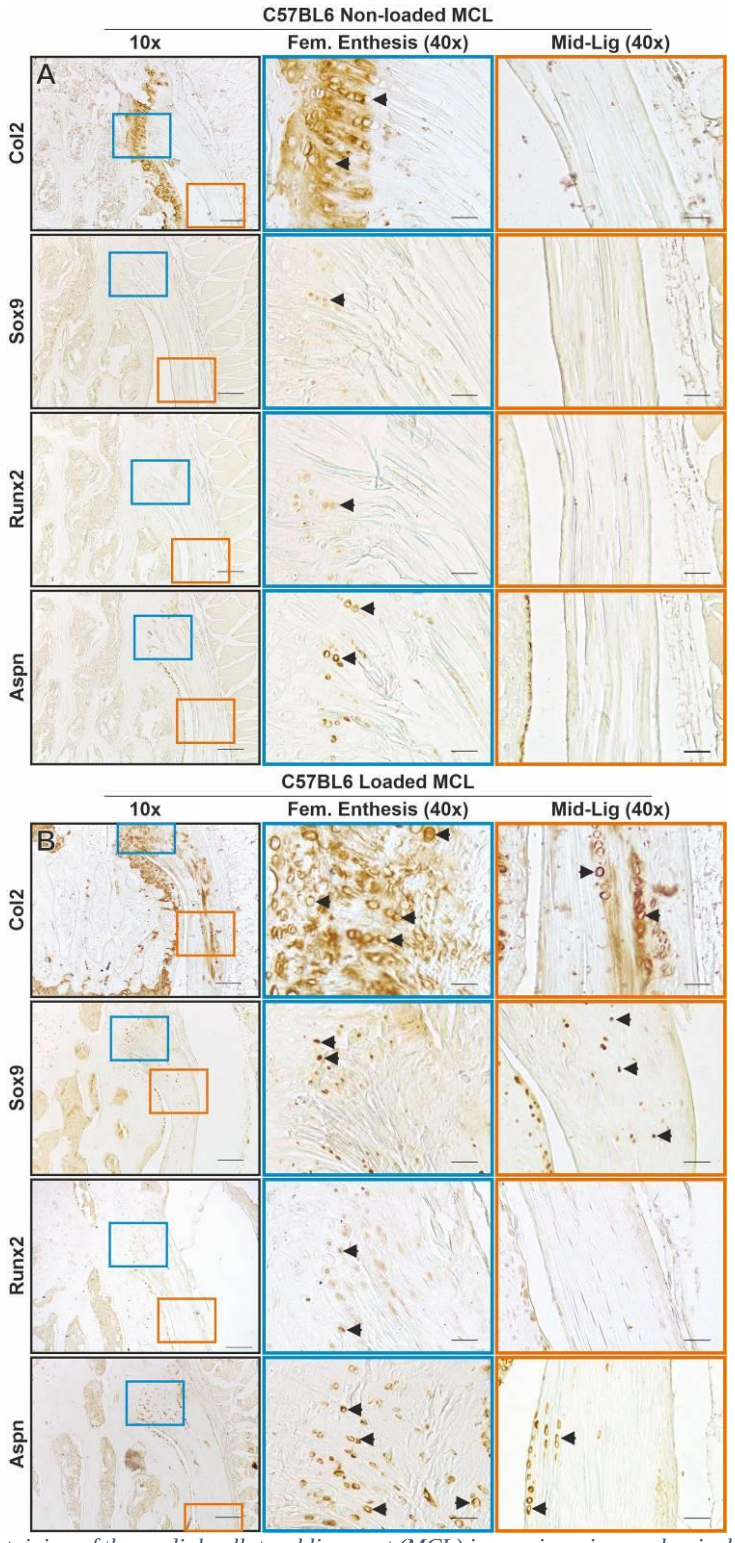

Figure 2.25 Immunostaining of the medial collateral ligament (MCL) in non-invasive mechanically loaded knee joints. Representative images of: (A) Healthy non-loaded knee joints had an MCL with structured COL2 deposition at the fibrocartilaginous zone of the femoral enthesis, and sparse SOX9, RUNX2 and ASPN staining (black arrows). In the mid-ligament region of the hleahty MCL, no COL2, SOX9, RUNX2 and ASPN staining was found. (B) OA loaded knee joint MCLs showed COL2 deposition which extended from the femoral enthesis into the MCL, as well as SOX9, RUNX2 and ASPN expression at the femoral enthesis (black arrow). The mid-ligament region also had COL2 deposition and SOX9 and ASPN expression (black arrows). Scale is 100 µm (10x) and 25 µm (40x).

2.3.3.3 Non-invasive mechanically loaded knee joint lateral menisci pathology

OA occurs mainly in the lateral compartment of the non-invasive mechanically loaded knee joint; hence the lateral menisci was analysed for OA pathology.

2.3.3.3.1 Toluidine blue staining

The lateral menisci of the healthy non-loaded joints demonstrated the expected meniscal structure, with hyaline cartilage layers (H), a central ossified region (O, orange region) and an outer fibrous region (F, red region) (Figure 2.26A). In the loaded knee joints post-trauma, the lateral menisci showed elongation of the central ossified region (Figure 2.26B). The fibrous region of the loaded knee joint lateral menisci showed a structure and rounded-cell morphology (black arrow) similar to the non-loaded knee joint (Figure 2.26B). Toluidine blue showed evidence of elongation of the ossified core of the lateral menisci in the loaded knee joints.

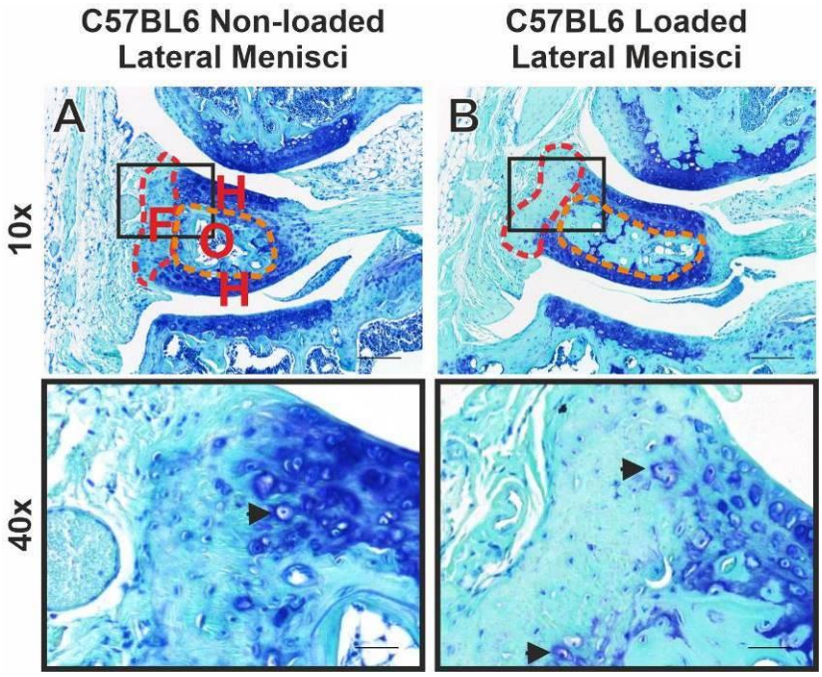

Figure 2.26 Histological staining of the lateral menisci in the non-invasive mechanically loaded knee joints using toluidine blue. Representative images of: (A) Healthy non-loaded knee joints had lateral menisci with toluidine blue staining the in outer hyaline cartilage layers (H) of the menisci and showed the expected ossified core (O) and fibrous region (F). (B) Loaded knee joints after four weeks post-trauma had lateral menisci with an expanded ossified core but similar toluidine blue staining. Fibrous region of the non-loaded and loaded knee joints showed similar structures with rounded-cell morphology only near the hyaline cartilage layers. Scale is 100 µm (10x) and 25 µm (40x).

2.3.3.3.2 Immunostaining

Immunostaining of the non-loaded healthy knee joints had lateral menisci with COL2 deposition in the previously mentioned hyaline cartilage region and ASPN expression in the outer meniscal regions (Figure 2.27A). Loaded knee joints post-trauma, showed a slight increase in COL2, SOX9 and ASPN expression in the upper fibrous region (black arrows) and also ASPN expression seemed to increase in the outer fibrous region near the capsular attachment (red arrow) (Figure 2.27B). Immunostaining showed only minor changes in matrix (COL2) and marker expression (SOX9 and ASPN) in the upper fibrous region of the lateral menisci of the loaded knee joint post-trauma.

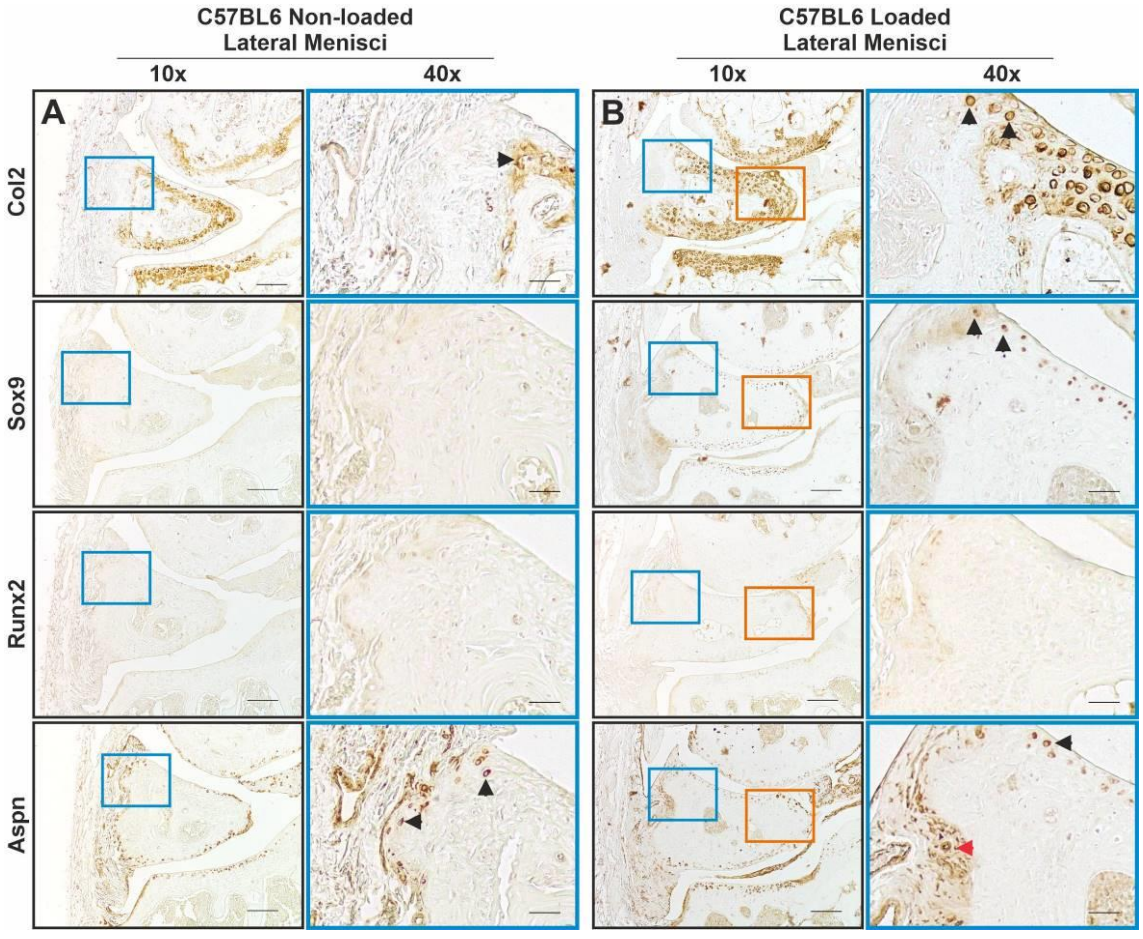

Figure 2.27 Immunostaining of the lateral menisci in non-invasive mechanically loaded knee joints of collagen type II (COL2), SOX9, RUNX2 and ASPN expression. Representative images of: (A) Healthy non-loaded knee joints had lateral menisci with col2 and ASPN staining in the hyaline cartilage region, and no SOX9 and RUNX2 staining. (B) Loaded knee joint post-trauma, had lateral menisci with COL2 deposition, SOX9 and ASPN staining extending from the hyaline cartilage region into the upper fibrous region (black arrows). There was also ASPN staining in the outer fibrous region near the capsular attachment. Scale is 100 µm (10x) and 25 µm (40x).

2.3.3.4 Summary of the non-invasive mechanically loaded knee joint OA pathology

In the non-invasive mechanically loaded knee joints we found structural and cellular changes in the ACL and MCL that emerged post-trauma. In the ACL of the mechanically loaded knee joints, there was toluidine blue staining, red collagen birefringence and rounded-cell morphology at the fibrocartilaginous zone of the ACL tibial enthesis, while the mid-ligament region also had toluidine blue staining and green collagen birefringence. In the MCL of the mechanically loaded knee joints, toluidine blue and red birefringence was present at the femoral enthesis and red birefringence was also present in the epiligament layer of the MCL mid-ligament region in areas of hyperplasia. In both the ACL and MCL of the mechanically loaded knee joints, there was COL2 deposition near the enthesis (ACL: tibial enthesis, MCL: femoral enthesis) and mid-ligament region, as well as SOX9 and ASPN expressing cells in the same regions. Lastly, in the lateral menisci of the mechanically loaded knee joints there was elongation of the ossified meniscal core. Overall, pathological changes in the ACL and MCL of mechanically loaded knee joints included changes in the matrix composition at the enthesis and mid-ligament regions and cellular marker expression.

.

2.3.4 Confirmation of a new OA model: CD1 murine model of spontaneous OA

As previously mentioned, CD1 mice are a novel spontaneous OA model. Briefly, CD1 OA knee joint pathology that has previously been described included cartilage degeneration, subchondral bone thickening and synovial hyperplasia mainly in the medial compartment of male 1-year-old CD1 mice [154]. Meniscal or knee ligament pathology in CD1 mouse knee joints have not been described to date. Therefore, we evaluated meniscal and knee ligament health and pathology during early OA development in this novel model, comparing younger 12-week-old male CD1 mice to older 24-week-old male CD1 mice. Younger 12-week-old CD1 mice were chosen as the control due to the heavy bodyweight of the CD1 mouse strain. CD1 bodyweight did increase during ageing with 24-week-old CD1 mice being heavier (14.2% weight difference) compared to the younger 12-week-old CD1 mice (Figure 2.28A).

2.3.4.1 Characterisation of OA in CD1 knee joints

2.3.4.1.1 Toluidine blue OA scoring

OA development was confirmed via the OARSI cartilage grading system and µCT quantification of joint space mineralisation. In the 24-week-old CD1 knee joints (n=10) there was significant cartilage degeneration, with cartilage lesions present in all mice and greater than 25% compartmental cartilage erosion (OA grade 4) occurring in 50% of the mice (Figure 2.28). This severe cartilage loss has not been previously reported at these time points in healthy mice knee joint including in CBA mice [158] and C57 mice [154, 173], but is comparable to spontaneous OA STR/ort mice knee scores which had cartilage erosion (OA grade 3) at 40-weeks-old [158].

In the 24-week-old CD1 knee joints, more cartilage lesions were seen in the medial compartment than in the 12-week-old CD1 knee joints (Figure 2.28C). In the medial tibial compartment, the maximum OA score was 0.3 ±0.2 and 3.1 ±0.6 for the 12 and 24-week-old CD1 knee joints respectively (Figure 2.28D). This is equivalent to no cartilage lesions in the 12-week-old knee joints, and up to 20% of articular cartilage loss in the 24-week-old knee joints in the medial tibial compartment of the CD1 mice. Furthermore, when comparing all knee compartments (whole joint), 50% (n=5) of the 24-week-old CD1 knee joints showed greater than 20% of articular cartilage loss (maximum OA score >3) (Figure 2.28F). The maximum score for the whole joint of the 24-week-old CD1 mice was 3.4 ±0.8 (Figure 2.28F), which is comparable to the maximum score of the STR/ort spontaneous OA mouse knee joint which was 2.6 ±1.1 at 26-weeks and also showed greater OA severity in the medial compartments [165]. Cartilage loss was not seen in the

CBA [153] and C57BL/6J [173] mice knee joints at 24-weeks, therefore this would suggest that the CD1 mice have early OA development similar to that of spontaneous OA models.

When comparing the 12 and 24-week-old knee joints of the CD1 mice, the mean and maximum score of the whole joint demonstrated significant increases ($p \leq 0.001$ and $p \leq 0.0001$ respectively) in the OA score of the 24-week-old CD1 mice knee joints (Figure 2.28E-F). The same was true for the summed mean and summed maximum OA scores of the whole joint which also confirmed significant increases ($p \leq 0.001$ for both) in the OA score of the 24-week-old CD1 knee joint (Figure 2.28G-H). OARSI cartilage scoring confirmed that OA development in the knee joints of 24-week-old CD1 mice was significantly higher than in the younger 12-week-old CD1 mice. 24-week-old CD1 mice knee joints had greater variation of OA score as the maximum overall OARSI score varied from 0 to 1 in the 12-week-old CD1 knee joints and from 1 to 6 in the 24-week-old CD1s (Figure 2.28F). This variation is equivalent to healthy thick cartilage seen in most young CD1s (OA score 0), to minor fibrillations in the cartilage (OA score 1), to complete loss of AC and subchondral bone exposure (OA score 6, maximum score) in some of the older CD1 mice knee joints (see Figure 2.28B). Overall, OA progression was demonstrated in the 24-week-old CD1 mice knee joints, particularly in the medial compartment.

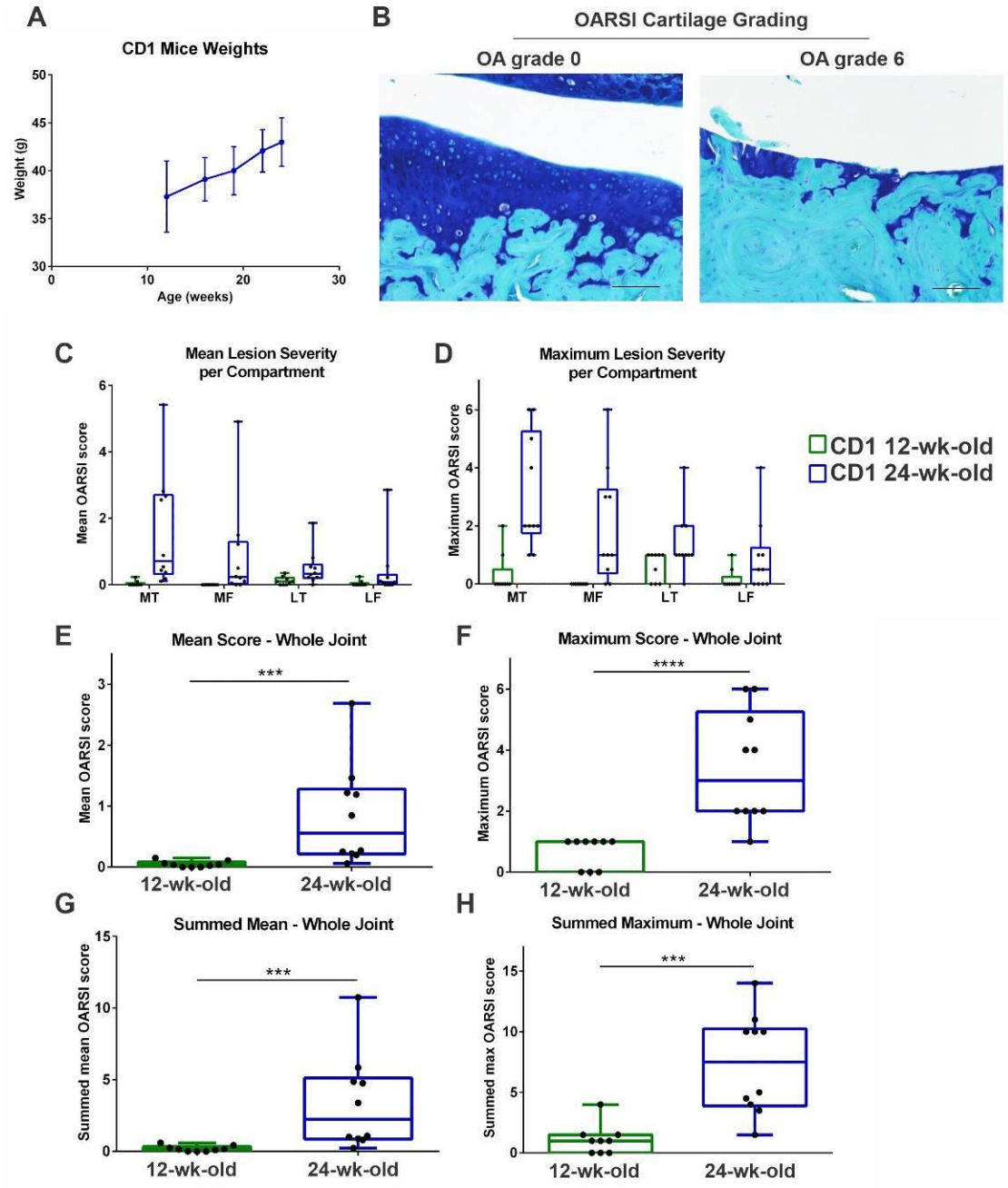

Figure 2.28 Mice bodyweights and OARSI cartilage scoring of 12 and 24-week-old CD1 mice. (A) CD1 mice weights increased 14.2% in the 24-week-old CD1 compared to the 12-week-old CD1 mice. (B) OARSI cartilage lesion scoring ranged from of healthy cartilage (OA grade 0) to complete loss of articular cartilage (OA grade 6). Scale is 50 µm. (C-D) Mean and maximum OARSI cartilage score per compartment revealed higher mean and maximum scores in the medial compartments (MT and MF) of the 24-week-old CD1 knee joints compared to the lateral compartments (LT and LF). (E-F) Mean and maximum OARSI score of the whole joint was significantly higher in the 24-week-old CD1 mice knee joints ($p \leq 0.001$ and $p \leq 0.0001$ respectively). (G-H) Summed mean and maximum OARSI scores of the whole joint confirmed significantly higher scores in the 24-week-old CD1s ($p \leq 0.001$ for both). Unpaired non-parametric Mann-Whitney test was used for statistical analysis.

2.3.4.1.2 Joint space mineralisation analysis

Quantification of joint space mineralisation using µCT was significantly increased ($p \leq 0.001$) in the 24-week-old CD1 mice knee joints compared to the younger 12-week-old knee joints (Figure 2.29A). 3D µCT images revealed increased mineralisation in the medial side of the 24-week-old CD1 mice (Figure 2.29B). More specifically, mineralisation can be seen in the anterior and posterior horn of the medial menisci (orange arrows) and in the medial collateral ligament (blue arrows) at both OA grade 4 and 6 (Figure 2.29B). This is similar to the findings from the OARSI cartilage score which increased in the medial compartment of the 24-week-old CD1 knee joints (Figure 2.28C-D). Joint space mineralisation has been previously associated with OA progression [165]. OARSI scoring and µCT joint space mineralisation confirmed OA development in the 24-week-old CD1 mice compared to the 12-week-old mice.

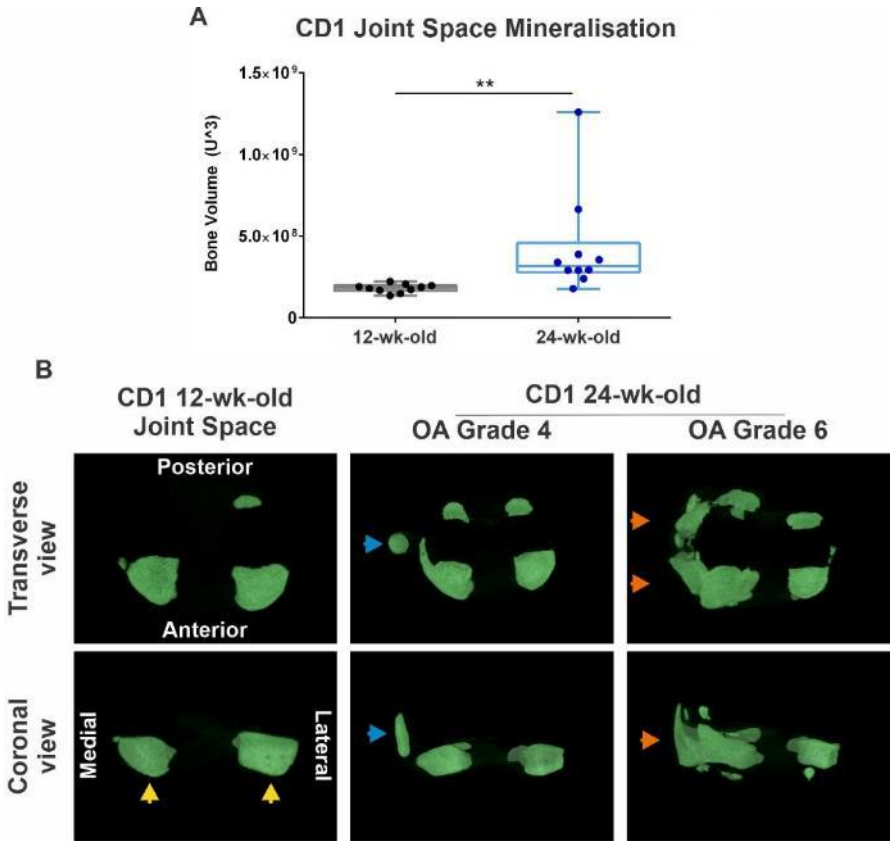

Figure 2.29 Knee joint space mineralisation in 12 and 24-week-old CD1 mice. (A) Quantification of joint space mineralisation showed significantly higher bone volume in the 24-week-old CD1 mice ($p \leq 0.001$). Unpaired non-parametric Mann-Whitney test was used for statistical analysis. (B) 3D reconstruction of µCT images of joint space showed mineralisation in the anterior horn of the medial and lateral menisci of the 12-week-old CD1 mice (yellow arrows). Increased mineralisation was visible in the OA grade 4 and 6 CD1 24-week-old medial collateral ligament (blue arrows) and in the medial menisci (orange arrows).

2.3.4.2 Knee ligament and meniscal pathology in the CD1 OA mouse model

CD1 mice histological analysis included toluidine blue, PR and immunostaining of the ACL, MCL and medial menisci. The medial collateral ligaments and menisci were analysed as OARSI cartilage lesion severity (Figure 2.28) and µCT joint space mineralisation (Figure 2.29) was higher in the medial femorotibial compartments. The ligaments and menisci of the 24-week-old CD1 knee joints were categorised based on OA score and compared to the healthy 12-week-old CD1 mice knee joints, allowing for description of structural and cellular changes during OA progression.

2.3.4.3 CD1 mice anterior cruciate ligament (ACL) pathology

2.3.4.3.1 Toluidine blue staining

Toluidine blue staining was used to analyse ACL structure and cellular morphology in 12-week-old and 24-week-old CD1 knee joints. 12-week-old CD1 murine knee joints had an organised ACL structure with aligned collagen fibres and toluidine blue staining extending from the attachment site to the mid-ligament region (Figure 2.30A). The tibial attachment site had a delineated fibrocartilaginous zone (black arrow) with rounded-shaped cells (yellow arrow), and spindle-shaped cells (purple arrow) in the mid-ligament region (Figure 2.30A). In the 24-week-old CD1 knee joints with OA grade 4, ACL structure and cell morphology were irregular, and changes included misalignment of the fibres and an increase in the 'rounded' cell types near the tibial attachment site and in the mid-ligament region (yellow arrows) (Figure 2.30B). In OA grade 6 CD1 knee joints, the ACL had complete toluidine blue staining in all regions of the ligament, suggestive of substantial proteoglycan deposition, and 'rounded' cell types near the tibial attachment site (Figure 2.30C). It is worth noting that the ACL displayed better fibre alignment in the OA grade 6 knee joints compared to the OA grade 4 knee joints, (Figure 2.30B-C), which demonstrates the variability of ACL pathology in this CD1 spontaneous OA model.

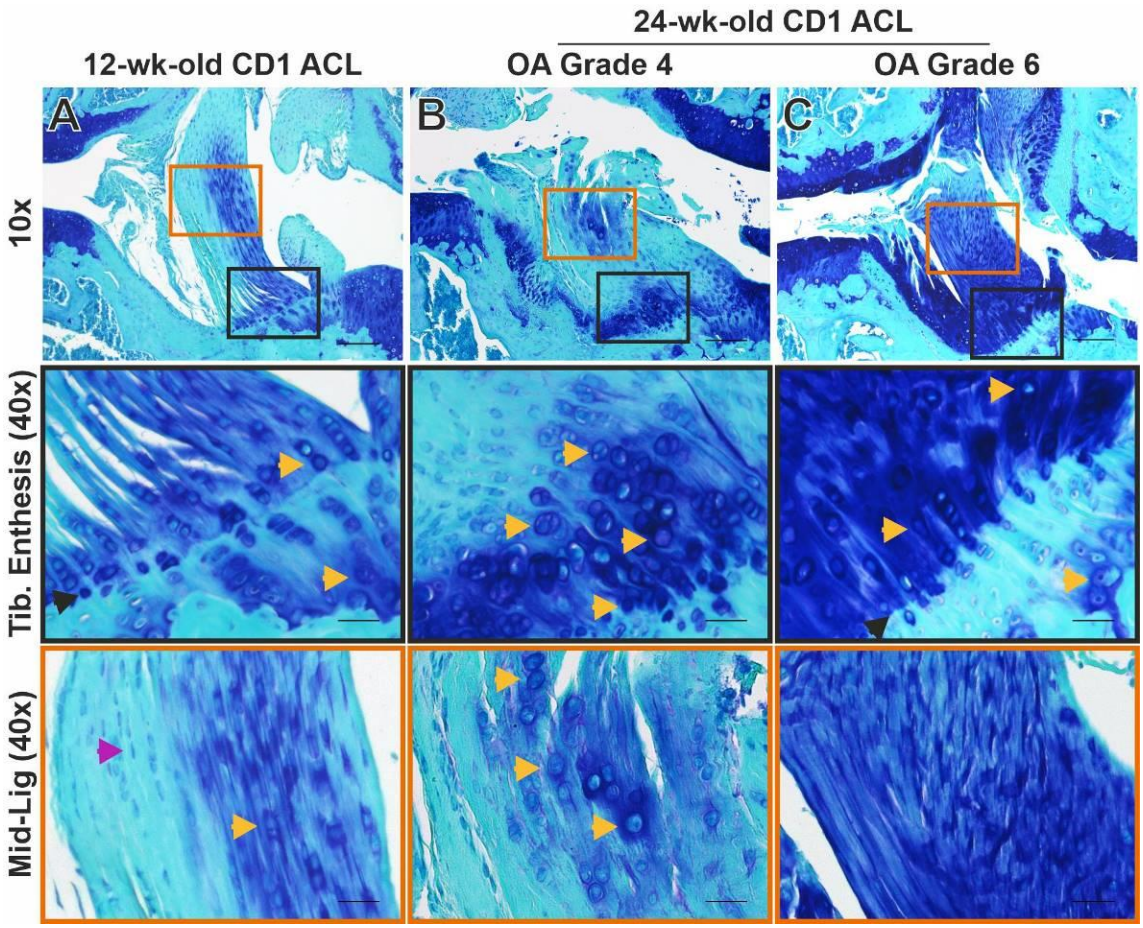

Figure 2.30 Histological staining of the anterior cruciate ligament (ACL) in CD1 mice using toluidine blue staining. Representative images of: (A) Healthy 12-week-old CD1 ACL had fibre alignment and some toluidine blue staining extending from the tibial enthesis to the mid-ligament region. The delineated fibrocartilaginous zone (black arrow) had rounded cell morphology (yellow arrows) and the mid-ligament region had spindle-shaped fibroblasts (purple arrow) and some rounded-cell types (yellow arrow). (B) CD1 OA grade 4 ACL had severe fibre misalignment, and toluidine blue and rounded-cell morphology in the mid-ligament region (yellow arrows). (C) CD1 OA grade 6 ACL had toluidine blue staining throughout the ligament, as well as cells with rounded-cell morphology at the tibial enthesis (yellow arrow). Scale is 100 µm (10x) and 25 µm (40x).

2.3.4.3.2 PR staining

PR staining was used to analyse collagen birefringence in the ACL of 12-week-old and 24-week-old CD1 knee joints. CD1 12-week-old mice had an organised ACL with light red collagen staining and polarised light showed green birefringence throughout the ACL and yellow birefringence near the tibial enthesis (blue arrow) (Figure 2.31A). CD1 24-week-old OA grade 4 knee joints had ACLs with structural changes, including extensive red collagen staining, rounded cell morphology (yellow arrows) and red birefringence throughout the ACL, (Figure 2.31B). In CD1 knee joints with OA grade 6, polarised light showed green birefringence in the mid-ligament region with red birefringence in the outer epiligament layers of the ACL (Figure 2.31D). Collagen birefringence in 24-week-old CD1 ACLs varied independent of OA grade.

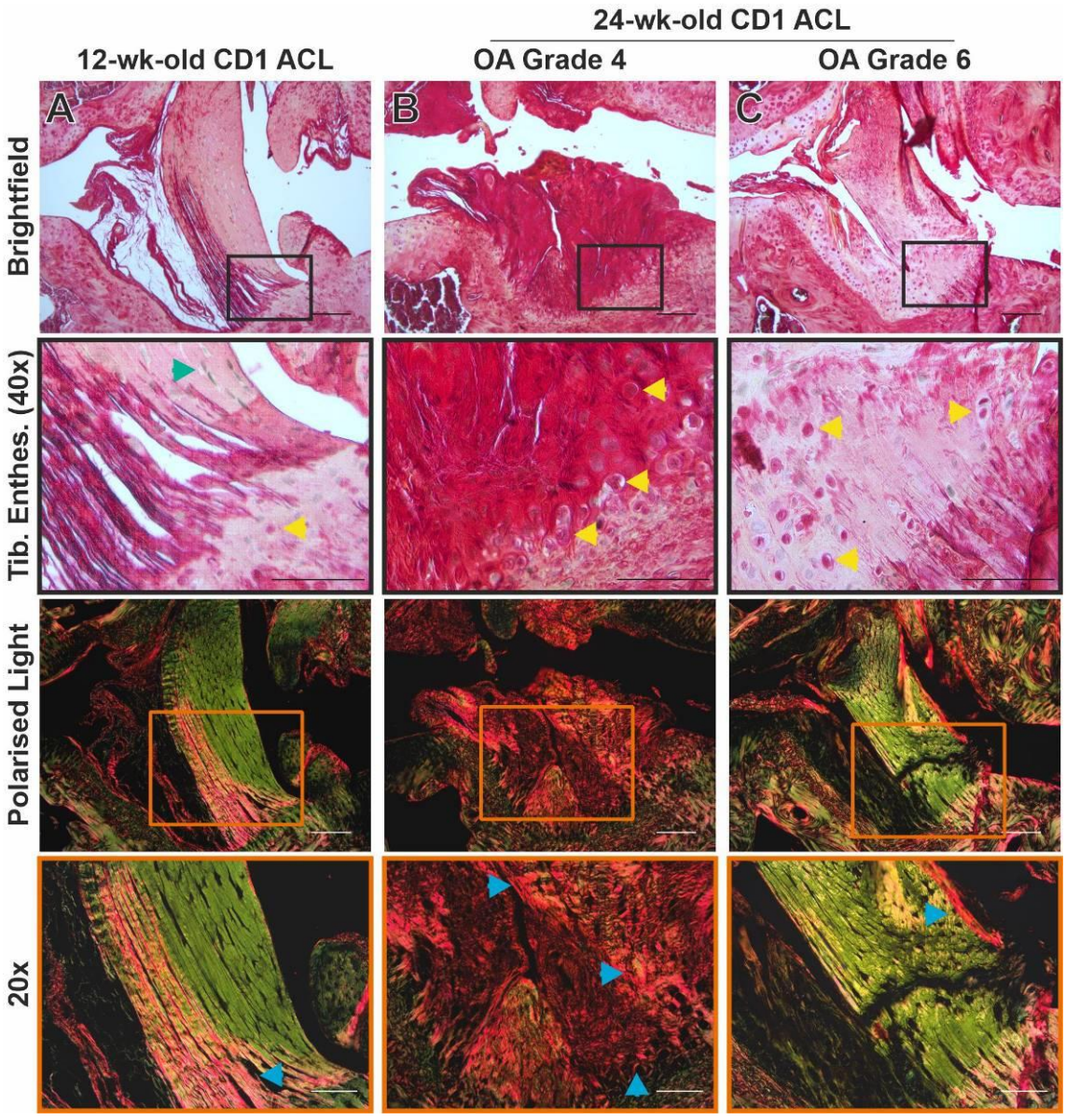

Figure 2.31 Histological staining of the anterior cruciate ligament (ACL) in CD1 knee joints using picrosirius red. Representative images of: (A) Healthy 12-week-old CD1 ACL showed light red staining within the ACL and darker red staining near the tibial enthesis near spindle-shaped fibroblasts (green arrow). Polarised light showed mainly green birefringence and some yellow birefringence near the tibial attachment site (blue arrow). (B) OA grade 4 CD1 knee joints had ACLs with dark red collagen staining and rounded cell morphology (yellow arrows) throughout the ligament. Polarised light showed red birefringence throughout the ACL (blue arrows). (C) CD1 OA grade 6 ACL had light red collagen staining and thick fibrocartilaginous zone with rounded-shaped cells (yellow arrows). Polarised light showed mainly green birefringence throughout the ACL with red birefringence in the outer epiligament layer (blue arrow). Scale is 100 µm (10x) and 50 µm (20x, 40x).

2.3.4.3.3 Immunostaining

Immunostaining was used to compare COL2 staining and SOX9, RUNX2 and ASPN expression in the ACLs of 12-week-old and 24-week-old CD1 knee joints. Healthy 12-week-old CD1 ACLs had COL2 staining in the fibrocartilaginous enthesis extending towards the ligament, along with sparse SOX9 and ASPN staining at the enthesis (black arrows) (Figure 2.32A). In OA grade 4 knee joints of 24-week-old CD1 mice, there was a distinct layer of COL2 deposition at the fibrocartilaginous zone of the ACL tibial enthesis, along with prevalent SOX9, RUNX2 and ASPN expression in the same fibrocartilaginous region (black arrows) (Figure 2.32B). COL2, SOX9, RUNX2 expression extended to the ACL fibroblast near the tibial enthesis (purple arrow) (Figure 2.32B), as well as in an inflamed disorganised region adjacent to the tibial enthesis (black arrow) (Figure 2.32B, inflamed region). In OA grade 6 CD1 knee joints, COL2 deposition increased in a dense fibrocartilaginous layer at the ACL tibial enthesis (black arrow) and in adjacent tissue surrounding the ACL tibial enthesis (red arrow) (Figure 2.32C). Additionally, SOX9, RUNX2 and ASPN were only present in sparse areas near the ACL tibial enthesis (Figure 2.32C).

In the ACL mid-ligament region of the healthy 12-week-old CD1 knee joints, COL2 staining was found, however SOX9, RUNX2 and ASPN were not present (Figure 2.34A). Similarly, in OA grade 5 CD1 knee joints, COL2 deposition was found in the mid-ligament region of the ACL of (black arrows) and in the epiligament region of the ACL (Figure 2.34B).

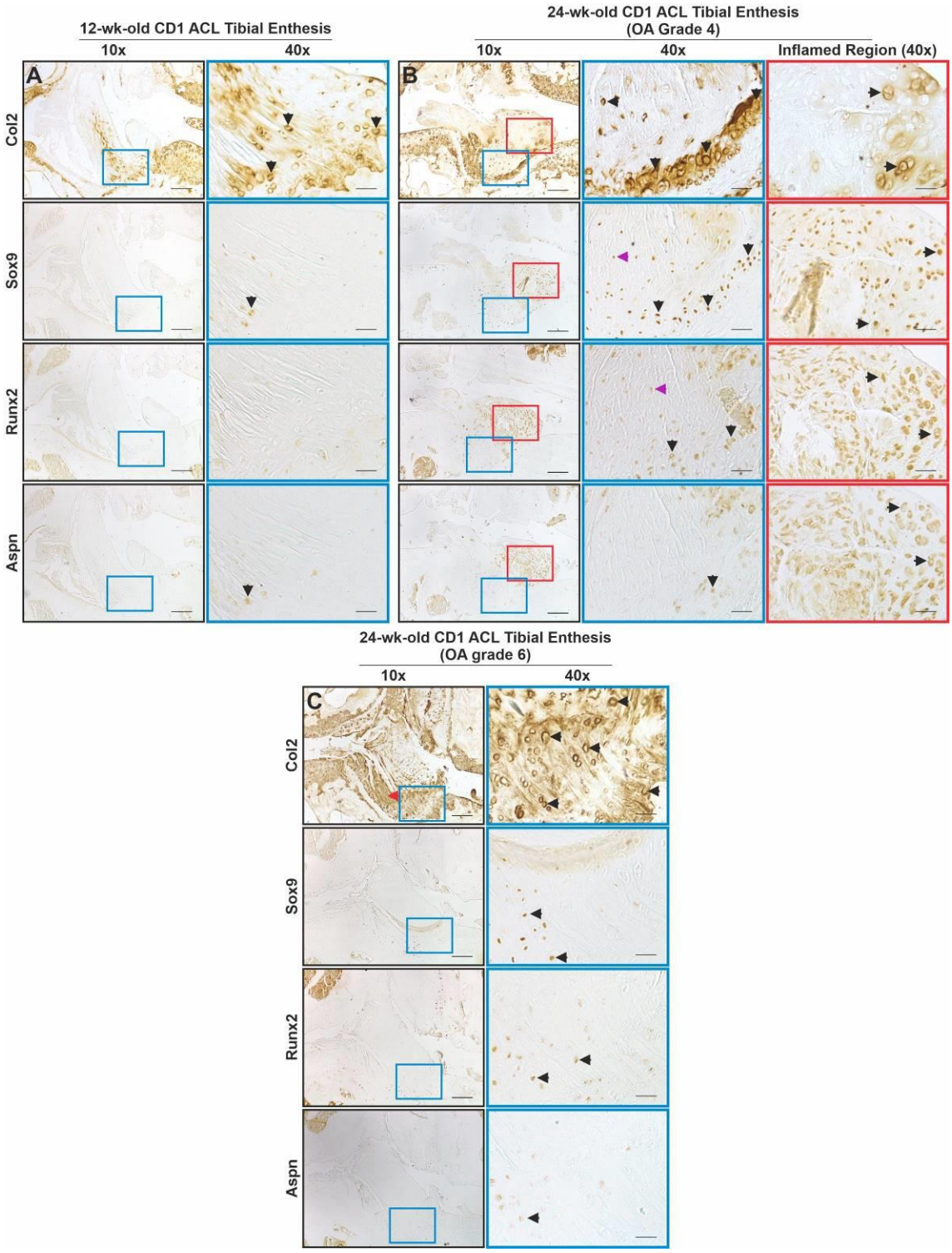

Figure 2.32 Immunostaining of the anterior cruciate ligament (ACL) tibial enthesis in CD1 knee joints. Representative images of: (A) Healthy 12-week-old CD1 ACL showed some COL2 deposition extending from the tibial enthesis along with sparse SOX9 and ASPN expression. (B) OA grade 4 CD1 ACLs had a thick layer of COL2 deposition at the tibial enthesis as well as SOX9 and RUNX2 expression (black arrows) which extended further into the ACL ((purple arrows). (C) OA grade 6 CD1 ACL had a dense layer of COL2 deposition at the tibial enthesis and sparse SOX9, RUNX2 and ASPN expression. Scale is 100 µm (10x) and 25 µm (40x).

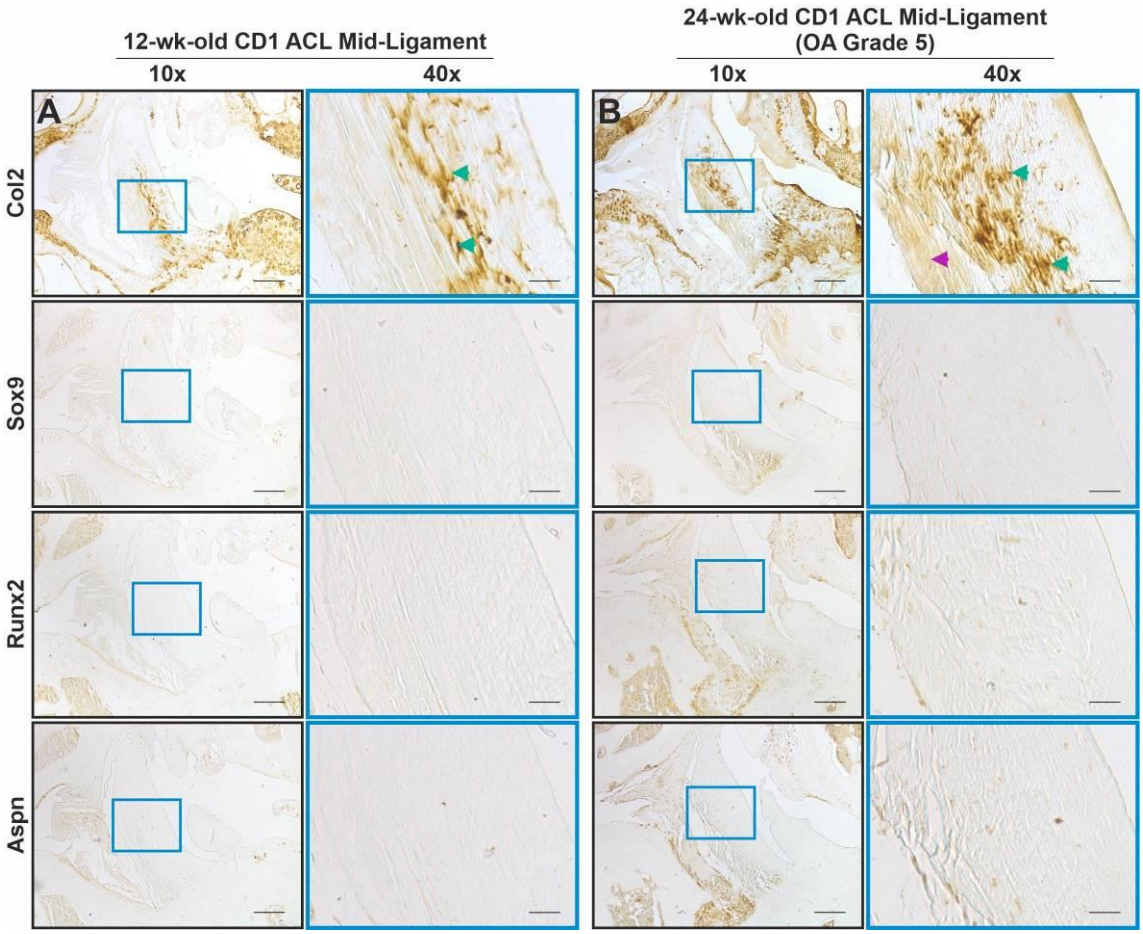

Figure 2.33 Immunostaining of the anterior cruciate ligament (ACL) mid-ligament region in CD1 knee joints. Representative images of: (A) Healthy 12-week-old CD1 ACL showed COL2 deposition in the mid-ligament region. SOX9, RUNX2 and ASPN were not expressed. (B) Similarly, OA grade 5 CD1 had COL2 deposition in the ACL mid-ligament region and no SOX9, RUNX2 and ASPN expression as well as COL2 staining in the epiligament region (purple arrow). Scale is 100 µm (10x) and 25 µm (40x).

2.3.4.4 CD1 mice medial collateral ligament (MCL) pathology

2.3.4.4.1 Toluidine blue staining

Toluidine blue staining of the MCLs from CD1 mice showed changes in the 24-week-old experimental group compared to the 12-week-old mice. The 12-week-old CD1 MCLs showed organised collagen fibre alignment and some toluidine blue staining at the tibial enthesis (yellow arrows) (Figure 2.34A). Meanwhile, the 24-week-old CD1 knee joints had MCLs with evidence of hyperplasia, toluidine blue staining (red arrows) and potential ossification (red region) (Figure 2.34B-C). OA grade 4 CD1 knee joints showed potential ossification near the MCL tibial enthesis, as well as some rounded-cell morphology in the MCL mid-ligament region (yellow arrow) (Figure 2.34B). OA grade 6 CD1 MCL presented severe hyperplasia with complete loss of fibre

arrangement, increased ‘rounded’ cell morphology near the tibial attachment site and in the mid-ligament region and possible bone formation in the mid-ligament region (Figure 2.34C).

2.3.4.4.2 PR staining

PR staining in the healthy 12-week-old CD1 mice had a light red staining and polarised light demonstrating a structured green birefringence at the MCL femoral attachment site with red birefringence in the upper epiligament layer (blue arrow) (Figure 2.35A). The MCL mid-ligament region of the 12-week-old CD1 mice had dark green birefringence (Figure 2.35A). OA grade 4 24-week-old CD1 mice showed dark red collagen staining throughout the MCL (yellow arrows) which correlated to red birefringence (blue arrows) (Figure 2.35B). OA grade 6 CD1 MCLs also showed dark red collagen staining, and a mixture of green and red birefringence mainly in areas of hyperplasia (blue arrows) (Figure 2.35C). Red birefringence in the OA MCLs indicate thicker collagen fibres not seen in the healthy 12-week-old MCLs.

2.3.4.4.3 Immunostaining

Immunostaining of healthy 12-week-old CD1 knee joints demonstrated an MCL femoral enthesis with organised COL2 staining and sparse expression of SOX9, RUNX2 and ASPN (Figure 2.36A). Additionally there was no presence of COL2, SOX9, RUNX2 or ASPN staining in the healthy MCL mid-ligament region. OA grade 4 CD1 knee joints had an MCL femoral enthesis similar to the healthy 12-week-old CD1 mice, however COL2 deposition, along with SOX9, RUNX2 and ASPN expression were evident in the MCL mid-ligament region (black arrows) (Figure 2.36B). OA grade 6 CD1 knee joints, COL2, SOX9, RUNX2 and ASPN staining was present near the MCL femoral enthesis and the MCL mid-ligament region, particularly in cells with ‘rounded’ morphology (black arrow) and in the outer epiligament layer (purple arrow) (Figure 2.37). Immunostaining indicates changes in COL2 deposition in the diseased MCLs of the CD1 mice, as well as changes in cellular markers indicating chondrogenesis and potential hypertrophy.

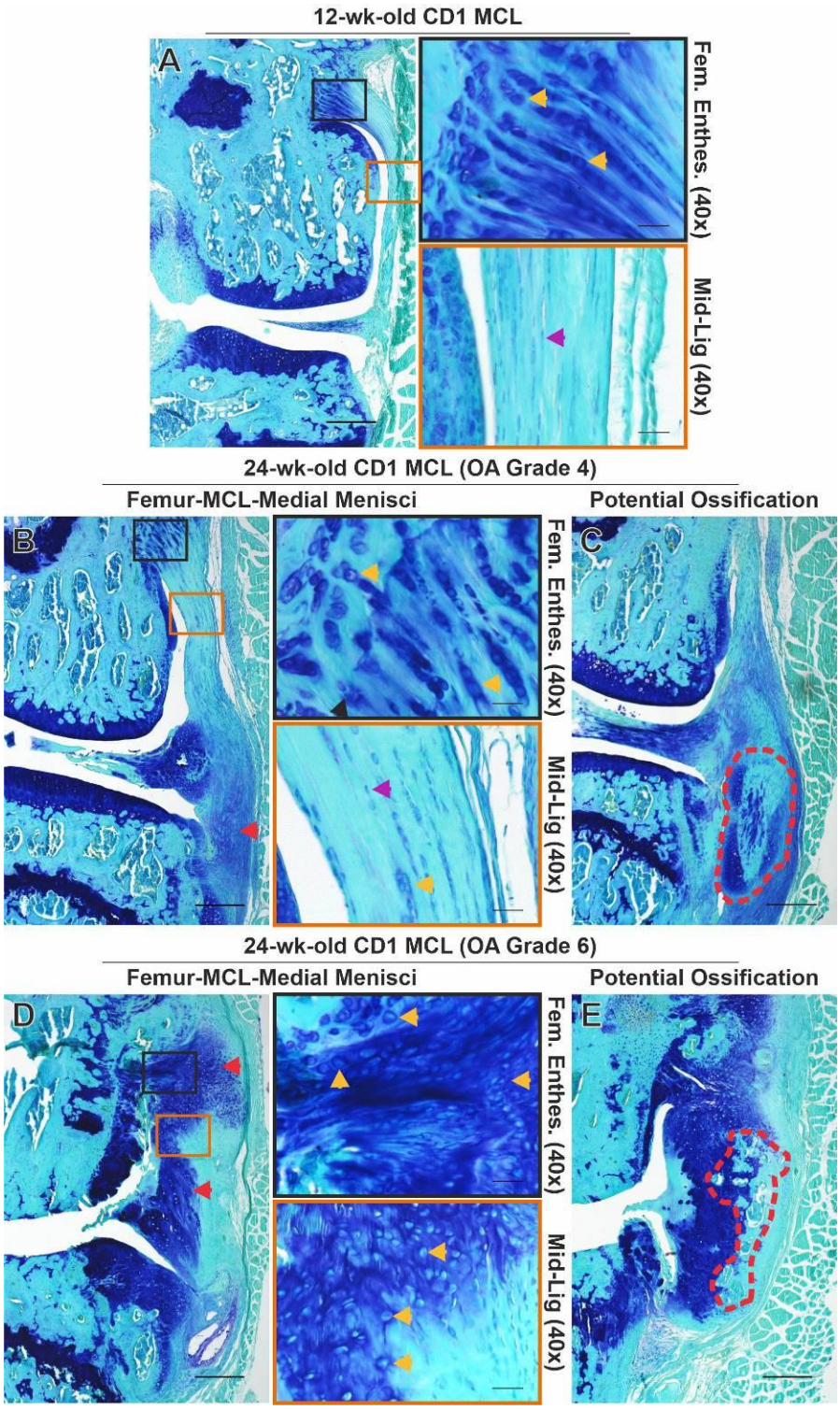

Figure 2.34 Histological staining of the medial collateral ligament (MCL) in CD1 knee joints using toluidine blue. Representative images of: (A) Healthy 12-week-old CD1 knee joints had an organised MCL with toluidine blue staining near the femoral enthesis (yellow arrows) and spindle-shaped fibroblasts in the mid-ligament region (purple arrow). (B) OA grade 4 CD1 MCLs showed rounded-cell morphology in the mid-ligament region (yellow arrow) and abnormal tissue growth (red region) including toluidine blue deposition (red arrow) near the tibial attachment. (C) OA grade 6 CD1 MCLs had severe hyperplasia throughout the MCL and rounded-cell morphology and toluidine blue staining near the femoral enthesis which extended to the mid-ligament region (yellow arrows). CD1 OA grade 6 also had evidence of bone formation in the mid-ligament regions (red region). Scale is 200 µm (4x) and 25 µm (40x).

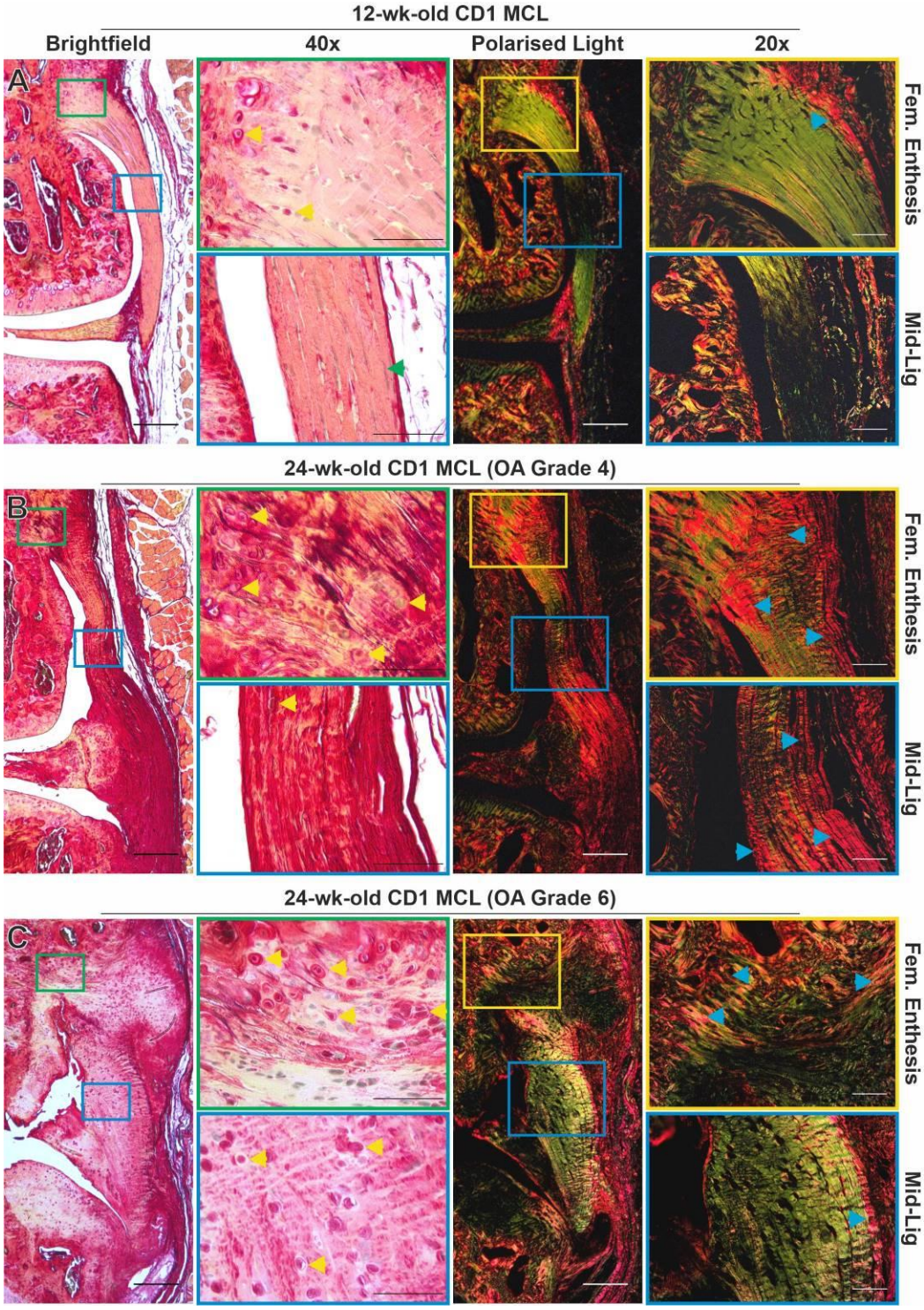

Figure 2.35 Histological staining of the medial collateral ligament (MCL) in CD1 knee joints using picrosirius red. Representative images of: (A) Healthy 12-week-old CD1 MCL showed light red collagen staining with spindle shaped fibroblasts (green arrow) and mainly green birefringence throughout the MCL with a small zone of red birefringence near the femoral enthesis (blue arrow). (B) CD1 OA grade 4 had dark red collagen staining which coincided with red birefringence near the femoral enthesis and in the mid-ligament region. (C) CD1 OA grade 5 showed thickening of the MCL and red collagen staining and red birefringence mainly in the outer region of the ligament near the femoral enthesis. (D) CD1 OA grade 6 had clear hyperplasia in the MCL and had light red collagen staining that matched green birefringence in the middle regions of the ligament and red collagen staining that matched areas of red birefringence in the outer regions. Scale is 200 µm (4x) and 50 µm (20x, 40x).

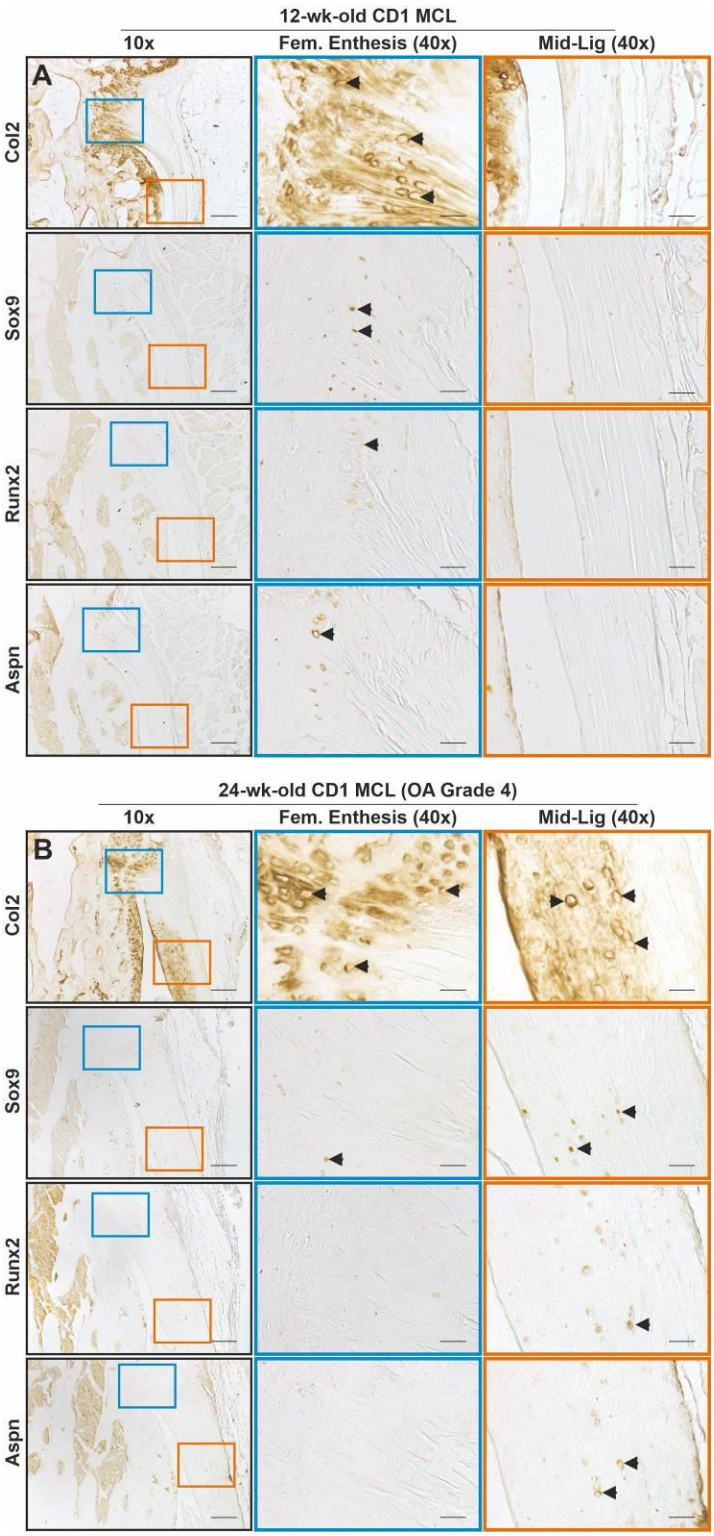

Figure 2.36 Immunostaining of the medial collateral ligament (MCL) in CD1 knee joints. Representative images of: (A) Healthy 12-week-old CD1 MCL showed some COL2 staining near the femoral enthesis and sparse SOX9, RUNX2 and ASPN expression (black arrows). No staining was found in the MCL mid-ligament region. (B) OA grade 4 CD1 MCLs had COL2 staining at the femoral enthesis and in the mid-ligament region. There was also SOX9, RUNX2 and ASPN expression in cells of the MCL mid-ligament region. Scale is 100 µm (10x) and 25 µm (40x).

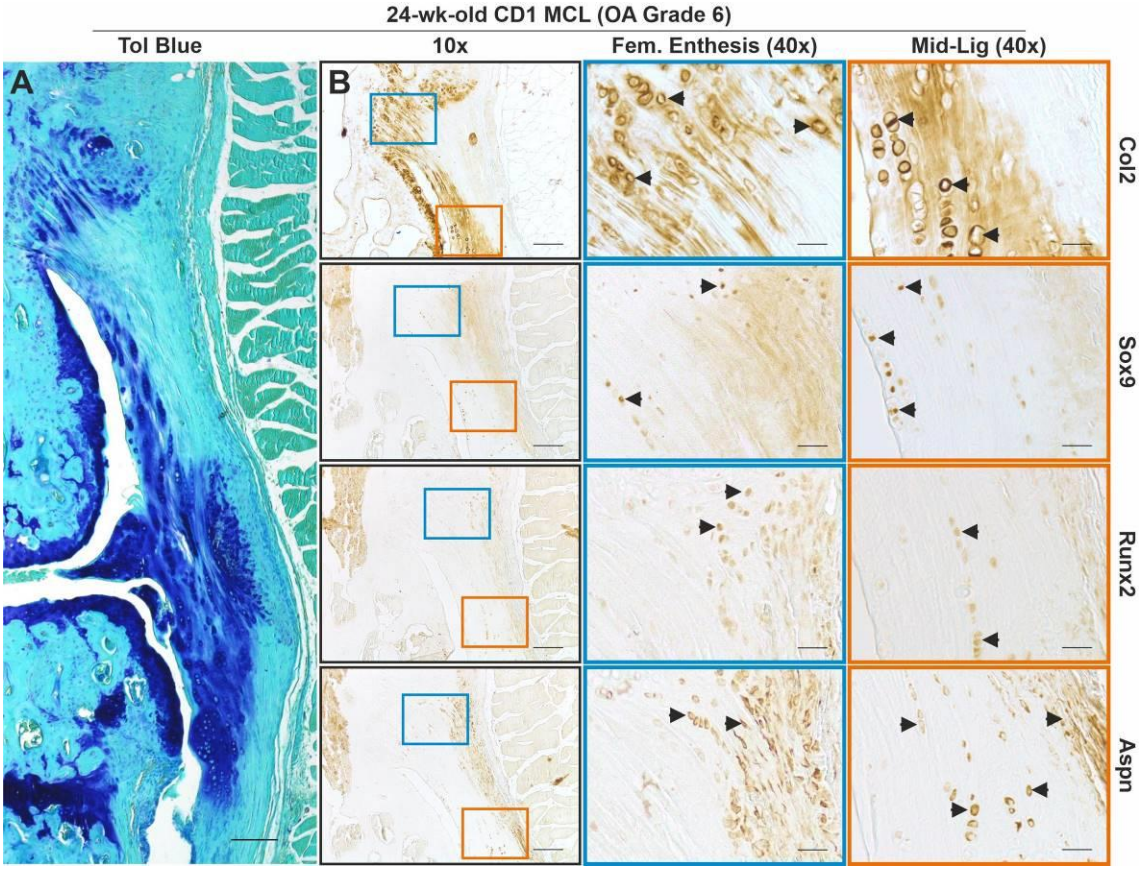

Figure 2.37 Toluidine blue (A) and immunostaining (B) of the medial collateral ligament (MCL) in CD1 OA grade 6 knee joints. Representative images of OA grade 6 CD1 MCLs had abundant COL2 deposition near the femoral attachment extending to the mid-ligament region. In these same regions SOX9, RUNX2 and ASPN were also present (black arrows), as well as in the epiligament layer (purple arrows). Additionally, areas of COL2 deposition seemed to match areas rounded-cell morphology (black arrows) and areas with toluidine blue staining (A, Tol Blue). Scale is 200 µm (Tol Blue), 100 µm (10x) and 25 µm (40x).

2.3.4.5 Medial menisci

2.3.4.5.1 Toluidine blue staining

Healthy12-week-old CD1 knee joints had medial menisci with the expected outer hyaline cartilage layers (H), central ossified region (O) and fibrous attachment (F, red region) (Figure 2.38A). At OA grade 4 of the 24-week-old CD1 knee joints, medial menisci showed hyperplasia of the fibrous region (red region), toluidine blue staining and 'rounded' cell morphology in the fibrous region (yellow arrows), as well as osteophyte formation at the anterior horn of the medial meniscus (red arrow) (Figure 2.38B). At OA grade 6 of the CD1 knee joint, there was further increase in toluidine blue staining, hyperplasia (red region), rounded-cell morphology (yellow arrows) and osteophyte formation (red arrow) in the medial menisci (Figure 2.38C). Toluidine blue staining indicated changes in the fibrous region of the OA CD1 medial menisci.

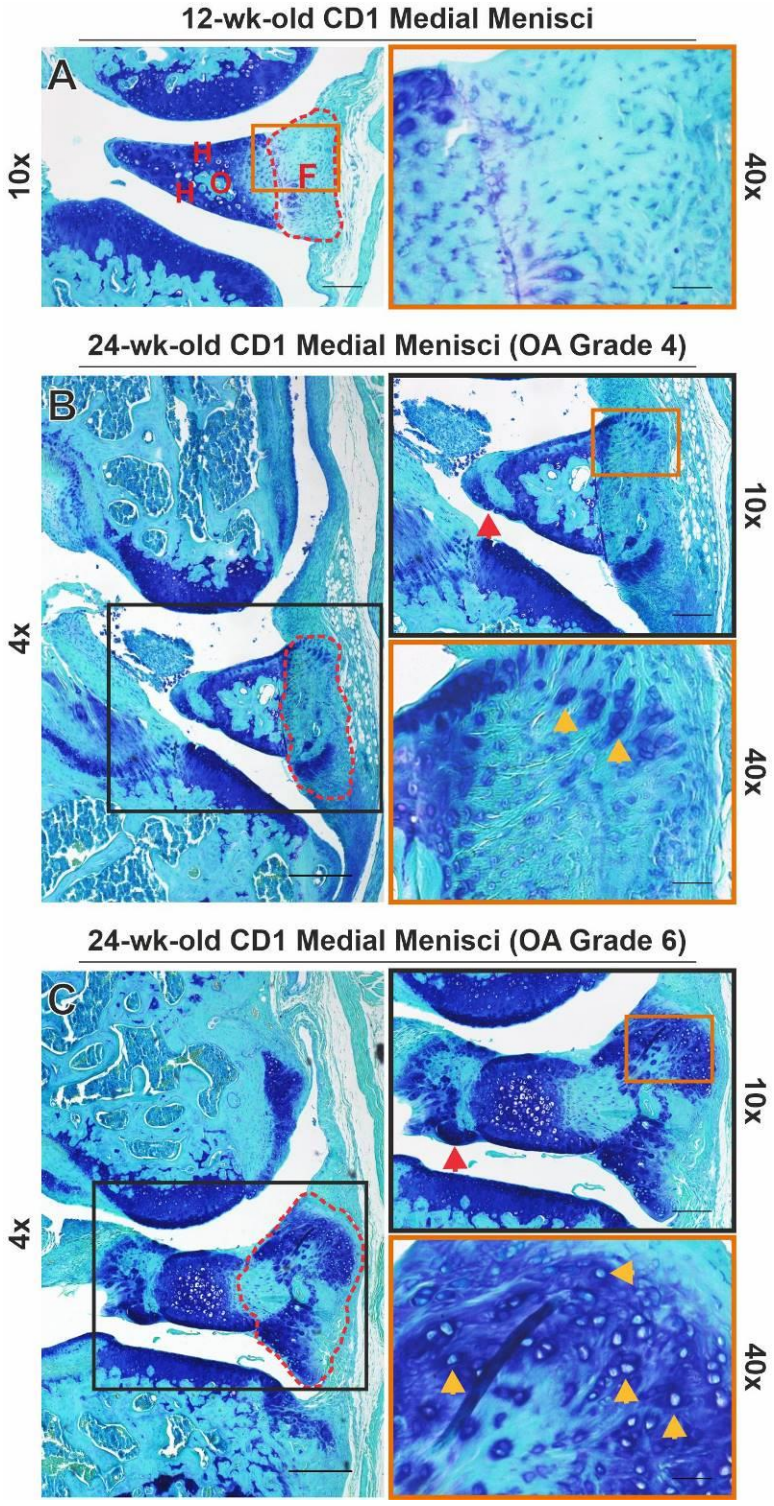

Figure 2.38 Histological staining of the medial menisci in CD1 knee joints using toluidine blue. Representative images of: (A) Healthy 12-week-old CD1 medial menisci had the expected hyaline cartilage regions (H), ossified core (O) and outer fibrous region (F, red region). (B) OA grade 4 CD1 medial menisci had expanded fibrous areas (red region) with toluidine blue staining and rounded-cell morphology (yellow arrows), as well as potential osteophyte formation at the anterior horn (red arrow). (C) OA grade 6 CD1 medial menisci had enlarged fibrous regions (red region) with abundant toluidine blue staining and rounded-cell morphology (yellow arrows), and also potential osteophyte formation at the anterior horn (red arrow). Scale is 200 µm (4x), 100 µm (10x) and 25 µm (40x).

2.3.4.5.2 Immunostaining

Immunostaining of the healthy 12-week-old CD1 menisci showed COL2 staining in the hyaline cartilage region as expected and sparse COL2, SOX9, RUNX2, and ASPN staining in the fibrous region (black arrows) (Figure 2.39A). In the enlarged fibrous region of the OA grade 4 CD1 medial menisci, COL2, SOX9, RUNX2 and ASPN staining was more prominent or evident in the outer fibrous regions and corresponding to areas with 'rounded' cell morphology (black arrows) (Figure 2.39B). As OA progressed, COL2 deposition spread throughout the entire medial meniscus and SOX9, RUNX2 and ASPN were also present in the outer fibrous regions (Figure 2.39C). Immunostaining of COL2 indicates a change in the ECM, meanwhile SOX9 and RUNX2 confirm chondrogenesis and potentially hypertrophy occurring in the fibrous regions of the OA CD1 medial menisci.

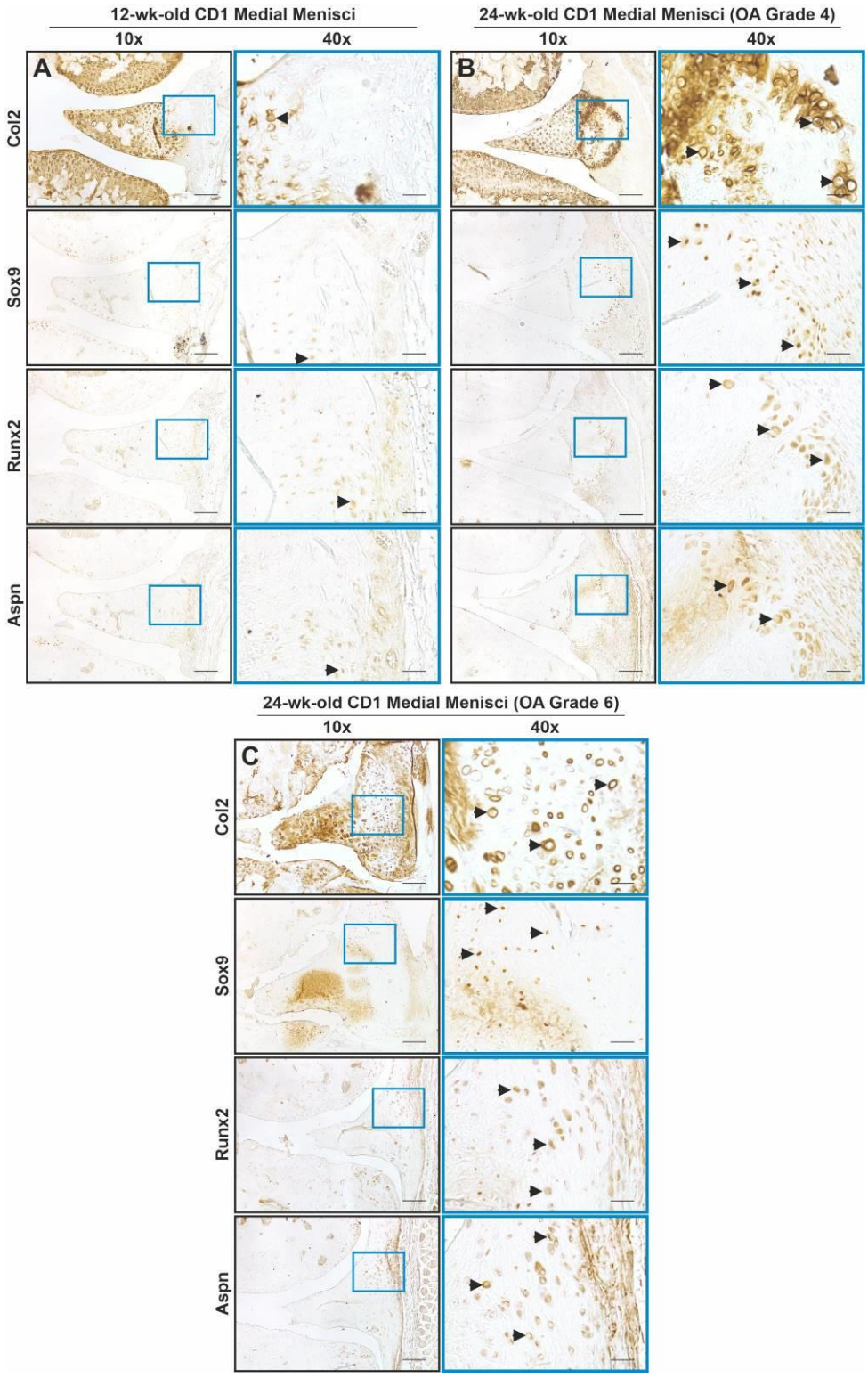

Figure 2.39 Immunostaining of the medial menisci in CD1 knee joints. Representative images of: (A) Healthy 12-week-old CD1 medial menisci had a COL2 staining in the hyaline cartilage layer and sparse staining of COL2, SOX9, RUNX2 and ASPN in the fibrous region (black arrow). (B) OA grade 4 CD1 medial menisci had COL2 which expanded into the fibrous region, and expression of SOX9, RUNX2 and ASPN in the same fibrous regions (black arrow). (C) CD1 OA grade 6 medial menisci had COL2 staining throughout the fibrous region as well as SOX9, RUNX2 and ASPN in the upper outer fibrous regions (black arrows). Scale is 100 µm (10x) and 25 µm (40x).

2.3.4.6 Summary of CD1 murine model and OA pathology

The CD1 murine model exhibited OA features in 24-week-old CD1 male mice which were not present in the 12-week-old CD1 male mice knee joints. This included a significantly higher OARSI score and joint space mineralisation, particularly in the medial knee compartment of the CD1 24-week-old mice. Knee ligament and meniscal pathology in the OA 24-week-old CD1 knee joint revealed ECM and cellular changes which included toluidine blue staining, red collagen birefringence and COL2 deposition and rounded-cell morphology with SOX9, RUNX2 and ASPN expression. In the ACL of CD1 knee joints these pathological changes occurred mainly in the tibial enthesis. In the MCL of CD1 knee joints, OA pathology included hyperplasia and potential ossification in the MCL mid-ligament region. Lastly in the medial menisci of the CD1 knee joints, hyperplasia was found in the fibrous region of the medial menisci.

Overall, we found changes in the CD1 knee ligament and menisci pathology in the ECM composition and COL2 deposition, complemented by changes in cellular markers which included markers for chondrogenesis and hypertrophy.

2.3.5 Summary of ligament and meniscal tissue pathology in all murine OA species

An overview of all pathological changes found in the murine spontaneous OA ACL, MCL and menisci can be seen in Table 2.3. Both spontaneous OA models (Str/ort and CD1 mice) had similar pathological changes in all ligaments which included TB staining, red birefringence and chondroid-like cells with COL2 deposition as well as SOX9 and RUNX2 expression. Furthermore, there were similarities in the medial menisci of both spontaneous OA models, which had a hypertrophic outer fibrous region. Differences between the spontaneous OA models included more variability in ligament pathology in the CD1 mice which varied with OA grade and in addition CD1 mice had no ASPN expression which was present in ACL and MCL of the Str/ort mice. Despite difference, both spontaneous OA models demonstrated pathological change occurring in the knee ligaments which coincided with chondroid-like cells which could play a role in OA progression.

Table 2.3 Anterior cruciate ligament (ACL), medial collateral ligament (MCL) and meniscal tissue pathology in murine spontaneous OA models: Str/ort mice and CD1 mice. Pathology was analysed using toluidine blue (TB) and picrosirius red (PR) staining and specific immunohistochemistry (IHC) markers which included COL2, SOX9, RUNX2 and ASPN.

OA	Mouse model	Stain or marker	Tissue		
			ACL	**MCL**	**Medial Menisci (MM)**
Spontaneous OA	**Str/ort mice** **(vs healthy CBA mice)**	Tol Blue (TB) staining:	Found in: • Mid-ACL region • ACL tibial enthesis OA progression: • Matrix disorder • Chondroid-like cells in mid-ACL region	Found in: • Mid-MCL region • MCL femur enthesis OA progression: • Chondroid-like cells in mid-MCL • MCL hypertrophy	Found in: • Outer fibrous region of MM OA progression: • Expanding outer fibrous region • Potential ossification
		Picrosirius Red (PR) staining:	Red birefringence: • Mid-ACL region	Red birefringence: • Mid-ACL region • MCL femur enthesis	N/A
		IHC: COL2, SOX9, RUNX2, ASPN	Tibial enthesis: • All markers present at OA grade 2 Mid-ACL: • All markers present at OA grade 4	Mid-MCL and femur enthesis: • All markers present at OA grade 5	Outer fibrous region: • COL2, SOX9 and ASPN expression at OA grade 5
	CD1 mice **(12-wk-old vs OA 24-wk-old)**	Tol Blue (TB) staining:	Found in: • Mid-ACL region • ACL tibial enthesis OA progression: • Chondroid-like cells in mid-ACL region • TB staining varied with OA grade	Found in OA grade 6: • Mid-MCL region • MCL femur enthesis OA progression: • Chondroid-like cells • Potential ossification	Found in: • Outer fibrous region of MM OA progression: • Expanding outer fibrous region • Chondroid-like cells
		Picrosirius Red (PR) staining:	Red birefringence: • Mid-ACL region in OA grade 4	Red birefringence: • Mid-MCL at OA grade 4	N/A
		IHC: COL2, SOX9, RUNX2, ASPN	Tibial enthesis: • COL2, SOX9, RUNX2 present at OA grade 4 Mid-ACL: • COL2 in OA and 12-wk-old ACLs	Mid-MCL: • All markers present at OA grade 4 and 6	Outer fibrous region: • All markers present at OA grade 4 and 6

Table 2.4 Anterior cruciate ligament (ACL), medial collateral ligament (MCL) and meniscal tissue pathology in murine post-traumatic OA models: destabilisation of the medial menisci (DMM) and non-invasive loading of the knee joint. Pathology was analysed using toluidine blue (TB) and picrosirius red (PR) staining and specific immunohistochemistry (IHC) markers which included COL2, SOX9 for the DMM mice and COL2, SOX9, RUNX2 and ASPN for the non-invasive loaded knee joints.

OA	Mouse model	Stain or marker	Tissue		
			ACL	**MCL**	**Menisci**
Post-traumatic OA	**DMM** **C57CBA mice 8 wks post-trauma vs contra-lateral leg**	Tol Blue (TB) staining:	OA progression: • Matrix disorder • Chondroid-like cells near ACL-tibia enthesis	OA progression: • Outer hypertrophic region • Potential ossification at OA grade 6	OA progression: • Expanding outer fibrous region • Ossification
		Picrosirius Red (PR) staining:	Red birefringence: • Mid-ACL region at OA grade 6	Red birefringence: • Throughout MCL at OA grade 6	N/A
		IHC: COL2, SOX9	Tibial enthesis: • Markers present at OA grade 4	MCL-femur enthesis: • Markers present at OA grade 6	Outer fibrous region: • Markers present at OA grade 4
	Non-invasive loading **C57BL/6J mice 4 wks post-trauma vs healthy**	Tol Blue (TB) staining:	Found in: • Mid-ACL region • ACL tibial enthesis OA progression: • Matrix disorder • Chondroid-like cells in mid-ACL region	Found in: • MCL femur enthesis of loaded MCL OA progression: • Chondroid-like cells	OA progression: • Expanding ossified core of lateral menisci
		Picrosirius Red (PR) staining:	Red birefringence: • ACL-tibial enthesis	Red birefringence: • MCL-femur enthesis • Outer mid-MCL	N/A
		IHC: COL2, SOX9, RUNX2, ASPN	Tibial enthesis and mid-ACL: • All markers present in loaded ACL • Including COL2 in the mid-ACL region	MCL-femur enthesis: • All markers present in loaded MCL Mid-MCL: • COL2, SOX9 and ASPN present	Outer fibrous region: • COL2 and SOX9 present in the lateral menisci

Pathological changes in the post-traumatic OA ligaments and menisci are summarised in **Error! Reference source not found.**. Both DMM and non-invasive loaded knee joints had similar pathologies in the ACL that included matrix disorganisation and chondroid-like cells with COL2 deposition and SOX9 expression as well as red collagen birefringence. However, in both post-traumatic OA models, ACL pathological changes occurred in different micro-anatomical locations. The non-invasive loaded ACLs had changes in the mid-ACL region, including COL2 deposition in the mid-ligament region which was not seen in the DMM ACLs. DMM mice had potential ossification occurring in the MCL and medial menisci. Both post-traumatic OA models had notable pathological changes to the ligaments which could indicate a compromised ligament function and potentially an active role in OA.

2.4 Discussion

This chapter has described abnormal pathology in murine knee ligaments and menisci in four distinct murine OA models which ranged from loss of collagen fibre alignment, hyperplasia, chondrogenesis and ossification, cell hypertrophy, and expression of endochondral ossification markers. These murine models included two post-traumatic OA models: the surgically induced DMM model [107] and the non-invasive mechanically loaded knee joint [153]. Additionally two spontaneous murine OA models were investigated: the STR/ort mice [152] and CD1 mice [154]. Knee ligament and meniscal pathology differed based on OA etiology. Herein we wanted to compare similarities and differences in OA pathology in murine knee ligament and menisci based on OA aetiology: spontaneous and post-traumatic.

2.4.1 Comparing OA models

2.4.1.1.1 Spontaneous OA

The CD1 murine model was a novel spontaneous OA model with similarities and differences to the STR/ort mice. OA in the CD1 mice was assessed by OARSI scoring and joint space mineralisation. Joint space mineralisation has been previously shown to increase with OA grade severity in St/ort mice [165], similar to our findings in the CD1 knee joints. Additionally, both spontaneous murine OA models (STR/ort and CD1) demonstrated OA predominantly in the medial knee compartments. In the medial compartment, both the MCL and medial menisci of the OA STR/ort and CD1 mice had similar pathologies that included hyperplasia, abnormal tissue growth and in more severe grades of OA, evidence of mineralisation and bone formation. OA developing in the medial of the knee compartments could be due to gait and greater weight bearing loads in the medial side as has been shown in human knee OA patients [174].

The ACL, MCL and medial menisci of both spontaneous OA murine knee joints, all showed increases in toluidine blue staining, which could suggest proteoglycan and GAG deposition [175]. Additionally the ACL and MCL in both spontaneous OA knee joints had increased red collagen birefringence particularly in the ACL mid-ligament region, indicative of collagen remodelling particularly thicker closely packed collagen fibres such as collagen type I [167]. Both spontaneous OA models showed COL2 deposition and SOX9, and RUNX2 expressing cells in areas of hyperplasia in the ACL tibial enthesis (Figure 2.4 and Figure 2.32), MCL enthesis and mid-ligament and regions (Figure 2.8 and Figure 2.36), and the medial menisci fibrous regions (Figure

2.10 and Figure 2.39). COL2, SOX9 and RUNX2 are indicative of endochondral ossification, and similarities in these OA markers between both spontaneous OA models could indicate a similar OA pathology.

Pathology differed in the ACL mid-ligament region, where OA STR/ort ACLs also showed COL2 deposition, and SOX9, RUNX2 and ASPN expression (Figure 2.5), however in the OA CD1 knee joints, only COL2 deposition was found in the ACL mid-ligament region but no SOX9, RUNX2 and ASPN expression (Figure 2.33). This implies that chondrogenesis and cellular hypertrophy driven by SOX9 and RUNX2 is not occurring in the CD1 spontaneous OA model in the mid-ligament region potentially suggesting a different ACL pathology compared to the STR/ort ACL. SOX9 is not the only regulator of COL2 and does not always correlate to COL2 expression as has been shown in human OA cartilage [176].

Additionally, there were differences in the healthy control knee joints. COL2 deposition was also present in the ACL mid-ligament region of the younger and healthy 12-week-old CD1 knee joints (Figure 2.33) but not present in the healthy CBA knee joints (Figure 2.5). Expression of the gene encoding COL2, *Col2a1* transcripts, have been previously detected in the ACL fibroblasts of both the STR/ort and CBA controls in all ages [177]. This would suggest that young CD1 mice are different to CBA mice in COL2 protein translation. The presence of COL2 in the young CD1 ACL could in part contribute to spontaneous OA development by altering mechanical properties of the ligament. This could highlight a difference in the ACL pathology in the STR/ort and CD1 knee joints but could also be due to differences in age (CD1: 24 weeks, STR/ort: 40 weeks), and weight. Further research is needed to better characterise the CD1 knee joints and determine pathological similarities and differences to the STR/ort and human OA models.

2.4.1.1.2 Post-traumatic OA

The post-traumatic OA models showed different severities of OA progression in different knee compartments. It is important to remember that DMM knee joints develop OA mainly in the medial knee compartments [107], and the non-invasive mechanically loaded knee joints in the lateral compartment [153]. The surgical DMM model showed severe OA pathologies including bone formation in the outer fibrous region of the medial menisci (Figure 2.17), however this bone formation did not occur in the lateral menisci of the mechanically loaded knee joints. Similarly, the ACL of the DMM model showed severe structural changes including collagen fibre misalignment, potential inflammation and red birefringence whereas the non-invasive

mechanically loaded knee joints retained fibre alignment and only had red birefringence near the ACL tibial enthesis. These findings suggest that the mechanically loaded knee joints showed less severe OA pathology compared to the DMM knee joints. We have previously shown that DMM knee joint OARSI score was 3.61 ±0.3 [165]. A previous study has also reported an OARSI score of 4 in CBA mice following non-invasive trauma [153]. The OARSI score of the non-invasive trauma on C57BL/6J mice at 6 weeks post-trauma has not been analysed, though a similar OARSI score between the two models would be expected.

The differences in pathology between the two post-traumatic models (DMM and loaded knee joints) could be due to differences in OA risk between the medial and lateral compartments. Differences could also be due to the different tissues affected, in the DMM model the medial menisci are destabilised, meanwhile in the non-invasive loading of the murine knee joint has been shown to affect the ACL, even resulting in ACL rupture at higher loads [178]. Further research is needed to determine how changes in both post-traumatic OA models affect the whole knee joint stability. In addition, it is important to note that both post-traumatic OA models had different controls. The non-invasive loading were compared to a control mouse group of the same strain that did not undergo trauma, meanwhile the DMM mice were compared to the opposite contralateral knee joint (left leg) from the same mice that underwent DMM surgery (right leg). While OARSI score and joint space mineralisation was lower in the contralateral knee joint [165], previously studies have shown that contralateral knee joints have a high risk of concomitant injuries [179], indicating that they could have underlying pathologies and are not necessarily a disease-free control.

Despite structural differences, both post-traumatic OA models demonstrated changes in rounded cell morphology. Immunostaining showed similar expression of cartilage-associated and chondrogenesis markers, COL2 and SOX9. In the ACL of both the DMM and the mechanically loaded knee joints, COL2 deposition and SOX9 expressing cells increased near the ACL tibial enthesis. In the mechanically loaded knee joints these markers extended further into the ACL mid-ligament region, as well hypertrophic marker RUNX2 and ligament-tendon SLRP marker ASPN. Unfortunately, RUNX2 and ASPN marker expression could not be validated in the DMM knee joints (see Section 2.2.2). Overall, the presence of COL2 deposition and SOX9 expression in the knee ligament and menisci of both post-traumatic OA models suggests that they share similar pathology despite having major structural differences.

2.4.2 Previous findings on ligament and meniscal OA mineralisation

Meniscal hyperplasia and ossification have been briefly reported in STR/ort mice [152, 160, 180] and more recently in the DMM mouse model [173], however they do not describe any changes in the ACL and the MCL. The description of knee OA in STR/ort mice includes reports of heterotopic calcification [152, 160]. In particular, an increased ossification centre in the medial menisci [152] and a positive association between MCL calcification and OA development [160]. These findings agree with our histological data of meniscal ectopic mineralisation and ossified nodules in the collateral ligaments (Figure 2.6). Meanwhile, murine DMM medial menisci have been previously shown to have severe fibrillation, erosion and calcifications [173]. This also matches our histological results and is further strengthened by our immunostaining findings, which provide insight into the ECM and cellular changes involved (Figure 2.18).

In humans, meniscal pathologies have been associated with ageing and OA [93]. Indeed, the meniscus commonly develops lesions in OA patients with no previous history of injury [181]. Although meniscal ossification is rare in humans and arises mainly from mechanical trauma [182], calcification is more common and found mainly in OA patients [183, 184]. In addition, aged and OA menisci showed changes in cellularity (with both areas of hyper- and hypocellularity), cell clustering and phenotype changes from fibroblast-like cells to round chondrocyte-like cells [184], similar to our findings in mouse OA. Similarities in meniscal pathologies between human and mouse OA support a favourable translatability between the species, despite clear meniscal structural differences.

Pathological changes in knee ligaments in murine models are consistent with changes noted in human joints [185, 186] and other species [119]. As previously mentioned (Section 2.1), human cruciate ligaments from OA knee joints show chondroid and cartilage metaplasia, involving a change in ligament cell phenotype to a more chondrocyte-like round cell morphologies with SOX9 and RUNX2 expression and COL2 formation [168, 169]. COL2 deposition in the mid-ligament region of the ACL in mice has, to our knowledge, never been reported, and yet it was evident in the spontaneous CD1 model and the non-invasive loading model. These findings are similar to that seen in the Dunkin Hartley guinea pigs, another spontaneous model of OA, in which COL2 deposition in the ACL preceded changes to the cartilage [121, 187]. Changes in COL2 formation could be related to SOX9 expression, a transcription factor necessary for chondrogenesis, which binds and regulates the *Col2a1* gene in chondrocytes [188] and regulates *Acan* gene promoters [189]. Further studies are needed to determine the mechanisms of pathological chondrogenesis in knee joint ligaments.

The pathological changes seen in the ligament and menisci of the OA mouse models has some similarities to endochondral ossification pathways. Endochondral ossification is the process by which cartilage mineralises and results in resorption and replacement by bone [190]. Typically this process begins with chondrocyte proliferation, initiated by SOX9 [188], then chondrocytes undergo further maturation and become hypertrophic, secreting a distinct matrix containing collagen type X and calcifying the matrix [190]. While chondrocytes die, due to lack of nutrients, they also direct surrounding stem cells to differentiate into osteoblasts which deposit the mineralised bone matrix [190]. RUNX2 is an important regulator at the later stages of endochondral ossification, promoting chondrocyte hypertrophy and controlling differentiation [191]. The presence of COL2, SOX9 and RUNX2, as well as evidence of bone formation in the OA ligament and meniscal tissue could be indicators of endochondral ossification occurring in these tissues. Future research should look at collagen type X secretion and mineralisation markers to confirm this possibility.

The presence of ASPN in the ACL, MCL and menisci of some of the murine OA knee joints, suggests that it could play a role in OA development. ASPN is a known tendon and ligament SLRP found localised around ligament fibroblasts [171]. ASPN expression has been previously known to increase in the cartilage of human OA patients, inhibiting TGF-β-induced expression of the *Col2a1* gene [170]. ASPN has also been found to increase in degenerated human intervertebral discs [192], yet its role is relatively unknown. ASPN deficient mice have thinner collagen fibrils and upregulation of collagen and other GAG [193], suggesting a role in ECM composition and mechanical properties. Additionally, ASPN is a negative regulator of periodontal ligament mineralisation, which has been shown to directly interact with BMP-2 [194]. ASPN could be involved in the prevention of chondrogenesis and mineralisation in the OA ligaments, though its effectiveness is unclear since chondrogenesis markers and bone formation were also found.

Other factors linked to ligament ossification include Indian hedgehog, WNT and inflammatory cytokines signalling [185, 186, 195]. It was also reported that *Col6a1* and *Runx2* may be common susceptibility genes in ligament ossification in the spine [196, 197] and both of these genes have also been linked to OA [198, 199]. Growth factor signalling has also been associated to ligament ossification in the spine, specifically the ligamentum flavum which connects adjacent vertebrae, and growth factors include recombinant BMP2 in rat spines [200] and BMP2, BMP4 and BMP7 signalling in the human spine [201]. TGF-β and BMPs are known regulators of endochondral ossification and fibrosis as well as being involved in OA development. Recently, epidermal growth factor signalling was linked to OA development comprising of ectopic chondro-osseous

pathologies in the ligament and meniscus [202]. Further research is needed to understand how all these factors interact during OA development.

2.4.3 Study limitations

There are certain limitations in the study design that could have improved the interpretation of our findings. In the post-traumatic OA models, the DMM surgery was performed on C57CBA mice, which differed from the C57BL/6 mice used for non-invasive mechanical loading. Additionally, tissue processing for the DMM knee joints differed from all the other OA models, which affected immunostaining protocols in the DMM mice. Lastly, the CD1 OA mice (24-week-old) were compared to their younger (12-week-old) and healthier CD1 mice which could have unknown pathologies, such as COL2 deposition seen in the 'healthy' CD1 ACL.

The biggest limitation in this study was the lack of ligament specific cellular markers. Analysis of important ligament ECM components such as collagen type I, collagen type III and small proteoglycans such as decorin and biglycan [80] could give us further insight into ligament ECM health and more specific pathological changes. However, these markers could not be validated for immunostaining analysis in murine knee joint, likely due to antibody sensitivity. Furthermore, better understanding of ligament cell populations and ligament fibroblast markers is imperative to further analyse the changes in rounded-cell morphology and SOX9, RUNX2 and ASPN expression seen many of the OA murine knee ligament cells.

2.5 Conclusion

This study has demonstrated structural and morphological differences and similarities in knee joint ligaments and menisci in post-traumatic and spontaneous murine OA models. In all spontaneous and post-traumatic OA models, we found ECM changes in the ACL and MCL that included proteoglycan deposition and collagen composition. These ECM changes were accompanied with cellular changes, indicated by rounded-cell morphology with SOX9 expression and COL2 deposition, markers of chondrogenesis. Furthermore, in the spontaneous OA STR/ort model and the post-traumatic OA non-invasive mechanically loaded model, cellular changes included hypertrophy (RUNX2 expression) and ASPN expression. SOX9 and RUNX2 expression indicate potential endochondral ossification in the ligaments which had never before been reported. Furthermore, we presented a novel spontaneous OA murine model: the CD1 mice. CD1 knee joints showed all the characteristics of OA, including joint space mineralisation, osteophyte formation, ossification in the MCL and medial menisci, and ACL ECM and cellular changes.

Our findings confirm that knee ligament and menisci health was affected during OA progression in both the post-traumatic and spontaneous OA models. These findings confirm that OA is a whole joint disease affecting all tissues in the knee joint, and knee ligaments and menisci could play a significant role in disease progression.

Chapter 3:
Mechanical Properties of the Murine Anterior Cruciate Ligament in Post-Traumatic and Spontaneous Osteoarthritic Models

3.1 Introduction

As in all matrix-rich tissue, ECM structure and function are closely related, particularly in ligaments. As previously mentioned, ligaments are composed of a collagen hierarchical structure consisting of collagen molecules, fibrils, fibres, fibre bundles and fascicles which make up the ligament unit [2]. Besides collagen, other structural ECM proteins such as proteoglycans, elastin and lysyl oxidase are also important components which interact with the fibrous collagenous bundles [2]. The mechanical behaviour of ligaments is viscoelastic and exhibit non-linear and linear behaviour when undergoing elongation (see Section 1.5, Figure 1.4) [2, 60]. Viscoelastic properties include strain rate sensitivity [61], stress-relaxation [59], creep [65] and hysteresis [66] (Figure 1.5). Viscoelastic behavior is mainly attributed to collagen interaction with ECM structural proteins such as proteoglycans and elastin [60, 69, 73]. Changes in the constituents of ligament structure can alter ligament function and mechanical behaviour which include changes to the ligament hierarchical structure [203] as well as collagen [141, 204], proteoglycan [205] and elastin content [28]. Previously, in Chapter 2, we demonstrated changes in the ligament ECM composition and cellular morphology during OA development in the murine knee joint. The consequences of the OA disease process on the mechanical behaviour of ligaments are not fully understood, therefore, our aim was to analyse the ligament mechanical behaviour in OA models.

To date, there are very few studies on the mechanical and viscoelastic properties of the human ACL in OA patients. A study by Hagena et al, found a decrease in elastic stiffness and ultimate load at failure in OA ligaments, along with an increase in viscoelastic stress-relaxation [138]. Another study found an increase in the elastic stiffness of the MCL and LCL ligaments in OA patients compared to non-arthritic cadaveric ligaments [140]. Therefore, changes in the knee ligament elastic stiffness during OA could depend on the type of ligament, such as cruciate or collateral ligaments which differ in structure and function [20]. Most other studies on human OA patients have focused on knee joint stiffness, such as varus and valgus knee stiffness, which did not change in OA patients [139] and dynamic knee joint stiffness during gait which increased in OA patients [206]. There is a clear need to better characterise the ligament viscoelastic and material properties during OA, to better understand disease progression during early stages of OA during age-related spontaneous OA and during post-traumatic OA, something not always possible with human ligament samples.

Several studies have analysed the mechanical properties of the ACL during OA development in different animal species, each offering deeper insight into disease pathology and ligament

mechanical changes. In the Dunkin Hartley guinea pig spontaneous OA model, mechanical tests found a decrease in the toe-region laxity of the ACLs [116]. In mice, Anderson-MacKenzie et al. found that STR/ort mice (spontaneous OA model) had weaker ACLs with a lower ultimate load, associated with increased collagen remodelling [114]. Furthermore, in collagen V mutant mice with secondary OA, Sun et al. reported decreased collagen fibril numbers in the ACL, along with a significant decrease in ultimate load and elastic stiffness [141], further confirmed in work by Connizzo et al. [204]. Most of these studies on ACLs focus on material properties, but do not fully address the viscoelastic properties of the toe-region which is physiologically relevant [60].

Murine models offer several advantages to study OA progression, including the ability to study disease progression in spontaneous OA models [114, 154] and more recently in post-traumatic OA [153]. The post-traumatic OA model developed by Poulet et al. [153] offers the ability to test the ACL mechanical properties post-trauma without invasive ACLT, which is the most common model of post-traumatic OA [102]. The ability to examine mechanical changes during disease progression in spontaneous OA will give further insight into the ACL degradation reported by Hasegawa et al [207] and the change in stiffness reported by Hagena et al [138]. This will elucidate the role of ligament function and ECM changes during OA pathology, important for future therapeutic applications for affected patients.

3.1.1 Hypothesis and aim

Due to our findings in Chapter 2, which included changes to the murine ACL ECM composition (COL2 deposition) and cell markers for chondrogenesis (SOX9 and RUNX2), we hypothesised there would be changes in the viscoelastic behaviour and material properties in both the murine spontaneous OA and post-traumatic OA ACLs.

The overarching aim for this study was to assess the mechanical viscoelastic behaviour and ultimate load of the ACL in healthy and spontaneous and post-traumatic murine OA models. To achieve this, the first aim was to create a testing setup and protocol appropriate for murine ACLs. Several aspects were included in this first aim, including determining the ideal knee flexion angle for mechanical testing, measuring the ACL length and cross-sectional area, and protocol design.

For mechanical analysis of the murine ACL, the aim was to analyse viscoelastic behaviour and material properties during OA progression in spontaneous and post-traumatic OA models. For viscoelastic behaviour the following properties were analysed: strain rate sensitivity, hysteresis, and stress-relaxation. For material behaviour, the ultimate load at failure was analysed.

Mechanical behaviour was compared between each OA group and appropriate control. Similarities and differences between the post-traumatic and spontaneous OA groups were discussed.

Overall, these aims should give us further insight into the viscoelastic behaviour and ultimate load material properties of the murine ACL and the effects of OA pathology.

3.2 Materials and Methods

3.2.1 Physiological range of murine knee flexion – Gait analysis

Gait analysis tests to determine the physiological range of motion in the murine knee joint was conducted on the data provided by Mr. Marrin, Dr. D'Aout and Prof. Bou-Gharios. X-ray reconstruction of moving morphology was recorded using two independent 60 kW Epsilon X-ray generators (EMD Technologies, CA), 16 inch image intensifier tubes (Thales, FR), X-Ray Tubes (Varian, USA) and Phantom Miro M120 video cameras (Vision Research, USA). X-ray images of gait were analysed using XMALab Software (Brown University, USA) and MatLab (MathWorks, R2018a Version 9.4, USA). Knee joint angles during gait was measured on B6CBAF1 mice (n=4) (Charles River). For each mouse, two gait trials were recorded and analysed. X-ray generator pulsed radiographic exposures at 120 frames per second, and video was recorded for a run length of approximately 3 seconds (Figure 3.A).

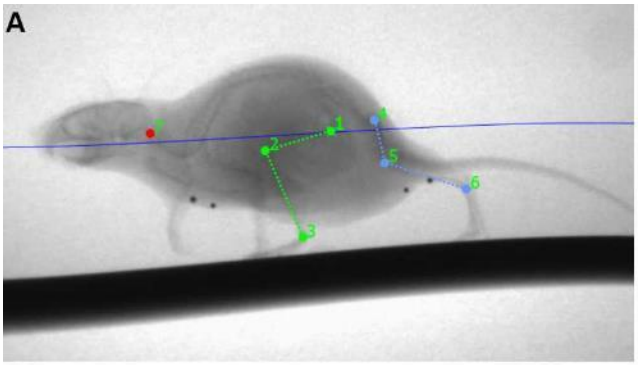

#	Marker	Anatomical Pt.
1	LHIP	Left Hip
2	LKNEE	Left Knee
3	LANK	Left Ankle
4	RHIP	Right Hip
5	RKNEE	Right Knee
6	RANK	Right Ankle
7	OCCI	Occiput

Figure 3.1 Setup for murine knee flexion measurements using x-ray reconstruction of moving morphology. X-ray images (A) were imported to XMALab software (Brown University, USA) where each anatomical point (Pt.) (B) was tracked at each frame during the normal mouse gait cycle. Anatomical points tracked were the following: left hip (1, LHIP), left knee (2, LKNEE), left ankle (3, LANK), right hip (4, RHIP), right knee (5, RKNEE), right ankle (6, RANK), and occiput (7, OCCI). The corresponding x,y,z location of each anatomical point was then imported to MatLab to create a 3D model of murine gait for the left and right hind-legs (C). Physiological knee range of motion during murine gait was calculated from the 3D models in MatLab (MathWorks, R2018a Version 9.4, USA).

Video files were opened in XMALab software for distortion correction, calibration and point digitising. Mouse gait was tracked at every frame at the following points: left hip, left knee, left

ankle, right hip, right knee, right ankle, and occiput (Figure 3.B). The resulting locations of each point were exported from XMALab as a 3D csv file that was then analysed as a matrix in MatLab where a 3D model could be created (Figure 3.C) and knee speed and knee joint flexion was measured at every frame. The results from this gait analysis of physiological murine knee flexion were used to determine the ideal angle for mechanical testing of the femur-ACL-tibia complex.

3.2.2 Experimental set-up for material testing of murine knee joints

Clamps were specifically designed for material testing of murine ACLs, using the femur-ACL-tibia complex. Clamp was designed based on past literature [114, 141, 204] and following advice from Dr. Snehal Shetye from the University of Pennsylvania. Clamps were designed using ProEngineer (Creo Elements/Pro, PTC, USA) with guidance from Mr. Eliasy and Mr. Janvier (Figure 3.2A). A 3D printed model of the clamp was manufactured in polylactic acid (Ultimaker, NL) for preliminary testing (Figure 3.2B). Clamps were modified to ensure ACL alignment and were manufactured in steel at the School of Engineering at the University of Liverpool (Figure 3.2C).

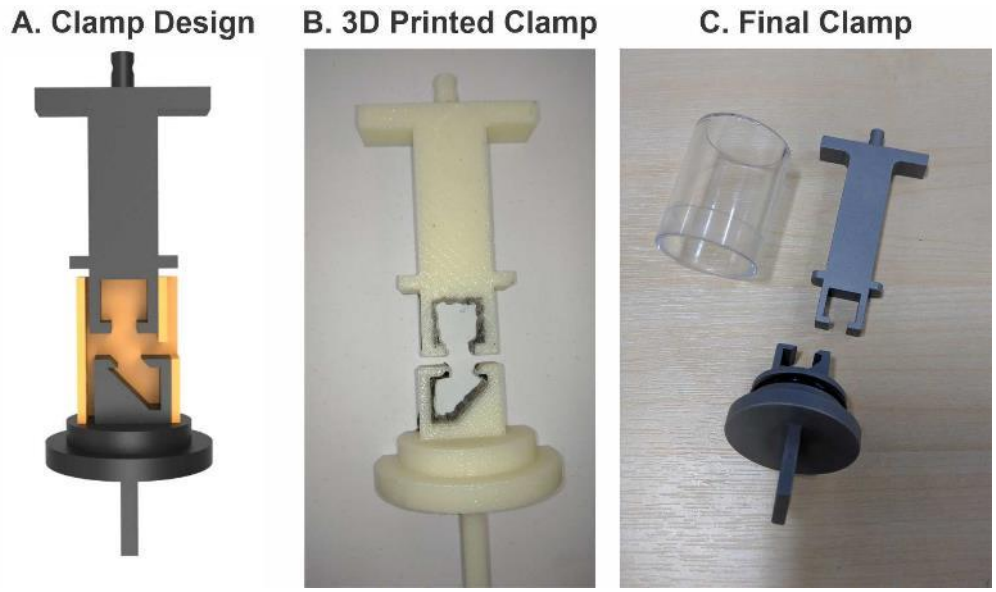

Figure 3.2 Instron clamp design and optimisation. Clamp prototypes were designed with ProEngineer (Creo Elements/Pro, PTC, USA) (A),a preliminary prototype was 3D printed (Ultimaker, NL) in polylactic acid (B), and then the final version was manufactured in medical grade steel (C) at the School of Engineering at the University of Liverpool. Design was based partly on past literature [141, 204].

3.2.3 Animals and tissue collection

3.2.3.1 Determination of sample size for material testing experiments

Preliminary studies were conducted using C57BL/6 12-week-old male mice (n=6) for a power analysis to determine the sample size necessary. Preliminary data (not shown here) of the tangent modulus-stress curve (at 2 MPa) was measured for each sample. Measurements of tangent modulus for all samples was normally distributed (Shapiro-Wilk test) with a standard deviation of 8.34 MPa. Power and Sample Size Software (version 3.1.6, Vanderbilt University) [208] was used to calculate ideal sample size. The hypothetical difference of the tangent modulus between control and OA group was assumed to be 15%. With these assumptions, we calculated the ideal sample size to be 6 experimental and 6 control subjects to be able to reject the null hypothesis that the population means of the experimental and control groups are equal with probability (power) 0.8 (Figure 3.3). The type I error probability associated with this test of this null hypothesis is 0.05. Though sample size needed for analysis was 6, however we tested more (n=8 or 10) to allow room for error in the setup of the sample (see Section 3.3.3).

Figure 3.3 Power and sample analysis. T-test was completed using Power and Sample Size Software (version 3.1.6, Vanderbilt University) [208]. By assuming a 15% difference in tangent modulus between control and OA groups, the predicted experimental sample size is 6.

3.2.3.2 Murine animal models

Both healthy and OA murine animal models were used in our study. Healthy ageing group were C57BL/6J mice at 12 and 24-weeks old. The murine OA models used in this study included a non-invasive post-traumatic OA model (with non-invasive loading) [153], and a novel spontaneous OA model (CD1 outbred mice) [154], (see Table 3.1). All mice were kept in the same

conditions in polypropylene cages, subjected to 12-hour light/dark cycles, at 21±2˚C and fed standard diet ad libitum. All procedures were performed in accordance with the UK Home Office guidelines and regulations under the Animals (Scientific Procedures) Act 1986 and local ethics committee (project license: P267B91C3). For tissue collection, all animals were euthanised by cervical dislocation. Murine hind legs were taken for micro-computed tomography (µCT) imaging analysis (see Section 3.2.4) or for ACL mechanical testing (see Section 3.2.5). The outer skin was removed from the murine hind legs, and samples were immediately stored in a -20C freezer until required for testing. Storage at -20C has been previously shown to not have effect on the viscoelastic and mechanical properties of ligaments in several animal models [78, 209].

3.2.3.3 Healthy ageing group (C57BL/6J mice).

In this chapter, male 12-week-old and 24-week-old C57BL/6J mice were used to represent normal ageing at the same age time points of the CD1 spontaneous OA mice. This would allow for analysis of healthy ageing, which could be compared to CD1 mice to determine if mechanical changes occurred due to age or OA progression, especially since CD1 mice are a novel spontaneous OA model. C57BL/6J mice at 12 to 24 weeks of age are not known to develop OA symptoms and at 6-months of age have healthy cartilage and a low OA score [154, 173]. For this study, male 12 and 24-week-old C57BL/6J mice (n=8) were obtained from Charles River (UK) and euthanised one day after arrival (see Table 3.1). Right legs were used for ACL mechanical testing, and left legs for µCT ACL measurements.

3.2.3.4 Spontaneous OA group (CD1 mice)

Male CD1 outbred mice were purchased from Charles River, UK. As shown in Chapter 2, CD1 mice develop spontaneous OA at 24-weeks of age, with significantly increased OARSI cartilage score and joint space mineralisation compared to the 12-week-old CD1 mice (Section 2.3.4). Mechanical properties of the ACL from a younger 12-week-old CD1 group was compared to an older 24-week-old group to determine differences within OA progression (Table 3.1). Male 12-week-old CD1 mice were euthanised one day after arrival (12-week-old group, n=10) and the remaining mice were aged for 12 more weeks (24-week-old group, n=10). Right legs were used for ACL mechanical testing, and left legs for µCT ACL measurements. Changes between 12 and 24-week-old ACLs in CD1 mice were briefly compared to changes between 12 and 24-week-old ACLs in the healthy aging group.

Table 3.1 Murine strain, gender, age and number for each group, including osteoarthritis (OA) and controls. Overall there were three main groups tested, a healthy ageing group (C57BL/6 male mice, 12 and 24-weeks-old), a spontaneous OA group (CD1 male mice, 24-weeks-old), and a post-traumatic OA group (C57BL/6 mice undergoing non-invasive loading of the knee joint). Each OA group also had a secondary healthy control: CD1 12-week-old mice previously shown not to develop OA (Section 2.6) and C57BL/6 non-loaded knee joint controls.

Group	Murine strain, gender	Age (n)	
		OA sub-group	Control sub-group
Healthy Ageing	C57BL/6J, male	N/A	12-week-old (n=8) 24-week-old (n=8)
Spontaneous OA	CD1, male	24-week-old CD1 (n=10)	12-week-old CD1 (n=10)
Post-traumatic OA	C57BL/6J male	Non-invasive loading, 18-week-old (n=12)	Non-loaded, 18-week-old (n=8)

3.2.3.5 Post-traumatic OA group (Non-invasive mechanical loading of C57BL/6 mice)

Non-invasive mechanical loading of the knee joint of C57BL/6J mice was used as a post-traumatic OA model. Progression of OA in this mouse model was described in Section 2.3.3 and has been published [153]. Non-invasive loading was performed on the right knee joints of ten-week-old C57BL/6J mice (Charles River, UK) (n=12), and a second group of C57BL/6J mice (n=8) which did not undergo treatment were used as a control group (Table 3.1). Briefly, axial compressive loads were applied consisting of 9N loads for forty cycles in each loading episode, and six loading episodes over a period of two weeks. Animals were euthanised at six weeks after the last loading episode, to ensure moderate OA progression. From the non-invasive loaded mice (n=12 total), eight of the right loaded legs were used for ACL mechanical testing (n=8), and four right loaded legs for µCT ACL measurements (n=4). From the non-loaded mice, right legs were used for ACL mechanical testing, and left legs for µCT ACL measurements.

3.2.4 Cross-sectional area (CSA) and length measurements of the murine ACL

Cadaveric knee joints for each murine group (see Table 3.1) were analysed with X-ray µCT to quantify the murine ACL length and cross-sectional area (CSA) at 90º knee flexion. 90º knee flexion was determined to be the optimal angle after gait measurements (see Section 3.3.1). For the healthy ageing and spontaneous OA group, ACL samples from the left knee joint (n=6) were scanned and analysed for CSA and length measurements. In the post-traumatic OA group, ACL samples from the right loaded knee joint were used (n=4), and in the healthy non-loaded control group ACL samples from the left knee joint were used (n=4). Previous studies have shown no difference in ACL measurements between left and right knee joints in humans [210], and the same was observed in preliminary studies on mice ACLs (data not shown here).

Prior to these analyses, the knee joints were defrosted and dissected under a microscope (Nikon SMZ-745, Japan), removing excess tissue and muscle until only the femur-ACL-tibia complex remained (Figure 3.4A), similar to the method previously published by Sun et al [141]. Following dissection, femur-ACL-tibia samples were submerged in Lipiodol contrast agent (Guerbet, FR) overnight at 4℃ before scanning the following day. The following day excess femur and tibia were removed using a scalpel (No. 11) to allow the sample to fit in a small straw holder filled with Lipiodol (Figure 3.4B). Dental wax (Boots, UK) and a putty adhesive (Blu Tack) (Bostik, UK) was used to keep the femur in place at a 90º with the ACL and tibia suspended vertically. The femur-ACL-tibia samples were then scanned with a 5µm isotropic voxel size (50kV, 200µA respectively, 0.5mm Aluminium filter; 0.6° rotation angle, no frame averaging) using a Skyscan 1172 µCT scanner (Bruker, BE). This protocol was similar to previously published methods to image mouse ligaments using phosphotungstic acid [211].

Images of the murine femur-ACL-tibia complex were reconstructed using the NRecon software and inspected with the Dataviewer software (Bruker, BE) (Figure 3.4C-E). A sagittal area of interest showing the femoral condyles-ACL-and tibia condyles was saved for analysis of the murine ACL length (Figure 3.4D). The ACL length was measured using the CTan software (Bruker, BE). A second area of interest of the entire ACL volume was selected in the Dataviewer software and saved in the axial plane for analysis of the ACL CSA (Figure 3.4E). The ACL CSA was measured using the CTan software at the ACL midsection. For each sample length and CSA was measured three times to ensure accuracy, and an average ACL length and CSA was calculated for each mouse group. This method was chosen to measure ACL length and CSA due to the small size of the mouse knee joint and ACL (~1mm length). The average measurement of ACL length and CSA for each group was used to calculate stress-strain. This method differs from past mechanical studies on mouse ACLs which measured each tested ligament using a custom laser-based device [141].

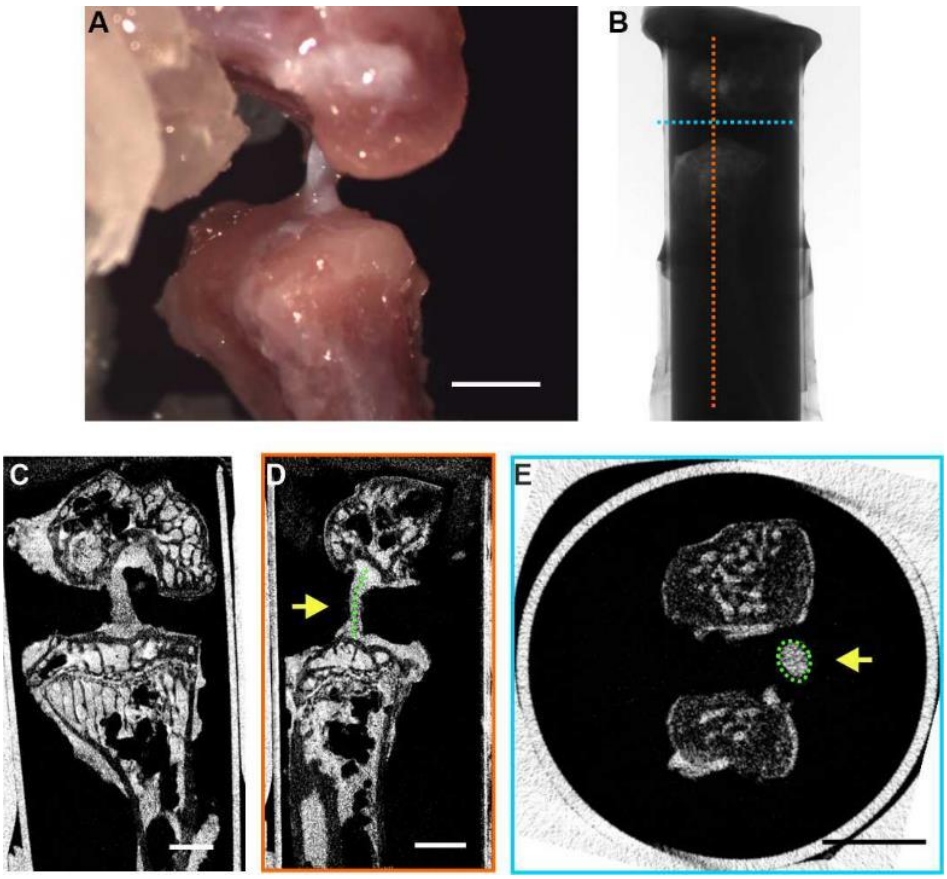

Figure 3.4 X-ray micro computed tomography (μCT) image analysis of the murine anterior cruciate (ACL). Length and cross-sectional area (CSA) were measured. (A) First the murine femur-ACL-tibia complex was dissected. (B) The sample was placed in a small holder submerged in Lipiodol (Guerbet, FR) contrast agent at a 90° knee flexion position. (C-E) Femur-ACL-tibia images were orientated in the coronal (C), sagittal (D, orange box) and axial (E, blue box) plane. (D) ACL length was measured in the sagittal plane (green line, yellow arrow). (E) Similarly, in the axial plane, the murine ACL CSA was selected (green line, yellow arrow) and measured at the mid-point of the ACL. Scale bar is 1mm for all images.

3.2.5 Sample preparation for tensile testing of the murine ACL

Frozen (-20°C) knee joints (see Table 3.1) from the right hind leg were used for mechanical testing of the ACL. Samples were defrosted at room temperature for twenty minutes. Meanwhile the test clamp fixture was assembled and oiled (sunflower oil). Once defrosted, the murine knee joint samples were immediately dissected under a dissection microscope (Nikon SMZ-745, Japan) whilst being kept hydrated with phosphate-buffered saline (PBS) (Gibco). All soft tissue, including muscle and patella, were removed around the femur, tibia and knee joint until the collateral ligaments were visible (Figure 3.5A). The collateral ligaments and then medial and lateral menisci were carefully removed (dissecting at the posterior horns and then the anterior horns) ensuring that the cruciate ligaments stayed intact. Excess muscle was removed until both cruciate ligaments were the only tissue remaining at their femoral and tibial insertions. Then lastly

the PCL was cut from the tibial attachment site and then from the femoral condyle. The remaining femur-ACL-tibia complex was ready to be placed in the test fixtures for tensile testing (Figure 3.5B).

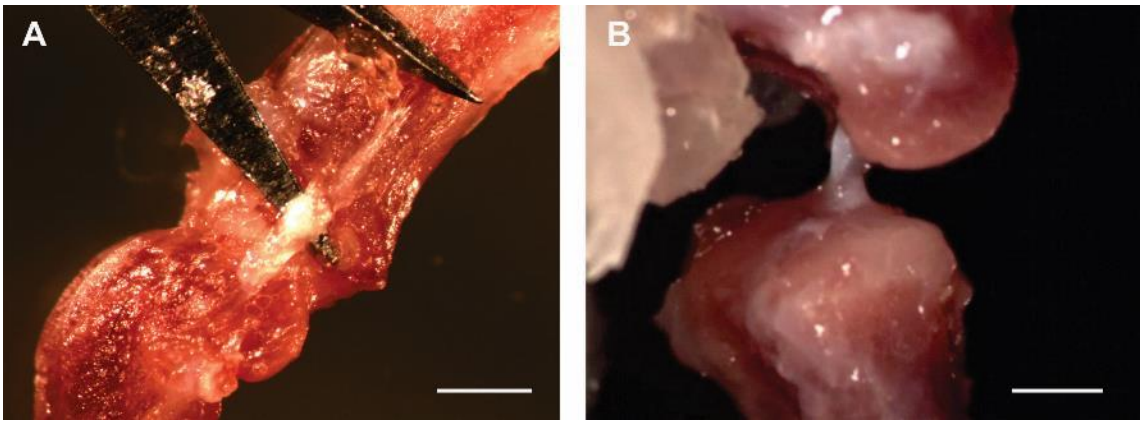

Figure 3.5 Dissection of the murine knee joint, for preparation of the femur-anterior cruciate ligament (ACL)-tibia complex. (A) First surrounding tissue around the knee joint was removed, including excess muscle, patellar tendon, and the collateral ligaments. (B) Then the menisci were removed by dissection at the meniscal horns, and lastly the posterior cruciate ligament was removed, leaving only the femur-ACL-tibia complex. Dissection protocol was similar to past studies on murine ACL mechanical testing [4]. Scale bar is 1mm for both images.

Poly(methyl methacrylate) (PMMA) (Technovit 6091) at the ratio of 1.74 g powder: 1 mL liquid was prepared in a fume hood and used to fix the femur and tibia samples to the clamp fixtures. A layer of PMMA was added to the two compartments and the sample was placed with the femur in the top compartment and the tibia in the bottom compartment (Figure 3.6A). The femur and tibia were placed at an estimated 90º angle using predefined guides in the fixture (Figure 3.6B&F), similar to the protocol used by Sun et al. [141]. Samples were quickly positioned, ensuring the ACL did not come into contact with the PMMA. Another layer of PMMA was applied to each compartment to ensure complete fixation of the femur and tibia. Once the PMMA hardened, the sample was briefly aligned under the dissection microscope (Nikon SMZ-745, Japan) to ensure a vertical ACL orientation (Figure 3.6C). The fixture with the sample was transferred to a dual column uniaxial material testing machine (Instron 3366, USA) (Figure 3.6D), the encasing outer plastic layer was adjusted to enclose the sample and PBS was added to ensure a hydrated ligament sample throughout testing (Figure 3.6E-F). Once ready, the tensile testing protocol commenced (Section 3.2.6). Once the tensile testing of the prepared sample was completed, a steel G-clamp

and a hammer were used to remove the PMMA and remaining tibia and femur sample (Figure 3.6G).

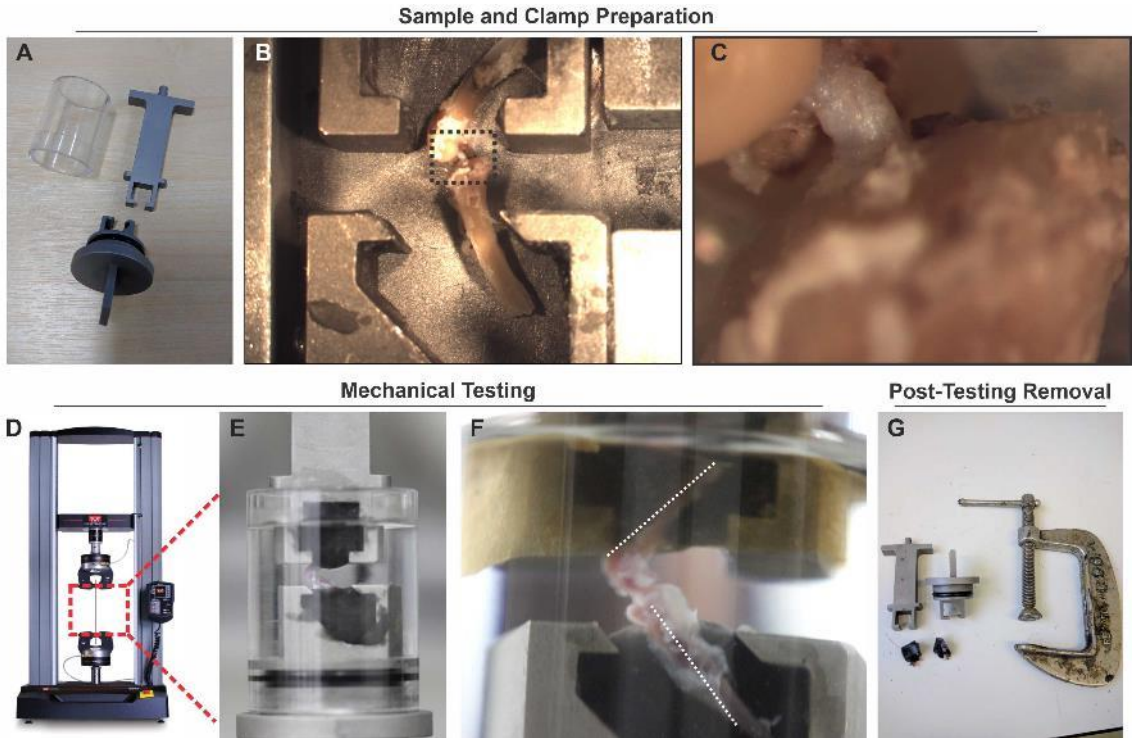

Figure 3.6 Experimental setup for mechanical testing of the murine ACL. Clamps were prepared in a fume hood (A), after which dissected femur-ACL-tibia complex samples were added at an approximate 90° knee flexion angle (B) and fixed in position using PMMA, similar to previous mechanical studies by Sun et al. [141]. ACL orientation was further adjusted under a microscope (C) to ensure a vertical ligament orientation. Clamps with the murine femur-ACL-tibia sample were transferred to a dual column uniaxial materials testing machine (Instron 3366) (D) and outer encasing layer was adjusted and the sample was submerged in phosphate buffered saline before mechanical testing commenced (E) and 90 degree knee flexion was further confirmed (F). Once the tensile testing was completed, the sample was forcefully removed using a G-clamp and a hammer (G).

3.2.6 Mechanical testing protocol to determine viscoelastic behaviour of the murine ACL

The mechanical testing protocol was chosen to determine murine ACL viscoelastic properties based on past literature of murine ligament mechanical properties [114, 141] and on canine cranial cruciate ligament mechanical testing [61]. For all mouse ACLs, the same uniaxial testing protocol was used in the materials testing machine (Instron 3366, USA) using a 10N load cell. Instron measured sample elongation and applied load. Firstly, a preload of 0.02N was applied to remove laxity in the ligament. Then a series of 10 preconditioning loads ensured ligaments were in a steady state condition [64] and removed alterations to viscoelastic behaviour due to freezing [78]. The 10 preconditioning load-unload cycles were applied at a strain rate of 1%/s to a maximum

load of 0.4N and then back to 0.02N with a resting period of 120 seconds before the next cycle (x10) (Figure 3.7).

Following preconditioning, strain rate sensitivity, stress-relaxation behaviour and ultimate load at failure were tested (Figure 3.7). Before strain rate testing, stress-relaxation and ultimate load at failure there was a resting period of 300 seconds to allow the ligament to return to a stable state. For strain rate testing, two load-unload cycles of three different strain rates (0.1%/s, 1%/s, and 10%/s) were followed by a 120 second rest time (Figure 3.7). Viscoelastic stress-relaxation was tested at 5% strain (applied strain at 1%/s) and elongation was maintained for 120 seconds (Figure 3.7). Lastly the final ultimate load at failure was tested at a strain rate of 1%/s until ligament rupture (Figure 3.7). Ligament rupture occurred at the ligament mid-section and was briefly analysed under a microscope following testing (data not shown). Strain rates were chosen based on past literature which ranged from 0.1%/s [141] to 100%/s [114]. Creep was not measured in this study, though it is an important viscoelastic property [2].

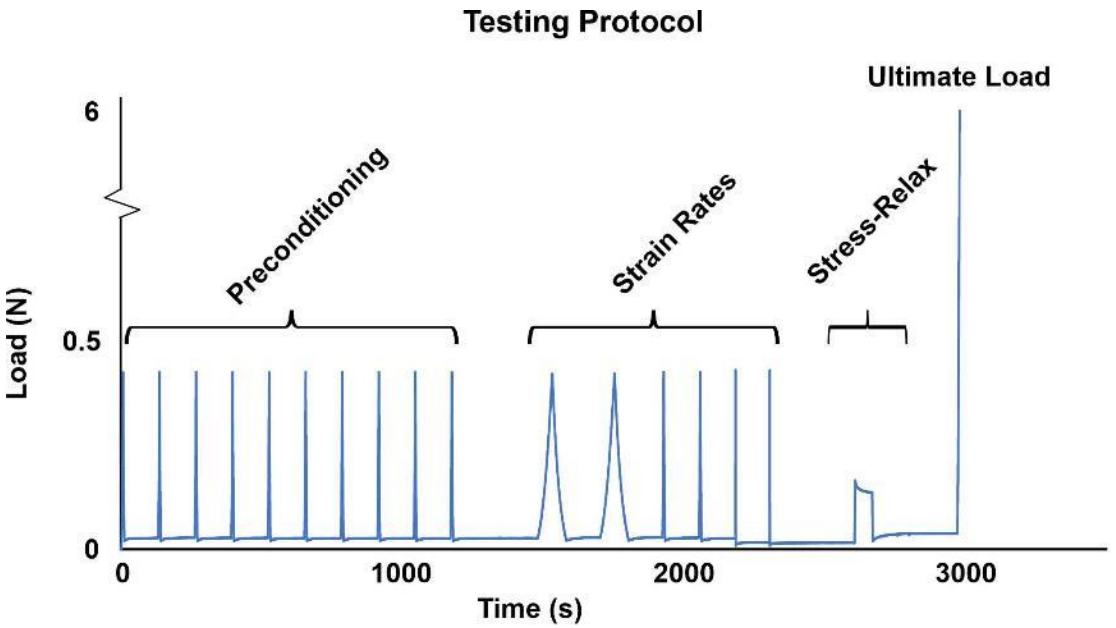

Figure 3.7 Mechanical testing protocol used for viscoelastic and material behaviour of murine anterior cruciate ligament (ACL). Ten preconditioning cycles were applied to ensure a stretched ligament at 1%/s strain rate. Then viscoelastic behaviours were tested including strain rate sensitivity and stress-relaxation. Different strain rates were tested (x2 for each strain rate) at 0.1%/s, 1%/s and 10%/s strain rates. For stress-relaxation the sample was loaded to 5% strain and elongation was held for 120 seconds. Lastly, the material behaviour of ultimate load to failure was tested at 1%/s until ACL rupture.

3.2.7 Analysis of the viscoelastic behaviour and ultimate load of the murine ACL

Analysis of the viscoelastic behaviour and ultimate load to failure of the murine ACLs was analysed using Excel (Microsoft) and GraphPad Prism (GraphPad Software, version 8.0.0).

3.2.7.1 Stress-strain

Stress-strain curves of each of the different strain rates was calculated from the elongation and applied force measurements for each strain rate (0.1%/s, 1%/s, and 10%/s) (see Figure 1.4). The second load-unload cycle was used for analysis [61]. Estimated CSA and length of the specific murine group ACL (see Section 3.3.2) were used for stress and strain calculations. Stress was calculated using Equation 3.1 and strain using Equation 3.2. The resulting stress-strain curve was then fitted to an exponential curve using the least squares method (from the root-mean-square error) (Equation 3.3). An exponential best-fit curve was chosen as it has been previously used to replicate the viscoelastic behaviour of soft-tissues [212], human ACLs [213] and more recently for canine cruciate ligament [61]. Stress-strain curves were plotted up to 3 MPa of stress to prevent extrapolation of data.

$$\sigma = \frac{F}{CSA} \tag{3.1}$$

Where σ is stress (MPa), F is the applied force (N) and CSA (mm^2) is the estimated cross-sectional area.

$$\varepsilon = \frac{\Delta L}{L_0} \tag{3.2}$$

Where ε is strain (mm/mm), ΔL is the change in elongation (mm) ($\Delta L = L_t - L_0$), and L_0 (mm) is the initial estimated ligament length.

$$\sigma = \mathrm{a}(\mathrm{e}^{\mathrm{b}\varepsilon} - 1) \tag{3.3}$$

Where ‘a’ and ‘b’ are coefficients.

3.2.7.2 Tangent modulus

From the exponential best-fit curve for each strain rate, the tangent modulus (slope of the stress-strain curve) was derived using Equation 3.4. Tangent modulus has been used to measure viscoelastic stiffness of the stress-strain curve for soft tissues, including the human sclera [214] and canine cruciate ligaments [61]. For the purposes of this study, tangent modulus was plotted

as a function of stress and then a best-fitted linear equation of the tangent modulus versus stress (Equation 3.5) was used when calculating the average tangent modulus between samples.

$$E_t = \frac{\Delta\sigma}{\Delta\varepsilon} \tag{3.4}$$

Where E_t is tangent modulus (MPa).

$$E_t(\sigma) = ax + b \tag{3.5}$$

Where E_t (σ) is the tangent modulus (MPa) equation as a function of stress, and 'a' and 'b' are coefficients.

3.2.7.3 Strain rate sensitivity

Ligaments and tendons are known to respond differently to variations in strain rate, a behaviour known as strain rate sensitivity [69] (see Figure 1.5A). To analyse stress-strain sensitivity, measurement of the stress-strain curve and tangent modulus was repeated for all the different strain rates. Furthermore, strain rate sensitivity was also analysed with normalised tangent modulus to account for deviation between samples. Normalised tangent modulus was calculated using the tangent modulus at 1%/s and 10%/s strain rates which was normalised to the 0.1%/s strain rate tangent modulus of the same sample using Equation 3.6. Normalised tangent modulus as a factor of stress was calculated for all samples, and an average normalised tangent modulus-stress curve was plotted for each murine group. This is similar to previous calculations done by Hama Rashid et al. on canine cruciate ligaments [61].

$$E_{norm} = \frac{E_t}{E_0} x\ 100 \tag{3.6}$$

Where E_{norm} is normalised tangent modulus (%), E_t is the tangent modulus at 1%/s or 10%/s strain rates, and E_0 is the tangent modulus at 0.1%/s strain rate.

3.2.7.4 Hysteresis

Ligaments also display hysteresis, another viscoelastic behaviour, referring to the loss of energy during a load and unload cycle [215]. In murine ACLs, hysteresis characterised as the area between the load and unload cycles (Figure 3.8), was measured using numerical integration, trapezoidal rule, similar to Rashid et al. [61]. Numerical integration calculated the area under the

curve of the load and unload cycle and the difference between the cycles was hysteresis. Hysteresis was measured at all strain rates (0.1%/s, 1%/s and 10%/s).

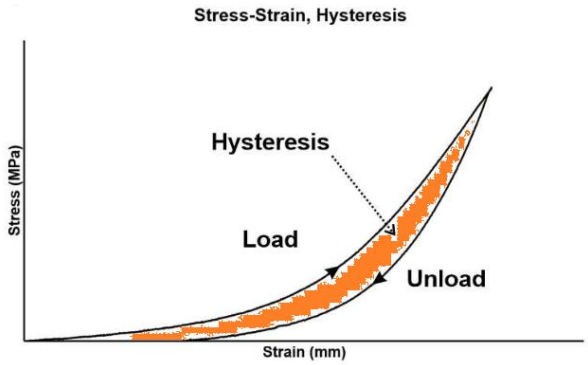

Figure 3.8 Representative viscoelastic hysteresis of the murine ACL. Hysteresis as represented by the load and unload stress-strain curves, demonstrates a loss of energy between the two cycles, measured as the area between the two curves (orange region). Hysteresis area was quantified using numerical integration [61].

3.2.7.5 Stress-relaxation

Stress-relaxation was used to measure the viscoelastic response to constant strain and the resulting decrease in stress (see Figure 1.5B). This nonlinear viscoelastic property has been previously modelled in ligaments [61, 216]. Stress-relaxation was measured when the load reached an estimated 5% strain (0.15N) (t=0). Stress was normalised by the peak stress at t=0 using Equation 3.7 and plotted as a function of log time. The resulting curve was fitted into a polynomial equation to determine the average normalised stress for all samples (Equation 3.8).

$$\sigma_{norm}(t) = \frac{\sigma_t}{\sigma_0} \tag{3.7}$$

Where $\sigma_{norm}(t)$ is the normalised stress-time function, σ_t is the stress, and σ_0 is the stress at t=0.

$$\sigma_{norm}(t) = ax^3 + bx^2 + cx + d \tag{3.8}$$

Where 'a', 'b', 'c' and 'd' are coefficients.

3.2.7.6 Ultimate load at failure

Lastly, ultimate load, also known as maximum load or failure load, a material property, was used as a measurement of maximum ligament strength [114, 141, 204] (see Figure 1.4, Failure region). Ultimate load at failure was measured for each murine sample using the 'MAX' function on Excel (Microsoft).

3.2.8 Statistical analysis and normality of data testing

Normality and statistical analysis were calculated using GraphPad Prism (GraphPad v8). Normality of data was tested using a Shapiro-Wilk test where a p-value ≤ 0.05 indicated statistical significance. For all other statistical analyses, a p-value ≤ 0.05 also indicated statistical significance.

For knee flexion and murine ACL length and CSA analysis, Shapiro-Wilk test showed normally distributed measurements for all groups. Statistical analysis of the physiological range of murine knee flexion involved an unpaired t-test (two-tailed) ($p \leq 0.05$) comparing the maximum and minimum knee flexion angles and gait speed between the left and right knee joints. In the ACL CSA and length measurements, an unpaired t-test ($p \leq 0.05$) was used to compare between control and test groups.

For comparison of ACL viscoelastic and material properties (stress-strain, tangent modulus, strain rate sensitivity, normalised strain rate sensitivity and stress relaxation), the area under the curve was calculated using numerical integration, trapezoidal rule [61], for each sample. Shapiro-Wilk test confirmed normally distributed data for the stress-strain area under the curve of the healthy ageing group 12-week-old and the spontaneous OA group 24-week-old ACLs. Data was not normally distributed for the area under the curve of the stress-strain curves for the healthy ageing 24-week-old ACLs, in the spontaneous OA 12-week-old ACLs, and in the post-traumatic OA group. Therefore, for stress-strain analysis, a nonparametric statistical test was performed (Mann-Whitney test). Lack of normality in these control samples is likely due to the standard deviation, potentially due to assumptions of equal ACL length and CSA.

All other ACL mechanical properties showed normal distribution, including tangent modulus, normalised tangent modulus, hysteresis, stress-relaxation and ultimate load. Therefore, statistical analysis was completed with an unpaired t-test (two tailed) ($p \leq 0.05$). Groups compared included: 12 versus 24-week-old ACLs in the healthy ageing group and in the spontaneous OA group, and non-loaded versus loaded ACLs in the post-traumatic OA group.

Furthermore, in the strain rate sensitivity analysis compared strain rate (0.1%/s, 1%/s and 10%/s) differences within the same group. A nonparametric Friedman test was used when comparing the area under the curve of stress-strain curves at the three different strain rates, followed by a Dunn's multiple comparison test ($p \leq 0.05$). Repeated measures ANOVA was used when comparing the area under the curve of the tangent modulus-stress curves at the same three different strain rates,

followed by multiple comparisons using Bonferroni post-hoc test ($p \leq 0.05$). When comparing the area under the curve of the normalised tangent modulus of the 1%/s and the 10%/s strain rates, a paired t-test (two-tailed) was used. A Friedman test, repeated measures ANOVA and paired t-test was possible since measurements were taken from the same ACL sample at different strain rates.

Changes in hysteresis within the same group at different strain rates were also tested with a repeated measures ANOVA, followed by a post-hoc Bonferroni multiple comparisons test ($p \leq 0.05$). Lastly, hysteresis was also tested as a continuous variable using Pearson's correlation test to determine a correlation coefficient (r). This was conducted for the hysteresis in the first five preconditioning cycles to measure correlation with increase in cycle in both the OA and control groups.

Overall, this statistical analysis compares differences and similarities between healthy control and OA ACLs, as well as similarities and differences within each group for strain rate sensitivity and preconditioning.

3.3 Results

3.3.1 Physiological range of murine knee flexion – Gait analysis

The physiological range of knee flexion in the mouse during gait was analysed to determine the ideal range of knee flexion for mechanical tensile testing of the ACL and CSA measurements. Using MatLab, a 3D model was created of the left and right hind-leg movement during gait of all (n=4) B6CBAF1 mice (Figure 3.9A). Knee flexion was calculated in radians and plotted at every frame for both legs (Figure 3.9B-C) from which the maximum and minimum angles of knee flexion were then calculated (Table 3.2).

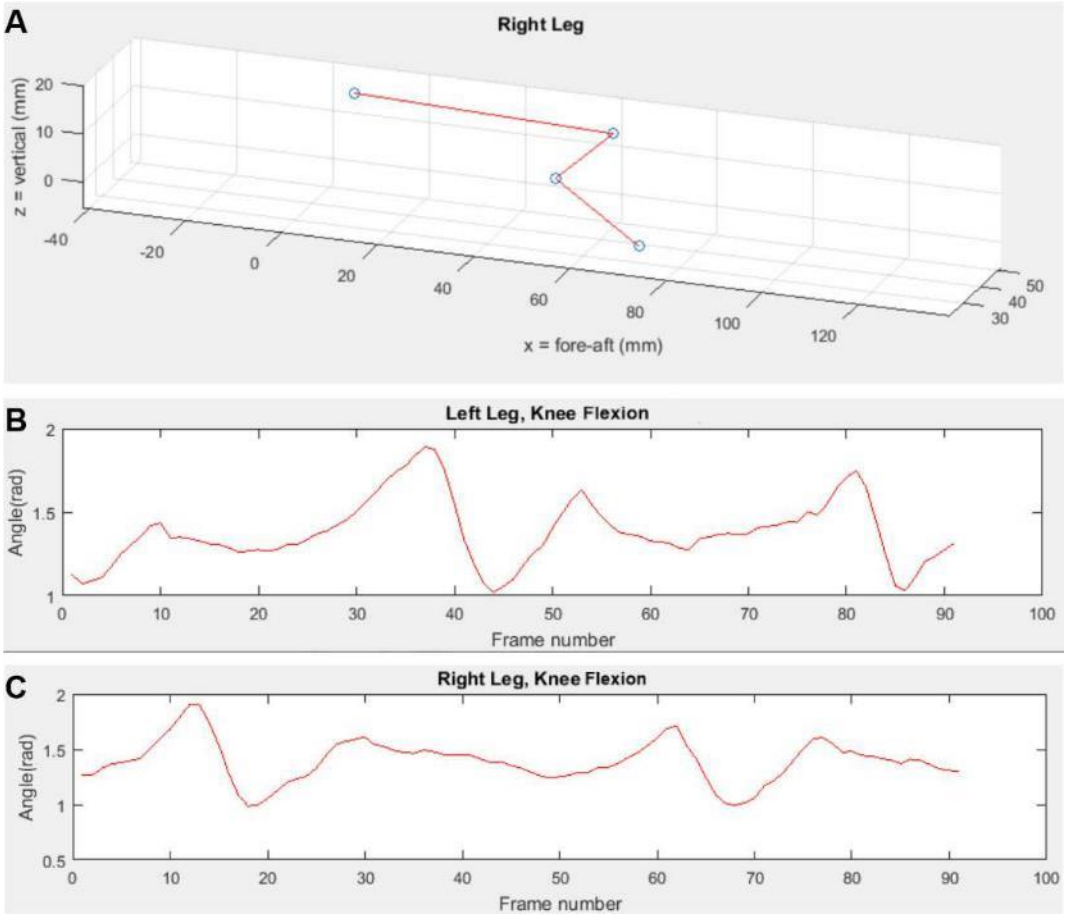

Figure 3.9 Representative images of murine knee flexion during gait. By tracking knee joint, hip, ankle and occiput points in each frame using XMALab (Brown University, USA) a 3D model of the left and right knee joint (A) was created using MatLab (MathWorks, R2018a Version 9.4, USA). From this model, knee flexion of the left (B) and right (C) knee joint were calculated as radians over frame number.

Maximum knee flexion was 100.82° in the left knee joints and 100.47° in the right knee joint (Table 3.2). Minimum knee flexion was 56.49° and 55.61° in the left and right knee respectively (Table 3.2). Maximum and minimum angles of knee flexion in both the left and right knee joints of the B6CBAF1 (n=4) mice were similar and showed no statistically significant differences in the maximum (p=0.96) and minimum angle of knee flexion (p=0.67) (Table 3.2). Furthermore, the speed of the left and right knee joints was also analysed, average gait speed was similar for both legs, 136 and 139 mm/s for the left and right knee respectively (p=0.73).

Overall, this data suggests that the physiological range of murine knee flexion during gait was between 55-100°. In order to remain within the physiological range, mechanical viscoelastic and material testing of the murine ACL was performed at 90° of knee flexion, because it allowed for uniform tensile testing along the axis of the ligament, similar to a previous study by Warden et al. [148].

Table 3.2 Angles of murine knee joint flexion and gait speed as determined by biplanar radiography. The average minimum (Min) and maximum (Max) knee flexion was calculated in degrees for both the left and right murine knee joint. Knee flexion ranged from 56.5 to 100.8° in the left knee, and 55.6 and 100.5° in the right knee joint. Relative standard deviation (RSD) ranged from 6.7% to 13.3%. No statistically significant differences were found between left and right knee in the Max knee flexion (p=0.96), Min knee flexion (p=0.67) and gait speed (p=0.73).

	Degrees (°)				Gait speed (mm/s)	
	Min	Max	Min	Max		
	Left Knee		Right Knee		Left knee	Right knee
Avg.	56.5	100.8	55.6	100.5	135.6	138.7
RSD (%)	8.8	13.3	6.7	11.5	24.3	19.1

3.3.2 Micro-computed tomography (µCT) imaging and measurement of the murine ACL length and cross-sectional area (CSA)

µCT imaging was used to measure the length and the CSA of the murine ACL, necessary for mechanical analysis. The murine ACL length for the healthy ageing 12-week-old and 24-week-old ACLs was 1.153 ±0.053 mm and 1.174 ± 0.060 mm respectively and differences were not statistically significant between the two groups (p=0.414) (Figure 3.10B-C). The length of the spontaneous OA 12-week-old and 24-week-old ACLs was 1.207 ±0.051 mm and 1.276 ± 0.031 mm respectively, a relative percent difference of 5.5% which was statistically significant (p=0.01) (Figure 3.10B-C). The ACL length of the post-traumatic OA non-loaded and loaded ACLs was 1.144 ±0.104 mm and 1.087 ±0.091 mm respectively and were not significantly different (p=0.077) (Figure 3.10B-C). Only the spontaneous OA 24-week-old ACLs showed a significant

increase in ACL length, which was not seen in the healthy ageing control group which could indicate a difference in skeletal maturity in this spontaneous OA group.

The CSA of the murine ACLs ranged between 0.097 mm^2 to 0.112 mm^2 based on the murine group (Figure 3.10A&C). When comparing the CSA between the murine groups and their respective controls, there were no statistically significant differences between the groups (healthy ageing group: p=0.648, spontaneous OA group: p=0.307, post-traumatic OA group: p=0.553). However, in the CSA measurements, there was relative standard deviation (RSD) which reached 16.2% in the post-traumatic OA non-loaded ACLs. High RSD suggests high variance within the samples which could be a potential source of error for calculations of stress and strain used in the mechanical analysis. The measurements for ACL length and CSA for each specific murine group (Figure 3.10C) were used in the mechanical analyses of stress-strain.

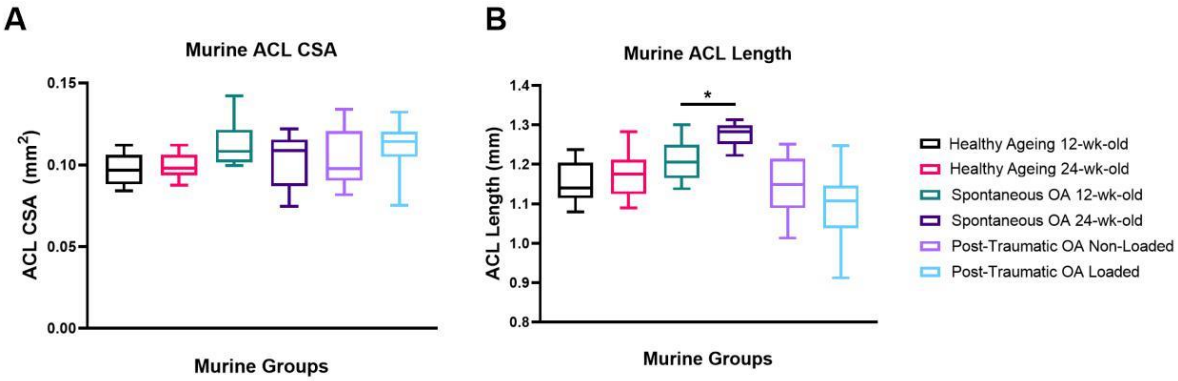

C

OA Group	Mouse group	ACL Length			ACL CSA		
		Length (mm)	RSD (%)	%diff	CSA (mm^2)	RSD (%)	%diff
Healthy Ageing	C57 12-wk-old	1.153	4.6	1.82	0.097	9.6	1.83
	C57 24-wk-old	1.174	5.1		0.099	14.6	
Spontaneous OA	CD1 12-wk-old	1.207	4.2	5.54	0.111	4.9	0.51
	CD1 24-wk-old	1.276	2.4		0.112	15.1	
Post-Traumatic OA	C57 Non-loaded	1.144	9.1	5.12	0.105	16.2	3.66
	C57 Loaded	1.087	8.4		0.109	16.1	

Figure 3.10 Measurement of the murine anterior cruciate ligament (ACL) length and cross-sectional area (CSA). Measurements were made in the healthy ageing, spontaneous and post-traumatic murine osteoarthritis (OA) groups. Murine ACL CSA (A) and length (B) were measured for each mouse group. Measurements of the ACL length (mm) and CSA (mm^2), relative standard deviation (RSD) and percent difference (%diff) between each group are summarised (C). There were statistically significant differences in ACL length within the spontaneous OA group (5.5% difference) (p=0.01).

3.3.3 Quality control of mechanical analysis

Preconditioning of the murine ACLs was used as a quality control step; samples that showed greater than 5% increased elongation during the preconditioning cycles were removed from analysis. All samples removed due to preconditioning can be seen in Sup Fig 1 (Appendix). In the healthy ageing group, two of the 24-week-old ACL samples were removed due to elongation increasing 6-7% (Sup Fig 1). In the spontaneous OA group, four samples were removed in the 12-week-old ACLs (7-10% increase in elongation), and two samples were removed in the 24-week-old group (6-7% increase in elongation) (Sup Fig 1) and an additional sample failed during dissection. In the post-traumatic OA group, one sample was removed from each group due to an increase in elongation ranging from 7-13% (Sup Fig 1). Increase in elongation was attributed to lack of fixation or slippage of the femur or tibia from the PMMA, resulting in increased elongation after every cycle. The total number of samples analysed for each group can be seen in Table 3.3. Representative preconditioning cycles for analysed samples can be seen in Sup Fig 2.

Table 3.3 Samples mechanically tested and analysed. Samples that had a greater than 5% increase in elongation during preconditioning were discarded from analysis. A summary of samples tested and analysed can be seen for each murine group. The preconditioning cycles of the removed samples can be seen in Sup Fig 1.

Murine Group	Samples Tested (n)	Samples Analysed (n)
Healthy Ageing group:		
12-wk-old ACLs	8	8
24-wk-old ACLs	8	6
Spontaneous OA group:		
12-wk-old ACLs	10	6
24-wk-old ACLs	10	7
Post-traumatic OA group:		
Non-loaded ACLs	8	7
Loaded ACLs	8	7

3.3.4 Viscoelastic behaviour and ultimate load at failure of the ACLs in the healthy ageing group (C57BL/6J 12 and 24-week-old ACLs)

The healthy ageing group were analysed to determine mechanical changes of the ACLs associated with ageing in a healthy murine group between 12 and 24-weeks-old, the same time points used in then CD1 spontaneous OA mice. C57BL/6J mice do not show symptoms of OA at 12-24 weeks of age [154, 173], hence differences within these two groups, if any, are likely to be due to ageing and not OA.

3.3.4.1 Stress-strain

Stress-strain curves of the loading cycle at strain rates of 0.1%/s, 1%/s and 10%/s showed the expected exponential nonlinear viscoelastic behaviour of the ACL (Figure 3.11) [61]. When comparing the healthy ageing 12-week-old and 24-week-old ACLs, there were no statistically significant differences in the stress-strain at 0.1%/s (p=0.65), 1%/s (p=0.69) and 10%/s (p=0.69) strain rates. General trend at all strain rates showed a slight increase in average stress in the 24-week-old ACLs, however this was not statistically significant. It is worth noting the large deviation seen in both samples, which reached up to 134% RSD in the 24-week-old ACLs and 118% RSD in the 12-week-old ACLs at 0.1%/s strain rate. Despite this deviation, these findings confirm no differences in the ACL stress-strain behaviour between the two age time points of the healthy ageing group.

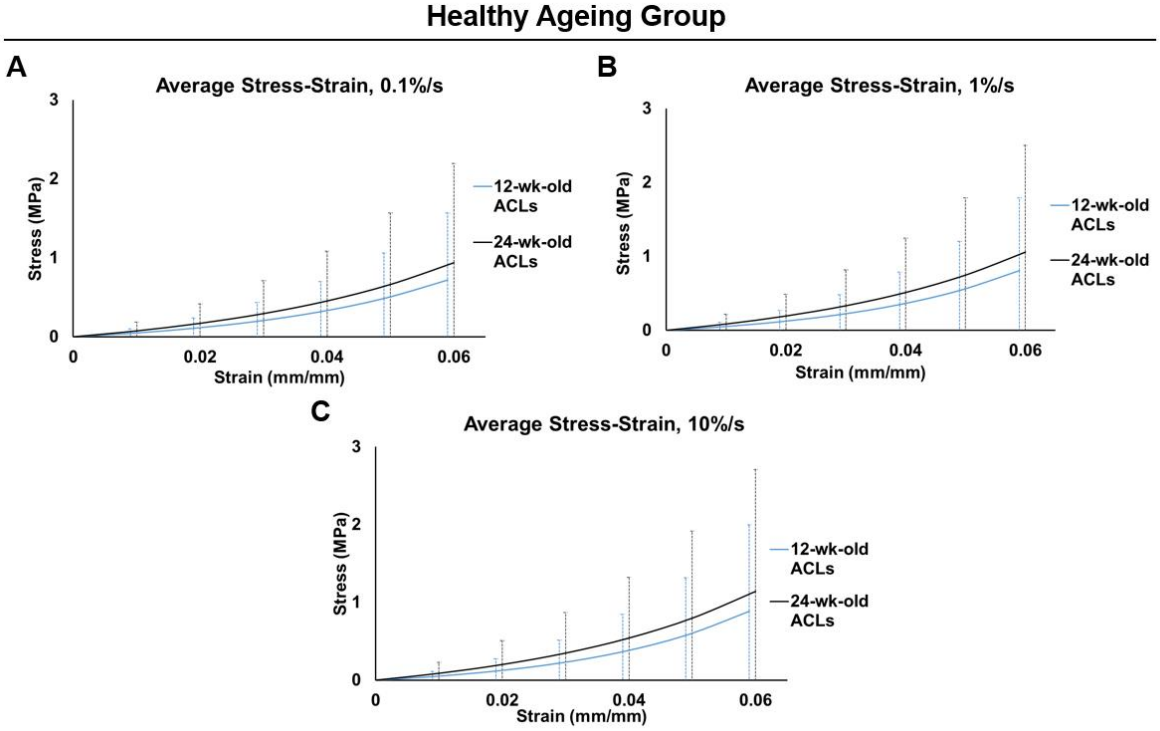

Figure 3.11 Average stress-strain curves of the murine healthy ageing group, 12 and 24-week-old ACLs, at different strain rates. Strain rates tested included 0.1%/s (A), 1%/s (B) and 10%/s (C). There were no statistically significant differences between the 12-week-old and 24-week-old ACLs at 0.1%/s (p=0.65), 1%/s (p=0.69) and 10%/s (p=0.69) strain rates. This suggests there were no changes in the stress-strain behaviour in the viscoelastic region for these two time points in the healthy ageing group.

3.3.4.1.1 Tangent modulus

Tangent modulus-stress curves measured stiffness in the murine ACLs at different points of stress. Figure 3.12 showed a linear increase in tangent modulus as stress increased in the healthy ageing group ACLs. There were no statistically significant differences between the tangent modulus of the 12-week-old and 24-week-old ACLs of the healthy ageing group at any strain rate (0.1%/s: p=0.68, 1%/s: p=0.75, and 10%/s: p=0.98). At 0.1%/s strain rate, at 2 MPa of stress (the same stress used for the power and sample size analysis) the average tangent modulus was 68 ±17 MPa and 70 ±13 MPa for the 12 and 24-week-old ACLs respectively (Figure 3.12A). This is a higher standard deviation than previously calculated in preliminary studies (8 MPa) and used in sample size calculations (see Section 3.2.3.1) which could affect the test power. Overall, these findings suggest that there were no differences in the tangent modulus and stiffness behaviour of the healthy ageing ACLs.

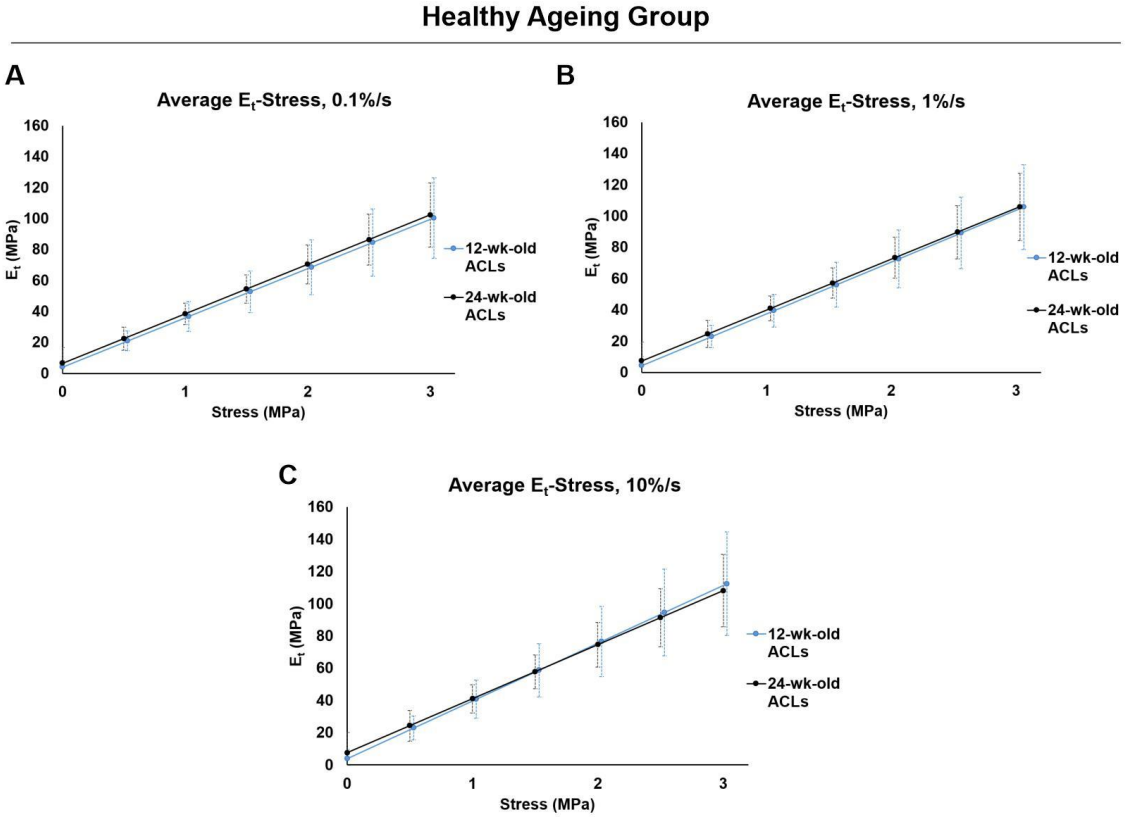

Figure 3.12 Average tangent modulus-stress curves of the murine healthy ageing group, 12 and 24-week-old ACLs, at different strain rates. Strain rates tested included 0.1%/s (A), 1%/s (B) and 10%/s (C). There were no statistically significant differences in the average tangent modulus of the 12-week-old and 24-week-old ACLs at any strain rate (0.1%/s: p=0.68, 1%/s: p=0.75, and 10%/s: p=0.98). Overall, stiffness did not change between the two healthy ageing ACL time points.

3.3.4.1.2 Stress-strain strain rate sensitivity

The strain rate sensitivity, a viscoelastic property, was analysed for each of the 12 and 24-week-old ACLs of the healthy ageing group. Generally, the average stress increased as the strain rate increased (Figure 3.13A-B). In the 12-week-old ACLs, when comparing the area under the curve of the stress-strain curves, the different strain rates were not significantly different (p=0.68). The same was also true in the same 24-week-old ACL at different strain rates (p=0.23). Post-hoc analysis (Dunn's multiple comparisons test) found no significant differences between any of the strain rates at both age groups. These results suggest a lack of strain rate sensitivity in the stress-strain curves for both healthy ageing ACLs.

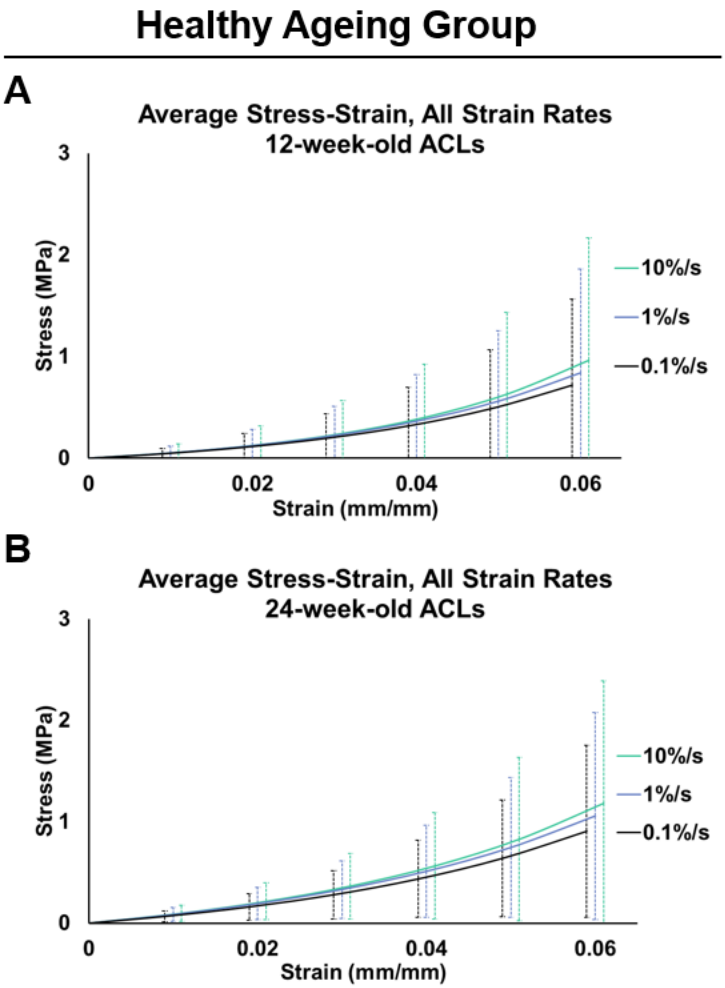

Figure 3.13 Average stress-strain curves at all strain rates (0.1%/s, 1%/s and 10%/s) to determine strain rate sensitivity in the murine healthy ageing group. Both 12-week-old (A) and 24-week-old ACLs (B) showed no statistically significant differences between strain rates (p=0.68 for 12-week-old and p=0.23 for 24-week-old). Statistical analysis would indicate no strain rate sensitivity in the stress-strain curves in both healthy ageing ACLs.

Strain rate sensitivity was further assessed in the tangent modulus-stress curves. Tangent modulus-stress curves showed an increase in tangent modulus in relation to the strain rate in both healthy ageing ACLs (Figure 3.14A-B). The difference in the tangent modulus between the different strain rates (0.1%/s, 1%/s and 10%/s) was statistically significant in both the 12-week-old ($p<0.01$) and 24-week-old ACLs ($p=0.01$) (Figure 3.14A-B). Post-hoc multiple comparisons revealed statistically significant differences between the 0.1%/s and 10%/s strain rates in both the 12-week-old ($p<0.01$) and 24-week-old ACLs ($p<0.01$). There were also statistically significant differences between the 1% and 10% strain rates in the 12-week-old ACLS ($p=0.03$) and in the 24-week-old ACLs ($p=0.04$). However, no statistically significant differences were found in average tangent modulus between the 0.1%/s and 1%/s strain rates in both ACLs (12-week-old: $p=0.31$, 24-week-old: $p=0.25$). Results from the tangent modulus-stress curves suggest strain rate sensitivity in both healthy ageing ACLs.

Strain rate sensitivity was further analysed in the normalised tangent modulus-stress curves (normalised to the 0.1%/s strain rate of each sample, see Section 3.2.7.3). In the 12-week-old ACLs, the difference between the 1%/s and 10%/s strain rates were statistically significant ($p<0.01$) (Figure 3.14C). The same was also true in the 24-week-old ACLs, where the difference in the normalised tangent modulus between the two strain rates was also statistically significant ($p<0.01$) (Figure 3.14D). Overall, this would suggest that at both ACLs of the healthy ageing group, the stress-strain, tangent modulus and normalised tangent modulus showed significant strain rate sensitivity, indicative that at these ageing time points there were no changes to viscoelastic strain rate sensitivity.

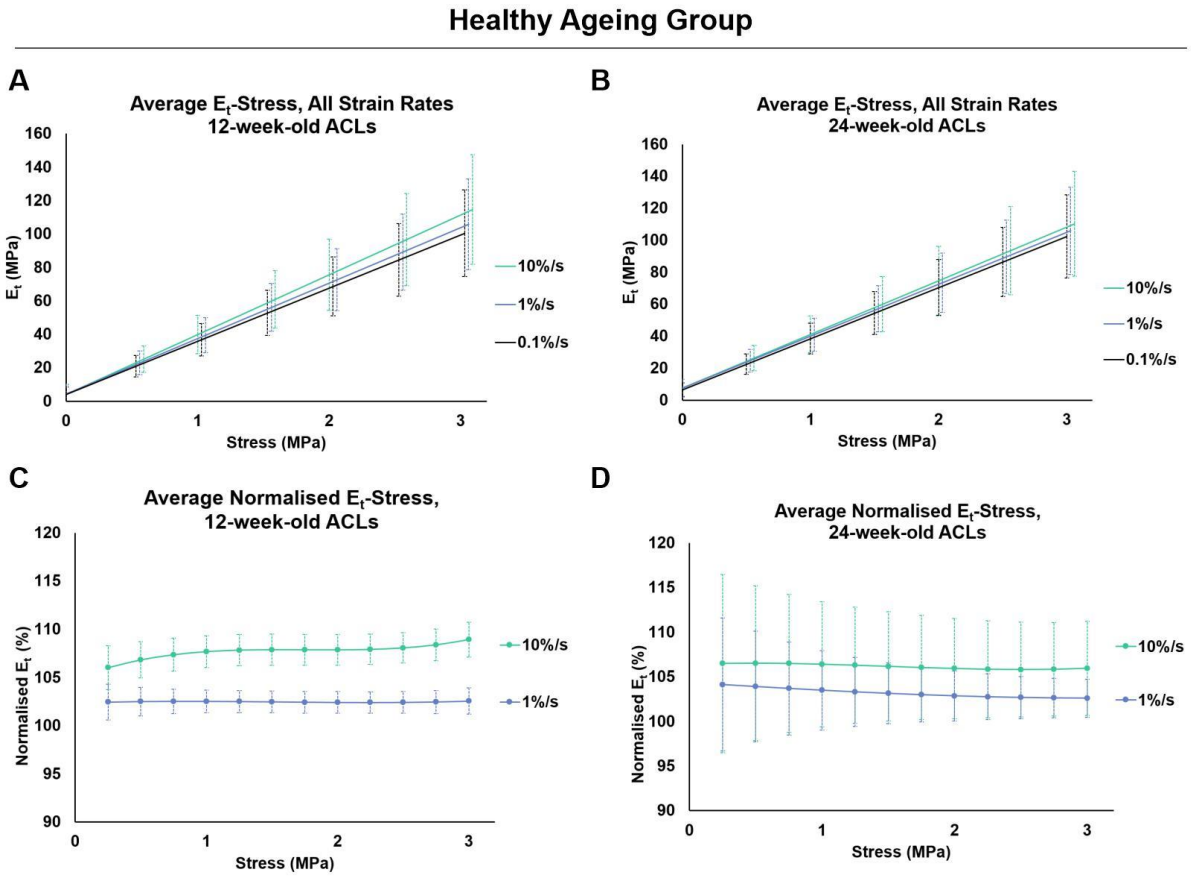

Figure 3.14 Average tangent modulus and normalised tangent modulus-stress curves comparing different rates (0.1%s, 1%/s and 10%/s) in the murine healthy ageing group to determine strain rate sensitivity. Average tangent modulus-stress curves of the 12-week-old (A) and 24-week-old (B) ACLs showed an increase in tangent modulus with increasing strain rate, both were statistically significant ($p \leq 0.01$ for both)). Normalised tangent modulus-stress curves of the 1%/s and 10%/s strain rates (normalised to the 0.1%/s strain rate) in the 12-week-old (C) and 24-week-old ACLs (D) also showed an increase in the 10%/s strain rate, which was statistically significant in both ACLs ($p<0.01$ for both). This would indicate strain rate sensitivity in both ACLs of the healthy ageing group.

3.3.4.2 Hysteresis

Viscoelastic hysteresis, a measurement of the energy lost during the load-unload cycle, was assessed at different strain rates (0.1%/s, 1%/s and 10%/s). When comparing the healthy ageing 12-week-old and 24-week-old ACLs, hysteresis was not statistically significant different at 0.1%/s ($p=0.20$), 1%/s ($p=0.14$) and 10%/s strain rates ($p=0.26$) (Figure 3.15). Additionally, at the 10%/s strain rate, hysteresis was negative for both healthy ageing ACLs, which would mean that the ligament released more energy than it stored, which is not possible. Negative hysteresis has previously been reported in human tendons [217, 218] often attributed to methodological inaccuracies. Overall, results suggested no differences in the hysteresis at different strain rates in the healthy ageing 12 and 24-week-old ACLs.

3.3.4.2.1 Hysteresis strain rate sensitivity

Hysteresis strain rate sensitivity was analysed in each of the healthy ageing ACLs (Figure 3.15). In the 12-week-old ACLs, strain rates had statistically significant differences ($p<0.01$). Post-hoc multiple comparisons also found significant differences between the 0.1%/s and 10%/s strain rates ($p<0.01$) and between the 1%/s and 10%/s strain rates ($p<0.01$), however no statistically significant difference was found between the 0.1%/s and 1%/s strain rates ($p>0.99$). Similarly, in the 24-week-old ACLs, strain rates were significantly different ($p<0.01$), and the same post-hoc analysis showed differences between the 0.1%/s and 10%/s strain rates and 1%/s and 10%/s strain rates ($p<0.01$ for both), but no differences between the 0.1%/s and 1%/s strain rates ($p>0.99$). In both healthy ageing ACLs, strain rate sensitivity was similar and did not change despite the different age points.

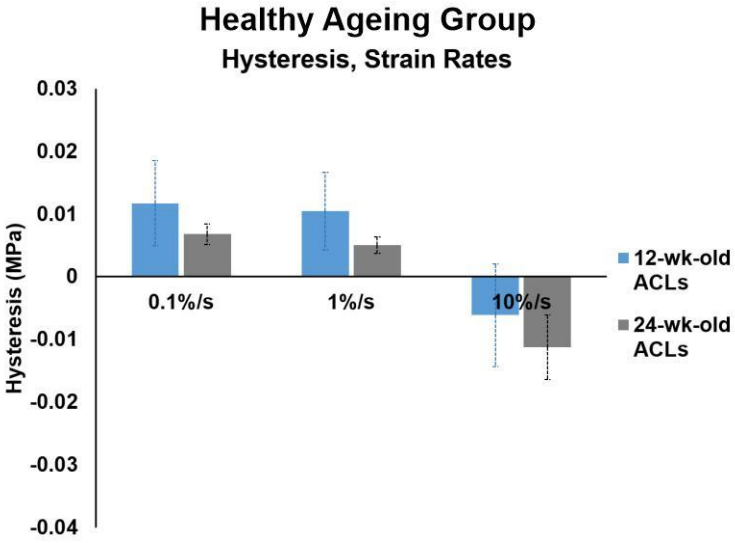

Figure 3.15 Hysteresis in the murine healthy ageing group, 12 and 24-week-old ACLs at different strain rates. Strain rates tested included: 0.1%/s, 1%/s and 10%/s. The average hysteresis and standard deviation increased in the 12-week-old ACLs compared to the 24-week-old ACLs, however this difference was not statistically significant at different strain rates. Furthermore, strain rate sensitivity analysis determined statistically significant differences between the strain rates at both the 12 and 24-week-old ACLs ($p<0.01$). This suggests similar hysteresis behaviour in both healthy ageing ACLs.

3.3.4.3 Stress Relaxation

Stress-relaxation was analysed with the average normalised stress (normalised to stress at t=0). Stress-relaxation showed no significance difference between the healthy ageing 12-week-old and 24-week-old ACLs ($p=0.69$) (Figure 3.16). Although there were no statistical differences between

the two age groups, the 24-week-old ACLs had slightly higher average normalised stress (Figure 3.16). Overall, similar stress-relaxation behaviour in both of these ACLs suggests that the age differences did not affect this viscoelastic behaviour.

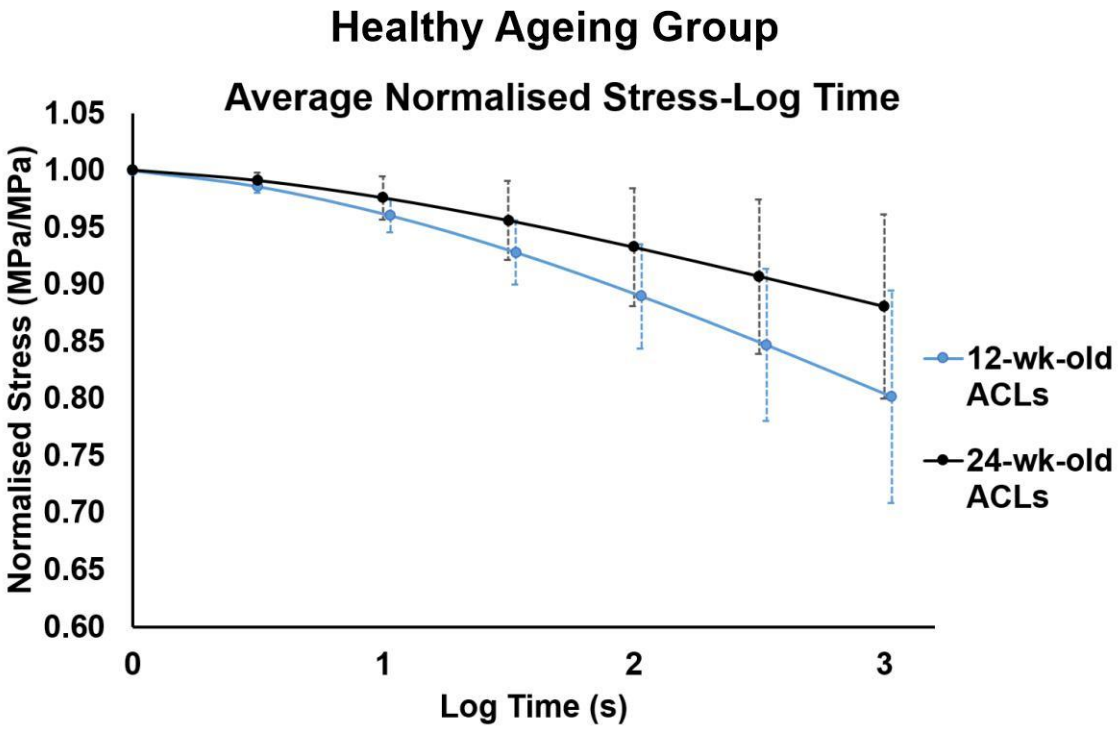

Figure 3.16 Normalised stress-log time curves of the healthy ageing 12 and 24-week-old ACLs to determine the viscoelastic stress-relaxation behaviour. Average normalised stress (normalised to stress at t=0) had no statistically significant differences between the 12 and 24-week-old ACLs (p=0.69). This would indicate that age differences in the ACLs did not result in changes to the viscoelastic stress-relaxation behaviour.

3.3.4.4 Ultimate load at failure

The ultimate load at failure was analysed as a measurement of overall ligament strength at forces above the normal physiological range. The ultimate load was 5.49 ±0.92 N and 5.08 ±1.62 N for the 12 and 24-week-old ACLs respectively, and both groups were not statistically different (p=0.58) (Figure 3.17). Furthermore, in the 24-week-old ACLs there was higher deviation equivalent to 32% RSD, almost double the 17% RSD of the 12-week-old ACLs. Overall, this data suggests no difference in the ultimate load and material properties of the healthy ageing ACLs.

Healthy Ageing Group

A

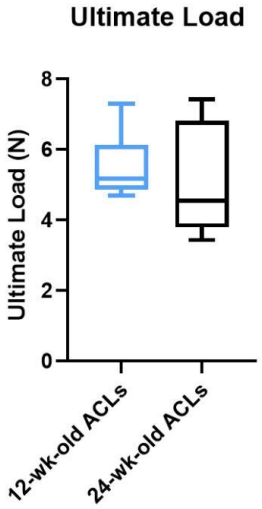

B

	12-wk-old ACLs	24-wk-old ACLs
Ultimate Load (N)	5.49	5.08
SD	0.92	1.62
P-value	0.575 (ns)	

Figure 3.17 Ultimate load (N) at failure of the healthy ageing group ACLs. Load to failure, also known as maximum load, was applied at 1%/s to 12 and 24-week-old ACLs until ligament failure. The average ultimate load applied was 5.49 ±0.92 N in the 12-week-old ACLs and 5.08 ±1.62 in the 24-week-old ACLs (A-B). Statistical analysis found no differences between the two age groups (p=0.575) (B). This would indicate similar material properties in the murine ACL at these two time points.

3.3.5 Viscoelastic behaviour and ultimate load at failure of the ACL in the spontaneous OA group (CD1 12 and 24-week-old ACLs)

In the spontaneous OA CD1 mice, we previously showed significantly higher OA cartilage scores and joint space mineralisation in the 24-weeks-old compared to the 12-week-old knee joints (see Chapter 2). For this spontaneous OA model, the material and viscoelastic properties of the CD1 12-week-old ACLs were compared to those of the 24-week-old ACLs, to analyse changes in the ligament mechanics during OA progression.

3.3.5.1 Stress-strain

The stress-strain curves showed the expected nonlinear exponential behaviour expected at the viscoelastic toe-region (Figure 3.18). For the 0.1%/s, 1%/s and 10%/s strain rates, there were no statistically significant differences between the 12 and 24-week-old ACLs (p=0.39 for 0.1%/s, p=0.36 for 1%/s and 10%/s) (Figure 3.18A-C). Overall, this indicates no difference in the stress-strain curves at the two CD1 age groups, despite increased spontaneous OA in the 24-week-old ACLs. This is similar to the stress-strain curves of the healthy ageing group (Figure 3.11).

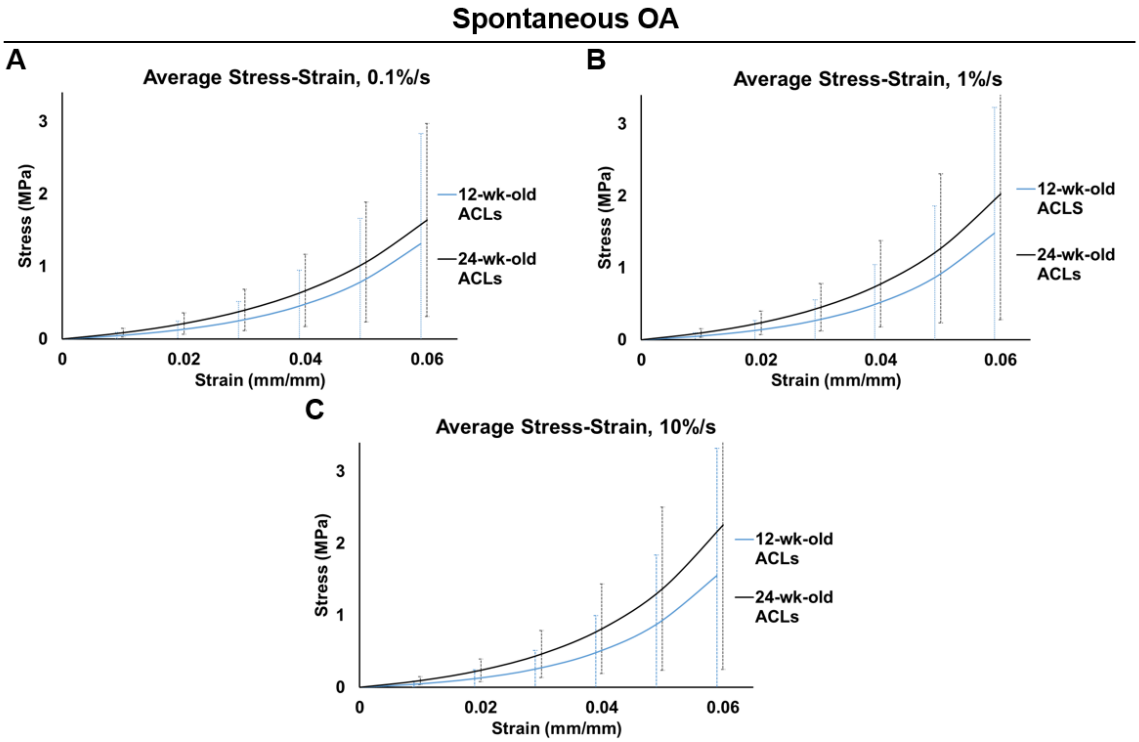

Figure 3.18 Average stress-strain curves of the murine spontaneous OA group, 12 and 24-week-old ACLs, at different strain rates. Strain rates tested included 0.1%/s (A), 1%/s (B) and 10%/s (C). There was no significant difference in the spontaneous OA group between the 12 and 24-week-old ACLs at 0.1%/s (p=0.39), 1%/s and 10%/s (p=0.36 for both). This would indicate that there were no changes between the 12 and 24-week-old spontaneous OA ACLs in the stress-strain behaviour.

3.3.5.1.1 Tangent modulus

Tangent modulus-stress curves demonstrated the expected increase in tangent modulus with increasing stress in the spontaneous OA ACLs (Figure 3.19). Average tangent modulus showed a general decrease in the 24-week-old ACLs compared to the 12-week-old ACLs, however the decrease in the 24-week-old ACLs was not statistically significant at 0.1%/s (p=0.38), 1%/s (p=0.50), and 10%/s (p=0.53) (Figure 3.19). Notably, the CD1 ACLs had high standard deviation at both age groups which could affect results; standard deviation reached 22 MPa and 20 MPa in the 12 and 24-week-old ACLs at 2 MPa of stress, which was higher than the expected standard deviation seen in the preliminary studies (8 MPa). Overall, this would confirm no change in stiffness between the 12-week-old and 24-week-old ACLs in the spontaneous OA group. This was similar to the tangent modulus-stress curves of the healthy ageing group which also found no differences between the 12 and 24-week-old ACLs.

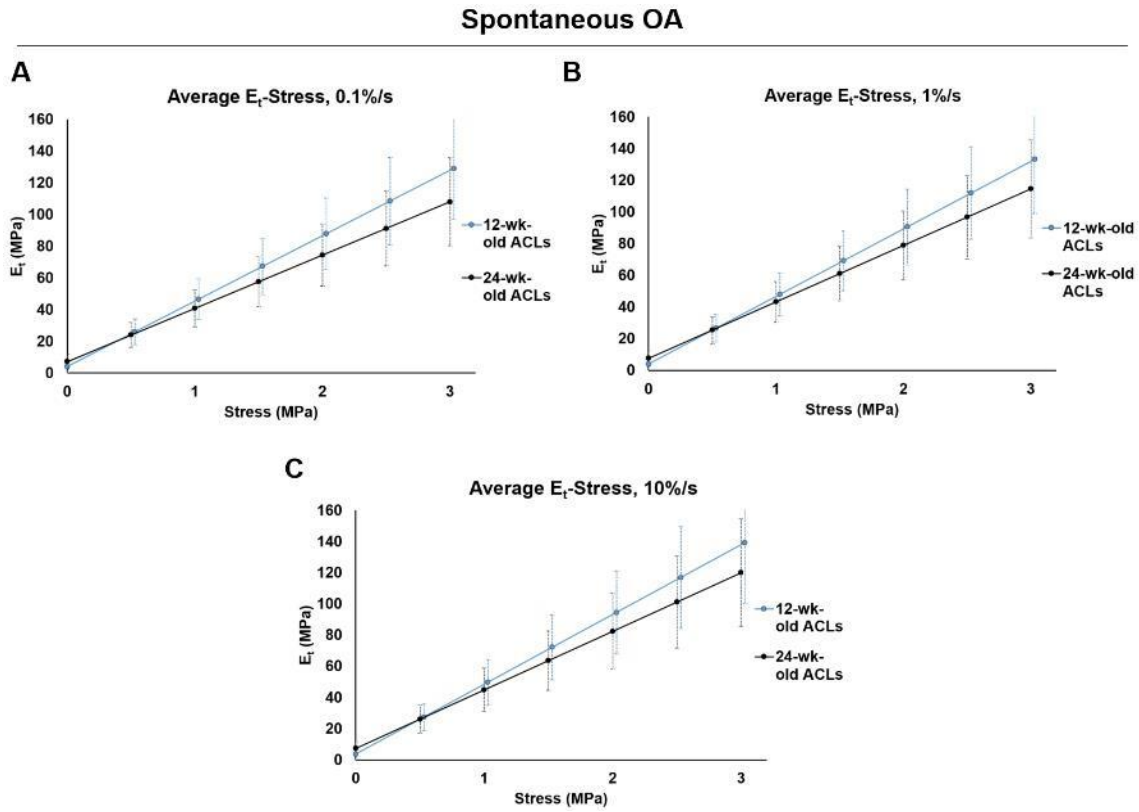

Figure 3.19 Tangent modulus-stress curves of the murine spontaneous OA group, 12 and 24-week-old ACLs, at different strain rates. Strain rates tested included 0.1%/s (A), 1%/s (B) and 10%/s (C) strain rates. Overall, the 24-week-old ACLs showed a decrease in average tangent modulus after 1 MPa of stress, however this decrease was not significantly different at 0.1%/s (p=0.38), 1%/s (p=0.50), and 10%/s (p=0.53). This indicates no changes in the stiffness behaviour at the toe-region of the ACL in the spontaneous OA group.

3.3.5.1.2 Stress-strain strain rate sensitivity

The stress-strain curves demonstrated a general increase in stress with increasing strain rate in the spontaneous OA 12 and 24-week-old ACLs (Figure 3.20A-B), however this was not statistically significant in both 12 (p=0.43) and 24-week-old (p=0.14) ACLs. Post-hoc multiple comparisons confirmed no significant differences between any strain rate for both age time points. This is similar to the findings seen in the healthy ageing group, which also found a lack of strain rate sensitivity in the stress-strain curves (Section 3.3.4.1.2).

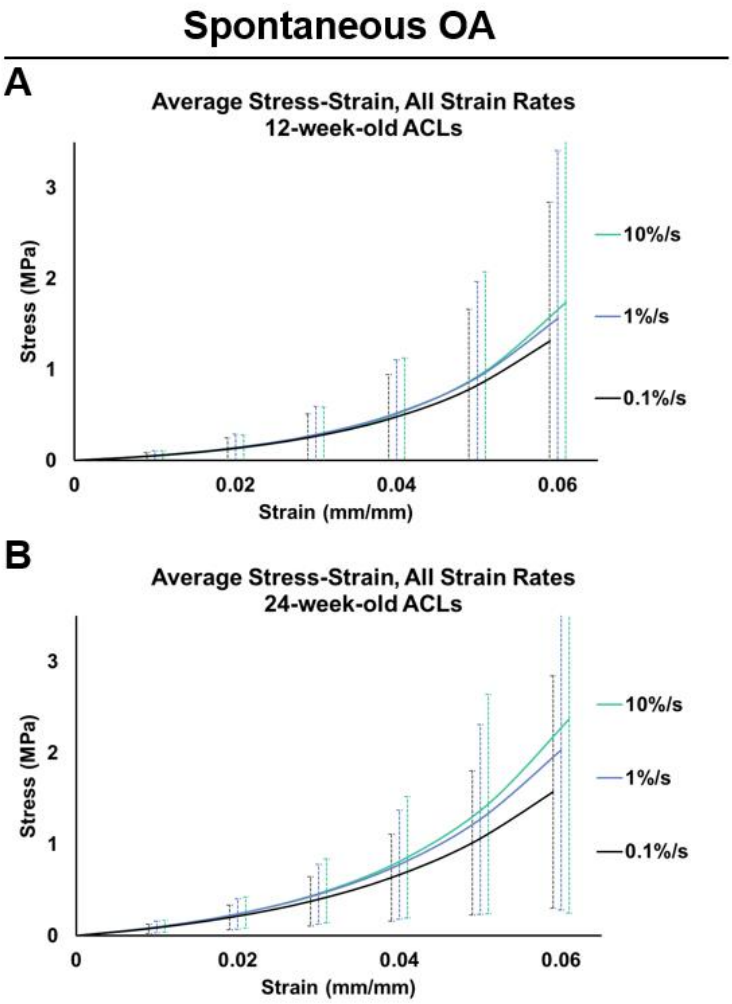

Figure 3.20 Average stress-strain curves of the murine spontaneous OA ACLs comparing all strain rates (0.1%/s, 1%/s and 10%/s) to determine strain rate sensitivity. Stress-strain showed a general stress increase with strain rate increase in the 12-week-old ACLs (A) and 24-week-old ACLs (B). However this increase was not statistically significant in the 12 (p=0.43) and 24-week-old ACLs (p=0.14). This would indicate a lack of strain rate sensitivity in both time points of the spontaneous OA ACLs.

Strain rate sensitivity was also assessed in the tangent modulus-stress curves of the spontaneous OA ACLs. The tangent modulus in the 12 and 24-week-old ACLs showed an increase in the average tangent modulus associated to an increase in strain rate (Figure 3.21A-B). In both the 12 and 24-week-old ACLs, strain rate differences were statistically significant (p=0.02 for 12-week-old ACLs, and p=0.01 for 24-week-old ACLs) (Figure 3.21A-B). Post-hoc multiple comparisons showed significant differences only between the 0.1%/s and 10%/s strain rates in both the 12-week-old and 24-week-old ACLs (p=0.01 for both). There was no significant difference between the 0.1%/s and 1%/s strain rates, as well as the 1%/s and 10%/s strain rates in both spontaneous

OA ACL age groups. This differs from the healthy ageing group ACLs where post-hoc analysis found significant differences between the 1%/s and 10%/s strain rates in both healthy ageing ACLs (Section 3.3.4.1.2). This would indicate a change in strain rate sensitivity at higher strain rates in the diseased spontaneous OA ACLs.

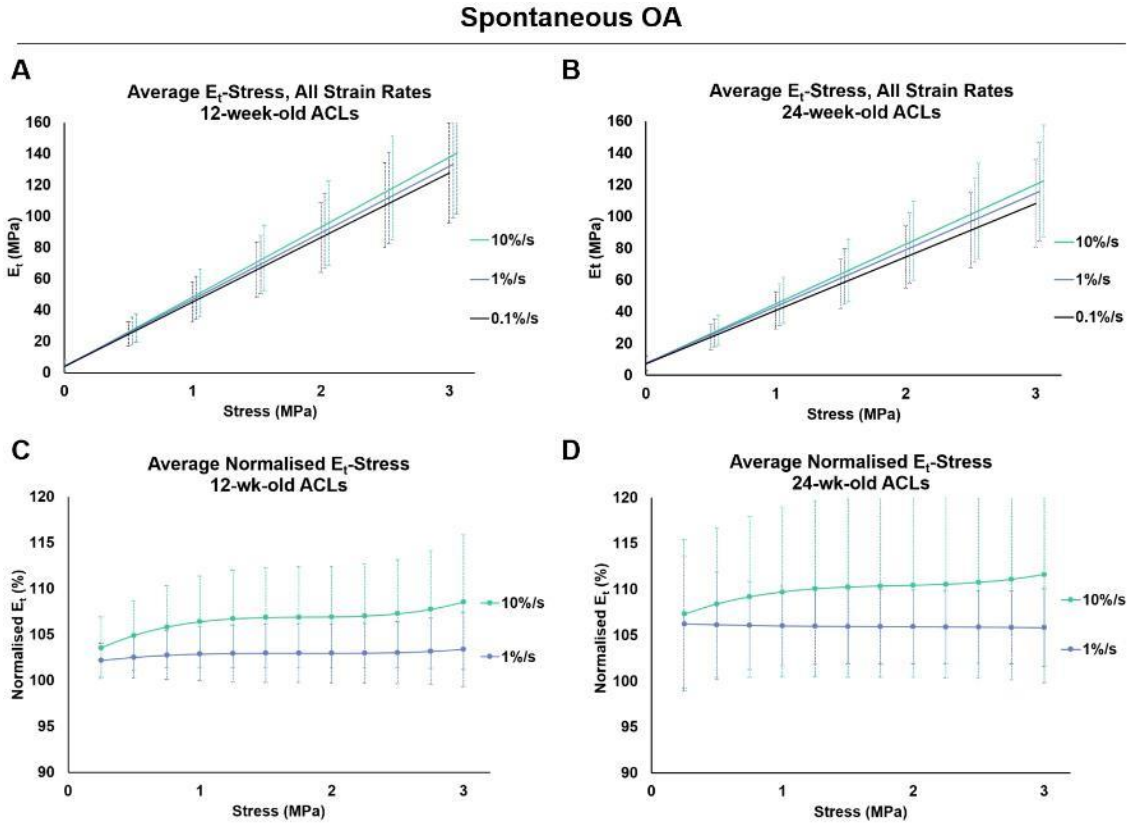

Figure 3.21 Average tangent modulus and normalised tangent modulus-stress curves comparing different rates (0.1%s, 1%/s and 10%/s) in the murine spontaneous OA group to determine strain rate sensitivity. Average tangent modulus-stress curves of the 12 (A) and 24-week-old ACLs (B) increased with strain rate, and differences between strain rates were statistically significant (12-week-old: p=0.02, 24-week-old: p=0.01), implying strain rate sensitivity in both ACLs. Normalised strain rate at 1%/s and 10%/s showed statistically significant differences in the 12-week-old ACLs (C) (p=0.02) but not in the 24-week-old ACLs (D) (p=0.11), indicative of a lack of strain rate sensitivity in the older 24-week-old ACLs of the spontaneous OA group.

Strain rate sensitivity was further analysed with normalised tangent modulus, which was compared between the 1%/s and 10%/s strain rates. In the spontaneous OA 12-week-old ACLs, differences in the 1%/s and 10%/s strain rates were statistically significant (p=0.02) (Figure 3.21C). In the spontaneous OA 24-week-old ACLs, differences in the 1%/s and 10%/s strain rates were not statistically significant (p=0.11) (Figure 3.21D). Normalised tangent modulus suggests a lack of strain rate sensitivity in the spontaneous OA 24-week-old ACLs, which was not seen in

the 12-week-old younger ACLs. This was different than the results of the healthy ageing group, which found strain sensitivity at both the 12 and 24-week-old ACLs (Figure 3.14) which could suggest that the lack of strain rate sensitivity in the normalised tangent modulus between the 1%/s and 10%/s strain rates could have occurred due to OA progression and not differences in age.

3.3.5.2 Hysteresis

Viscoelastic hysteresis was analysed at different strain rates (0.1%/s, 1%/s and 10%/s) in the spontaneous OA ACLs. There were no statistically significant differences between spontaneous OA 12 and 24-week-old ACLs at different strain rates (0.1%/s: p=0.82, 1%/s: p=0.93, 10%/s: p=0.80) (Figure 3.22). Furthermore, there was negative hysteresis in both CD1 age groups at the 10%/s strain rate, similar to the healthy ageing group and likely due to inaccuracies in the testing method [217, 218]. The lack of significant differences could be due to the high standard deviation in both spontaneous OA ACLs which was 91.2% and 74.2% RSD at 0.1%/s strain rate for the 12 and 24-week-old ACLs respectively. Overall, results suggest no changes in the viscoelastic hysteresis in the spontaneous OA group between the 12 and 24-week-old ACLs. This is similar to the healthy ageing ACLs, which also found no significant differences in the hysteresis at different strain rates (Figure 3.15).

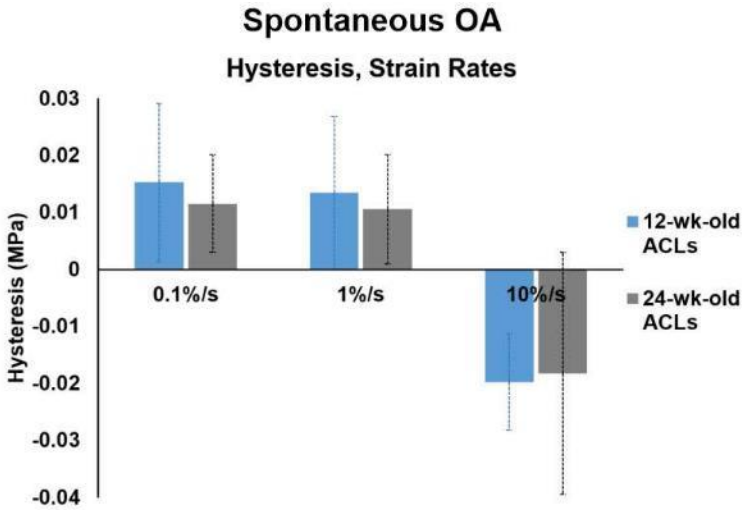

Figure 3.22 Viscoelastic hysteresis at different strain rates (0.1%/s, 1%/s and 10%/s) in the spontaneous OA 12 and 24-week-old ACLs. The average hysteresis was similar in both the 12 and 24-week-old ACLs, and the difference between the two groups was not significant at the different strain rates. Furthermore, hysteresis strain rate sensitivity showed significant differences between strain rates in the 12 and 24-week-old ACLs. This would suggest similar viscoelastic hysteresis in both ACLs in the spontaneous OA group.

3.3.5.2.1 Hysteresis strain rate sensitivity

Hysteresis strain rate sensitivity was analysed in the spontaneous OA ACLs (Figure 3.22). In the 12 and 24-week-old ACLs, strain rates were significantly different ($p<0.01$ for both). Post-hoc comparisons also determined significant differences between the 0.1%/s and 10%/s strain rates and between the 1%/s and 10%/s strain rates ($p<0.01$ for both). No statistically significant difference was found between the 0.1%/s and 1%/s strain rates ($p>0.99$ for both). Hysteresis strain rate sensitivity was found in both ACLs of the spontaneous OA group, similar to the findings of the healthy ageing group (Figure 3.15).

3.3.5.3 Stress-relaxation

The average normalised stress in the CD1 24-week-old ACLs seemed to decrease over time compared to the CD1 12-week-old ACLs, however this difference was not statistically significant ($p=0.60$) (Figure 3.23). This confirms that there were no significant changes to the stress-relaxation viscoelastic behaviour in the spontaneous OA group. This is similar to the stress-relaxation in the healthy ageing group ACLs, which also demonstrated no differences between the two healthy age groups (Figure 3.16).

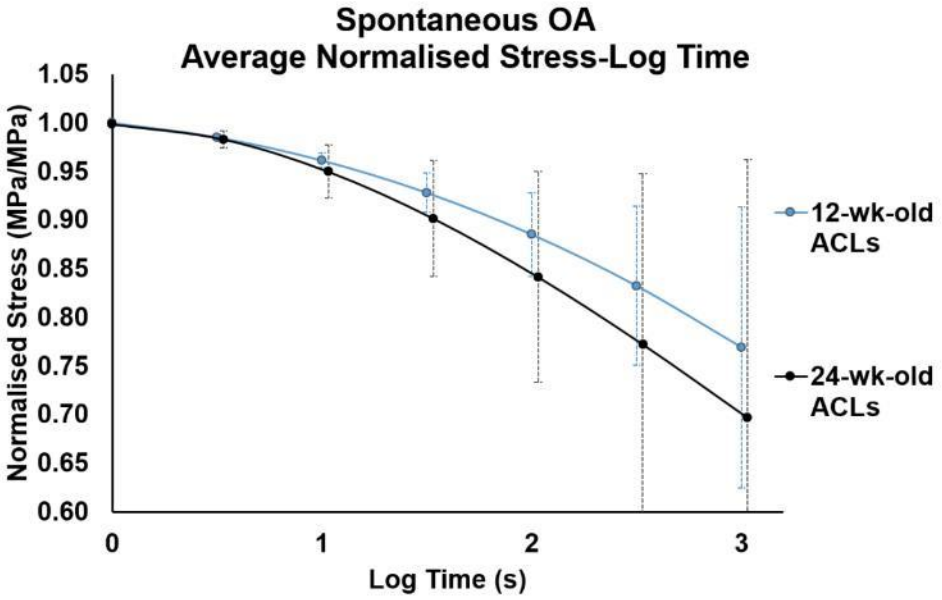

Figure 3.23 Normalised stress-log time curves of the spontaneous OA 12 and 24-week-old ACLs to determine viscoelastic stress-relaxation behaviour. The spontaneous OA 24-week-old ACLs had a lower normalised stress compared to the 12-week-old ACLs, however this decrease was not statistically significant (p=0.60). This would indicate no changes in the stress-relaxation behaviour in the spontaneous OA group.

3.3.5.4 Ultimate load at failure

The ultimate load at failure was similar in both the spontaneous OA group in the 12 and 24-week-old ACLs. The ultimate load in the ACLs was 6.98 ±1.18 N and 6.92 ±1.64 N in the 12 and 24-week-old ACLs respectively (Figure 3.24A-B). There were no statistically significant differences between the two groups (p=0.96). Overall, there were no differences in the ultimate load material property in the spontaneous OA group. This was similar to the ultimate load of the healthy ageing group which also had no difference in the ultimate load in both age groups (Figure 3.17).

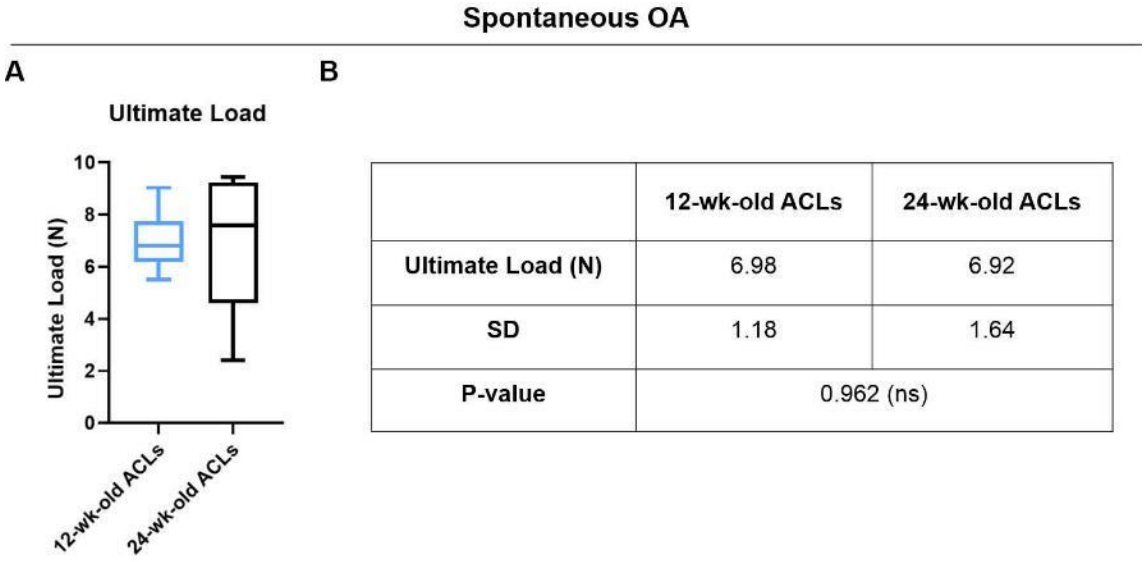

	12-wk-old ACLs	24-wk-old ACLs
Ultimate Load (N)	6.98	6.92
SD	1.18	1.64
P-value	0.962 (ns)	

Figure 3.24 Ultimate load (N) at failure of the spontaneous OA CD1 12 and 24-week-old ACLs. The average ultimate load at failure, also known as maximum load, was similar for both ACLs: 6.98 ±1.18 N in the 12-week-old ACLs and 6.92 ±1.64 in the 24-week-old ACLs (p=0.962). This would suggest no change to the material strength of the spontaneous OA ACLs.

3.3.6 Viscoelastic behaviour and ultimate load at failure of the ACL in the post-traumatic OA group.

Non-invasive loading of the murine C57BL/6J knee joint is an established post-traumatic OA model [27]. In this post-traumatic OA group, ACLs from loaded knee joints (i.e. loaded ACLs) were compared to healthy ACLs from a non-loaded control knee joint (i.e. non-loaded ACLs).

3.3.6.1 Stress-strain

Stress-strain curves at strain rate 0.1%/s, 1%/s and 10%/s showed exponential viscoelastic behaviour in the non-loaded ACL controls and a decreased stress-strain curve in the loaded ACLs (Figure 3.25). Despite this average stress decrease, statistical analysis found no significant differences at the 0.1%/s, 1%/s and 10%/s strain rates (p=0.38 for 0.1%/s, p=0.45 for 1%/s, p=0.48 for 10%/s) (Figure 3.25). This could be potentially due to the large standard deviation which was equivalent to 122% RSD in the non-loaded ACLs and 103% RSD in the loaded ACLs at 0.1%/s strain rate. Overall, these findings suggest there were no differences between the stress-strain curves of the healthy non-loaded and post-traumatic OA loaded ACLs.

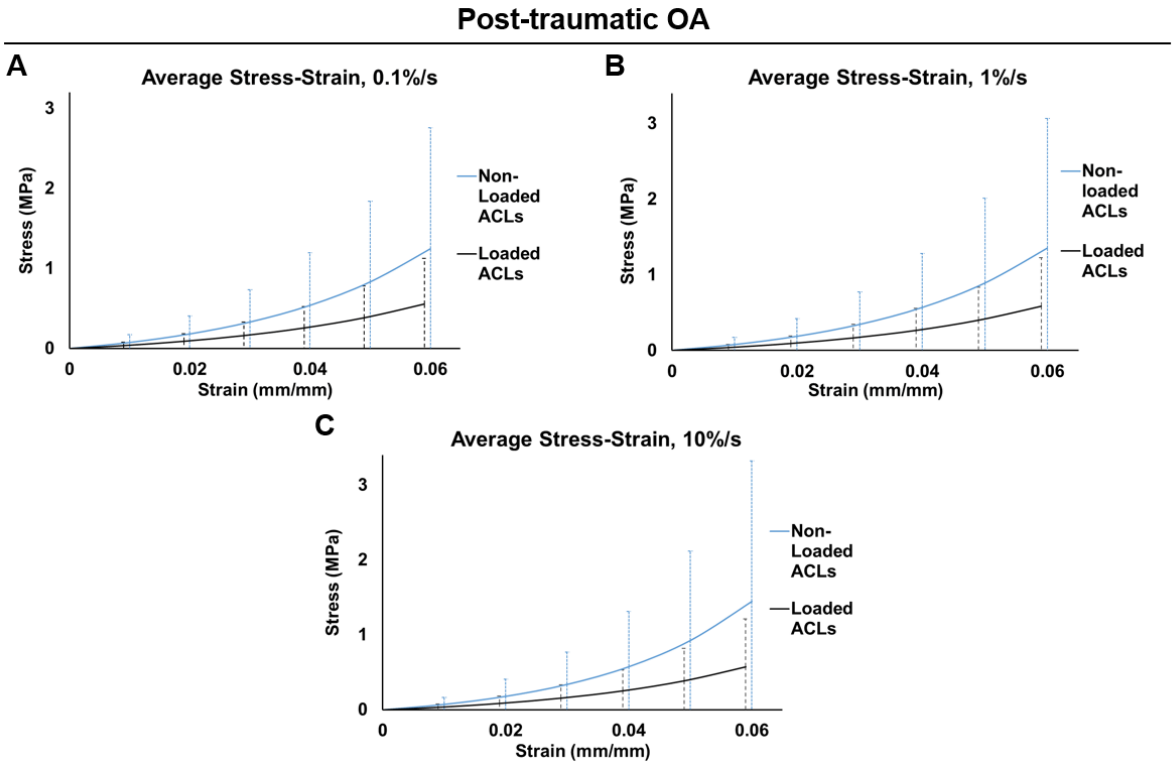

Figure 3.25 Average stress-strain curves of the healthy non-loaded and post-traumatic OA loaded ACLs at different strain rates.Strain rates included 0.1%/s (A), 1%/s (B) and 10%/s (C). Viscoelastic stress-strain behaviour showed a general decrease in the average stress of the loaded knee joint ACLs compared to the non-loaded ACLs, however this difference was not statistically significant at any strain rate (p=0.38 for 0.1%/s, p=0.45 for 1%/s, p=0.48 for 10%/s). This would indicate no changes in the viscoelastic stress-strain behaviour in the post-traumatic loaded ACLs.

3.3.6.1.1 Tangent modulus

Tangent modulus-stress curves of the loaded and non-loaded control ACLs showed a decrease in average tangent modulus in the loaded ACLs (Figure 3.26). Statistical analysis confirmed

significant reduction in the tangent modulus of the post-traumatic loaded ACLs at the 0.1%/s (p=0.03), 1%/s (p=0.02), and 10%/s (p=0.02) strain rates. Overall, this would suggest a significant reduction in the tangent modulus and stiffness of the post-traumatic OA loaded ACL compared to the healthy non-loaded ACL.

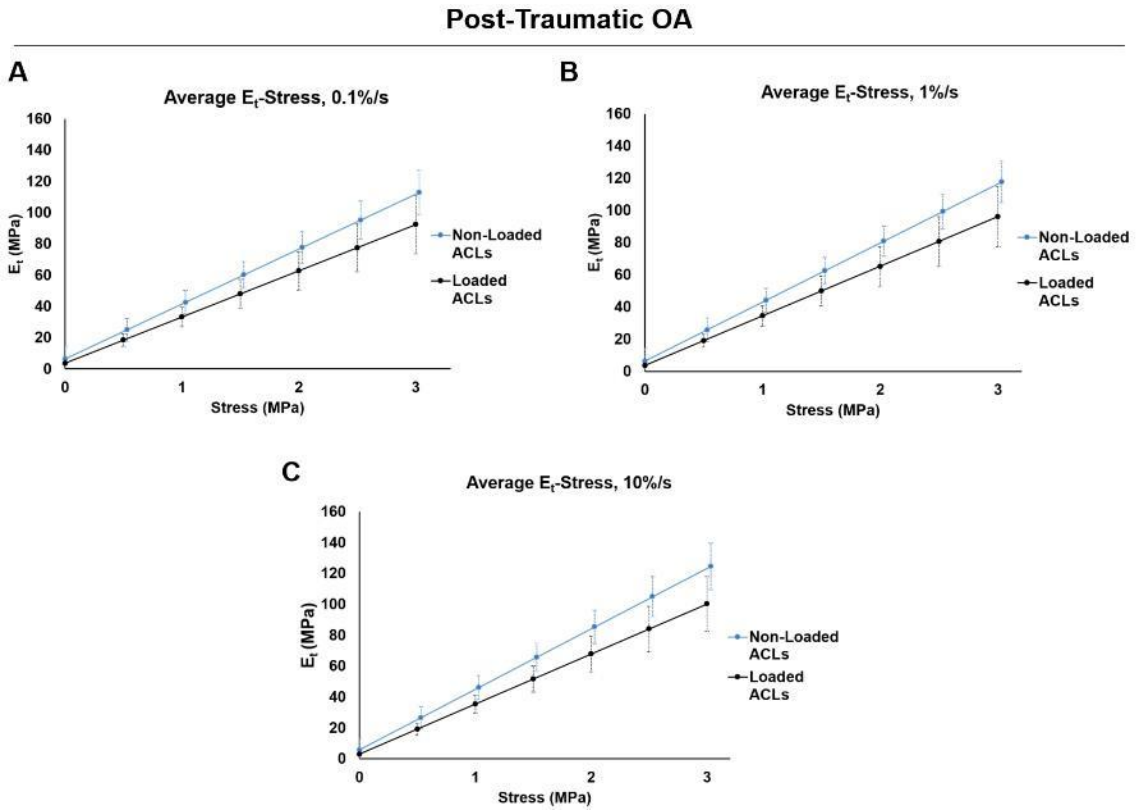

Figure 3.26 Tangent modulus-stress curves of the murine healthy non-loaded and post-traumatic OA ACLs, at different strain rates. Strain rates tested included 0.1%/s (A), 1%/s (B) and 10%/s (C). Overall, the loaded ACLs showed a significantly decreased average tangent modulus at the 0.1%/s (p=0.03), 1%/s (p=0.02), and 10%/s (p=0.02) strain rates. This indicates a decrease in stiffness in the viscoelastic toe-region of the post-traumatic OA ACLs.

3.3.6.1.2 Stress-strain strain rate sensitivity

Strain rate sensitivity was analysed in the stress-strain curves, the tangent modulus-stress curves and the normalised tangent modulus-stress curves. In the non-loaded and loaded ACLs, the stress-strain curves showed no statistical difference between the different strain rates in the non-loaded ACLs (p=0.74) and in the loaded ACLs (p=0.30) (Figure 3.27A-B). This would suggest a lack of strain rate sensitivity in both ACLs. Post-hoc analysis also confirmed no significant differences

between any of the strain rates. Overall, stress-strain behaviour found no strain rate sensitivity in both healthy and OA ACLs.

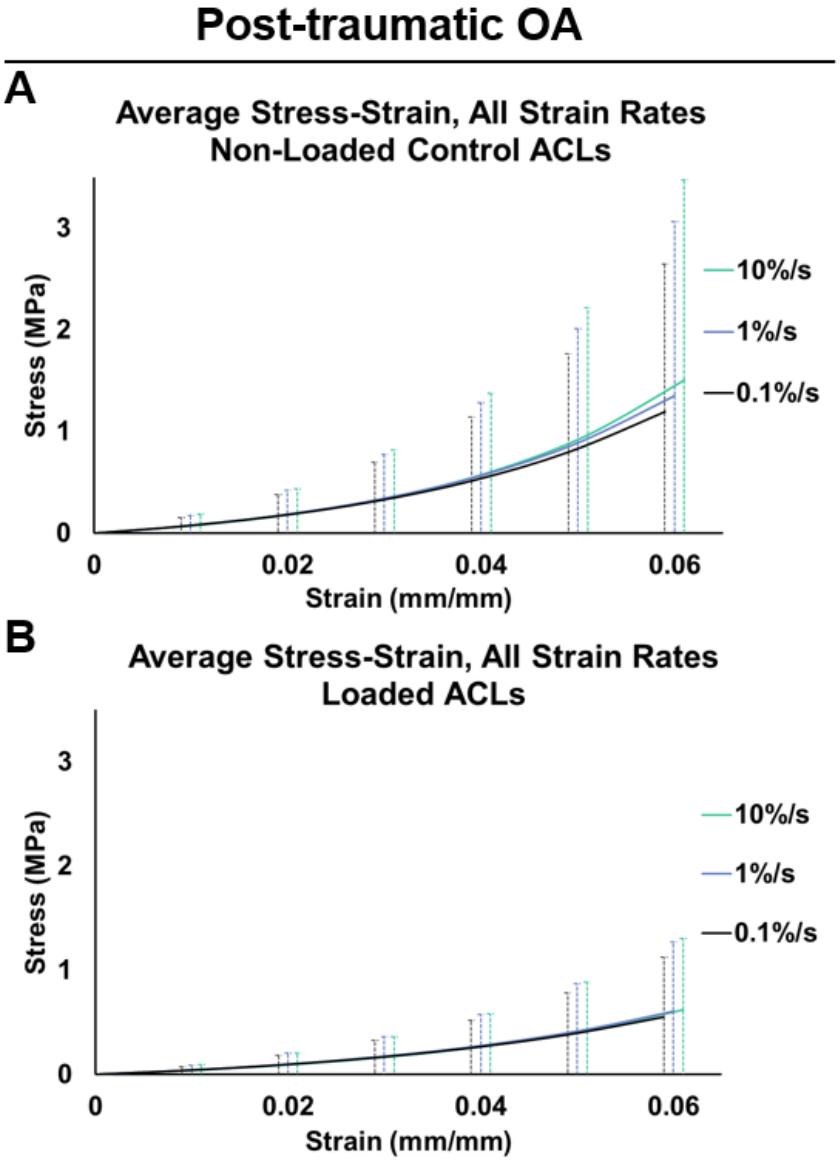

Figure 3.27 Average stress-strain curves of the murine healthy non-loaded and post-traumatic OA ACLs comparing all strain rates (0.1%/s, 1%/s and 10%/s) to determine strain rate sensitivity. Overall, there was no statistical significance in both the non-loaded (A) (p=0.74) and loaded (B) (p=0.30) knee joint ACLs. This would suggest no strain rate sensitivity in both the non-loaded and the post-traumatic OA loaded ACLs.

The tangent modulus-stress curve was another measure of strain rate sensitivity. In both the non-loaded control and loaded knee joint ACLs, the average tangent modulus increased as strain rate

increased (Figure 3.28). In the non-loaded control ACLs, strain rate differences were statistically significant ($p<0.01$) (Figure 3.28A). Post-hoc multiple comparisons further confirmed further significant differences between all of the strain rates, including between 0.1%/s and 1%/s, 0.1%/s and 10%/s and between 1%/s and 10%/s ($p<0.01$ for all) suggesting high strain rate sensitivity for the non-loaded ACLs. In the post-traumatic loaded ACLs, differences between strain rates were also statistically significant ($p<0.01$) (Figure 3.28B). However, post-hoc multiple comparisons reveals only statistically significant differences between the 0.1%/s and 10%/s strain rates ($p<0.01$), but no differences between the 0.1%/s and 1%/s and the 1%/s and 10%/s strain rates ($p=0.13$ for both). Therefore, tangent modulus-stress curves revealed a partial decrease in strain rate sensitivity for some of the strain rates of the post-traumatic OA loaded ACLs.

Tangent modulus was normalised for further analysis of the strain rate sensitivity. In the non-loaded control ACLs, the normalised tangent modulus of the 1%/s and 10%/s strain rates were significantly different ($p<0.01$) (Figure 3.28C). Meanwhile in the post-traumatic loaded ACLs, the normalised tangent modulus differences between the 1%/s and 10%/s strain rates were not statistically significant ($p=0.08$) (Figure 3.29D). These findings suggest that the normalised tangent modulus shows a lack of strain rate sensitivity in the post-traumatic loaded ACLs, compared to the healthy non-loaded control ACLs.

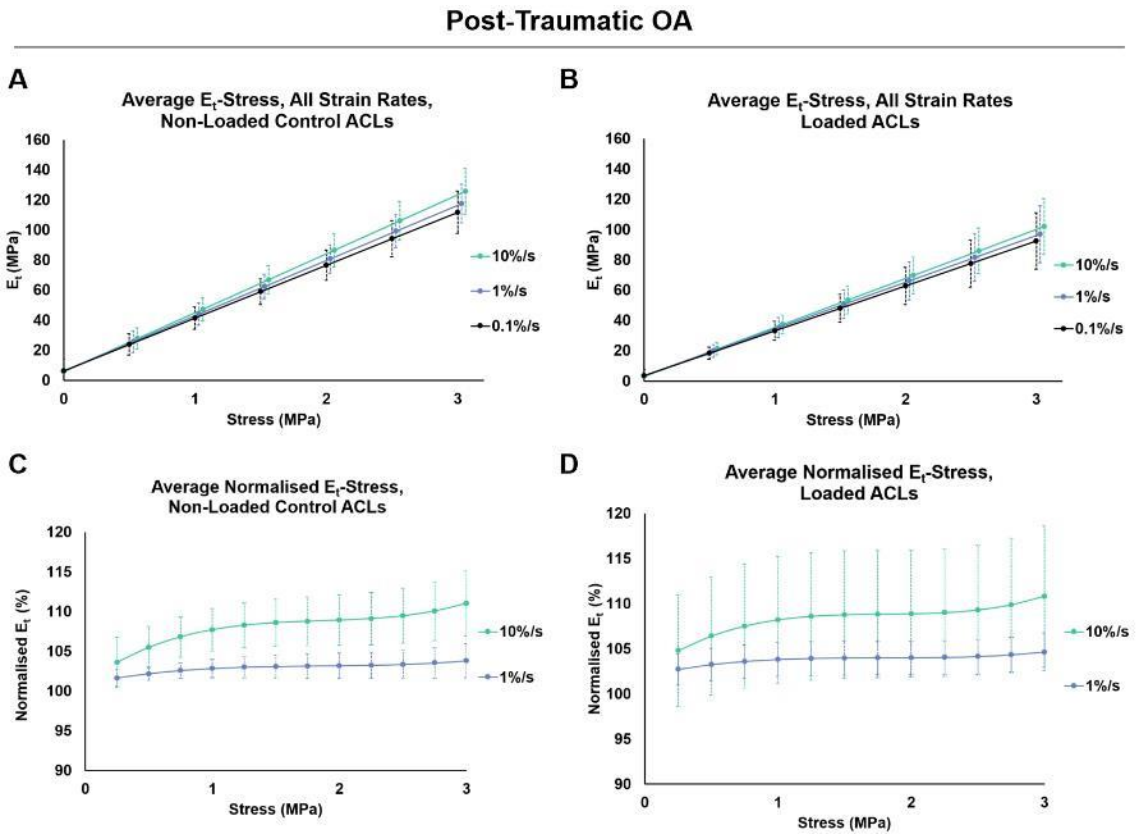

Figure 3.28 Average tangent modulus and normalised tangent modulus-stress curves comparing different rates (0.1%s, 1%/s and 10%/s) in the murine healthy and post-traumatic OA ACLs to determine strain rate sensitivity. Strain rates were significantly different in the tangent modulus of both the non-loaded (A) and loaded (B) knee joint ACLs ($p<0.01$ for both), suggesting strain rate sensitivity. In the normalised tangent modulus-stress curves, strain rate differences between the 1%/s and 10%/s strain rates were statistically significant in the non-loaded ACLs (C) ($p<0.01$) but were not in the loaded ACLs (D) ($p=0.08$). This would suggest a lack of strain rate sensitivity in the post-traumatic loaded ACLs at higher strain rates.

3.3.6.2 Hysteresis

Hysteresis was assessed at different strain rates (0.1%/s, 1%/s and 10%/s). When comparing the hysteresis between the non-loaded and loaded ACLs, the average hysteresis increased at all strain rates in the loaded ACLs (Figure 3.29). Although the average hysteresis increased in the loaded ACLs, the difference between the two groups was not statistically significant at 0.1%/s ($p=0.09$), 1%/s ($p=0.08$) and 10%/s ($p=0.88$). Like in the previous mouse groups, negative hysteresis was found in the 10%/s strain rate for both the non-loaded and loaded knee joint ACLs (Figure 3.29), possibly due to the low measurements and inaccuracies in the methodology [217, 218]. Overall, this data suggests, that there were no changes in hysteresis in the post-traumatic OA loaded ACLs at different strain rates.

3.3.6.2.1 Hysteresis strain rate sensitivity

Strain rate sensitivity was analysed in the hysteresis of non-loaded and post-traumatic loaded ACLs (Figure 3.29). Both the non-loaded and the loaded ACLs showed similar behaviour in strain rate sensitivity. Statistical analysis calculated significant differences between the strain rates in both the non-loaded and loaded ACLs ($p<0.01$). Post-hoc multiple comparison analysis also found significant differences between the 0.1%/s and 10%/s strain rates, as well as the 1%/s and 10%/s strain rates for both the non-loaded and loaded ACLs ($p<0.01$). This would suggest no changes in strain rate sensitivity behaviour of viscoelastic hysteresis in the post-traumatic OA loaded ACLs.

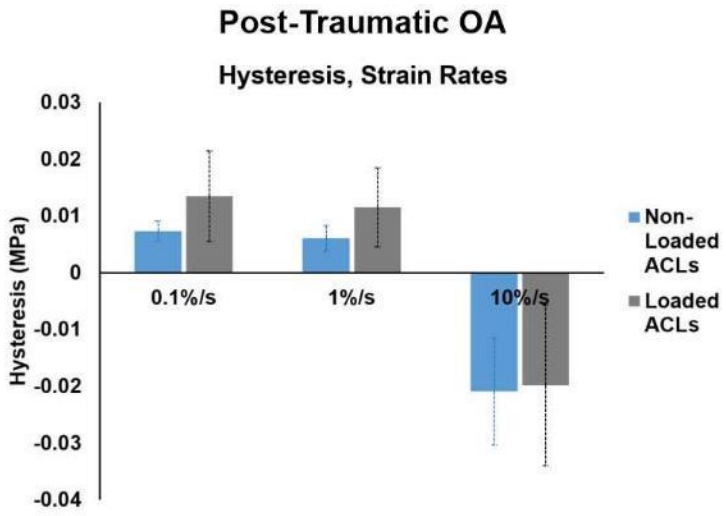

Figure 3.29 Viscoelastic hysteresis at different strain rates (0.1%/s, 1%/s and 10%/s) in the healthy non-loaded and post-traumatic loaded OA ACLs. The average hysteresis and standard deviation increased in the loaded ACLs compared to the non-loaded ACLs, however this difference was not significant at the different strain rates (0.1%/s: p=0.09, 1%/s: p=0.08, 10%/s: p=0.88). Furthermore, strain rate sensitivity analysis determined statistically significant differences between the strain rates at both the non-loaded control ACLs and post-traumatic loaded ACLs (p<0.01). This would suggest no changes to the viscoelastic hysteresis behaviour in the post-traumatic OA loaded ACLs.

3.3.6.3 Stress Relaxation

Stress-relaxation curves showed a decrease in the normalised stress in the loaded ACLs compared to the non-loaded control ACLs (Figure 3.30). Statistical analysis confirmed a significant difference between the non-loaded and loaded stress-relax curves ($p=0.04$). This data indicates that there was a reduction in the stress-relaxation response of the post-traumatic loaded ACLs resulting in more relaxed ligaments compared to the healthy non-loaded ACLs.

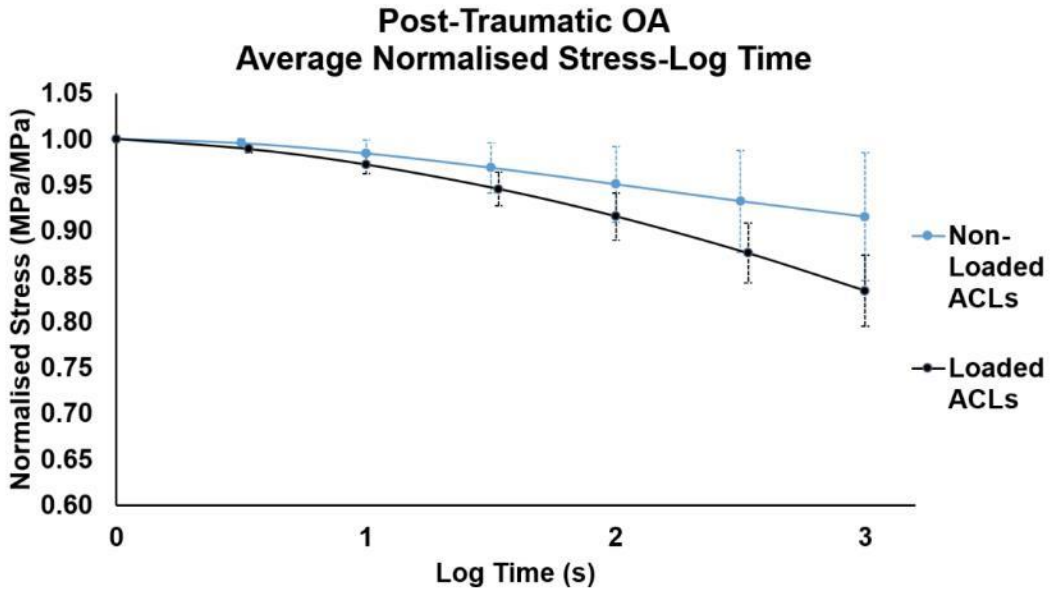

Figure 3.30 Normalised stress-log time curves of the healthy non-loaded and post-traumatic OA ACLs to determine viscoelastic stress-relaxation behaviour. Overall the loaded ACLs had a lower normalised stress compared to the non-loaded ACLs. This decrease was statistically significant (p=0.04) and would suggest a reduction in the stress-relaxation behaviour of the post-traumatic loaded ACLs.

3.3.6.4 Ultimate load at failure

The ultimate load was similar in both the non-loaded controls and loaded ACLs. The ultimate load for the non-loaded control ACLs was 6.17 ±1.91 N and for the loaded ACLs the ultimate load was 6.10 ±2.51 N (Figure 3.31A-B). The small differences between the two groups were not statistically significant (p=0.96) (Figure 3.31B). In addition, both ACLs had high standard deviation equivalent to 41% and 31% RSD, for the loaded and non-loaded ACLs respectively. Overall, this data suggests no statistically significant differences in the ultimate load and material strength between the non-loaded control and loaded ACLs.

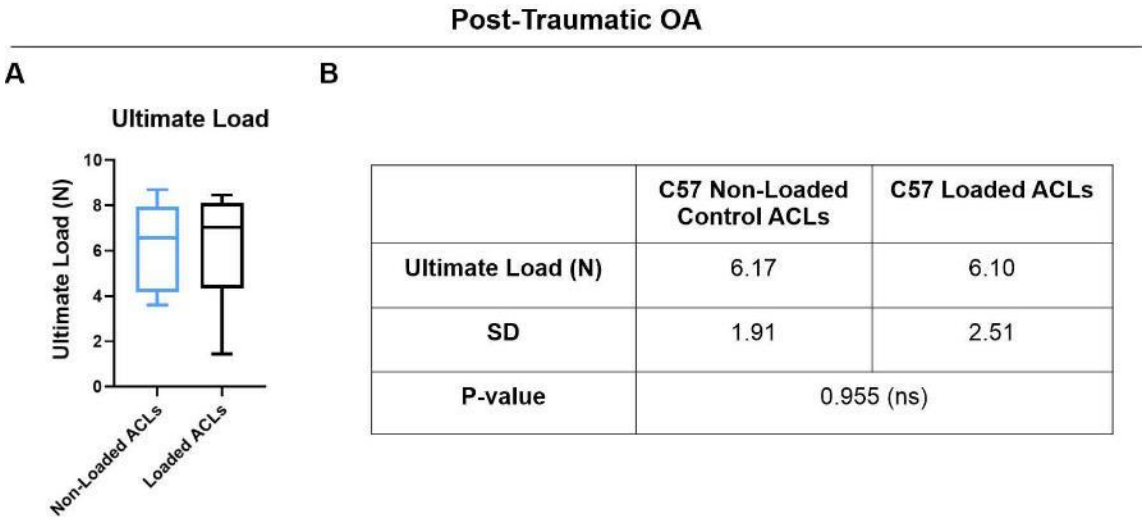

	C57 Non-Loaded Control ACLs	C57 Loaded ACLs
Ultimate Load (N)	6.17	6.10
SD	1.91	2.51
P-value	0.955 (ns)	

Figure 3.31 Ultimate load (N) at failure of the healthy non-loaded and post-traumatic OA ACLs. The average ultimate load, also known as maximum load, was 6.17 ±1.91 N in the non-loaded ACLs and 6.10 ±2.51 in the loaded ACLs. There was little difference between the two ACLs, and statistical analysis confirmed no significant differences (p=0.955). This would suggest no changes in the ultimate load and material strength of the post-traumatic loaded ACLs.

3.3.7 Summary of results

In summary, viscoelastic strain rate sensitivity decreased during OA progression in both the spontaneous and post-traumatic OA group. More specifically, strain rate sensitivity was not significantly different between the higher strain rates (1%/s vs 10%/s) in the normalised tangent modulus-stress (normalised to the 0.1%/s strain rate) in the 24-week-old ACLs of the spontaneous OA group and in the post-traumatic loaded ACLs (Table 3.4). This lack of normalised strain rate sensitivity was not seen in the 24-week-old ACLs from the healthy aging group, indicating that this loss of strain rate sensitivity was due to OA progression. Most viscoelastic properties, such as stress-strain, tangent modulus, hysteresis and stress-relaxation and material properties (ultimate force at failure) were not significantly different between the 12 and 24-week-old in the healthy ageing group and in the spontaneous OA group (Table 3.4). In the post-traumatic OA group, comparing healthy non-loaded to post-traumatic loaded knee joint ACLs, there were significant difference in the viscoelastic tangent modulus and stress-relaxation, indicating further viscoelastic changes in this post-traumatic OA model.

Table 3.4 Summary of ACL viscoelastic and mechanical tests and results for each murine group. Murine groups included the healthy ageing group, the spontaneous OA group (both with 12 versus 24-week-old ACLs), and the post-traumatic OA group (non-loaded vs loaded ACL). Viscoelastic and mechanical properties measured included stress-strain, tangent modulus, hysteresis, stress-relaxation, ultimate load at failure and strain rate sensitivity.

Viscoelastic and mechanical test	**Healthy Ageing Group**		**Spontaneous OA Group**		**Post-traumatic OA Group**	
	12-week-old	24-week-old	12-week-old	24-week-old	Non-loaded	Loaded
	Significance? (p value)					
Stress-strain	No		No		No	
Tangent modulus	No		No		**Yes (p=0.02 for 1%/s)**	
Stress-strain strain rate sensitivity (0.1%/s, 1%/s, 10%/s)	No (p=0.68)	No (p=0.23)	No (p=0.43)	No (p=0.14)	No (p=0.74)	No (p=0.30)
Tangent modulus-stress strain rate sensitivity (0.1%/s, 1%/s, 10%/s)	Yes (p<0.01)	Yes (p=0.01)	Yes (p=0.02)	Yes (p=0.01)	Yes (p<0.01)	Yes (p<0.01)
Normalised tangent modulus-stress strain rate sensitivity (1%/s vs 10%/s)	Yes (p<0.01)	Yes (p<0.01)	Yes (p=0.02)	**No (p=0.11)**	Yes (p<0.01)	**No (p=0.08)**
Hysteresis	No		No		No	
Hysteresis strain rate sensitivity (0.1%/s, 1%/s, 10%/s)	Yes (p<0.01)	Yes (p<0.01)	Yes (p<0.01)	Yes (p<0.01)	Yes (p<0.01)	Yes (p<0.01)
Stress-relaxation	No (p=0.69)		No (p=0.60)		**Yes (p=0.04)**	
Ultimate load at failure	No (p=0.58)		No (p=0.96)		No (p=0.96)	

3.4 Discussion

We hypothesized a change in the viscoelastic behaviour of the post-traumatic and spontaneous OA ACLs. This hypothesis was partially proven correct, as statistically significant differences were found in the normalised tangent modulus-stress strain rate sensitivity of the spontaneous OA ACLs, and in the normalised tangent modulus-stress strain rate sensitivity, tangent modulus and stress-relaxation of the post-traumatic OA ACLs. There were no changes in the viscoelastic behaviour between the aged ACLs of the healthy ageing group, confirming that the viscoelastic changes seen in the spontaneous OA model are involved in OA progression and not differences in ageing.

3.4.1 Age-related ACL mechanics

In the healthy ageing group, there were no statistically significant differences in the viscoelastic behaviour and ultimate load in the ACLs between the 12 and 24-week-old mice, implying that at these age time points, there were no changes to the viscoelastic or material properties of murine ACLs.

Reports of viscoelastic behaviour of ligament or tendons change with age vary, and likely depend on the specific ligament and age differences [205, 219, 220]. Connizzo et al. found minimal differences in the viscoelastic properties with age in murine supraspinatus tendons, including no changes in the midsubstance moduli of 90, 300 and 570 day-old tendons [205]. Other studies have shown that age can affect ligament and tendon mechanical behaviour. In pig tendons, mature tendons had an increase in tensile strength and stiffness compared to newborn pigs [221]. In rat tail tendons, ultimate load and elastic stiffness were highest in the 12-month-old rats compared to the 1, 2 and 4-month-old rats and viscoelastic hysteresis decreased with age [220]. In rabbit medial collateral ligaments, increased stress-relaxation was evident in the 3-month-old rabbit ligaments and no differences were noted in the 6, 9 and 12-month-old rabbits [219].

Clinical research studies in humans have also reported age-related changes in ligament mechanical behaviour and properties [15, 222]. A general decrease in ligament strength has been reported by Woo et al., including a decrease in linear stiffness and ultimate load in the ACL of middle and older age adults compared to younger adults [15]. Meanwhile, in the Achilles' tendon, mechanical strength and elastic stiffness were shown to increase during childhood [222]. Both of these human studies showed an increase in linear-elastic stiffness in ligament and tendon but did not measure

viscoelastic stiffness or behaviour. Together, all these findings suggest that age-related mechanical changes could be species-dependant and ligament-specific, as well as being based on tissue maturation and age difference.

Our results indicate that in the healthy C57BL/6J mice ACLs there were no significant changes between the 12 and 24-week-old ACLs. In these mice, skeletal maturity is reached at about 4 months (16-weeks) [223], therefore at 12-weeks-old, the ACLs are nearing skeletal maturity and at 24-week-old are fully matured. This potential difference in skeletal maturity did not result in statistically significant differences in the viscoelastic and material behaviours of the murine ACL.

3.4.2 OA-related ACL mechanics

Viscoelastic behaviour of the OA murine ACLs showed changes in the strain rate sensitivity and stress-relaxation properties. Specifically, there was a decrease in strain sensitivity in the normalised tangent modulus-stress between strain rate 1%/s and 10%/s in both the post-traumatic OA ACL (Figure 3.28) and spontaneous OA ACL (Figure 3.21) which was not evident in any of the healthy ageing group ACLs (Figure 3.14). These findings indicate similar losses in normalised tangent modulus-stress strain rate sensitivity at higher strain rates in both the post-traumatic and spontaneous OA model. Hence disease pathology in both OA models is resulting in the loss of viscoelastic strain rate sensitivity. Loss of strain rate sensitivity suggests a change in the ECM components, which, as described in Chapter 2, include COL2 and proteoglycan deposition.

Changes in ligament viscoelasticity and ECM raises new questions on the ligament biomechanical response and its importance in OA disease progression. It is well documented that cells respond to force to the ECM and mechanical stimuli and the corresponding mechano-regulation mainly comprises of matrix deposition, rearrangement and removal [224]. Tendon cells in particular have been shown to sense and respond to mechanical stimuli, including cyclic strain which upregulates collagen synthesis [225] and MMP1 expression [226]. Therefore, it follows, if ligament strain rate sensitivity decreases and ECM changes during OA, mechanical stimuli and cellular response could also be affected. How cells respond to matrix viscosity is a new and emerging field of mechanobiology [227]. Understanding the mechanotransduction pathways of ligament fibroblasts is critical to comprehend the passive or active role of the ligament in OA progression.

Additional changes in the viscoelastic behaviour were seen in the post-traumatic OA loaded ACLs when compared to the healthy non-loaded ACLs. These changes included a significant decrease in the tangent modulus (Figure 3.26) at all strain rates of the loaded ACL, implying a decrease in

viscoelastic stiffness in the post-traumatic ACL. Changes in ligament elastic stiffness have been previously associated with changes to collagen [69], which were previously seen in Chapter 2, including COL2 deposition (Figure 2.22) and thicker collagen birefringence (Figure 2.20). Biologically, it is well documented that cells can sense and respond to ECM stiffness [228], but how ligament cells respond to ECM stiffness in OA is unknown. As previously mentioned, tendon cells can adapt to mechanical stimuli to adjust the ECM stiffness [225, 226], therefore it is likely that ligament cells are driving this ECM stiffness change seen post-trauma.

Furthermore, stress-relaxation curves (Figure 3.30) were significantly decreased in the post-traumatic loaded ACLs compared to the non-loaded ACLs, which would indicate an increase in relaxation. and changes in viscoelastic stress-relaxation has been previously associated with GAG [229] and proteoglycan depletion [69]. Changes in stress-relaxation of the ECM can regulate scaffold remodelling and bone formation, as has been shown in rats with implanted hydrogels with different stress-relaxation properties [230]. Therefore, similar ECM changes in the ligaments could be driving the chondrogenesis and potential ossification seen in OA ligaments. Further research is necessary, to understand which specific ECM components are causing a loss in ECM stress-relaxation as well as the underlying cellular pathways.

There are very few studies on the ligament mechanics of human knee OA patients. Changes in the ACL viscoelastic behaviour in human OA and rheumatoid knees, has only been reported once previously where Hagena et al. found an increase in relaxation during stress-relaxation [138]. These results in human OA ACLs are similar to our findings of stress-relaxation in the post-traumatic OA murine model (Figure 3.30). This confirms similar viscoelastic mechanical pathology between murine and human OA. However, Hagena et al. also found a decrease in ultimate load at failure in the ACL of knee OA and rheumatoid patients [138], which was not seen in the murine post-traumatic (Figure 3.31) and spontaneous OA models (Figure 3.24). These differences could arise from different methodologies, or different time points of analysis.

Changes in strain rate sensitivity in ACLs from OA knee joints have not been previously reported. A reduction in strain rate sensitivity has been previously reported in proteoglycan depleted canine ACLs [61], and decorin and biglycan depleted tendons [69, 73]. It is possible that changes to the ACL proteoglycan composition during OA could affect viscoelastic behaviour. Decorin and biglycan depleted mice had altered mechanical properties, including decreased strain rate sensitivity and increased relaxation during stress-relaxation in the mouse tail tendons [69, 73] and in the flexor digitorum longus tendon [80]. Hama Rashid et al. found a decrease in stress-relaxation in GAG depleted canine cruciate ligaments [61]. The role of proteoglycans and GAG

on viscoelastic behaviour is still debated. We previously reported an increase in ASPN expression, a SLRP, in both murine OA models (see Chapter 2), however ASPN lacks GAG chains [193] usually associated with increased viscosity [231]. Further research is needed to fully map proteoglycan composition in the ACL during OA.

It is also possible that multiple ECM components are driving this viscoelastic change, including COL2 deposition. Collagen is generally a determinant factor in the elastic properties of ligaments [69]. Furthermore, COL2 molecules are generally flexible and have a lower elastic modulus (stiffness) than collagen type I molecules [232]. COL2 deposition could in theory explain a decrease in stiffness found in the post-traumatic OA ACL. Furthermore, collagen remodelling has been previously shown in spontaneous OA murine models [114], and it is a known process in OA. Pathways driving proteoglycan and collagen deposition could be related, therefore understanding these biological processes is key.

There have been a few studies on the ACL of spontaneous OA models, such as Dunkin Hartley guinea pig [116] and STR/ort mice [114]. Quasnichka et al. studied the Dunkin Hartley spontaneous OA guinea pig model and analysed critical deformation, a measurement of the size of the toe-region which significantly increased in the spontaneous OA model [116]. Change in the toe-region critical deformation, would likely be reflected in the tangent modulus of the viscoelastic behaviour, however in our murine spontaneous OA model, we did not find any changes in the tangent modulus. Quasnichka et al. compared the Dunkin Hartley guinea pigs to healthy Bristol Strain 2 guinea pigs, at multiple time points from 3 to 36-week-old ACLs [116]. In contrast, our study on the murine spontaneous OA group focused on OA progression, comparing mechanical changes to a younger ACL from the same spontaneous OA strain. In the Dunkin Hartley guinea pig model, ACL critical deformation preceded cartilage degeneration and was associated with higher collagen turnover at young ages compared to the healthy Bristol strain 2 [116]. The ACLs from STR/ort mice, a spontaneous OA model, had a decreased ultimate load as well as increases in MMP2, a collagenase involved in collagen turnover [114]. Similar to the study by Quasnichka et al [116], STR/ort mice were compared to the healthier CBA mouse strain [114]. Changes in the ultimate load material property of the STR/ort spontaneous OA mice were not found in the CD1 spontaneous OA model (Figure 3.24). This could be in part because our study did not compare the ultimate load of the spontaneous OA model to a healthy model.

Further research is needed to determine age-related pathology in the CD1 murine spontaneous OA model. It is possible that ECM changes had already occurred in the 12-week-old CD1 ACLs and could explain the lack of differences in the other viscoelastic properties (hysteresis, stress-

relaxation and tangent modulus) when comparing the CD1 12 and 24-week-old ACLs. In Chapter 2, CD1 12-week-old ACLs showed COL2 immunostaining within the ligament mid-region, which was not found in the healthy ACL groups (non-loaded controls, CBA controls). It is possible that direct comparison with the healthy ageing group would lead to a better understanding of ligament mechanical properties in the early stages of spontaneous OA.

Overall, this research is a step closer to characterising ligament viscoelastic behaviour in healthy and OA ligaments. This will allow for a more applicable understanding of ligament ECM pathology and its correlation with mechanical function. In the future mechanical properties will be important for OA diagnosis and for more effective tissue engineered ligament models.

3.4.3 Limitations

There are several limitations in our study design and measurements. It is important to note that most studies previously mentioned use slightly different testing protocols including different preconditioning cycles, strain rates, knee flexion angle and methods for measurement of the ligament length and CSA. An additional limitation in our methods, was the assumption of similar ACL length and CSA within groups, which could affect the accuracy of the calculations for the stress-strain curve. Most other studies on murine ACL mechanics measured the CSA and length for each individual sample [114, 141, 204], which was not feasible in our setup. These inaccuracies could account for the negative hysteresis we found in the faster 10%/s strain rate of all our murine models, but despite inaccuracies these measurements were reproducible.

Negative hysteresis is another phenomena which has been previously reported in human tendons and ligaments [45, 46] as well as in canine tendons [233] but has never been entirely explained. As mentioned previously, most literature dismisses negative hysteresis because it implies a net positive energy return which should not exist and attributes it to testing inaccuracies such as overshoot and equipment limitations [45, 46]. Testing innacuracies are possible in the murine ACL due to low hysteresis measurements (~0.01 MPa) and the small ACL length (1.1-1.2 mm, see Figure 3.10). However, the strain rates tested in this study are well within the boundaries of strain rates previously tested on mice tendons [69]. Furthermore, our results showed consistent negative hysteresis only in the faster 10%/s strain rates (in both repeats) and at areas of high stress, similar to what was reported previously in the human Achilles tendon [217]. While it is possible that all previous studies had similar testing inaccuracies, this does not rule out the possibility that measurements of negative hysteresis could be amplified by underlying ligament physiology. Past

studies in human skin have attributed negative hysteresis to varying viscoelastic properties [234], the same could also apply to the ACL and differences in its ligament bundles or fascicles. Understanding the causes for negative hysteresis at high strain rate could give further insight into soft tissue mechanics and merits further investigation.

Another limitation in mechanical testing includes the variability in testing protocols. Preconditioning procedures are not standardised for ligament mechanical testing. Sun et al. used 0.1%/s to 0.04N [141], and other previous studies by Warden et al. used 1 Hz (100%/s) to 1% strain for preconditioning [148]. In this study, the 10 preconditioning load-unload cycles were applied at a strain rate of 1%/s to a maximum load of 0.4N (Figure 3.7). The 0.4 N maximum load was chosen during preliminary testing which showed that this load was within the elastic limits and showed the full 'toe region' of the viscoelastic behaviour of the murine ACL.

Another potential limitation is the variability in OA progression in the spontaneous OA model. As previously shown (see Chapter 2), maximum OA cartilage lesion scores of the spontaneous OA 24-week-old knee joint ranged from a score 6 to 1 (Figure 2.28). This is equivalent to minor fibrillations in the cartilage (OA score 1), to complete loss of AC and subchondral bone exposure (OA score 6, maximum score). OA score varied greatly, as expected for a spontaneous OA model, and could result in large variations of the ACL mechanical properties. Analysis of OA progression for each sample (before or after mechanical testing) might allow for better correlation of OA and mechanical changes. We attempted to score cartilage after mechanical testing using Indian ink [175], however our results for cartilage scoring were inconclusive. The post-traumatic OA model offers less variability in OA score. The maximum OARSI cartilage lesion score has been reported to be 4 at 3-weeks post-trauma [153] and 3 at 6-weeks post-trauma [164]. It is possible that differences between the spontaneous and post-traumatic OA models could be due to differences in OA variability and progression. These factors could influence the analysis of viscoelastic behaviour in the ligaments and need to be studied carefully.

3.5 Conclusions and future work

Mechanical testing of the ACLs revealed that ACL function changed in OA knee joints. Viscoelastic strain rate sensitivity decreased in both the post-traumatic and spontaneous OA murine models, indicating that a change in viscoelastic ligament function occurs in both OA types. Changes in the strain rate sensitivity of the ACL in both OA models is, to our knowledge, a novel finding. There were additional viscoelastic changes in the post-traumatic OA model including a decrease in viscoelastic stiffness and an increase in relaxation during stress-relaxation which could lead to further OA progression. These findings support the theory that the ACL has an important role in OA progression, and that the OA is a whole joint disease affecting all surrounding tissues of the knee joint [6].

Further research is needed to determine the overall implications of how changes in the ACL viscoelastic properties affect knee stability and mechanics, as well as the mechanical pathological changes which are leading to changes in viscoelastic behaviour. Particularly, research on the proteoglycan compositional changes and involved pathways is necessary as it has been previously linked to changes to strain rate sensitivity in tendons [69, 73] and canine ACLs [61]. To do this, we need a better understanding of the ligament biological components, including cell populations and mechanical sensors which control pathological changes in the ligament structure and function.

Additionally, changes in the viscoelastic behaviour of the ACL occurred in the spontaneous OA model. Therefore, changes in the ligament pathology can occur spontaneously, without the need for traumatic intervention. Further characterisation of the CD1 spontaneous OA model is needed, to determine if ACL mechanical changes precede cartilage degeneration or vice-versa. There is also a need to determine similarities and differences in the pathology between post-traumatic and spontaneous OA necessary for future clinical applications.

Chapter 4:
Exploring Ligament and Synovial Fibroblast Subpopulations and Transcriptional Markers using Single-Cell RNA-Sequencing

4.1 Introduction

The knee joint is composed of highly-interconnected specialised connective tissues of which the exact cellular makeup is only recently starting to be discovered [235-237]. In OA, disease pathogenesis affects all knee joint tissues including cartilage, ligaments and synovium and has thus been termed a 'disease of the joint as an organ' [6]. In Chapter 2, we observed changes in murine OA ligament, including ligament cell morphology and marker expression. However, ligament cell populations and markers in the healthy ligament and knee joint are not well characterised. Fibroblasts have emerged as particularly important, namely unravelling fibroblast heterogeneity to discover complex biological functions [238, 239]. To further elucidate the role of ligament cells during OA progression, it is necessary to identify the fibroblasts present in healthy ligaments.

Ligament fibroblasts and potentially other cell types play an important role in ligament development and homeostasis [2, 240]. Ligaments are composed of a dense ECM with complex hierarchical fibre organisation where dispersed ligament fibroblasts, named ligamentocytes, are the predominant ligament cell-type [2]. Ligamentocytes play an active role in ligament physiology, responsible for matrix synthesis during development and regeneration [240] and cell-cell communication [241]. Besides ligamentocytes, other ligament cell types are present in the more vascular overlying epiligament layer, which contains mast cells, adipocytes and neurovascular cells [33]. Additionally, there is evidence of a ligament stem cell population, including vascular stem cells [242] and other ligament specific stem cell populations [46]. Ligaments host a complex cellular makeup and yet current knowledge of ligament cell markers is limited. Tendon-ligament markers, generally grouped together due to similarities in the tissues, include development and adult tissue markers such as SCX, TNMD and MKX [53, 243]. Ligament-fibroblasts remains poorly defined, particularly in their subpopulation heterogeneity, transcriptional markers and pathways.

The synovial membrane is another specialised connective tissue that lines the inside of the knee joint capsule which surrounds the cruciate ligaments and neighbours the collateral ligaments [5]. The synovium is comprised primarily of synovial fibroblasts, also known as fibroblast-like synoviocytes, which are interspersed with synovial macrophages [244]. The synovial fibroblasts are responsible for the production of synovial fluid, an important lubricant for knee joint movement [244] and provide structural support and supply of nutrients to the joint [5]. The second most prominent cell type found in the synovial lining are the synovial macrophages, which have

an important role for innate immune responses [244] and have a unique relationship with synovial fibroblasts. Synovial fibroblasts have been shown to carry innate immune receptors and are well equipped to sense pathogens and tissue damage [245] and are also involved in disease regulation [109]. Other cell populations in the synovium can be found in an outer sub-lining interstitial layer rich in nerve cells [244] as well as immune cells that include lymphocytes and dendritic cells [244]. Several synovial-specific fibroblast markers have been identified, mostly through bulk genetic analysis, such as podoplanin, *Thy1* (*Cd90*), cadherin-11 (*Cdh11*) and *Cd34* [246]. Similar to the ligaments, healthy synovial fibroblasts remain largely unresolved. Synovium and ligaments are both are rich in fibroblasts but likely to be playing different roles in knee joint homeostasis [2, 245]. Identification of heterogeneous fibroblast subpopulations and markers in ligaments and synovium is needed to elucidate underlying joint organ pathology and potential biomarkers and future therapeutic targets.

Recent technological advances have allowed mapping of transcriptomic markers with high-resolution using single-cell RNA-sequencing (scRNA-seq). scRNA-seq is a relatively novel methodology in the transcriptomics field which can uncover a comprehensive high-resolution transcriptional snapshot of a tissue sample [247]. The high-resolution individual cell approach allows for the discovery of complex and rare cell populations, when compared to traditional bulk RNA sequencing [248] and allows for a true mapping of cell types and subpopulations. This technique has recently revealed fibroblast heterogeneity in mouse tendons [236] and human synovium [237, 249-251].

Transcriptomic single-cell analysis of mouse tendons and human synovial samples has identified important subpopulations and markers. In pooled human tendons, four cell types were identified including tendon fibroblasts that had a further five subpopulations [235]. In murine Achilles tendons, 11 unique cell types were identified with two tendon fibroblast subpopulations [236]. Additionally, in diseased and healthy human knee joint synovial tissues, 18 unique cell populations were found including four fibroblast subpopulations [237]. This population varied slightly from another study on human synovial-derived cells which found 13 unique cell populations and three synovial fibroblast subpopulations [249]. Both of these studies reveal the heterogeneity of tendon and synovial fibroblasts. Heterogeneity is an important aspect for biological function and for the development of new therapies for disease [238, 239]. For this reason, creating a single-cell transcriptional atlas is a necessary step forward for the understanding of functionally important connective tissue such as ligament and synovium. scRNA-seq has not, until now, been used to profile cell populations of murine ligament and synovial tissue.

4.1.1 Aims of the study

The overarching aim of this chapter was to generate a ligament and synovium-derived cellular atlas using healthy C57BL/6J adult male mice, with a focus on fibroblast heterogeneity. To achieve this aim, scRNA-seq was used due to its power in resolution and ability to detect rare cell populations [247, 252].

Several more specific goals were set for successful scRNA-seq. Firstly the ideal method of cell isolation from the fibrous ligament and synovial membrane and joint capsule tissue, was determined. This is an important step to ensure extraction encompasses all cells with high quality RNA reads [247]. Secondly, a downstream analysis workflow was created to classify major cell populations in both ligament and synovial fibroblast subpopulations, which was done following already established Seurat workflows [253]. Thirdly, each fibroblast subpopulation was further classified based on highly expressed transcriptional markers and predicted canonical pathways and upstream regulators [254]. Finally, we aimed to validate our findings by confirming a rare but distinct ligament fibroblast subpopulation using a transgenic fluorescent reporter mouse line.

4.2 Materials and Methods

4.2.1 Animal and ligament and synovial tissue collection for scRNA-seq

All procedures complied with Animals (Scientific Procedures) Act 1986 and local ethics committee. Male 3-month-old C57BL/6J mice were obtained from Charles River (UK) and were housed in the specific pathogen free biological services unit at the University of Liverpool, kept in polypropylene cages, subjected to 12 hour light/dark cycles, at 21±2˚C and fed standard diet ad libitum. Mice were euthanized one day after arrival by exposure to carbon dioxide.

Mice cadavers were immediately prepared for tissue collection by removing the skin and exposing the hindlimbs. Using a dissecting microscope, excess muscle from the pelvic limbs was dissected until the fibrous layer of the joint capsule and collateral ligaments were visible (Figure 4.A). Firstly, the murine synovial sample was collected which consisted of the whole outer joint capsule (made up of the fibrous and synovial layers). The joint capsule was carefully dissected using surgical micro-scissors (Agar Scientific) from where the synovial membrane meets the collateral ligament to as close as possible to the patella which was repeated for both the medial and lateral side of the joint capsule (Figure 4.B). The sample was stored temporarily in an eppendorf with Dulbecco's Modified Eagle Medium (DMEM, Thermo) media. Murine synovial samples from both legs and multiple mice (n=3) were pooled together into one sample (total n=6 knees).

Murine ligament samples were then collected. First the lateral and medial collateral ligaments were dissected using surgical micro-scissors (Figure 4.C) and placed in a separate eppendorf with DMEM media. The knee was further dissected, menisci and all excess tissue were removed cleaned until only the cruciate ligaments remained (Figure 4.D). Cruciate ligaments were cut using micro-scissors, first from the tibial enthesis and then the femoral enthesis and collected. Murine cruciate ligament samples were transferred to the eppendorf with the collateral ligaments and DMEM media. Murine collateral and cruciate ligaments from both pelvic limbs and multiple mice (n=3) were pooled together (total n=6 knees) to make one murine ligament sample.

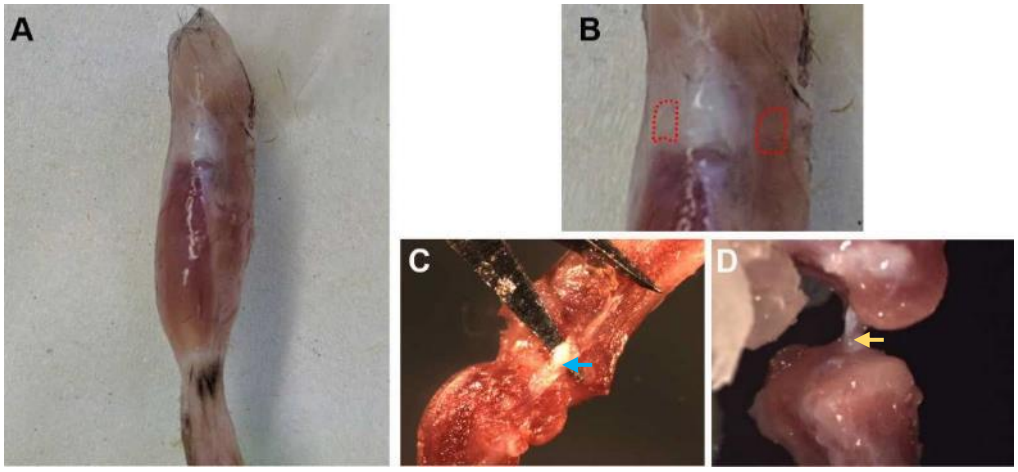

Figure 4.1 Micro-dissection of murine knee joint synovial membrane and ligaments. (A) Murine pelvic limbs were isolated. (B) Excess muscle was removed until fibrous joint capsule (red region) was visible. Joint capsule including the fibrous synovial layer were dissected. (C) The medial and lateral collateral ligaments (blue arrow) were dissected and collected. (D) Then the anterior and posterior cruciate ligaments (yellow arrow) were dissected and collected. All collateral and cruciate ligaments were pooled together (n=6 knees total).

4.2.2 High-quality cell isolation from ligament and synovial tissue

Cell isolation protocol was based on recently published work on tendon scRNA-seq [251]. This protocol was optimised for protease concentration, digestion incubation time, filter size, and spin speed; the optimal protocol was chosen based on cell viability, cell yield, amount of debris and single-cell clustering (see Section 4.3.1 for an evaluation of cell isolation protocols). Both ligament and synovial tissue samples were digested to obtain a viable single cell suspension. Two cell isolation protocols are shown in this chapter, first the preliminary cell isolation protocol that yielded low cell numbers and high debris. The preliminary cell isolation protocol consisted of mincing the ligament and synovium samples and transferring to a 1mL cell digestion buffer with 3 mg/mL collagenase type I, 8 mg/mL collagenase type II, 2 mg/mL dispase II, and 2 mg/mL trypsin. Tissue digestion lasted for 1 hour at 37ºC in a vigorous shaking water bath. 0.5mL of DMEM media with 10% fetal bovine serum (FBS) was added to the sample and then passed through a 70 µm cell strainer (Sigma) was used. Cells were spun down at 700 G for 5 minutes. Supernatant was removed and cells resuspended with 50 µL of DMEM media with 10% FBS.

For the final optimised protocol, pooled samples were finely minced using a scalpel and transferred to an eppendorf with 1mL protease solution of collagenase type I (6 mg/mL), collagenase type II (16 mg/mL), and dispase II (4 mg/mL) in DMEM. Both samples were digested for 30 minutes at 37ºC using a vigorous shaking water bath. Trypsin was then added (0.2 mg/mL final concentration, Sigma) for a further 10 minutes incubation. After digestion, 0.5 mL of DMEM

media with 10% FBS was added, samples were passed through a 40 µm cell strainer (Sigma). Cells from each sample were then transferred to separate eppendorf tubes and spun at 500 G for 5 minutes. The supernatant was removed and cells were re-suspended with 50 µL of DMEM media with 10% FBS (volume was adjusted based on expected cell retention for each tissue sample).

The amount of debris, cell viability, clustering and concentration was assessed using the Luna-FL Dual Fluorescence Cell Counter (Logos). 18 µL of the resuspended sample was taken and mixed with 2 µL of acridine orange/ propidium iodide stain (Logos). 10 µL of this mixture was then added to a Luna Cell Counting Slide (Logos) and loaded for automated counting. Cell counting and viability was critical for successful sequencing and to measure the final cell concentration. Samples were then ready for single cell library preparation.

4.2.4 Single-cell library creation and RNA sequencing of ligament and synovial samples

scRNA-seq combines single-cell encapsulation with current RNA-sequencing and gene expression profiling [247]. Though there are several approaches, the 10x Genomics method used here partitions cells with unique 10x barcoded gel beads using a microfluidic platform. Each barcoded cell is consequently encapsulated with oil emulsion mixing primers containing an Illumina R1 sequence, a unique molecular identifier, and a dT primer sequence with cell lysate and Master Mix. This incubation produces full-length barcoded cDNA which are then sequenced to generate libraries. Due to the 10x barcoding, individual reads can then be associated to each individual partition. When applied successfully, this method can analyse RNAs from large populations of cells and expose critical transcriptional differences of individual cells within these populations.

Libraries were prepared through a collaboration with the University of Liverpool Centre for Genomics Research by Dr. Margaret Hughes. Chromium Single Cell 3' Reagent Kit Protocol (version 2, 10x Genomics) was used following the steps of the manufacturer. 10,000 cells were targeted for recovery in the protocol, mixed with reagents and processed using a Chromium Controller (10x Genomics). Following library preparation and quantification, libraries were sequenced by an Illumina NovaSeq using an S4 chemistry flow cell (paired-end, 2x150bp sequencing) to generate approximately 2500 million read-pairs per lane.

4.2.5 Single-cell RNA-seq analysis of ligament and synovial cell samples

Gene expression matrices were generated by Dr. Luca Lenzi from the Center for Genomic Research at the University of Liverpool. Matrices were generated using the Cell Ranger pipeline (version 3.0.2, 10x Genomics) and were aligned with mm10 transcriptome (C57BL/6J reference genome). Cell Ranger and Loupe Cell Browser (version 3.1.0, 10x Genomics) was used for the initial pre-processing, to determine quality of reads and total counts of unique molecular identifiers (UMI) plotted in t-distributed stochastic neighbour embedding (t-SNE). Downstream analysis was done with RStudio version 1.2.5019 (2019) and the Seurat 3.1.1 R package, which was designed for quality control and analysis of scRNA-seq data, particularly for identification of heterogeneity [253]. An example of the RScript used is provided in the appendix (Sup Fig 3).

For ligament-derived single-cell analysis, cells with <200 unique feature counts and >40% mitochondrial counts were filtered out. This is similar to past studies [250, 251], though it also includes a high number of mitochondrial counts. Filtering is necessary to remove artefacts from cell isolation method and ensure high quality reads [253]. Data from the remaining 2,165 ligament cells was then normalised ('LogNormalize' function, 10,000 scale factor) and scaled (linear transformation, 'ScaleData' function). Dimensionality reduction was then applied using principal component analysis (PCA), a statistical methodology that can summarise larger datasets into smaller summary indices called principal components. PCA is the most popular dimension reduction method used for Seurat [253]. Elbow and Jackstraw plots were used to determine 'dimensionality' of the dataset and find significant principal components. From this, the first 20 principal components were used for population clustering ('FindNeighbors' function, dims 1 to 20) ('FindClusters' function, 0.5 resolution) and then clusters were visualised using non-linear dimensional reduction method called uniform manifold approximation and projection (UMAP).

Synovium-derived single-cell analysis followed the same method as that used for the ligaments with modifications to optimise for the synovium quality read. Synovium cells with <200 and >3000 unique features, in addition to >10% mitochondrial counts, were filtered out. After filtering, reads from the remaining 3,229 cells were normalised, scaled, and dimensionality reduction applied (PCA) using the same parameters used on ligament cells. Elbow and Jackstraw plots determined significance of the first 20 principal components (dims 1 to 20). Population clustering was then completed using the same parameters used on ligament cells (0.5 resolution) and visualised with UMAP.

Both ligament and synovium samples were examined separately but followed the same workflow for cluster analysis. First clusters were classified using known cell type markers. Cell type markers were the following: collagen type 1 alpha 2 (*Col1a2*) a marker for fibroblasts, platelet/endothelial cell adhesion molecule-1 (*Pecam1*) a marker for endothelial cells, haemoglobin alpha adult chain 1 (*Hba-a1*) for red blood (RB) cells, protein tyrosine phosphatase receptor type C (*Ptprc*) for immune cells, myelin protein zero, (*Mpz*) for nerve cells, paired box Pax-7 (*Pax7*) for satellite cells, integrin alpha-IIb (*Itga2b*) for platelet cells, and myotilin (*Myot*) for muscle cells. A summary of markers and related references can be seen in Table 4.1.

Table 4.1. Cell markers used for cluster cell type identification. The following markers were used: Col1a2 for fibroblasts, Pecam1 for endothelial cells, Hba-a1 for red blood cells, Ptprc and CD14 for immune cells, Mpz for nerve cells, Pax7 for satellite cells, Itga2b for platelet cells, Myot for muscle cells.

Marker	Cell Type	Reference
Collagen type 1 alpha 2 (Col1a2)	Fibroblasts	[236, 255]
Platelet/endothelial cell adhesion molecule-1 (*Pecam1*, also known as *Cd31*)	Endothelial cells	[256]
Haemoglobin alpha adult chain 1 (*Hba-a1*)	Red blood cells	[257]
Protein tyrosine phosphatase receptor type C (*Ptprc* also known as *Cd45*)	Immune cells	[258]
Cluster of differentiation 14 (*Cd14*)	Immune cells (monocytes)	[259]
Myelin protein zero (*Mpz*)	Nerve cells	[260]
Paired box protein Pax-7 (*Pax7*)	Satellite cells	[261]
Integrin alpha-IIb (*Itga2b*, also known as *Cd41*)	Platelet cells	[262]
Myotilin (*Myot*)	Muscle cells	[263]

Differential expression analysis was used to determine marker differences between clusters. Non-parametric Wilcoxon rank sum test is widely used in differential expression analysis of scRNA-seq datasets [264] and was used in all differential expression analysis unless otherwise noted. Firstly, differential expression analysis ('FindMarkers' function) of each cluster compared to all other clusters was used to identify major cell types. The second differential expression analysis ('FindMarkers' function) was between all fibroblast clusters and all other clusters to evaluate fibroblast-specific markers within the tissue. The fibroblast clusters were then selected and segregated for further analysis. The third differential expression analysis ('FindMarkers' function) was completed between only the fibroblast clusters, comparing one fibroblast cluster to all other

fibroblast clusters to determine fibroblast cluster-specific markers. The top markers from each analysis were quantified using feature plots, violin plots, ridge plots, dot plots and heatmaps ('FeaturePlot', 'VlnPlot', 'RidgePlot', 'DotPlot' and 'DoHeatmap' function).

Lastly, ligament and synovial fibroblast subpopulations were integrated using the SCTransform Seurat workflow to allow direct comparison of both fibroblast populations. SCTransform workflow uses an improved normalisation workflow ('SCTransform', 'PrepSCTIntegration', 'FindIntegrationAnchors', and 'IntegrateData' function) [253]. This is similar to past studies that integrated different tendon samples together [235, 236]. Then the integrated data can be visualised using the standard visualisation and clustering workflow ('RunPCA', 'RunUMAP' function). Differential expression analysis was then used to determine marker differences between the ligament and synovial fibroblasts ('FindMarkers' function). Integration and top markers were visualised as before ('FeaturePlot', 'VlnPlot' function).

4.2.6 Enriched canonical pathway analysis and predicted upstream regulators and activation scores

Pathway analysis of the top predicted canonical pathways and upstream regulators was completed with Ingenuity Pathway Analysis (IPA) software (Qiagen). Differential expression data consisting of the gene marker identity and the average log fold change was converted from R to a csv file ('write.csv' function). Differential expression data files were created for each fibroblast subpopulation using the top markers with an adjusted p-value $\leq 10^{-20}$, this is similar to past approaches for IPA analysis [254]. A core analysis was initiated; the data was imported to the IPA software. An initial pathway analysis was run using the following parameters: Ingenuity Knowledge Base (Genes), species (all), tissues and cell lines (all). Two comparison analysis were then completed between the core analysis of ligament fibroblasts (L.F1, L.F2, L.F3, L.F4 and L.F5) (Section 4.3.2.9) and synovial fibroblasts (S.F1, S.F2, S.F3 and S.F4) (Section 4.3.3.8). Core analysis and comparison analysis showed enriched canonical pathways, predicted upstream regulators, associated diseases and functions, networks and other analyses. Enriched canonical pathways were ranked based on the predicted activation score among all clusters. Activated upstream regulators were ranked based on predicted activation scores.

4.2.7 Transgenic *Acan*-Cre-tdTomato murine reporter model of ACAN expression for validation of an *Acan*-expressing cell subpopulation

Acan gene enhancer transgenic murine line (*Acan*-Cre-tdTomato) was used to spatially explore ACAN expression in murine ligament tissue and confirm the presence of an *Acan*-fibroblast subpopulation. This mouse line was provided by Professor George Bou-Gharios and Dr. Ke Liu. Animal work was completed in accordance with UK Home Office regulations and the Animals (Scientific Procedures) Act 1986. Mice were housed in the specific pathogen free biological services unit at the University of Liverpool. An inducible *Acan*-Cre strain was created using a highly conserved -10kb *Acan* enhancer [265] (10kb upstream of *Acan* transcriptional start site) paired with a tamoxifen inducible Cre ($CreER^{T2}$). This murine strain has been previously characterised [266, 267]. *Acan*-Cre murine strain was bred with Rosa26–tdTomato strain (R26R–tdTomato, JAX7914), creating a red fluorescent *Acan*-Cre-tdTomato reporter.

Male 8-week-old *Acan*-Cre-tdTomato mice were used to visualise cellular location of ACAN expression in cartilage and in ligaments. At 8 weeks of age, recombination of *Acan*-$CreER^{T2}$-tdTomato was induced using tamoxifen. Tamoxifen was administered intraperitoneally at a dose of 1mg/10g body weight three times at intervals of 48 hours. Mice were euthanized 2 weeks after tamoxifen injection and knee tissue (left and right hind legs) was collected for histology.

4.2.7.1 Tissue preparation and histology of Acan-Cre-tdTomato murine reporter

Knee joint tissue samples from *Acan*-Cre-tdTomato mice was prepared for histology by Professor George Bou-Gharios and Dr. Ke Liu. Samples were fixed in 4% paraformaldehyde overnight at 4°C and decalcified in 15% EDTA for two weeks. Tissue samples were then cryoprotected in 30% sucrose/PBS solution overnight at 4°C followed by 30% sucrose/PBS: optimal cutting temperature compound (1:1) solution overnight at 4°C. Samples were then embedded in optimal cutting temperature compound (TissuTek, Sakura) coronally, solidified with dry ice and stored at -80°C. This is a similar protocol for tissue preparation used previously [268].

Frozen *Acan*-Cre-tdTomato knee tissue samples were sectioned and analysed for the purpose of this study. Knee samples were cryo-sectioned (Cryostat, Leica) at -20°C cutting 7 µm thick sections of the whole knee joint and slides were stored at -20°C away from light until imaged.

4.2.7.2 Fluorescent imaging of Acan-Cre-tdTomato murine reporter

Slides were mounted with Vectashield antifade mounting medium with DAPI (Vector Laboratories) to visualise nuclei. Slides were imaged with a Zeiss M1 fluorescent microscope using the following excitation and emission filters: tdTomato (Ex. 543 nm, Em. 581 nm), DAPI (Ex. 405 nm, Em. 461). Images of brightfield, tdTomato and DAPI were saved individually and overlaid using Zen Imaging Analysis software. Images of cruciate ligaments and collateral ligaments were taken to determine spatial expression of *Acan*-expressing cells in the ligaments.

4.3 Results

4.3.1 Evaluation of ligament and synovium cell isolation quality

As previously mentioned, cell isolation from healthy murine ligament and synovial tissue samples was optimised for high cellular yield and quality (see Section 4.2.2). Isolation of live cells of sufficient quality for scRNA-seq has previously been done on murine tendons [236, 251] and is a critical step for high quality RNA reads. The preliminary protocol of cell isolation consisted of lower protease concentration (except higher trypsin concentration), longer incubation time, larger filter size and faster spin speed. This yielded low cell counts (~10,000 cells for ligament, ~12,000 cells for synovium), low cell viability (65.5% for ligament, 63.7% for synovium) and cell clustering (≤80% single-cell clusters for both samples) (Figure 4.2). The synovium sample also showed bulky masses of debris (Figure 4.2B) and cell clustering including 1.2% of >5-cell clusters (Figure 4.2D). Cell quantity and quality was low in the preliminary cell isolation protocol.

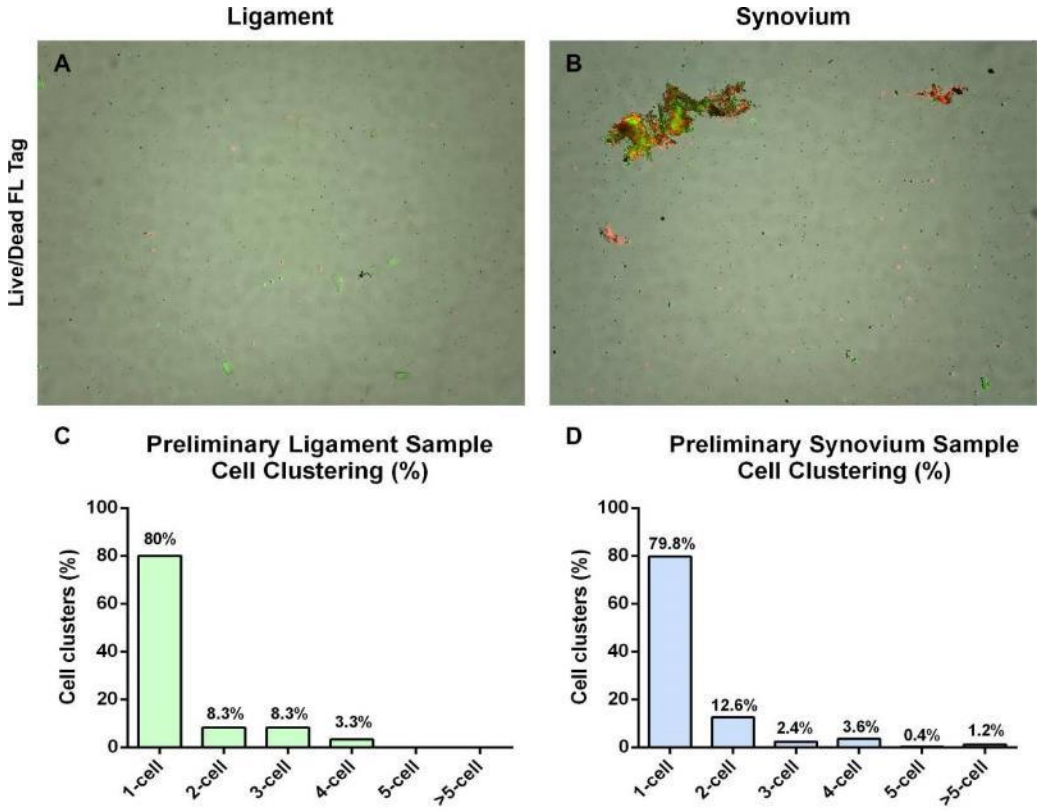

Figure 4.2 Analysis of cell viability and clustering for cell isolation protocol optimisation. (A) Live/Dead fluorescence images where green are viable and red are dead cells of ligament samples protocol showed low cell numbers (10,000 cell yield) and low viability (65.5%). (B) The synovium sample also had low cell yield (12,000 cells), high debris, cell clumping, and high dead (red) fluorescence tag (63.7% viability). (C-D) Cell clustering analysis showed ≤80% single-cell clusters for the ligament and synovium sample. Preliminary cell isolation protocol needed further optimisation.

The final cell isolation protocol (see Section 4.2.2) yielded reproducible cell isolation with sufficient cell numbers, high cell viability and low debris. Images from the automated cell counting (Figure 4.3A-B) confirmed high quality of cells for both samples. Pooling knee joint tissue samples from three healthy male mice yielded enough cells (40,000) from both ligament and synovium samples with a final concentration of 560 cells/µL and 720 cells/ µL respectively. Fluorescence cell counting also confirmed high viability of 89.2% for ligament-derived cells and 88.4% for synovial-derived cells (Figure 4.3A-B) and low cell clustering including >90% 1-cell clusters (Figure 4.3C-D). Therefore high quality cell clusters were confirmed, necessary to ensure high-quality RNA reads.

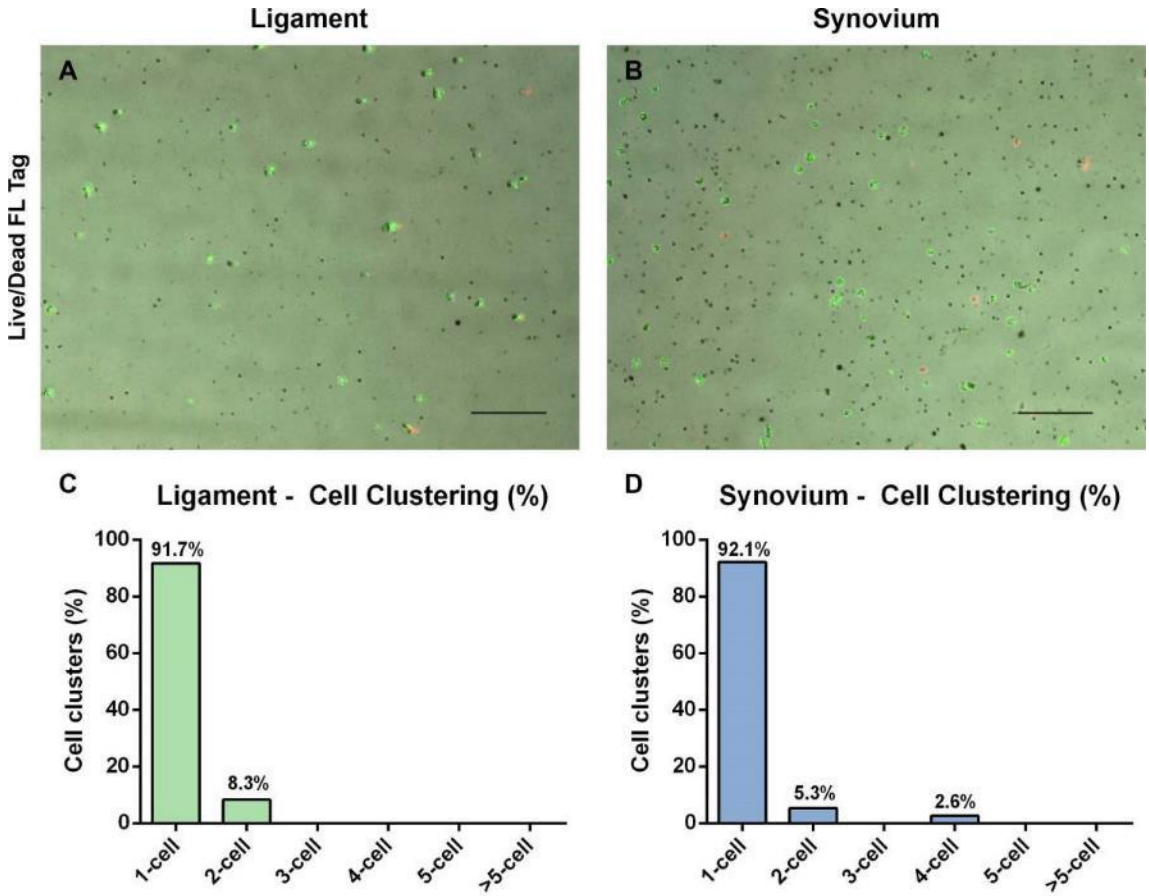

Figure 4.3 Analysis of cell viability and clustering for the final cell isolation protocol. (A-B) Live/Dead fluorescent images (where green are live cells, and red are dead cells) of cells isolated from (A) ligament sample and (B) synovium sample showed highly viable (green) cells, calculated as 89.2% viability for ligament cells and 88.4% viability for synovial cells. (C-D) Cell clustering analysis confirmed high single-cell clusters including (C) 91.7% 1-cell clusters for the ligament cells and (D) 92.1% 1-cell clusters for the synovial cells.

4.3.2 Analysis of ligament-derived cell populations and markers

Ligament-derived cell populations were initially analysed for quality control initially using Loupe Cell Browser to determine the quality of reads and total counts of UMIs. Cells were then further characterised based on downstream analysis following the standard Seurat workflow for cell identification and gene expression analysis [253], similar to recent papers on tendon cell populations [236, 251]. Pre-processing analysis and downstream analysis revealed numerous cell populations and distinct fibroblast subpopulations.

4.3.2.1 Quality control of ligament-derived library reads

Initial quality control post-sequencing with Loupe Cell Browser confirmed 5,574 ligament-derived cells were analysed with a mean of 109,289 reads per cell and a median of 287 genes per cell. This was a relatively low cell retention from the expected 10,000 cells and could be due to sample debris or the cell isolation protocol. Each individual cell was visualised using unguided t-SNE and labelled with their UMI counts which represented the absolute number of observed transcripts from each cell. UMI counts ranged from 2000 to 8000 counts (Figure 4.4A), where cells with higher UMI counts likely have higher RNA content. The t-SNE plot aggregated cells with similar gene expression profiles (Figure 4.4A).

Sequencing saturation and median genes per cell increased and an eventually plateaued at higher mean reads per cell (Figure 4.4B-C) and confirmed high sequencing saturation and therefore high fraction library complexity from our mean reads per cell, an important factor to ensure recovery of lowly expressed transcripts, particularly from rare cell populations. These initial results verified successful library creation and sequencing of ligament-derived cells, ready for downstream analysis.

4.3.2.2 Identification of ligament cell types and subpopulations

Seurat downstream analysis of ligament-derived cells filtered out low quality reads including low unique features and high mitochondrial genes. This filtering resulted in a remaining 2,165 ligament cells which were categorised into 20 distinct clusters using modularity optimisation techniques and visualised using UMAP (Figure 4.5A).

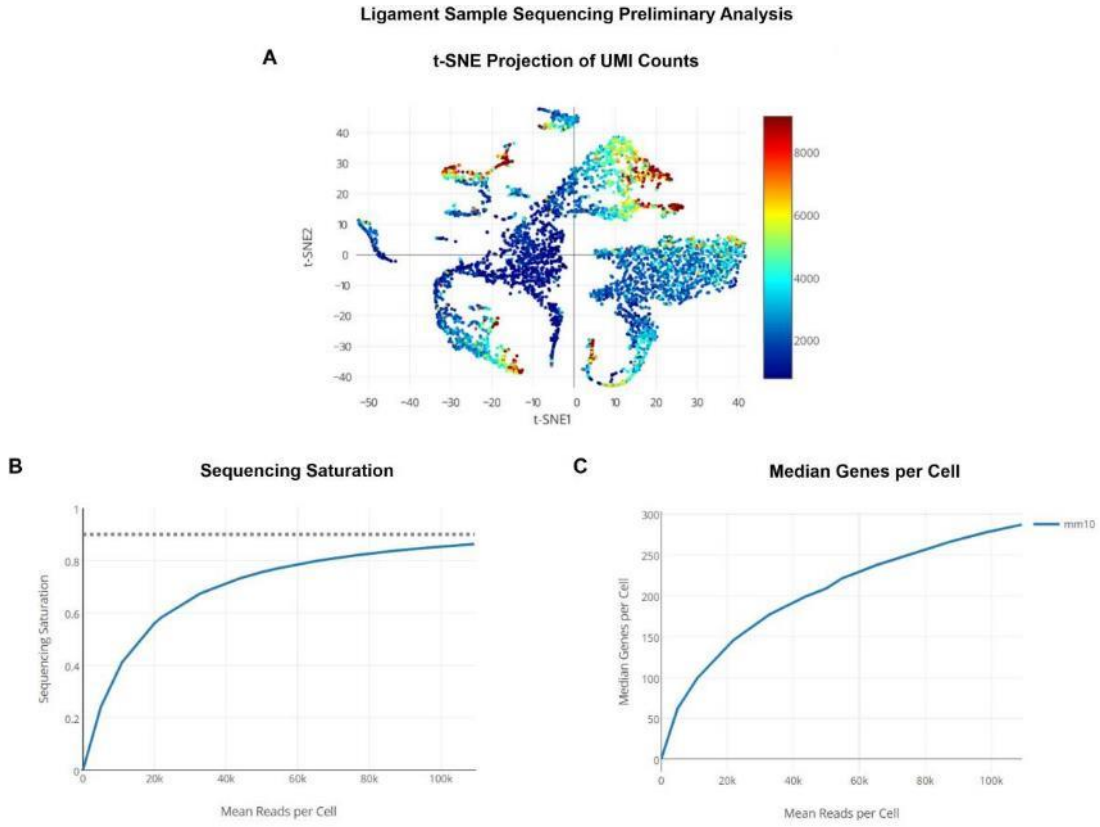

Figure 4.4 Quality control post-sequencing of the ligament-derived cells. (A) Unguided t-distributed stochastic neighbour embedding (t-SNE) projection of unique molecular identifiers (UMI) counts for each individual ligament-derived cell showed a range from 2000-8000 counts. This confirms a high number of absolute transcripts read for all the ligament-derived cells. (B) High sequencing saturation was confirmed and increased with the number of mean reads per cell. (C) Median genes per cell also increased as mean reads per cell increased. This confirmed successful library creation and high mean reads per cell an indicator of library complexity.

Each cluster was identified based on the presence of known cell-type markers (see Section 4.2.5 and Table 4.1 for details on known cell markers). Cell-type markers revealed nine distinct ligament cell-types (Figure 4.5): five fibroblast clusters (based on *Col1a2* gene expression), five immune cell clusters (based on *Ptprc* gene expression), three endothelial cell clusters (based on *Pecam1* gene expression) and two RB cell clusters (based on *Hba-a1* gene expression) (Figure 4.5B-E). The remaining clusters comprised of one nerve cell cluster (based on *Mpz* gene expression), one satellite cell cluster (based on *Pax7* gene expression), one platelet cell cluster (based on *Itga2b* gene expression), one muscle cell cluster (based on *Myot* gene expression) and one unidentified cell cluster (Figure 4.5F). Average expression and percent cell expression of each cell type marker within each classified cluster can be seen in Figure 4.5F.

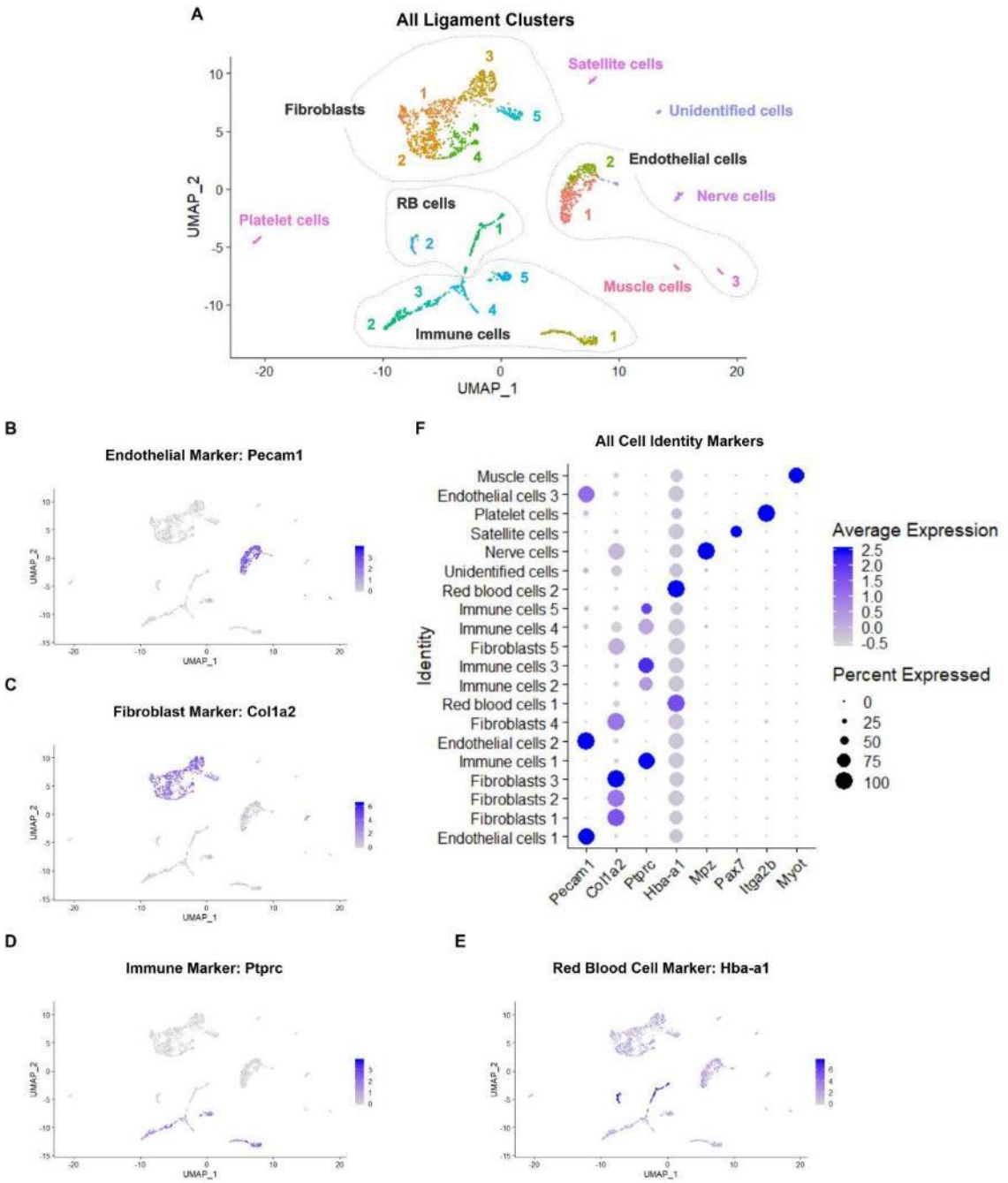

Figure 4.5 Identified ligament-derived cell populations. (A) Uniform manifold approximation and projection (UMAP) of all ligament clusters colored, numbered and labelled by cell type. Cell types included fibroblasts, endothelial cells, immune cells, nerve cells, red blood (RB) cells, satellite cells, platelet cells, muscle cells and an unidentified cluster. (B-E) The cell identification markers included Pecam1 for endothelial cells (B), Col1a2 for fibroblasts (C), Ptprc for immune cells (D) and Hba-a1 for RB cells (E). (F) Dot plot of all cell type markers also included the remaining identification markers: Mpz for nerve cells, Pax7 for satellite cells, Itga2b for platelet cells and Myot for muscle cells.

The top differentially expressed markers of each ligament cell-type cluster highlighted gene expression differences within similar cell types including the fibroblasts. The top three markers

of each fibroblast cluster show some overlap between all cell clusters (Figure 4.6A). Fibroblast cluster 1 markers included STEAP family member 4 (*Steap4*), complement component 1 s-subcomponent (*C1s1*) and cytoglobin (*Cygb*) (Figure 4.6A). Fibroblast cluster 2 markers included endosialin (*Cd248*), endothelial protein C receptor (*Procr*) and peptidase inhibitor 16 (*Pi16*) (Figure 4.6A). Fibroblast cluster 3 markers included thrombospondin 4 (*Thbs4*), cartilage intermediate layer protein 2 (*Cilp2*) and coiled-coil domain-containing protein 3 (*Ccdc3*) (Figure 4.6A). Fibroblast cluster 4 markers included immunoglobulin superfamily containing leucine-rich repeat protein 2 (*Islr2*) and immunoglobulin-like domain containing receptor 2 (*Ildr2*) and also olfactomedin-like 2A (*Olfml2a*) (Figure 4.6A). Fibroblast cluster 5 markers included leucine-rich repeat-containing G-protein coupled receptor 6 (*Lgr6*), tumor necrosis factor receptor superfamily member 11B (*Tnfrsf11b*, also known as osteoprotegerin) and hyaluronan and proteoglycan link protein 1 (*Hapln1*) (Figure 4.6A). Fibroblasts will be analysed in more detail in Section 4.3.2.3.

Ligament-derived immune cell clusters also had different transcriptional profiles with unique markers. The top differentially expressed markers of the immune clusters showed some overlap between the immune cell cluster 3 and 4 (Figure 4.6B). Immune cluster 1 had neutrophil-associated markers such as matrix metallopeptidase 9 (*Mmp9*) [269] and matrix metallopeptidase 8 (*Mmp8*) [270] and other lesser known markers such as solute carrier family 7 member 11 (*Slc7a11*) (Figure 4.6B). Immune cluster 2 and 3 showed macrophage-associated markers. Immune cluster 2 markers included macrophage associated markers such as folate receptor beta (*Folr2*) [271], mannose receptor C-type 1 (*Mrc1*) [272] and carbonyl reductase 2 (*Cbr2*) [273] (Figure 4.6B). Immune cluster 3 markers included macrophage and monocyte-associated markers such as C-C chemokine receptor type 2 (*Ccr2*) [274], macrophage-expressed gene 1 (*Mpeg1*) [275] and phospholipase D family member 4 (*Pld4*) [276] (Figure 4.6B). Although there was overlap in markers between immune cluster 3 and 4, immune cluster 4 markers included membrane-spanning 4-domains subfamily A3 (*Ms4a3*) an early myeloid marker [277] and lesser known markers such as *1700020L24Rik*, and cystatin-F (*Cst7*) (Figure 4.6B). Immune cluster 5, the least numerous, comprised of a B lymphocyte associated markers, such as immunoglobulin lambda constant 3 (*Iglc3*) [278], B-cell antigen receptor complex-associated protein (*Cd79a*) [278] and B-lymphocyte antigen (*Ms4a1*, encoding CD20) [278] (Figure 4.6B).

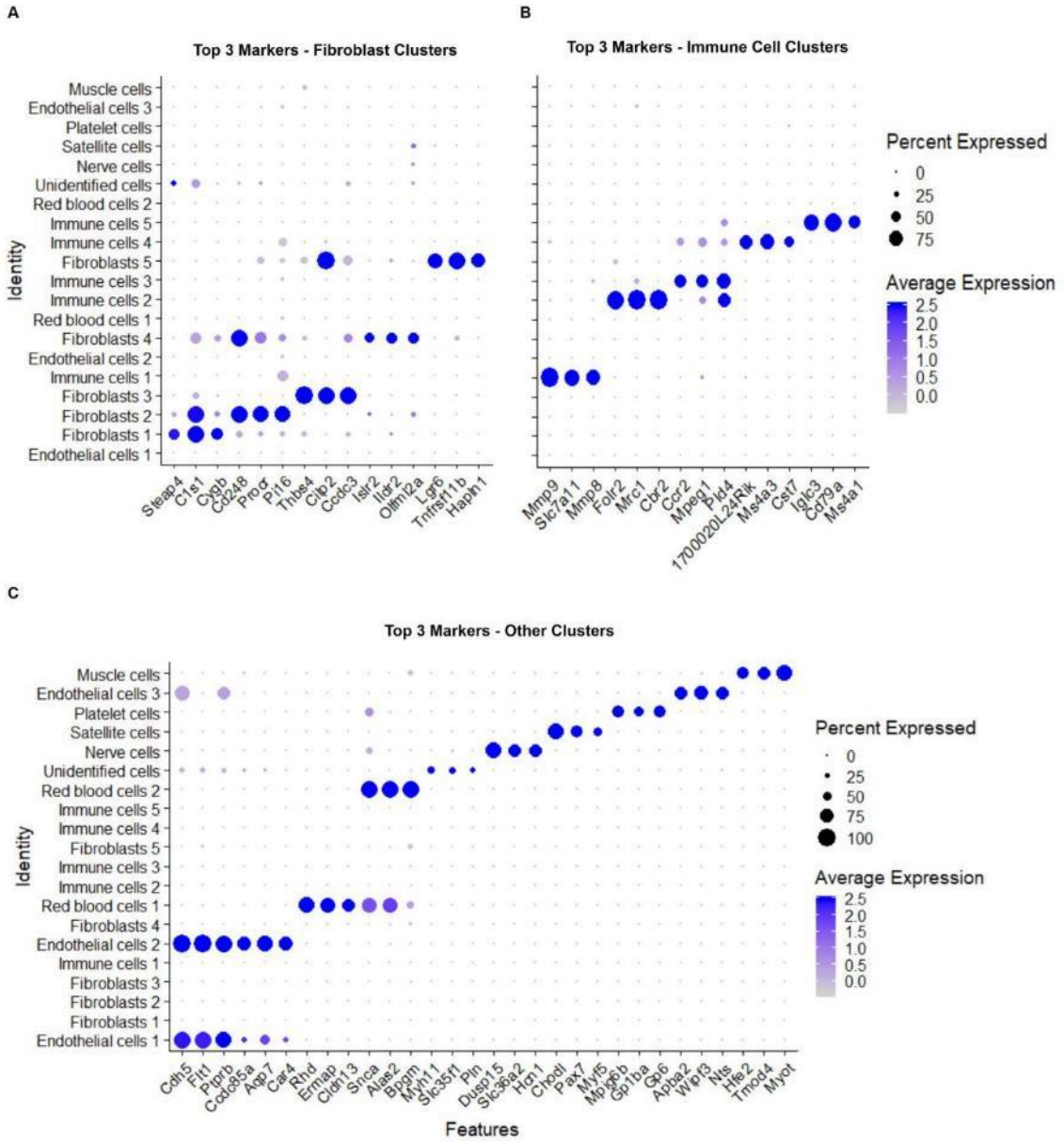

Figure 4.6 Dot plot of the top three differentially expressed markers of all ligament cell clusters for cluster identification. (A) The top three markers of the fibroblast clusters showed some overlap in marker expression between fibroblast clusters. (B) The top markers of the immune cell clusters showed high specificity except between immune cluster 3 and 4. (C) The top markers of the remaining endothelial, red blood (RB), unidentified, nerve, satellite, platelet, and muscle cell clusters showed high specificity except for the endothelial and RB clusters. High specificity could indicate distinct cell subpopulations.

The three endothelial cell clusters were identified based on high expression of *Pecam1* (Figure 4.5). Endothelial cell cluster 1 included vascular-endothelial markers such as vascular-endothelial cadherin (*Cdh5*, encoding VE-Cadherin also known as CD144) [279], vascular endothelial growth factor receptor 1 (*Flt1*, encoding VEGFR-1) [280] and vascular endothelial protein tyrosine phosphatase (*Ptprb*, encoding VE-PTP) [279] (Figure 4.6C). Endothelial cell cluster 2 included a

range of lesser-known markers such as coiled-coil domain containing 85A (*Ccdc85a*), aquaporin 7 (*Aqp7*) and carbonic anhydrase 4 (*Car4*) (Figure 4.6C). Endothelial cell cluster 3 included neuronal-associated makers such as amyloid beta A4 precursor protein-binding family A2 (*Apba2*) [281] and neurotensin (*Nts*) a marker associated with smooth muscle contraction [282] (Figure 4.6C). The dot plot showed overlap in markers between endothelial cluster 1 and 2 (Figure 4.6C) suggesting similar expression profiles.

The remaining clusters included a range of cell types and generally distinct top marker expression. This included two RB cell clusters (RB 1: *Rhd, Ermap, Cldn13*; RB 2: *Snca*, *Alas2*, *Bpgm*), a nerve cell cluster (*Dusp15*, *Slc36a2*, *Hcn1*), a satellite cell cluster (*Chodl*, *Pax7*, *Myf5*), platelet cell cluster (*Mpig6b*, *Gp1ba*, *Gp6*) and a muscle cell cluster (*Hfe2*, *Tmod4*, *Myot*). Lastly, an unidentified cell cluster (*Myh11*, *Slc35f1*, *Pln*) had distinct markers from a range of associated cell-types, from smooth muscle markers such as Myh11 [283] to stem cells marker such as Foxd3 (not shown here) [284] and neural crest markers such as Sox10 (not shown here) [285]. Except for the RB cell clusters, all other clusters had distinct and cluster-specific marker expression (Figure 4.6C). Cluster-specificity of the top markers supports the idea that each cluster is a transcriptionally diverse subpopulation.

4.3.2.3 Analysis of ligament fibroblast markers

Ligament fibroblasts subgroups were separated (based on *Col1a2* expression) (Figure 4.7A). Downstream analysis with Seurat (see Section 4.2.5) found five distinct ligament fibroblast clusters, labelled L.F1 (258 cells), L.F2 (240 cells), L.F3 (219 cells), L.F4 (135 cells), and L.F5 (78 cells) respective of cluster size (Figure 4.7B).

Ligament fibroblast markers were determined via differential expression analysis of all fibroblast clusters compared to all other ligament cell-type clusters (see Section 4.2.5). A heatmap of the top 20 markers confirmed marker specificity to the fibroblast clusters (Figure 4.7C). Fibroblast-marker specificity was slightly lower in the L.F5 cluster which had low or negative expression of *Col1a1, Serpinf1, Serping1, Clec3b* and *Fstl1* (Figure 4.7C). Despite this, prominent fibroblast ECM markers were present in L.F5 cluster including decorin (*Dcn*), *Col1a2* and *Col3a1* as well as high expression of other significant fibroblast collagens (*Col6a1, Col6a2, Col5a2*) (Figure 4.7C). Differences in the L.F5 transcriptional makeup cluster could suggest it is a distinct fibroblast subpopulation. Additional analysis of each individual fibroblast cluster is necessary to differentiate each cluster and their potential role.

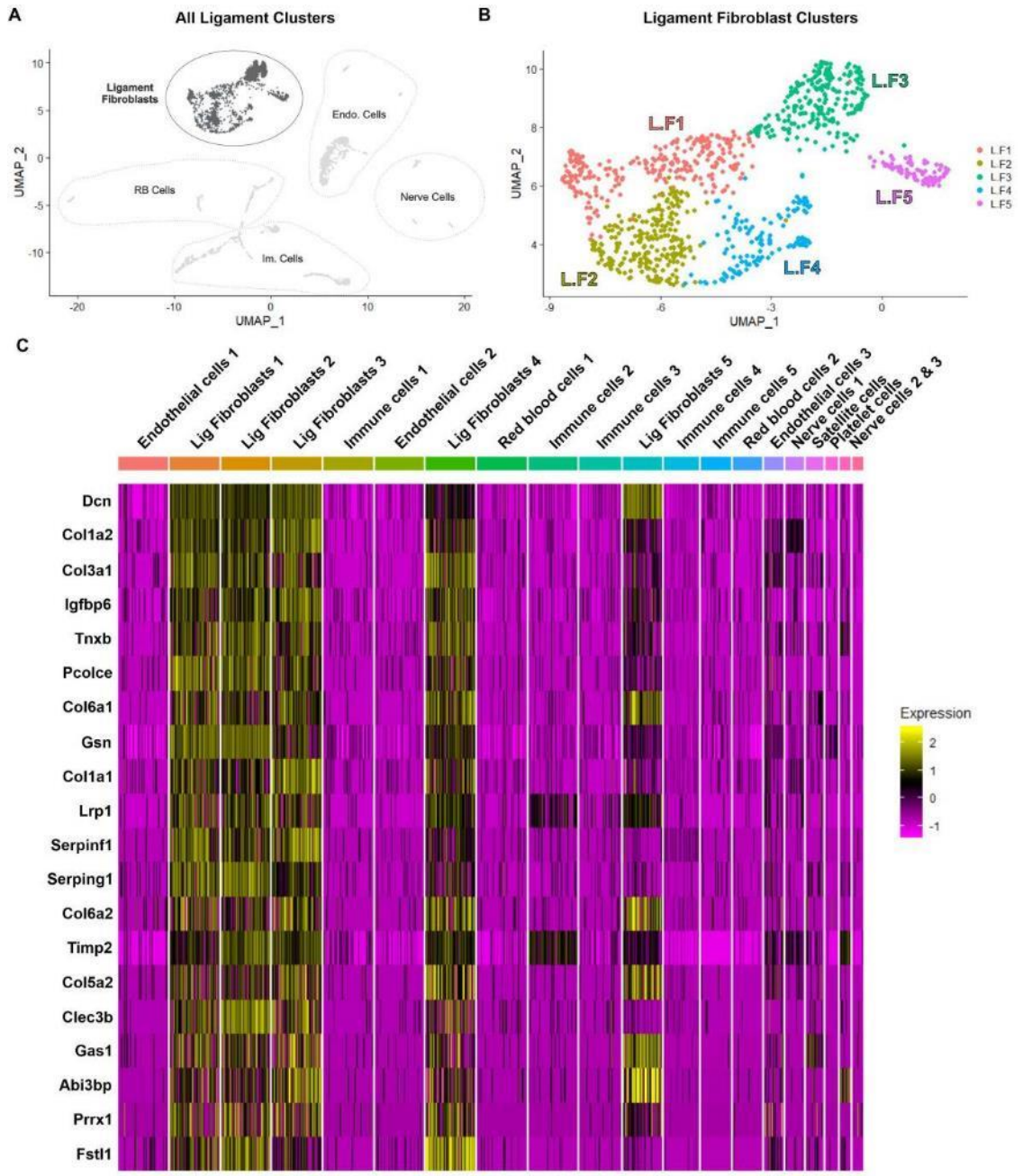

Figure 4.7 Ligament fibroblasts subgroups and the top differentially expressed fibroblast markers. (A) 'Ligament Fibroblasts' clusters expressing Col1a2 were further analysed. (B) Ligament fibroblast subgroups were five in total according to Seurat downstream analysis and labelled LF1 to LF5. (C) Heatmap of the top 20 ligament fibroblast markers calculated via differential expression analysis included: Dcn, Col1a2, Col3a1, Igfbp6, Tnxb, Pcolce, Col6a1, Gsn, Col1a1, Lrp1, Serpinf1, Serping1, Col6a2, Timp2, Col5a2, Clec3b, Gas1, Abi3bp, Prrx1 and Fstl1. The heatmap demonstrated high expression and specificity for the fibroblast clusters.

4.3.2.4 Ligament fibroblast 1 (L.F1) subpopulation

L.F1 cluster was the largest ligament fibroblast cluster made up of 258 cells (Figure 4.8A). Differential expression analysis between L.F1 and the remaining fibroblast clusters found unique

high-expressing markers such as six transmembrane epithelial antigen of prostate 4 (*Steap4*), hemicentin 2 (*Hmcn2*), gamma-glutamyltransferase 5 (*Ggt5*), chemokine CXC motif ligand 14 (*Cxcl14*), secreted frizzled-related protein 1 (*Sfrp1*), and glypican 3 (*Gpc3*) (Figure 4.8B). A heatmap of the top 20 differentially expression L.F1 markers confirmed specificity to the L.F1 cluster but also a minor overlap with L.F2 markers indicating a similarity between the two clusters (Figure 4.8C).

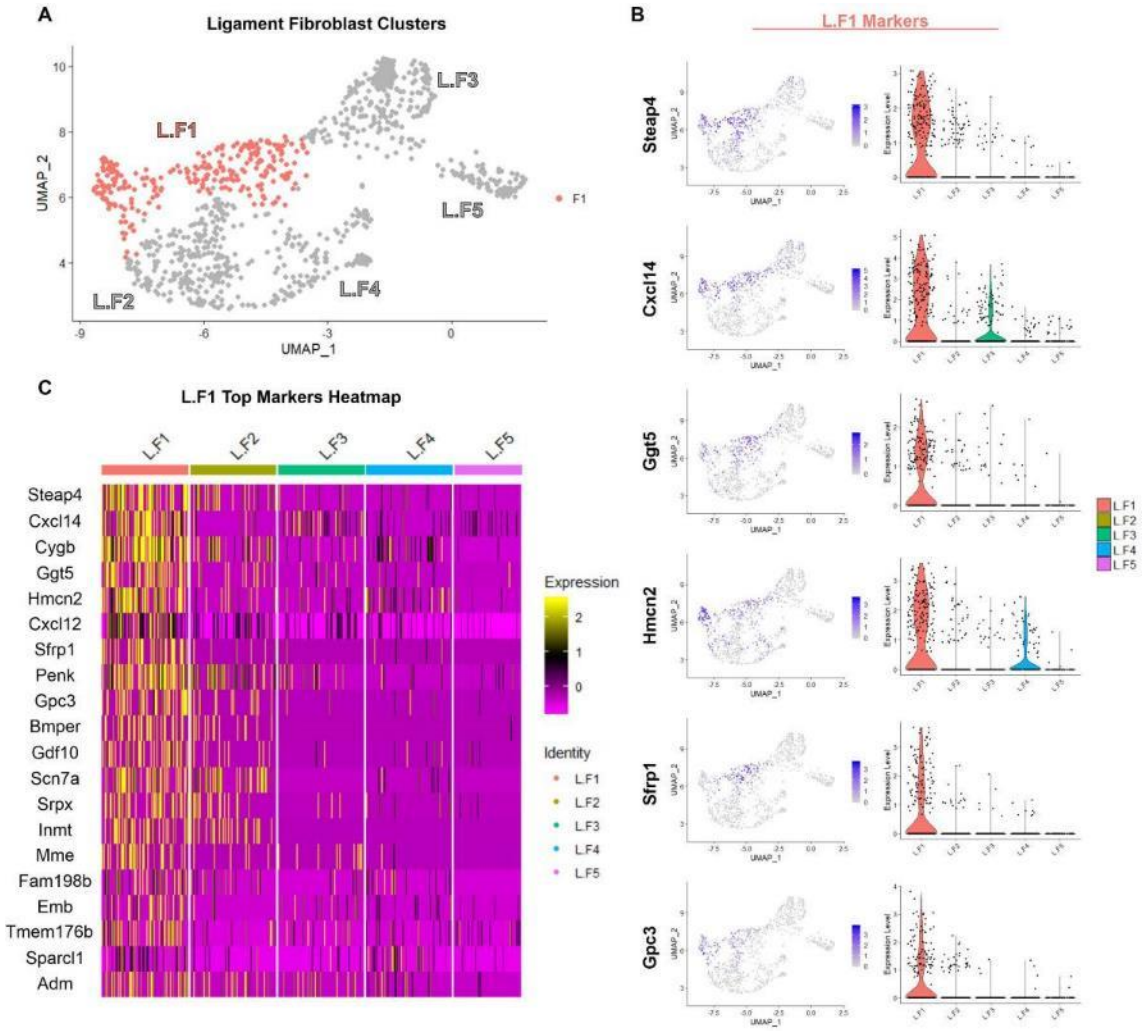

Figure 4.8 The top differentially expressed markers of the ligament fibroblast 1 (L.F1) cluster. (A) Uniform manifold approximation and projection (UMAP) of L.F1 and the other fibroblast cells. (B) Feature and violin plot comparing the top differentially expressed L.F1 markers: Steap4, Cxcl14, Ggt5, Hmcn2, Sfrp1, and Gpc3. (C) A heatmap of the top 20 differentially expressed L.F1 markers included Steap4, Cxcl14, Cygb, Ggt5, Hmcn2, Cxcl12, Sfrp1, Penk, Gpc3, Bmper, Gdf10, Scn7a, Srpx, Inmt, Mme, Fam198b, Emb, Tmem176b, Sparcl1 and Adm. Heatmap confirmed marker specificity for the L.F1 cluster with minor overlap with the L.F2 cluster, indicating potential transcriptional similarities between the two clusters.

4.3.2.5 Ligament fibroblast 2 (L.F2) subpopulation

Differential expression analysis of L.F2 cluster (240 cells) identified L.F2-specific markers. These gene expression markers included peptidase inhibitor 16 (*Pi16*, encoding CD364) and IL-1 receptor type II (*Il1r2*), sphingomyelin phosphodiesterase 3 (*Smpd3*), transmembrane protein 26 (*Tmem26*), endo-beta-N-acetyl-glucosaminidase (*Engase*) and allograft inflammatory factor 1-like (*Aif1l*). L.F2 cluster heatmap showed overlap with the L.F4 cluster (Figure 4.9C) indicating potential transcriptional similarities between the two clusters.

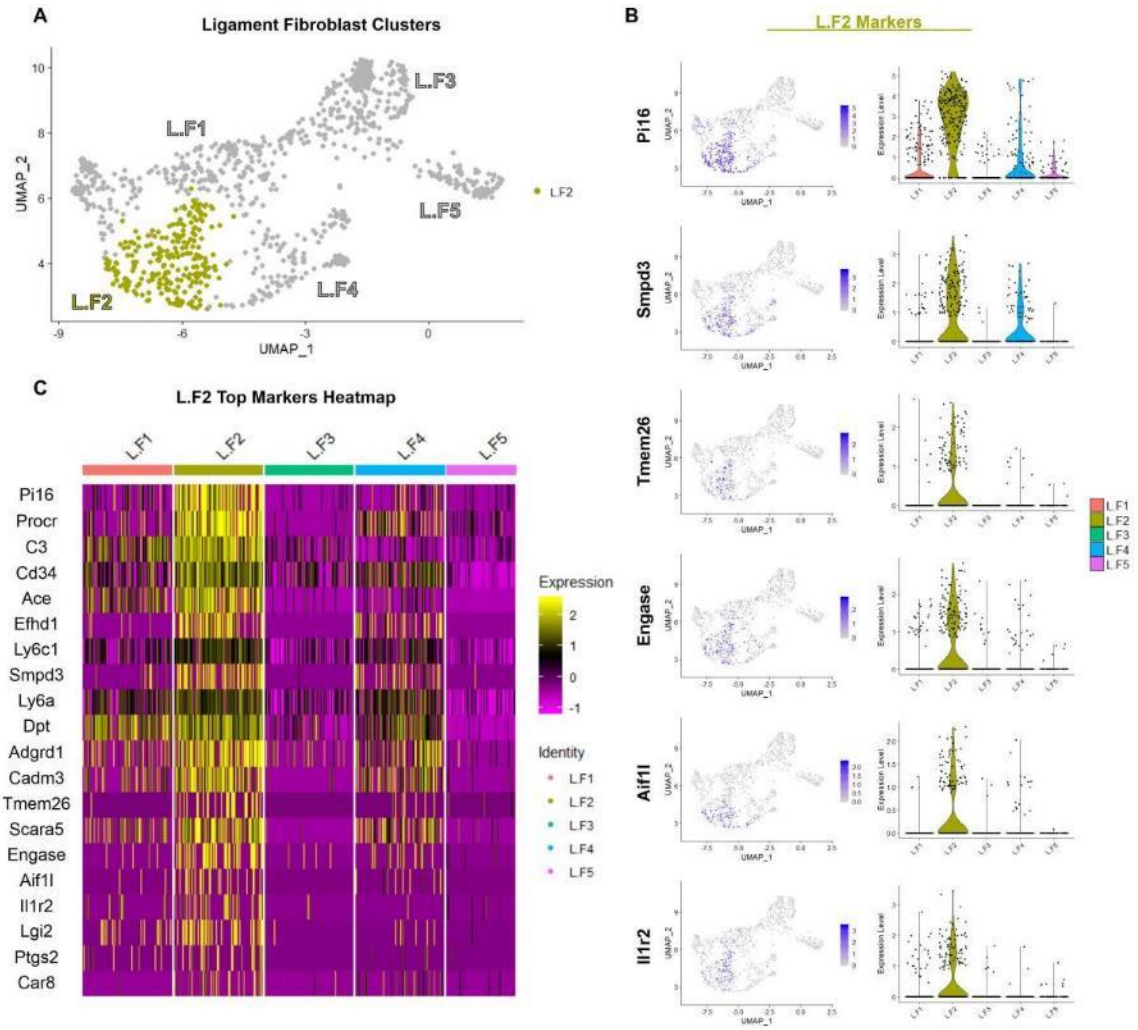

Figure 4.9 The top differentially expressed markers of the ligament fibroblast 2 (L.F2) cluster. (A) Uniform manifold approximation and projection (UMAP) of L.F2 and other fibroblast cells. (B) Feature and violin plot of the top differentially expressed L.F2 markers: Pi16, Smpd3, Tmem26, Engase, Aif1l, Il1r2. (C) A heatmap of the top differentially expressed L.F2 markers showed some overlap with L.F4, indicating transcriptional similarities between the two clusters. The top 20 differentially expressed markers included Pi16, Procr, C3, Cd34, Ace, Efhd1, Ly6c1, Smpd3, Ly6a, Dpt, Adgrd1, Cadm3, Tmem26, Scara5, Engase, Aif1l, Il1r2, Lgi2, Ptgs2 and Car8.

4.3.2.6 Ligament fibroblast 3 (L.F3) subpopulation

Differential expression analysis of the L.F3 cluster (219 cells) (Figure 4.10A) found cluster-specific markers such as scleraxis (*Scx*), tenomodulin (*Tnmd*), mohawk (*Mkx*), fibromodulin (*Fmod*), glycoprotein thrombospondin-4 (*Thbs4*), myosin light chain kinase (*Mylk*) (encoding kinase-related protein, telokin), keratocan (*Kera*), and leptin receptor (*Lepr*) (Figure 4.10B-C). A heatmap of the top 20 differentially expressed L.F3 markers confirmed cluster specificity (Figure 4.10C).

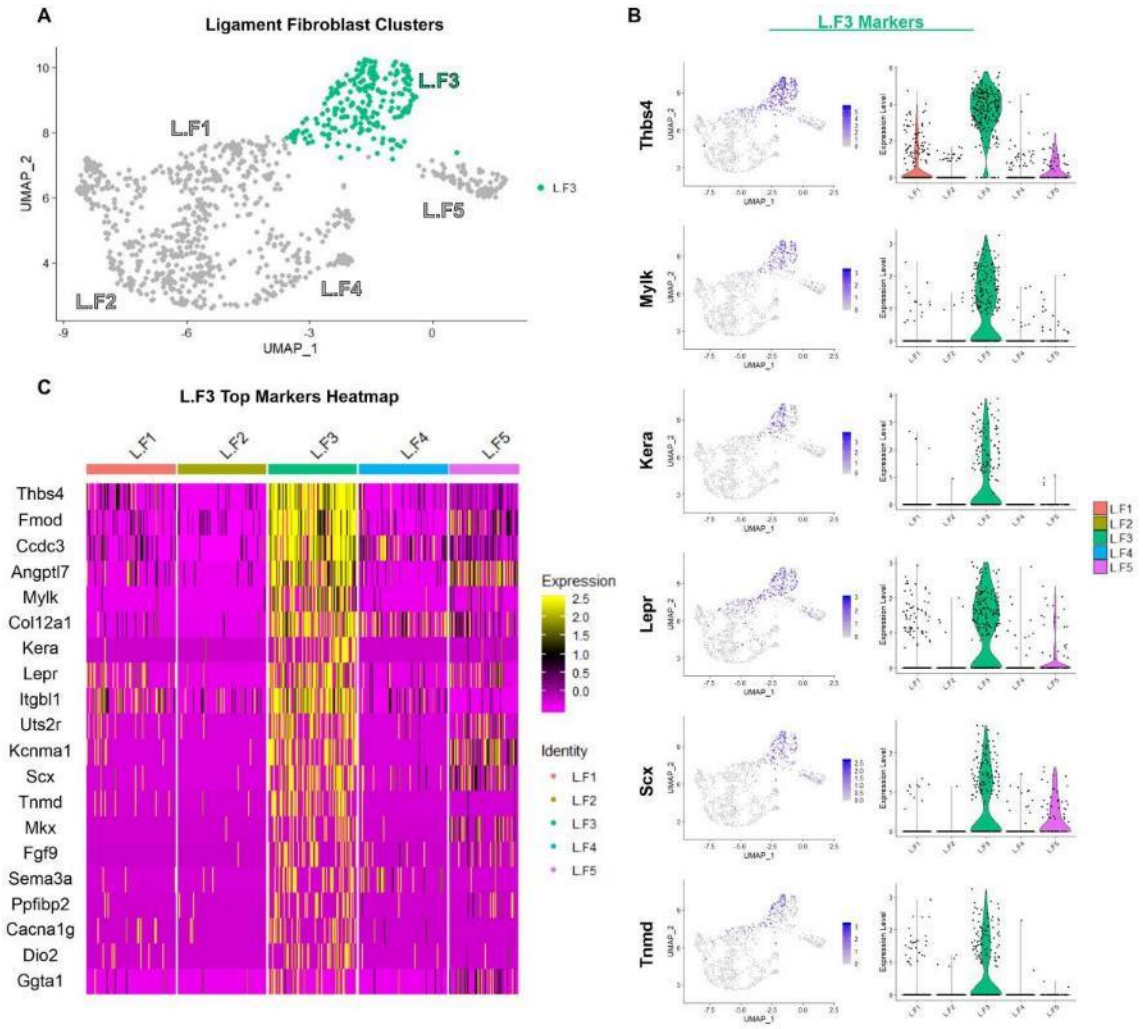

Figure 4.10 The top differentially expressed markers of the ligament fibroblast 3 (L.F3) cluster. (A) Uniform manifold approximation and projection (UMAP) of L.F3 and other fibroblast cells. (B) Feature and violin plot of the top differentially expressed L.F3 markers included Thbs4, Mylk, Kera, Lepr, Scx, and Tnmd. (C) A heatmap of the top 20 differentially expressed L.F3 markers showed cluster-specific markers. The top 20 differentially expressed markers included Thbs4, Fmod, Ccdc3, Angptl7, Mylk, Col12a1, Kera, Lepr, Itgbl1, Uts2r, Kcnma1, Scx, Tnmd, Mkx, Fgf9, Sema3a, Ppfibp2, Cacna1g, Dio2 and Ggta1.

4.3.2.7 Ligament fibroblast 4 (L.F4) subpopulation

The top differentially expressed L.F4 subpopulation (135 cells) markers included immunoglobulin superfamily containing leucine-rich repeat 2 (*Islr2*), immunoglobulin-like domain receptor 2 (*Ildr2*), hemicentin-1 (*Hmcn1*, encoding Fibulin-6), integrin beta 3 (*Itgb3*, encoding CD61), olfactomedin-like 2A (*Olfml2a*), and ovarian carcinoma immunoreactive antigen domain 2 (*Ociad2*) (Figure 4.11B). A heatmap of the top 20 differentially expressed markers confirmed high expression and cluster-specificity (Figure 4.11C).

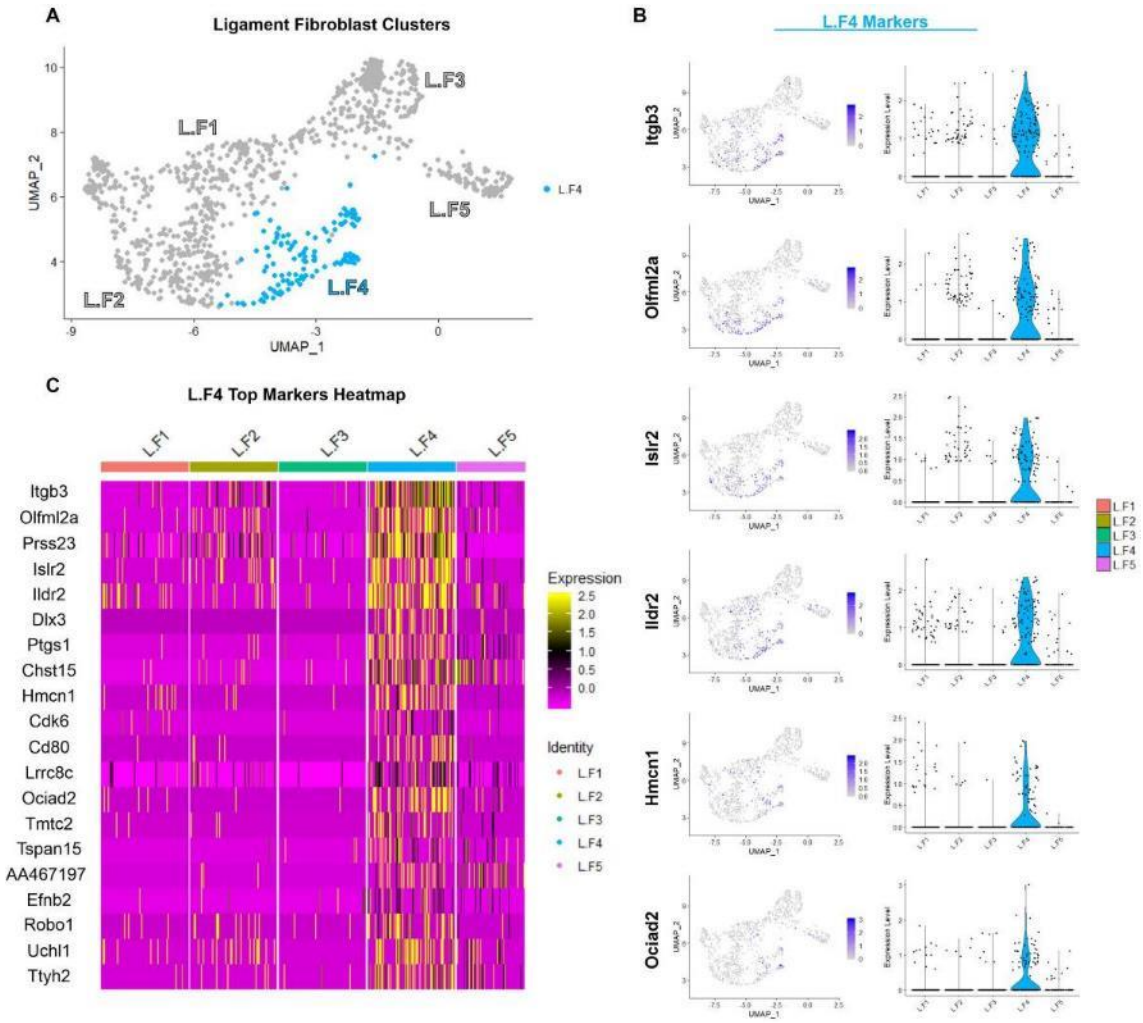

Figure 4.11 The top differentially expressed markers of the ligament fibroblast 4 (L.F4) cluster. (A) Uniform manifold approximation and projection (UMAP) of L.F4 and other fibroblast cells. (B) Feature and violin plot of the top differentially expressed L.F4 markers: Itgb3, Olfml2a, Islr2, Ildr2, Hmcn1, and Ociad2. (C) A heatmap of the top 20 differentially expressed L.F4 markers shows L.F4 cluster specificity. Top 20 differentially expressed markers included Itgb3, Olfml2a, Prss23, Islr2, Ildr2, Dlx3, Ptgs1, Chst15, Hmcn1, Cdk6, Cd80, Lrrc8c, Ociad2, Tmtc2, Tspan15, AA467197, Efnb2, Robo1, Uchl1 and Ttyh2.

4.3.2.8 Ligament fibroblast 5 (L.F5) subpopulation

L.F5 was the smallest subpopulation of fibroblasts (Figure 4.12A) made up of 78 cells. The top differentially expressed markers included cartilage associated markers such as *Acan* and hyaluronan and proteoglycan link protein 1 (*Hapln1*, encoding CRTL1). Other L.F5 markers included leucine-rich repeat-containing G-protein coupled receptor 6 (*Lgr6*), Egl nine homolog 3 (*Egln3*), melanotransferrin (*Meltf*, encoding CD228) and tumor necrosis factor receptor superfamily member 11b (*Tnfrsf11b*) (Figure 4.12B). A heatmap showed high specificity and expression for the top 20 differentially expressed L.F5 markers (Figure 4.12C). Other cartilage markers specific to L.F5 included transcription factor Sox-9 (*Sox9*) and COL2 alpha 1 (*Col2a1*) both of which were highly expressed and specific (Figure 4.12D-E). These cartilage-associated markers indicate a cluster-specific transcriptional shift in this fibroblast subpopulation.

4.3.2.9 Enriched canonical pathways and predicted upstream regulators

The top 20 enriched canonical pathways of the healthy murine ligament fibroblast clusters predicted by the IPA software revealed similar signalling pathways. GP6 signalling pathway received the highest activation scores in all ligament fibroblast clusters (Table 4.2). The same was also true for the cardiac hypertrophy signalling, dendritic cell maturation, and OA pathways (Table 4.2). The only signalling pathways that had predicted inactivation was WNT/β-catenin (L.F1, L.F3, L.F5) and RhoGDI signalling pathways (L.F4) (Table 4.2). Furthermore, there were six canonical pathways that were activated in both L.F2 and L.F4 (Table 4.2), confirming the close relationship between the two clusters seen previously (Figure 4.9C). From the top 20 enriched canonical pathways, the only pathways that were unique to one cluster were the integrin signalling pathway (L.F4), the fibroblast growth factor (FGF) signalling pathway (L.F5) and the RhoGDI signalling pathway (L.F4). Canonical pathway analysis did not reveal major differences in the pathways of the murine ligament fibroblast subpopulations.

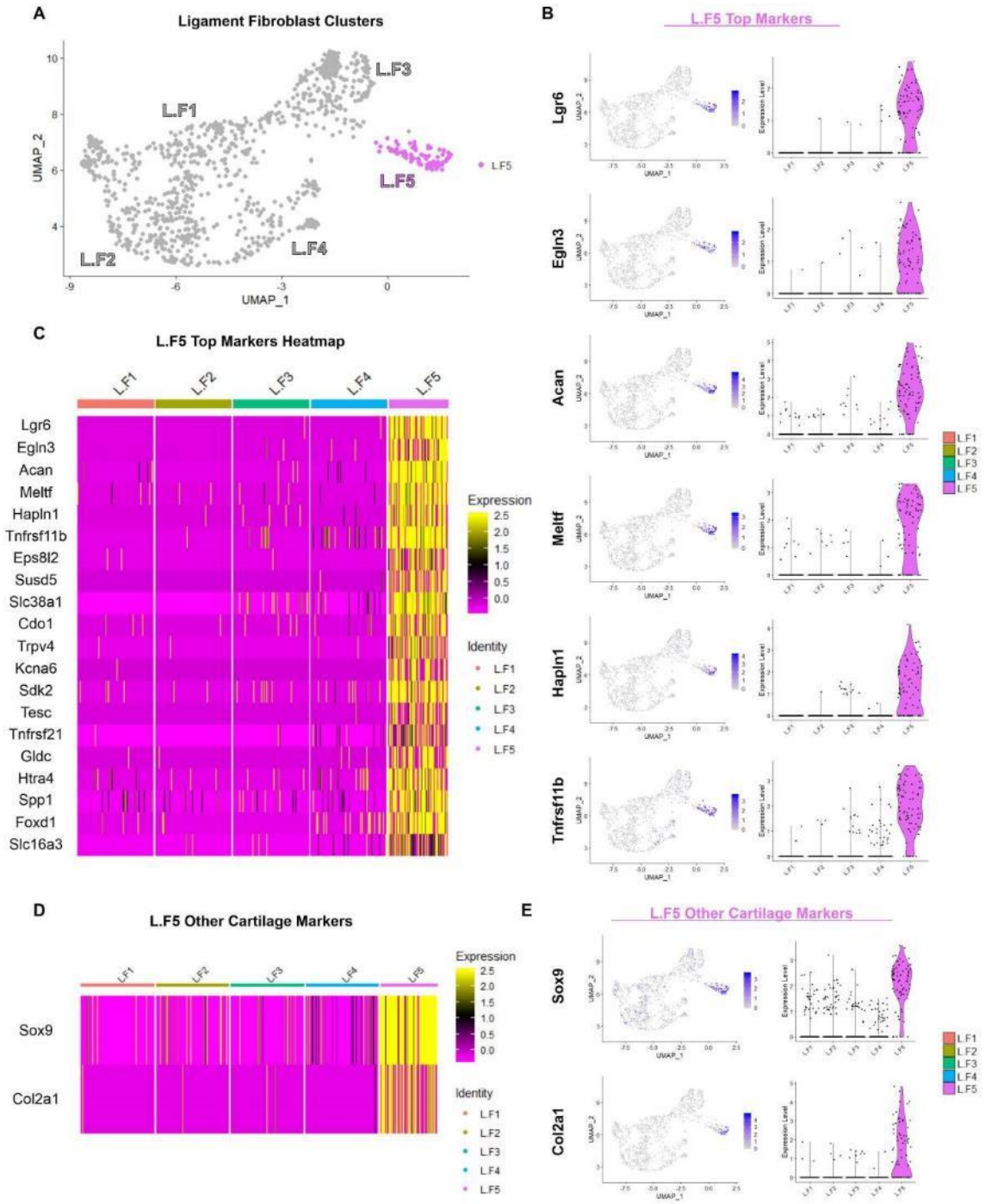

Figure 4.12 The top differentially expressed markers of the ligament fibroblast 5 (L.F5) cluster. (A) Uniform manifold approximation and projection (UMAP) of the L.F5 cluster relative to other ligament fibroblast clusters. (B) Feature and violin plot of the top differentially expressed L.F5 markers: Lgr6, Egln3, Acan, Meltf, Hapln1 and Tnfrsf11b. (C) A heatmap of the top differentially expressed markers: Lgr6, Egln3, Acan, Meltf, Hapln1, Tnfrsf11b, Eps8l2, Susd5, Slc38a1, Cdo1, Trpv4, Kcna6, Sdk2, Tesc, Tnfrsf21, Gldc, Htra4, Spp1, Foxd1 and Slc16a3. (D) A heatmap of cartilage-associated markers Sox9 and Col2a1 show L.F5 specificity. (E) Feature and violin plot of Sox9 and Col2a1 confirm L.F5 specificity and expression of both cartilage markers.

Table 4.2 Predicted enriched canonical pathways for each ligament fibroblast cluster. Canonical pathway activation revealed similarities between the ligament fibroblast clusters. The respective activation z-score of each canonical pathway was colour graded: red is positive and blue is negative. Enriched canonical pathway analysis was predicted with Ingenuity Pathway Analysis (IPA) software.

Top 20 Enriched Canonical Pathways	Activation z-score				
	L.F1	L.F2	L.F3	L.F4	L.F5
GP6 Signalling Pathway	3.464	2.828	3.606	3.317	3.317
Cardiac Hypertrophy Signalling (Enhanced)	2.449	3	2.646	2	3.873
Dendritic Cell Maturation	2.236	2	2.449	2.449	2
Synaptogenesis Signalling Pathway	2	2.449	2.449	2.53	N/A
NF-κB Signalling	2	2.646	N/A	N/A	2
Osteoarthritis (OA) Pathway	1	2.111	1.342	1.265	0.688
Glioblastoma Multiforme Signalling	N/A	2.236	N/A	2.236	1.342
Colorectal Cancer Metastasis Signalling	N/A	3	N/A	2.449	N/A
IL-8 Signalling	N/A	2.449	N/A	2.828	N/A
ILK Signalling	N/A	2.646	N/A	2.53	N/A
STAT3 Pathway	2	2.646	N/A	N/A	N/A
Cholecystokinin/Gastrin-mediated Signalling	N/A	2	N/A	2	N/A
Apelin Liver Signalling Pathway	2	N/A	2	N/A	N/A
Sphingosine-1-phosphate Signalling	N/A	2	N/A	2	N/A
WNT/β-catenin Signalling	-1	0	-0.447	0.447	-1.667
Leukocyte Extravasation Signalling	N/A	1	1	1.414	N/A
Integrin Signalling	N/A	N/A	N/A	2.828	N/A
Glioma Invasiveness Signalling	N/A	1	N/A	1.667	N/A
FGF Signalling	N/A	N/A	N/A	N/A	2.449
RhoGDI Signalling	N/A	N/A	N/A	-2.449	N/A

Predicted upstream regulators for each ligament fibroblast cluster were also assessed using IPA software. The top six predicted activated upstream regulators were very similar among all the clusters and included transforming growth factor beta 1 (*Tgfb1*) which was activated in all ligament fibroblast subpopulations (Table 4.3). The total number of activated upstream regulators for each ligament fibroblast cluster was highly variable and the percentage of those regulators which were also activated in other ligament fibroblast cluster confirmed a high overlap of upstream regulators (from 38.8-80.0%) (Table 4.3). The top cluster-specific upstream regulators were determined based on their predicted activation score. These ligament fibroblast subpopulation-specific upstream regulators could provide insight into cluster-specific roles (Table 4.3) and are discussed in Section 4.4.1.

Table 4.3 Predicted activated upstream regulators in the ligament fibroblast subpopulations. The total number of predicted activated upstream regulators varied between clusters. The top six predicted activated upstream regulators were similar between in all ligament fibroblast clusters. The top five cluster specific activated upstream regulators for each ligament fibroblast cluster could provide insight into cluster-specific roles. Activated upstream regulators were predicted with Ingenuity Pathway Analysis (IPA) software.

	Predicted Activated Upstream Regulators		
Cluster	**Total #**	**Top 6**	**Top 5 Cluster Specific**
L.F1	201	*Ccr2, Ikbkb, Tgfb1, Ikbkg, Prl, Twist1*	*Mafb, Tcr, Eif4e, Cpxm1, Stat*
L.F2	278	*Pdgf Bb, Prl, Sp1, Il1B, Egf, Tp53*	*Fgf7, Lhx1, F3, F7, Tlr3*
L.F3	135	*Tgfb1, Ccr2, Htt, Hif1A, Twist1, Tgf Beta*	*Id2, Otx2, Hoxd3, Atf6, Neurog1*
L.F4	205	*Tgfb1, Tp53, Il1B, F2, Il5, Sp1*	*Kmt2d, Ret, Il15, Sox11, Ptpn3*
L.F5	228	*Tgfb1, Ctnnb1, Tgf Beta, Bmp2, Hif1A, Pgr*	*Nfat5, Bmpr1b, Bmpr1a, Gper1, Cav1*

4.3.3 Analysis of synovium-derived cell populations and markers

Similar to the ligament cell populations, synovium-derived cell populations were analysed via scRNA-seq using the same cell isolation protocol (Section 4.2.2), library creation and sequencing method (Section 4.2.4), and analysis method (Section 4.2.5).

4.3.3.1 Quality control of synovial-derived library reads

Synovium-derived cells post-sequencing had a final output of 6,228 cells with 99,451 reads per cell and a median of 1,624 genes per cell which was a lower cell retention than the 10,000 cells expected but enough for further analysis. Overall, t-SNE projection showed several aggregations of synovial cells and the absolute number of UMI counts ranged from 2,000 to 10,000 counts per cell (Figure 4.13A), slightly higher than the UMI counts for the ligament-derived cells (Figure 4.4). Sequencing saturation and median genes per cell both show an increase and plateau as the mean reads per cell increases (Figure 4.13B) which suggested high fraction library complexity and confirms successful library creation.

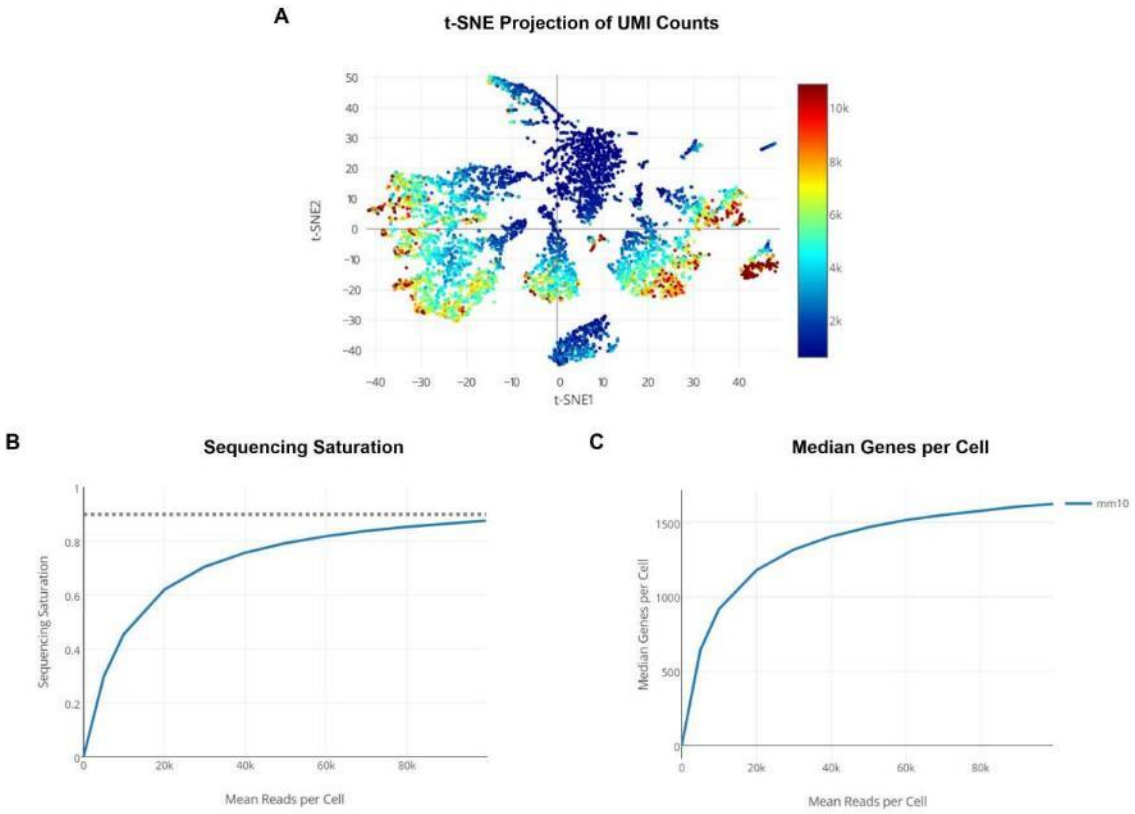

Figure 4.13 Quality control post-sequencing of the synovial-derived cells. (A) Unguided t-distributed stochastic neighbour embedding (t-SNE) projection of unique molecular identifiers (UMI) counts for each synovial-derived cell showed a range from 2000 to 10,000 counts. (B) High sequencing saturation was confirmed and increased with the number of mean reads per cell. (C) Median genes per cell also increased as mean reads per cell increased. This confirmed successful library creation and high library complexity.

4.3.3.2 Identification of synovial cell types and subpopulations

Seurat downstream analysis of synovial-derived cells filtered out low quality reads including low unique features and high mitochondrial genes (see Section 4.2.5). This filtering resulted in a remaining 3,229 synovial cells which were categorised into 11 unique cell clusters using modularity optimisation techniques and visualised using UMAP (Figure 4.14A).

The 11 clusters were classified based on the presence of certain cell markers (see Section 4.2.5). Cell identification markers showed 4 distinct cell types (Figure 4.14A). These consisted of four fibroblast clusters (based on *Col1a2* and *Col3a1* expression), five immune cell clusters (based on *Ptprc* and *Cd14* expression, one endothelial cell cluster (based on *Pecam1* expression) and one RB cell cluster (based on *Hba-a1* expression) (Figure 4.14B). Average marker expression and cell percentage expression can be seen in Figure 4.14C.

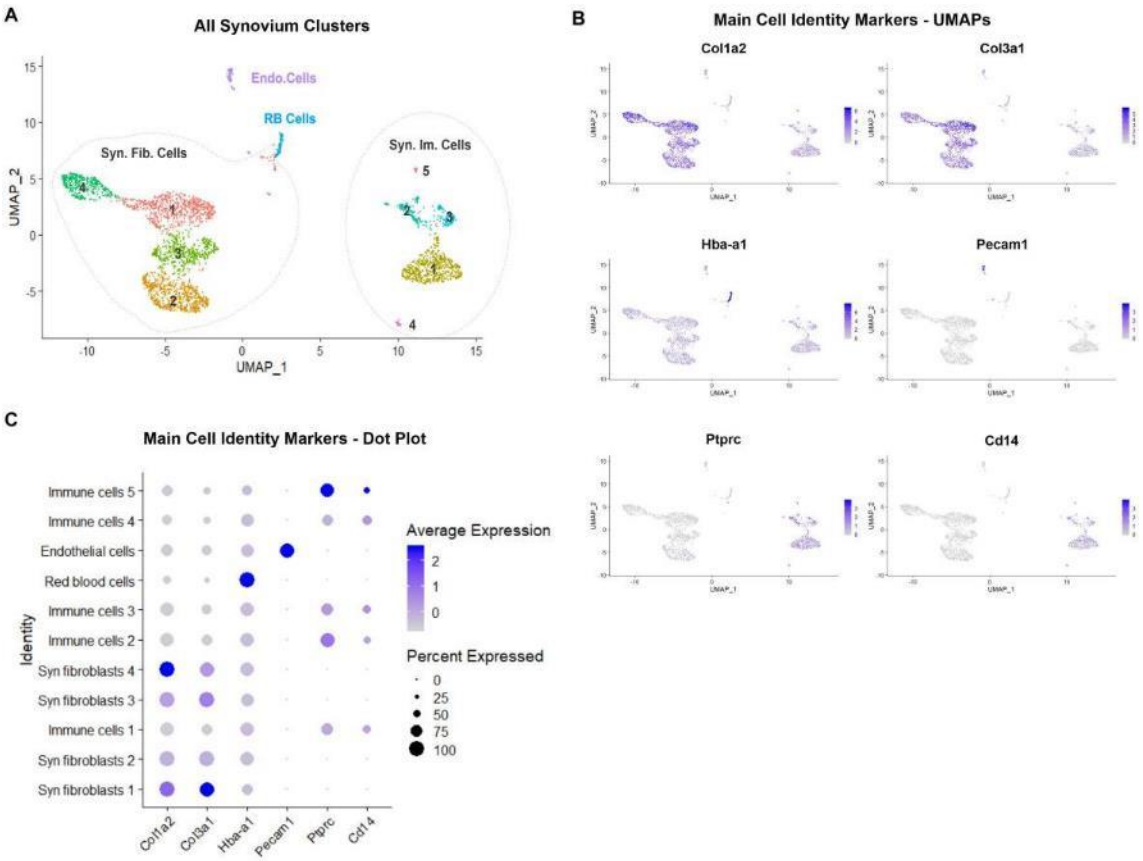

Figure 4.14 Overview of synovium-derived cell types. (A) Uniform manifold approximation and projection (UMAP) of all synovial cell clusters colored, numbered and labelled by cell type. (B) Major known cell type markers were visualised with feature plots to classify clusters and included Col1a2 and Col3a1 for fibroblasts, Hba-a1 for red blood cells, Pecam1 for endothelial cells, and Ptprc (Cd45) and Cd14 for immune cells. (C) Dotplot of the major cell identity markers quantified expression of these identification markers in each synovial cell cluster.

The top three markers of each cluster based on differential expression analysis are summarised in Figure 4.15. Top markers for synovial fibroblast cluster 1 (S.F1) included fibroblast markers *Steap4*, *Col3a1* and *Gsn* (Figure 4.15A). These markers were similarly expressed in ligament fibroblasts including *Steap4* in L.F1 (Figure 4.8). Synovial fibroblast cluster 2 (S.F2) markers consisted of phospholipase A1 (*Pla1a*), epidermal growth factor-containing fibulin-like ECM protein 1 (*Efemp1*) and annexin A3 (*Anxa3*) (Figure 4.15A). Markers for synovial fibroblast cluster 3 (S.F3) were ECM protein 1 (*Ecm1*), annexin A8 (*Anxa8*) and synovial fibroblast marker *Cd34* (Figure 4.15A). Synovial fibroblast cluster 4 (S.F4) markers included angiopoietin-related protein 7 (*Angptl7*), keratocan (*Kera*) and coiled-coil domain-containing protein 3 (*Ccdc3*) (Figure 4.15A). All the S.F4 markers were cluster-specific and were also present in the ligament (L.F3 cluster, Figure 4.10). Overall, many of the synovial-derived fibroblast markers were also

expressed in the ligament-derived fibroblasts, indicating similar transcriptional similarities in the fibroblasts of the two tissues. Fibroblast clusters will be explored in more detail in Section 4.3.3.3.

The five synovial immune clusters had markers associated to macrophages. Synovial immune cluster 1 top differentially expressed markers included macrophage associated markers such as platelet factor 4 (*Pf4*, encoding CXCL4), coagulation factor XIII A (*F13a1*) and complement C1q subcomponent subunit A (*C1qa*) [238] (Figure 4.15C). All the top differentially expressed immune cluster 1 markers overlapped with immune cluster 4 (Figure 4.15C), suggesting similar transcriptional profiles. Immune cluster 2 markers included napsin-A (*Napsa*) a dendritic cell marker [238], and lesser known markers such as phospholipase B domain containing 1 (*Plbd1*) and class II histocompatibility antigen M beta 1 chain (*H2-DMb1*) (Figure 4.15C). The top differentially expressed markers of immune cluster 2 were also expressed in immune cluster 3, indicating similar transcriptional profiles (Figure 4.15C). Immune cluster 3 top differentially expressed markers included inflammatory and macrophage associated markers such as regulator of G-protein signalling 1 (*Rgs1*) [286] and chitinase-like protein 3 (*Chil3*) [287] and lesser known markers such as signal-regulatory protein beta 1C (*Sirpb1c*) (Figure 4.15C). Immune cluster 4 differentially expressed markers also included inflammatory and macrophage associated markers such as v-set and immunoglobulin domain containing 4 (*Vsig4*) [288] and oxidised low-density lipoprotein receptor 1 (*Olr1*, encoding LOX-1) [289] as well as leukocyte-associated immunoglobulin-like receptor 1 (*Lair1*, encoding CD305) [290] (Figure 4.15C). Immune cluster 5 top differentially expressed markers also consisted of inflammatory and macrophage associated markers such as aconitate decarboxylase 1 (*Acod1*) [291] and resistin-like gamma (*Retnlg*) [292] and also a lesser known marker *AC110211.1* (Figure 4.15C). Overall, overlap between the top differentially expressed markers from immune cluster 1 and 4 and immune cluster 2 and 3 indicate transcriptional similarities between those clusters.

The two remaining synovial cell clusters were the RB cell cluster and the endothelial cell cluster. The top three differentially expressed markers for the RB cluster consisted of delta-aminolevulinate synthase 2 (*Alas2*), alpha-synuclein (*Snca*) and solute carrier family 4 member 1 (*Slc4a1*) (Figure 4.15B). The top three differentially expressed markers for the endothelial clusters were vascular endothelial cadherin (*Cdh5*, encoding CD144), kinase insert domain receptor (*Kdr*, encoding VEGFR2) and *Pecam1*, the previously mentioned endothelial marker (Figure 4.15B). Synovial RB and endothelial markers showed high cluster-specificity (Figure 4.15B) suggesting distinct cell populations.

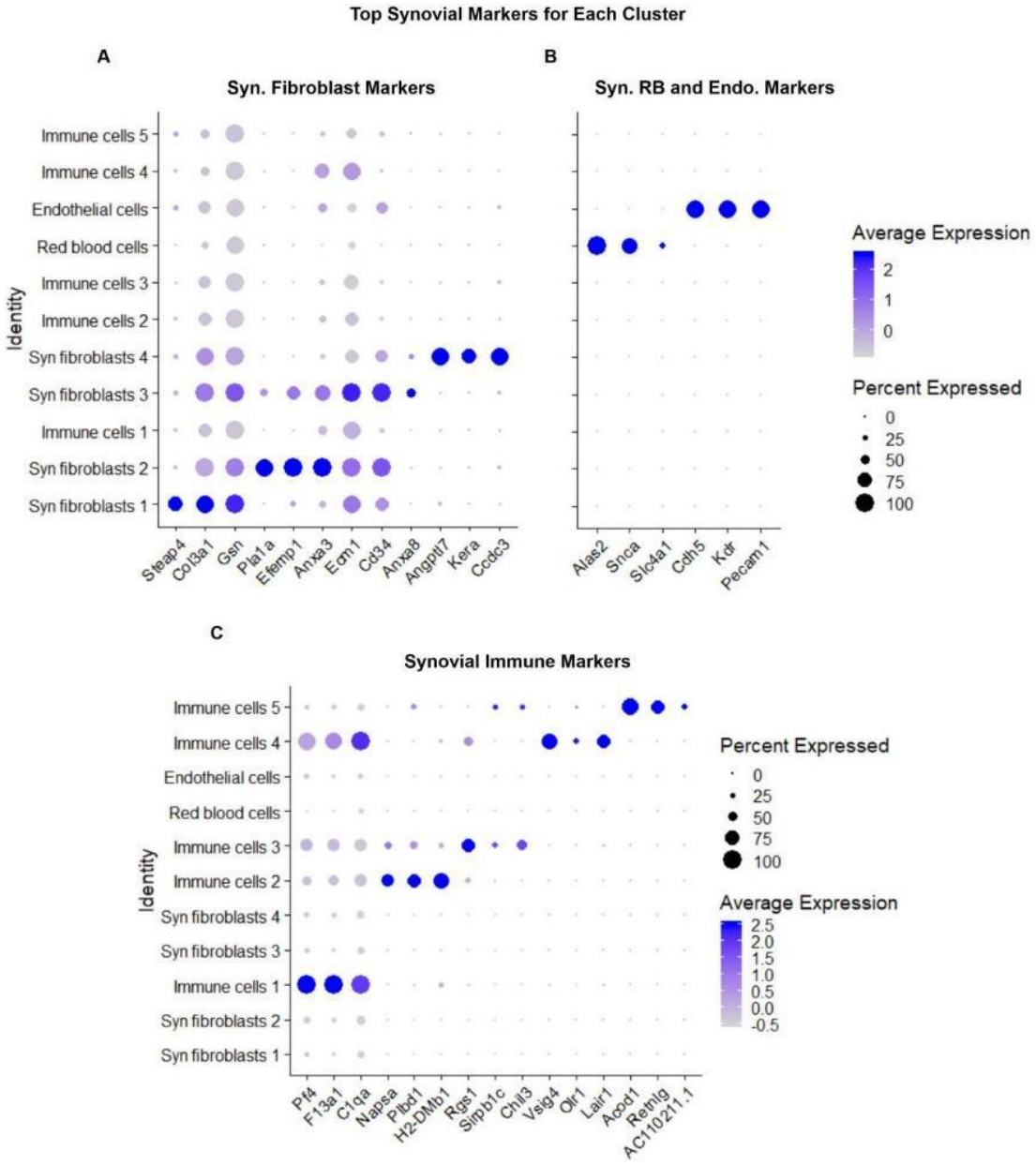

Figure 4.15 Dot plot of the top three differentially expressed markers in each synovial cell cluster. (A) Dot plot of the top three differentially expressed markers in the synovial fibroblast clusters showed overlap in expression between the clusters. (B) Dot plot of the top three differentially expressed markers from the synovial red blood and endothelial cell clusters were cluster specific. (C) Dot plot of the top three differentially expressed markers in the synovial immune cell clusters showed overlap in expression between immune cluster 1 and 4 and immune cluster 2 and 3. Overlap in expression indicates similar transcriptional profiles between the clusters.

4.3.3.3 Analysis of synovial fibroblast markers

Synovial fibroblast subgroups were selected (Figure 4.16A) based on the high expression of *Col1a2* and *Col3a1* (Figure 4.14). The four identified synovial fibroblast clusters were labelled S.F1 (730 cells), S.F2 (587 cells), S.F3 (478 cells) and S.F4 (354 cells) respective of cluster size

(Figure 4.16B). Differential expression analysis between the synovial fibroblast clusters and other cell-type clusters revealed synovial fibroblast specific markers. A heatmap of the top 20 differentially expressed fibroblast markers from murine synovium samples confirmed specificity to the fibroblast clusters and high expression (Figure 4.16C). Notable differences were only present in S.F4 which had low or negative expression of *Gsn, Fstl1, C3, Dpt* and *C1s1* which could suggest a divergence of this cluster (Figure 4.16C).

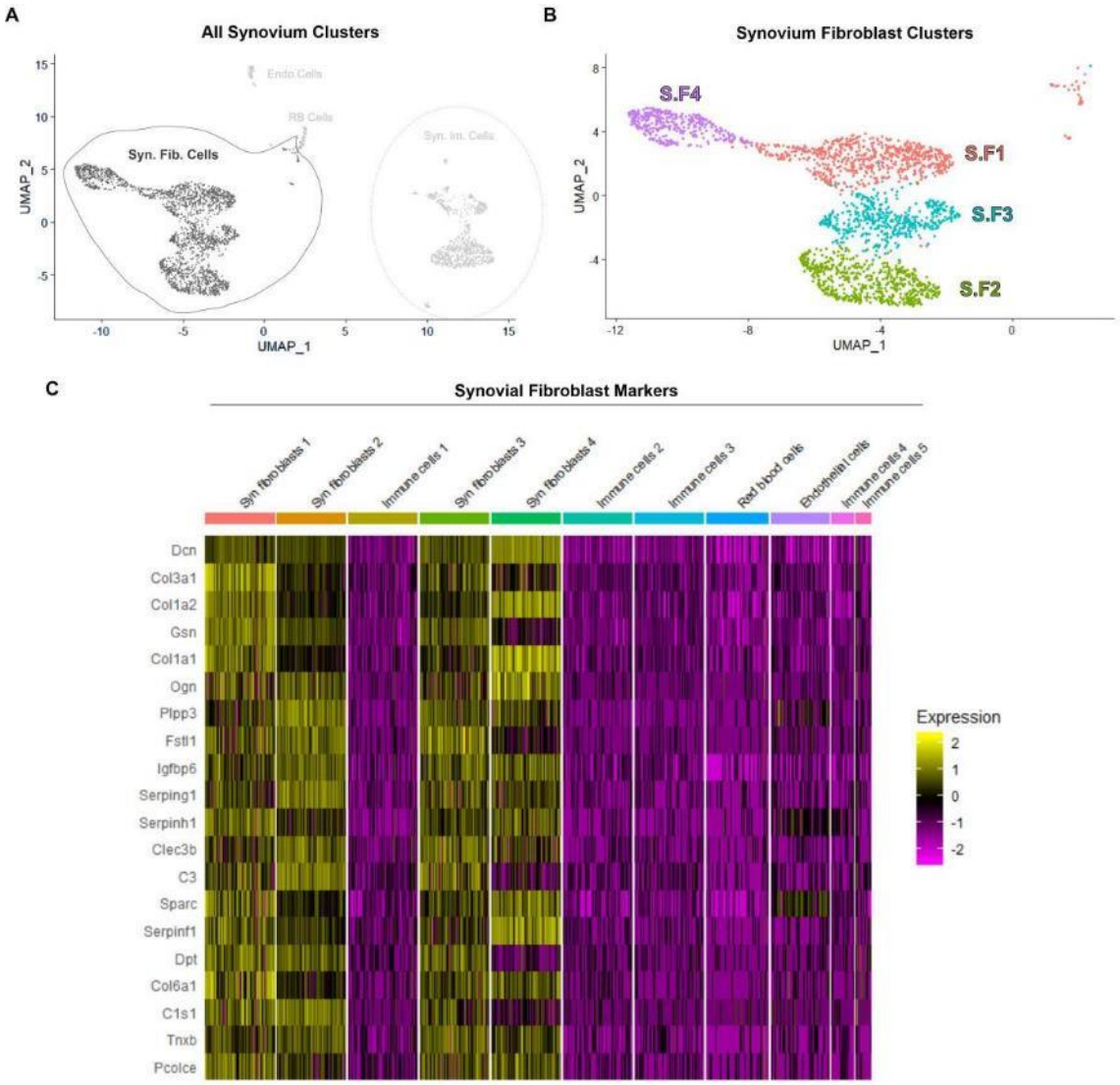

Figure 4.16 Synovial fibroblasts subgroups and the top differentially expressed fibroblast markers. (A) Synovial fibroblast cells were identified based on Col1a2 and Col3a1 expression. (B) Seurat downstream analysis found four distinct synovial fibroblast clusters labelled S.F1 to S.F4. (C) Differential expression analysis between the synovial fibroblast clusters and all other synovial cell types determined the following top 20 synovial fibroblast markers: Dcn, Col3a1, Col1a2, Gsn, Col1a1, Ogn, Plpp3, Fstl1, Igfbp6, Serping1, Serpinh1, Clec3b, C3, Sparc, Serpinf1, Dpt, Col6a1, C1s1, Tnxb, Pcolce. The heatmap confirmed specificity of these markers to the fibroblast clusters.

4.3.3.4 Synovial fibroblast 1 (S.F1) subpopulation

Differential expression analysis of the S.F1 cluster (730 cells) found markers such as growth differentiation factor 10 (*Gdf10*), BMP endothelial regulator (*Bmper*), Sparc-like protein 1 (*Sparcl1*), matrix metalloproteinase 3 (*Mmp3*), embigin precursor (*Emb*) and metalloreductase STEAP family member 4 (*Steap4*) (Figure 4.17B). *Steap4* was previously noted as a L.F1 marker (Figure 4.8). A heatmap of the top 20 differentially expressed S.F1 markers demonstrated specificity to the S.F1 cluster, though a few markers (*Cxcl14* and *Lum*) were also expressed in S.F4 (Figure 4.17C).

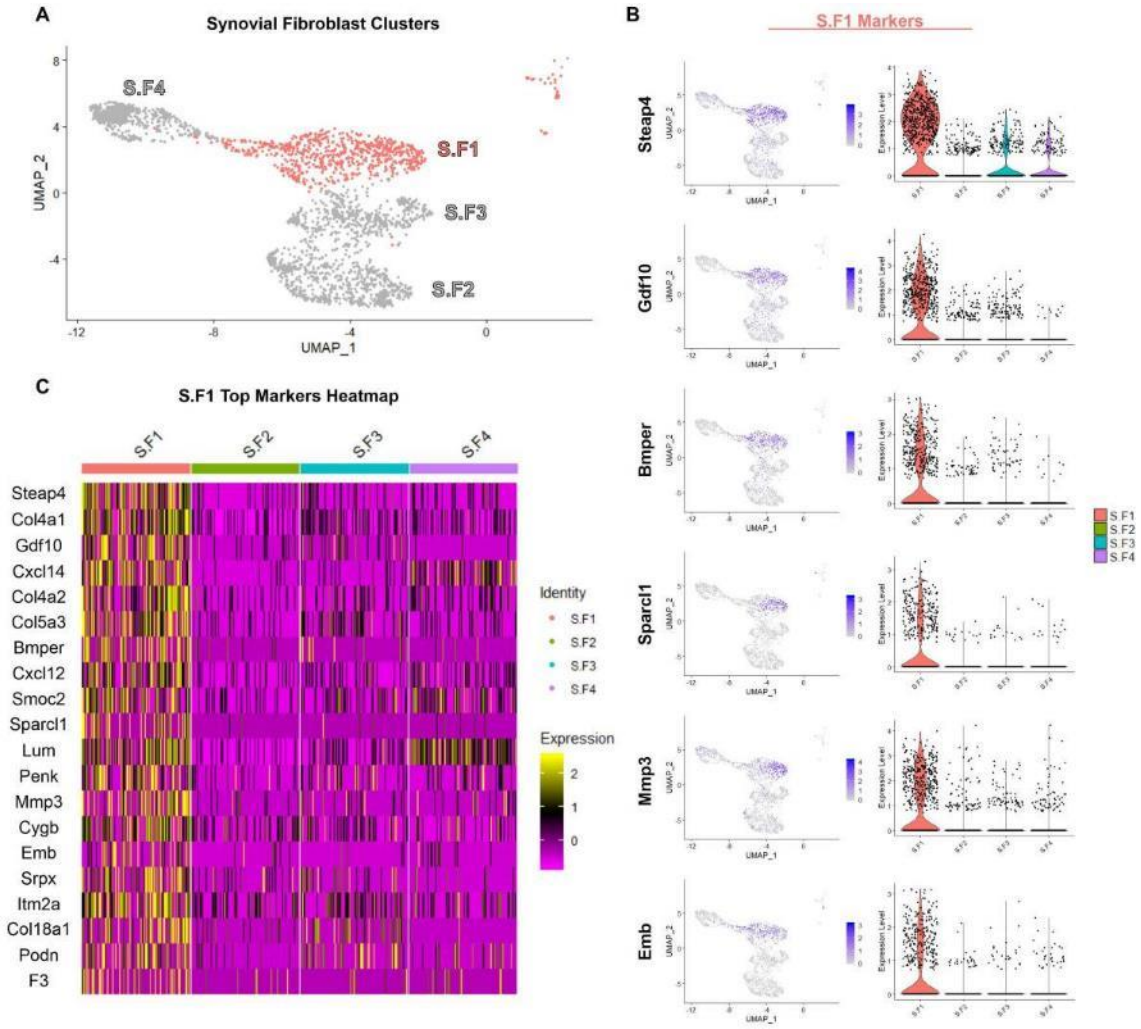

Figure 4.17 The top differentially expressed markers of the synovial fibroblast 1 (S.F1) cluster. (A) Uniform manifold approximation and projection (UMAP) of S.F1 relative to the other fibroblast clusters. (B) Feature and violin plot showing expression of the top differentially expressed S.F1 markers which included Steap4, Gdf10, Bmper, Sparcl1, Mmp3, and Emb. (C) A heatmap of the top 20 differentially expressed S.F1 markers showed high expression and specificity for S.F1 and included Steap4, Col4a1, Gdf10, Cxcl14, Col4a2, Col5a3, Bmper, Cxcl12, Smoc2, Sparcl1, Lum, Penk, Mmp3, Cygb, Emb, Srpx, Itm2a, Col18a1, Podn and F3.

4.3.3.5 Synovial fibroblast 2 (S.F2) subpopulation

S.F2 cluster (587 cells) differentially expressed markers (Figure 4.18A) included suprabasin (*Sbsn*), placenta-specific protein 8 (*Plac8*), brain acid soluble protein 1 (*Basp1*), electrogenic sodium bicarbonate cotransporter 1 (*Slc4a4*, encoding NBCe1), carbohydrate sulfotransferase 1 (*Chst1*), and aldehyde dehydrogenase 1 family member A3 (*Aldh1a3*) (Figure 4.18B). A heatmap of the top 20 differentially expressed S.F2 markers demonstrated specificity of markers to the S.F2 cluster, though some markers such as *Efemp1*, *Dpp4*, *Smpd3* and *Emilin2* were also expressed in S.F3 (Figure 4.18C).

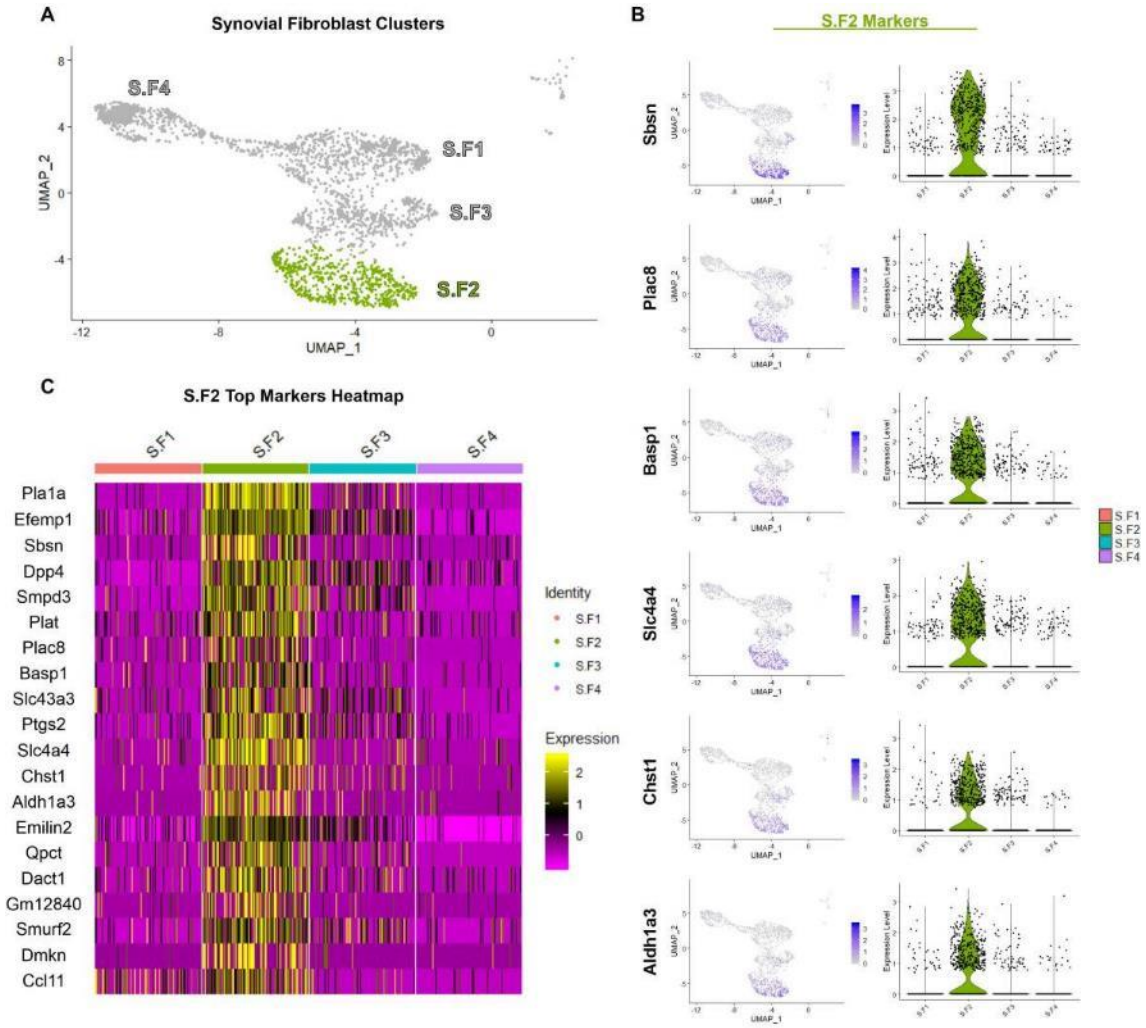

Figure 4.18 The top differentially expressed markers of the synovial fibroblast 2 (S.F2) cluster. (A) Uniform manifold approximation and projection (UMAP) of S.F2 cells relative to the other fibroblast clusters. (B) Feature and violin plots of the top differentially expressed S.F2 markers which included Sbsn, Plac8, Basp1, Slc4a4, Chst1, and Aldh1a3. (C) A heatmap of the top 20 differentially expressed markers included Pla1a, Efemp1, Sbsn, Dpp4, Smpd3, Plat, Plac8, Basp1, Slc43a3, Ptgs2, Slc4a4, Chst1, Aldh1a3, Emilin2, Qpct, Dact1, Gm12840, Smurf2, Dmkn and Ccl11. Markers showed specificity for S.F2 with some overlap with S.F3 (Efemp1, Dpp4, Smpd3).

4.3.3.6 Synovial fibroblast 3 (S.F3) subpopulation

The top differentially expressed markers for the S.F3 cluster (478 cells) included annexin A8 (*Anxa8*), calcitonin receptor-like receptor (*Calcrl*), stathmin 4 (*Stmn4*), hyaluronan synthase 2 (*Has2*), t-box transcription factor 5 (*Tbx5*) and ankyrin repeat domain-containing protein 29 (*Ankrd29*) (Figure 4.19B). Moreover, heatmap of the top 20 differentially expressed S.F3 markers showed little specificity to S.F3 and repeated overlap with the S.F2 cluster (Figure 4.19C), suggesting a similar transcriptional profile between the two clusters.

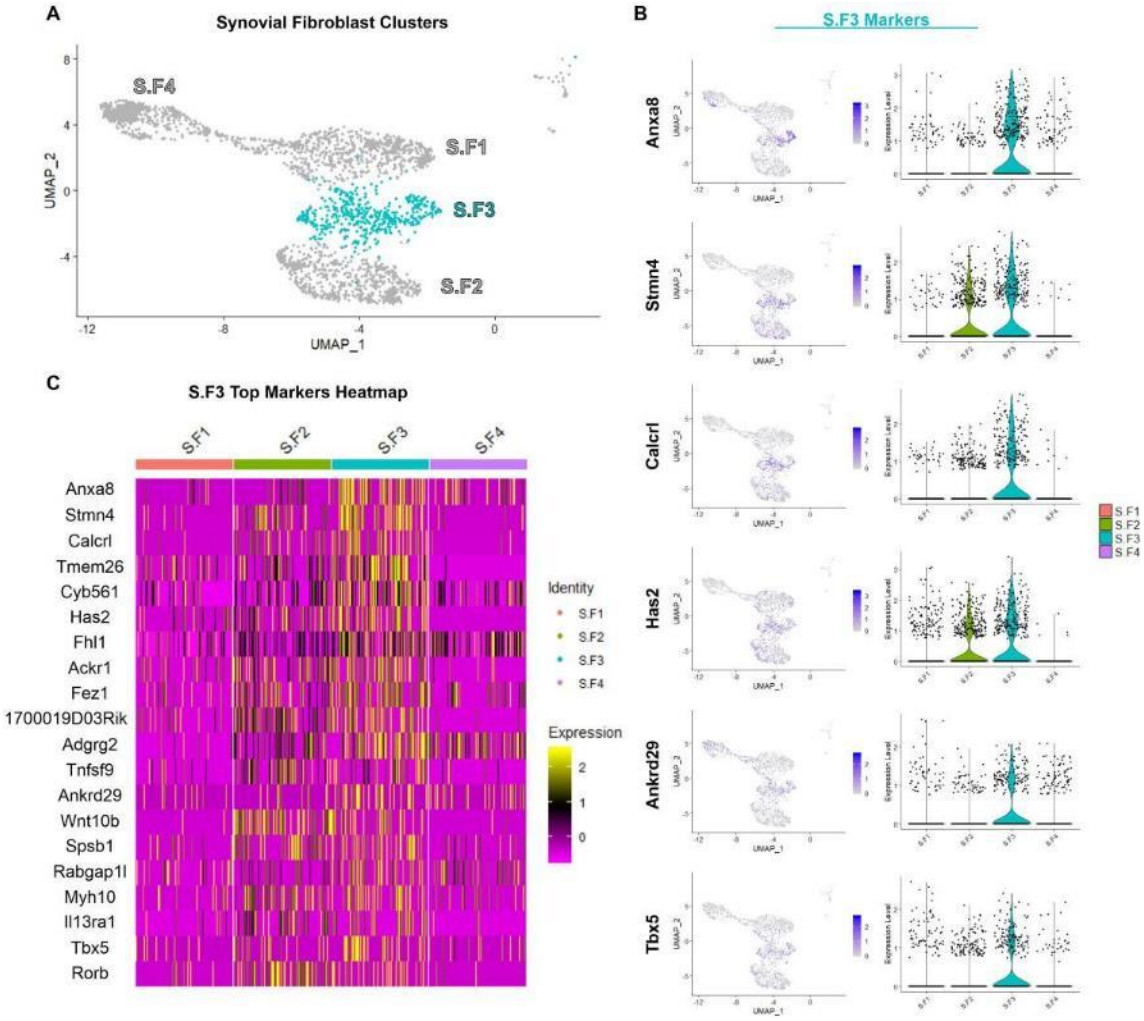

Figure 4.19 The top differentially expressed markers of the synovial fibroblast 3 (S.F3) cluster. (A) Uniform manifold approximation and projection (UMAP) of the S.F3 cluster relative to other synovial fibroblast clusters. (B) Feature and violin plots of the top differentially expressed S.F3 markers included Anxa8, Stmn4, Calcrl, Has2, Ankrd29, and Tbx5. (C) A heatmap of the top 20 differentially expressed markers included: Anxa8, Stmn4, Calcrl, Tmem26, Cyb561, Has2, Fhl1, Ackr1, Fez1, 1700019D03Rik, Adgrg2, Tnfsf9, Ankrd29, Wnt10b, Spsb1, Rabgap1l, Myh10, Il13ra1, Tbx5 and Rorb. Heatmap showed that the top differentially expressed S.F3 markers were also expressed in the S.F2 cluster, suggesting similar transcriptional profiles.

4.3.3.7 Synovial fibroblast 4 (S.F4) subpopulation

The top differentially expressed markers for the S.F4 cluster (354 cells) included cartilage intermedia layer protein 2 (*Cilp2*), collagen type X1 alpha 1 (*Col11a1*), calcium-activated potassium channel subunit (*Kcnma1*), coiled-coil domain-containing 3 (*Ccdc3*), fin bud initiation factor homolog (*Fibin*), and *Kera* (Figure 4.20B). *Kera* marker expression was also present in the L.F3 cluster (Figure 4.10B). Other tendon-associated markers were also present in the S.F4 heatmap including *Scx*, *Fmod* and *Tnmd* (Figure 4.20C). A heatmap further showed high specificity of the markers to the S.F4 cluster (Figure 4.20C).

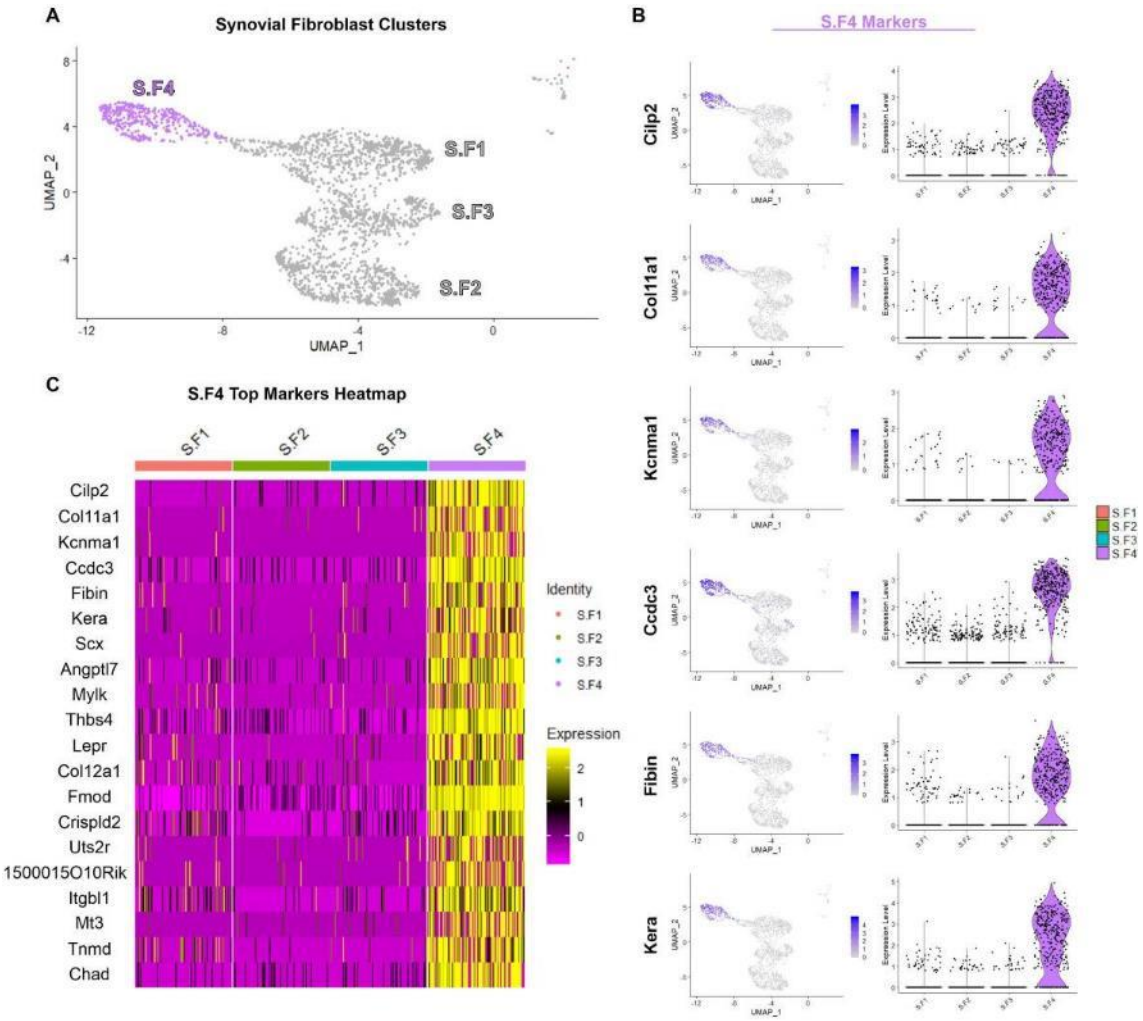

Figure 4.20 The top differentially expressed markers of the synovial fibroblast 4 (S.F4) cluster. (A) Uniform manifold approximation and projection (UMAP) of the S.F4 cluster relative to the other synovial fibroblast clusters (B) Feature and violin plots of the top differentially expressed S.F4 markers included Cilp2, Col11a1, Kcnma1, Ccdc3, Fibin, and Kera. (C) A heatmap of the top 20 differentially expressed S.F4 markers included Cilp2, Col11a1, Kcnma1, Ccdc3, Fibin, Kera, Scx, Angptl7, Mylk, Thbs4, Lepr, Col12a1, Fmod, Crispld2, Uts2r, 1500015O10Rik, Itgbl1, Mt3, Tnmd, and Chad. Heatmap showed that marker expression was specific to S.F4.

4.3.3.8 Enriched canonical pathways and predicted upstream regulators

The top 20 predicted enriched canonical pathways according to IPA software analysis revealed similar signalling pathways between the synovial fibroblast clusters as can be seen in Table 4.4. Cardiac hypertrophy, colorectal cancer metastasis, GP6 and IL-8 signalling pathways received the highest predicted activation scores in all clusters (Table 4.4). Signalling pathways with predicted inactivation included PTEN signalling, endocannabinoid cancer inhibition and PPARα/RXRα activation pathways (Table 4.4). Canonical pathway analysis showed similar enriched pathways in the synovial fibroblast clusters.

Table 4.4 Predicted enriched canonical pathways for each synovial fibroblast cluster.The respective activation z-score for each canonical pathway was graded color scale where red is positive and blue is negative. Canonical pathway analysis was completed with Ingenuity Pathway Analysis (IPA) software.

Top 20 Enriched Canonical Pathways	Activation z-score			
	S.F1	S.F2	S.F3	S.F4
Cardiac Hypertrophy Signalling (Enhanced)	3.051	5	3.051	1.807
Colorectal Cancer Metastasis Signalling	3.464	4.359	2.449	1.414
GP6 Signalling Pathway	3.9	2.111	2.333	3
IL-8 Signalling	2.333	4	3	0.707
Glioblastoma Multiforme Signalling	2.646	3.051	1.342	1.414
STAT3 Pathway	2.333	2.333	2.646	1
CXCR4 Signalling	2.236	3	2	1
Cardiac Hypertrophy Signalling	1.633	3.207	2.236	1.134
ILK Signalling	1.633	3.411	2.333	0.333
PTEN Signalling	-2.236	-2.449	-1.633	-1.342
Cholecystokinin/Gastrin-mediated Signalling	2	3.317	2.236	N/A
Endocannabinoid Cancer Inhibition Pathway	-2	-2.121	-0.447	-2.646
NF-κB Signalling	2.121	1.732	2.333	1
Role of NFAT in Cardiac Hypertrophy	1.342	1.897	2	1.89
Acute Phase Response Signalling	2.333	3	N/A	-1.414
Thrombin Signalling	N/A	3.464	2.236	1
Adrenomedullin signalling pathway	1.342	1.508	2.236	1.414
IL-6 Signalling	2.828	3.162	N/A	-0.378
Osteoarthritis Pathway	1.265	2.683	1.265	1.155
PPARα/RXRα Activation	-1.897	-2.333	-1.414	-0.707

Upstream regulators predicted by IPA software analysis also sound similar upstream regulators in the synovial fibroblast clusters (Table 4.5). The top five upstream regulators all overlapped with other clusters except for *Mycn* which was a top activated and cluster specific upstream regulator of S.F2 (Table 4.5). Similar to the ligament fibroblasts, synovial fibroblast clusters had similar upstream regulators that overlapped between clusters. Furthermore, cluster specific upstream regulators were predicted by IPA software and were ranked based on the highest activation score.

Table 4.5. Predicted activated upstream regulators in the synovial fibroblast subpopulations. The total number of predicted activated upstream regulators varied between clusters. The top five predicted activated upstream regulators based on activation score showed similar activated regulators in all synovial fibroblast clusters. The top five cluster specific activated upstream regulators for each synovial fibroblast cluster was determined based on activation score.

	Predicted Activated Upstream Regulators		
Cluster	**Total #**	**Top 5**	**Top 5 Cluster Specific**
S.F1	597	*Tgfb1, Ctnnb1, Tp53, Xbp1, Edn1*	*Cpxm1, Nr5a2, H2afb3, Il11, Skil*
S.F2	609	***Mycn**, Il1b, Vegf, Pdgf bb, Nfkb*	***Mycn**, Rps15, Tbk1, Crem, Tlr7*
S.F3	294	*Sp1, Vegf, Egf, Tp53, Ctnnb1*	*Lhx1, Ascl1, Srebf2, Nkx2-1, Dcn*
S.F4	308	*Tgfb1, Wnt3a, Sp1, Htt, Tgf Beta*	*Hoxd3, Otx2, Wls, Tmpo, Mdm2*

4.3.4 Confirmation of Aggrecan (ACAN)-expressing ligament cell subpopulation

ACAN expression was analysed using an *Acan*-Cre-tdTomato transgenic murine model, which allows for indirect monitoring of *Acan* transcriptional activity using fluorescently labelled induced ACAN expression with a tdTomato reporter [266]. Fluorescent images of the *Acan*-Cre-tdTomato medial tibial cartilage, a positive control, demonstrated the expected ACAN tdTomato expression in the cartilage chondrocytes and surrounding niches (Figure 4.21). These findings confirm *Acan*-Cre-tdTomato as a working ACAN expression reporter model.

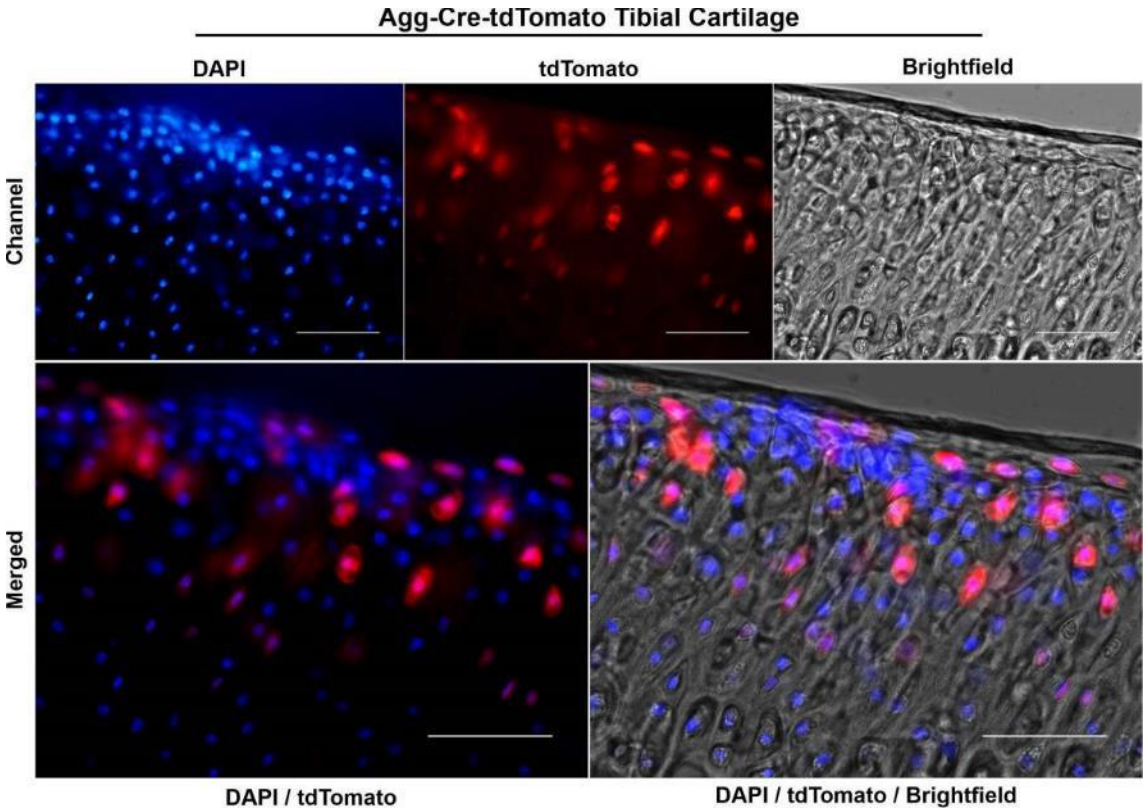

Figure 4.21 Fluorescent images of the murine Aggrecan (Acan)-Cre-tdTomato medial tibial cartilage. Fluorescence showed ACAN expression in the articular cartilage chondrocytes and the surrounding pericellular matrix. Fluorescent images show chondrocyte nuclei (DAPI) (blue), ACAN expression from an induced Acan-Cre enhancer with a tdTomato reporter (tdTomato) (red), brightfield and merged images. Scale bar is 50 µm.

ACAN expression was then analysed in murine knee ligaments (n=4) using the established *Acan*-Cre-tdTomato reporter model. ACAN expression was found in the PCL in specific ligament cells in the midsection of the ligament (Figure 4.22). These findings would suggest a unique ligament cell subpopulation identified with an ACAN marker, confirming the results from the scRNA-seq analysis of a cartilage-like *Acan*-L.F5 subpopulation (Figure 4.12).

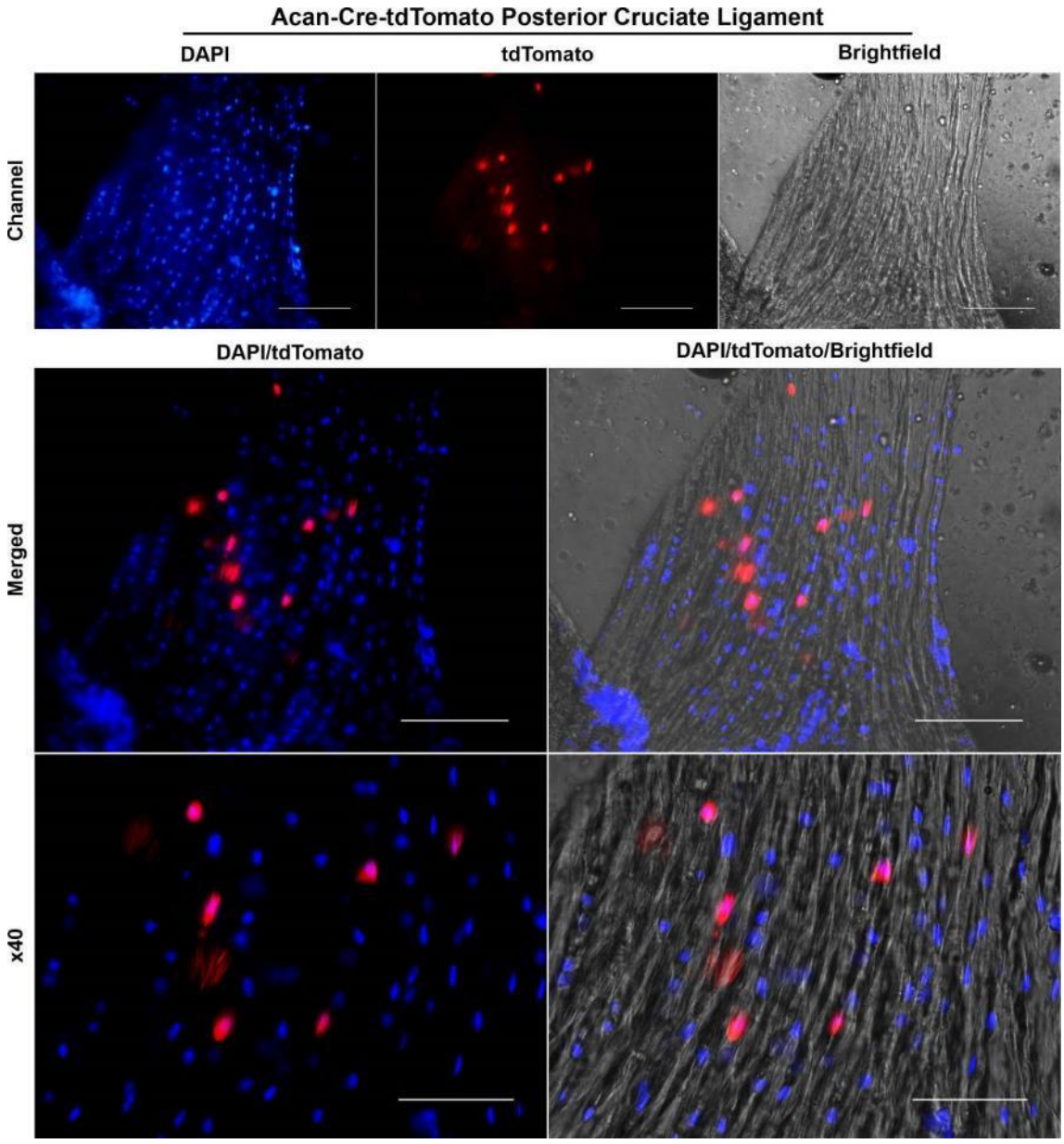

Figure 4.22 Fluorescent images of Aggrecan (Acan)-Cre-tdTomato posterior cruciate ligament. Fluorescence reveals ACAN expression in certain subpopulations of ligament cells in the mid-ligament region. Fluorescence shows all ligament nuclei staining (DAPI) (blue), ACAN expression from an induced Acan-Cre enhancer with a tdTomato reporter (tdTomato) (red), and brightfield and merged images. Scale bar is 100 µm for the channel and merged images, and 50 µm for x40 images.

4.3.5 Comparison of ligament and synovial fibroblasts

Ligament and synovial fibroblast datasets were integrated and compared using the SCTransform Seurat integration workflow [253]. Integration of the two datasets was confirmed in Figure 4.23A. Side by side comparison of the datasets revealed similar UMAP approximation between the L.F1 and S.F1 cluster, as well as between the L.F2, L.F4, S.F2 and S.F3 clusters, and between the L.F3, L.F5 and S.F4 clusters (Figure 4.23B). UMAP approximation indicate similar transcriptional profiles between these clusters. This confirms our past findings of similar markers between ligament and synovial fibroblast subpopulations (Figure 4.7 and Figure 4.16).

Differential expression analysis between ligament fibroblasts and synovial fibroblasts revealed potential tissue specific fibroblast markers. The top five differentially expressed markers upregulated in the ligament fibroblasts included *Cilp2*, *Ccdc3* and *Thbs4*, however these markers were also upregulated in the synovial S.F4 cluster (Figure 4.23C) indicating that these markers are not tissue specific. Ligament fibroblast markers cytokine-like 1 (*Cytl1*) and osteopontin (*Spp1*) were upregulated and downregulated in the L.F5 cluster only and were not expressed in any of the synovial fibroblast clusters, suggesting potential ligament subpopulation specific fibroblast markers.

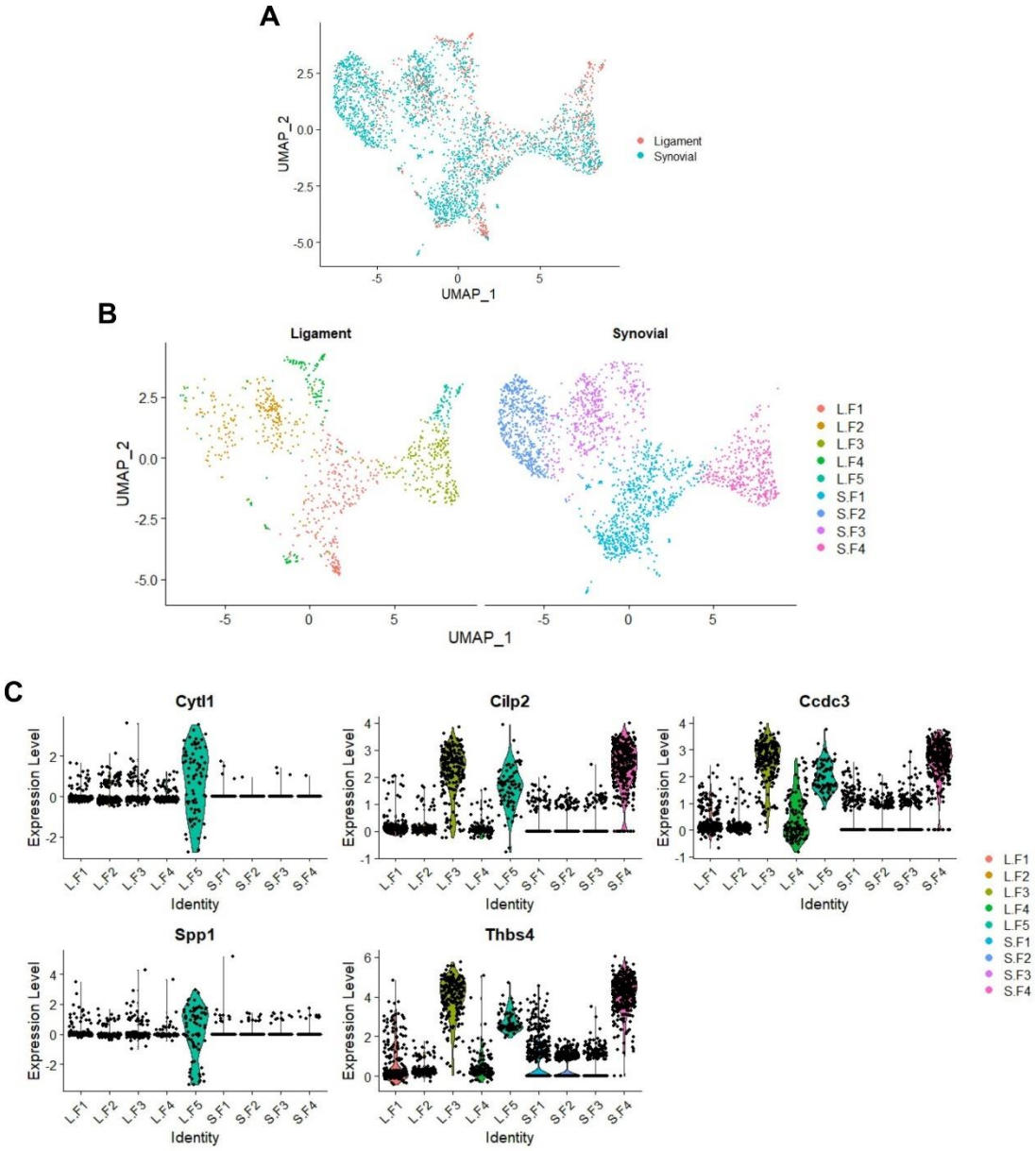

Figure 4.23 Integrated ligament and synovial fibroblasts and differential expression analysis. (A) Uniform manifold approximation and projection (UMAP) of the integrated ligament (red) and synovial (green) fibroblast dataset. (B) UMAP of the integrated ligament and synovial datasets split by tissue type and color coded by cluster identity (L.F1-5 and S.F1-4). (C) Differential expression analysis of the top five markers upregulated in the ligament fibroblast dataset included Cytl1, Cilp2, Ccdc3, Spp1 and Thbs4. Violin plot of these markers showed that Cytl1 and Spp1 were mainly expressed in the L.F5 subpopulation but not in the synovial fibroblasts.

4.3.6 Summary of results

Summary of ligament and synovial cell populations and fibroblast subpopulations can be seen in Table 4.6. Ligament-derived cells had nine distinct cell populations from which there were five fibroblast subpopulations (L.F1-5). Synovial-derived cells had four distinct cell populations and had four fibroblast subpopulations (S.F1-4). Fibroblast specific markers and upstream regulators are summarised in Table 4.6, as well as the potential role of each fibroblast subpopulation which are further discussed in Section 4.4.1-2.

Table 4.6 Summary of murine ligament and synovial cell populations and fibroblast subpopulations. Ligament-derived cells consisted of nine cell types with five fibroblast subpopulations (L.F1-5). Synovium-derived cells had four distinct cell types and four fibroblast subpopulations (S.F1-4). The top differentially expressed specific markers, upstream regulators and potential roles of each fibroblast subgroup are summarised.

Tissue	Cell types	Fib. clusters (# cells)	Specific markers	Upstream regulators	Potential role
Ligament	**9 cell types:** Fibroblasts Immune cells Endothelial cells Red blood cells Platelet cells Nerve cells Satellite cells Muscle cells Unidentified cells	L.F1 (258)	*Steap4, Cxcl14, Ggt5, Hmcn2, Sfrp1, Gpc3*	*Mafb, Tcr, Eif4e, Cpxm1, Stat*	Mineralisation-related
		L.F2 (240)	*Pi16, Smpd3, Tmem26, Engase, Aif1l, Il1r2*	*Fgf7, Lhx1, F3, F7, Tlr3*	Inflammatory-related
		L.F3 (219)	*Thbs4, Mylk, Kera, Lepr, Scx, Tnmd*	*Id2, Otx2, Hoxd3, Atf6, Neurog1*	Tendon-related
		L.F4 (135)	*Itgb3, Olfml2a, Islr2, Ildr2, Hmcn1, Ociad2*	*Kmt2d, Ret, Il15, Sox11, Ptpn3*	Sensory-related
		L.F5 (78)	*Lgr6, Egln3, Acan, Meltf, Hapln1, Tnfrsf11b*	*Nfat5, Bmpr1b, Bmpr1a, Gper1, Cav1*	Cartilage-related
Synovium	**4 cell types:** Fibroblasts Immune cells Red blood cells Endothelial cells	S.F1 (730)	*Steap4, Gdf10, Bmper, Sparcl1, Mmp3, Emb*	*Cpxm1, Nr5a2, H2afb3, Il11, Skil*	Regulatory-related
		S.F2 (587)	*Sbsn, Plac8, Basp1, Slc4a4, Chst1, Aldh1a3*	*Mycn, Rps15, Tbk1, Crem, Tlr7*	Neuronal-related
		S.F3 (478)	*Anxa8, Stmn4, Calcrl, Has2, Ankrd29, Tbx5*	*Lhx1, Ascl1, Srebf2, Nkx2-1, Dcn*	Intermediary subpopulation
		S.F4 (354)	*Cilp2, Col11a1, Kcnma1, Ccdc3, Fibin, Kera*	*Hoxd3, Otx2, Wls, Tmpo, Mdm2*	Tendon-related

4.4 Discussion

This study identified cell populations from murine ligament and synovial tissue and analysed fibroblast subpopulations and their transcriptional markers and associated pathways. Ligament-derived cell populations had nine distinct cell types which included fibroblasts with five subpopulations (L.F1-5) (Figure 4.5). The L.F5 subpopulation markers contained *Acan* expression (L.F5) (Figure 4.12) which was confirmed by an *Acan*-Cre-tdTomato transgenic reporter mouse line (Figure 4.22). In the synovial-derived cells, four different cell types were discovered, from which fibroblasts had four subpopulations (S.F1-4) (Figure 4.14). Synovial fibroblast markers had numerous overlaps with the ligament fibroblasts, and comparison of the ligament and synovial fibroblasts confirmed overlap in fibroblast heterogeneity and identified ligament subpopulation specific markers.

4.4.1 Ligament fibroblast subpopulations and potential roles

Ligament fibroblast subpopulations had distinct markers and associated roles. This included a mineralisation-related (L.F1), inflammatory-related (L.F2), tendon-related (L.F3), sensory-related (L.F4) and cartilage-related (L.F5) subpopulations. The associated roles of these subpopulations are based on current literature, but many markers remain unknown particularly within ligament tissue.

The L.F1 cluster was made up of 258 cells which accounted for 28% of all ligament fibroblasts. The top L.F1 differentially expressed markers (Figure 4.8) included markers associated with mineralisation such as *Steap4* [293], *Sfrp1* [294] and *Gpc3* [295]. Some of these markers are also expressed in developing mouse tendons including *Steap4* [296], *Gpc3* [297] and *Cxcl14* [298]. The predicted L.F1-specific upstream regulators comprised of *Mafb, Tcr, Eif4e, Cpxm1* and *Stat*. Of these, *Mafb* encodes a transcriptional factor involved in regulating osteoblast differentiation [299]. L.F1 markers and upstream regulators indicate an important mineralisation and developmental role of this subpopulation.

The L.F2 cluster, which represented 26% of all ligament fibroblasts, had differentially expressed markers (Figure 4.9) suggesting an inflammatory role. Markers associated with inflammatory regulation are *Pi16* (CD364) [300], *Aif1l* [301] and *Il1r2* [302] which is also expressed in developmental tenocytes [303]. From the predicted L.F2-specific upstream regulators, several are involved in immune response and inflammatory pathways, such as *F3* and *F7* [304] as well as

Tlr3 [305]. The presence of these markers and upstream regulators suggest an inflammatory-related role for this fibroblast subpopulation.

Tendon-ligament associated markers were differentially expressed in the L.F3 subpopulation which correspond to 24% of all ligament fibroblasts (Figure 4.10). This included the presence of *Mkx*, *Scx* and *Tnmd* which are established tendon-ligament markers [52, 243]. *Scx*, *Tnmd* and *Mkx* expression was found in two distinct murine Achilles tendon fibroblast subpopulations [236], whereas our results revealed that these markers were concentrated in one ligament fibroblast subpopulation (L.F3). Other tendon associated markers in the L.F3 subpopulation included *Thbs4* [306], *Fmod* [307]; and *Kera* [308]. Predicted L.F3-specific upstream regulators included *Id2*, *Otx2*, *Hoxd3*, *Atf6*, *Neurog1*. *Id2* is a SCX regulator during early development [309]. *Neurog1* and *Otx2* are known neuronal differentiation regulators [310, 311]. L.F3 specific upstream regulators showed tendon and neuronal development regulators, but failed to show further pathways, likely because many of these pathways are still undiscovered. The presence of multiple tendon-associated markers and upstream regulators suggests a more tendon-like role for the L.F3 subpopulation.

The L.F4 cluster comprised of 14% of all ligament fibroblasts. The top six differentially expressed L.F4 markers (Figure 4.11) included *Islr2, Ildr2, Hmcn1, Itgb3, Olfml2a*, and *Ociad2*. From these markers, *Islr2* is expressed in murine neural tissue [312] and *Ildr2* in murine immune cells [313]. *Hmcn1* is found in many tissues but also anchors mechanosensory neurons [314]. Furthermore, predicted L.F4 upstream regulators included *Il15*, an immune regulator [315], and *Ret* and *Sox11*, known neuronal mechanosensor regulators [316, 317]. The presence of immune and neuronal markers (including mechanosensory) could indicate an important sensory role for this L.F4 subpopulation.

The L.F5 subpopulation was the least numerous cluster and consisted of 8% of all ligament fibroblasts. The presence of established cartilage-specific cell markers such as *Acan*, *Sox9* and *Col2a1* in the L.F5 subpopulation (Figure 4.12) indicate a unique cartilage-like role for this cluster. Many of these markers have been previously shown in the transitional fibrocartilaginous region of the ligament-bone insertion site [318]. However, spatial confirmation of an ACAN-expressing subpopulation of cells was found in the mid-ligament region of the PCL in the murine ACAN-Cre-tdTomato reporter line (Figure 4.22). Even though this was the smallest subpopulation, equivalent of 8% of ligament fibroblasts and 4% of all ligament-derived cells across 4 different knee ligaments from 6 pooled knee joints, histological sections revealed 8 adjacent ACAN expressing cells in the PCL (Figure 4.22). These results confirm the powerful

resolution of single-cell sequencing. However, it is possible that specific fibroblasts subpopulations are more common in certain knee ligaments or micro-anatomical sites and warrants further investigation via spatial analysis or single-cell analysis of each individual ligament. Spatial analysis is also important, as our findings confirmed that an *Acan*-subpopulation of fibroblast cells were not only found in the ligament fibrocartilaginous region as previously thought but also in the mid-ligament region of healthy ligaments. ACAN-expressing cells were also previously found in healthy canine ACLs [20] and could be indicative of compressive load occurring in the mid-ligament region.

Though this was the smallest ligament fibroblast cluster, *Acan*-fibroblasts could play an important role in murine ligament homeostasis and disease progression. *Acan, Sox9* and *Col2a1* gene expression was elevated in the overuse tendinopathy model in rats [319]. Similarly ACAN, SOX9, and COL2 protein expression has been described in the ACL mid-ligament region in OA patients [207]. SOX9 and COL2 protein markers were also found in the murine spontaneous and post-traumatic OA ligaments (Chapter 2). This could suggest an important role in OA for this L.F5 subpopulation. Furthermore, L.F5-specific canonical pathway included the FGF pathway and L.F5-specific upstream regulators included two BMP receptors (*Bmpr1b, Bmpr1a*). Both FGF and BMP signalling are involved in chondrogenesis [320]. These findings confirm an important cartilage-like role for the L.F5 subpopulation and indicate potential pathways in ligament OA progression.

4.4.2 Synovial fibroblast subpopulations and potential roles

Synovial fibroblast clusters included a regulatory-related (S.F1), neuronal-related (S.F2) and a tendon-related (S.F4) subpopulation as well as an intermediary subpopulation (S.F3).

In the S.F1 subpopulation, made up of 34% of all synovial fibroblasts, the top differentially expressed markers included *Gdf10, Bmper, Sparcl1, Mmp3, Emb* and *Steap4* (Figure 4.17). From these markers, four are associated with disease progression: *Mmp3* and *Sparcl1* are upregulated in OA synovial fluid [321, 322], *Steap4* is present in rheumatoid arthritis synovium [323] and *Gdf10* is found in OA and rheumatoid arthritis synovial fibroblasts [324]. Furthermore, of the predicted S.F1-specific upstream regulators, *Il11* is an inflammatory cytokine [325]. The relationship of S.F1 markers with disease progression suggests an important regulatory role for this large subpopulation.

S.F2 consisted of 27% of all synovial fibroblasts and its top differentially expressed markers (Figure 4.18) *Basp1* and *Slc4a4* have been linked to neuronal activity [326, 327]. *Basp1* is also associated with rheumatoid arthritis in murine synovial fluid [328]. Furthermore, *Chst1* marker is involved in the immune response [329]. From the S.F2 predicted upstream regulators, *Mycn* regulates neurogenesis [330] and is involved in disease progression including rheumatoid arthritis and OA [331]. Other upstream regulators, *Tbk1* and *Tlr7* regulate the innate immune response and are expressed in the synovium of rheumatoid arthritis patients [332, 333]. S.F2 markers and upstream regulators suggest a potential neuronal and immune activity for the S.F2 subpopulation.

The S.F3 subpopulation consisting of 22% of all synovial fibroblasts, had top differentially expressed markers which largely lacked specificity and were also expressed in the S.F2 cluster (Figure 4.19). From the top differentially expressed S.F3 markers, two are associated with neuronal pathways including *Stmn4* [334] and *Calcrl* [335]. Another marker, *Has2* is expressed in healthy synovium and downregulated in OA and rheumatoid arthritis synovium [336]. *Tbx5*, another S.F3 marker, is upregulated in rheumatoid arthritis synovium [337]. From the predicted S.F3 upstream regulators, several regulate neuronal differentiation including *Lhx1* [338] and *Ascl1* [339]. Other S.F3 specific upstream regulators included *Dcn* a known ligament SLRP marker [2]. S.F3 markers indicate that S.F3 has a role in neuronal activity and disease pathways similar to the S.F1 and S.F2 subpopulations suggesting that S.F3 is an intermediary subpopulation.

The S.F4 subpopulation was the smallest synovial fibroblast cluster comprising 16% of all synovial fibroblast. Its top differentially expressed markers (Figure 4.20) included markers associated with other knee joint tissues, such as *Kera, Scx, Fmod* and *Tnmd* which are tendon-associated markers [308] and *Col11a1* which is found in multiple skeletal tissues including tendon [340]. *Cilp2* is another S.F4 marker usually expressed in the cartilage intermediate layer and in the OA synovial membrane [341].Though these markers are associated with neighbouring tissue, *Fmod* and *Tnmd* are also expressed in healthy synovial fibroblasts [342, 343]. Furthermore, predicted upstream regulators of S.F4 included *Otx2*, a neuronal regulator [311], which was also found in the L.F3 subpopulation. S.F4 markers and upstream regulators indicate a tendon-like role of the S.F4 subpopulation. The presence of cartilage and tendon-associated markers in S.F4 could be due to contamination, however the fact that some of these markers have been found in synovial fibroblasts would suggest otherwise.

4.4.3 Ligament versus synovial fibroblast markers and subpopulations

Fibroblast markers were first analysed separately in both ligament and synovial-derived cells. Ligament fibroblast markers showed many of the known tendon-ligament markers such as *Dcn*, *Col1a2*, *Col3a1*, *Col1a1*, *Col6a1*, *Col6a2* and *Col5a2* (Figure 4.7) which make up the dense ECM structure of the ligament [2]. The top 20 synovial fibroblast markers (Figure 4.16) had numerous overlaps with the top 20 ligament fibroblast markers (65%). Similar markers included *Dcn, Col3a1, Col1a2, Gsn, Col1a1, Fstl1, Igfbp6, Serping1, Clec3b, Serpinf1, Col6a1, Tnxb* and *Pcolce*. These results reinforce that ligament and synovial fibroblast markers are similar in their transcriptional profiles.

Overlap between ligament and synovial fibroblast extended to their subpopulations. From the top 20 differentially expressed S.F1 markers (Figure 4.17), 50% of them were also in the top 20 differentially expressed L.F1 markers (Figure 4.8). From the S.F4 top 20 differentially expressed markers (Figure 4.20), 65% were also highly differentially expressed in the L.F3 cluster (Figure 4.10). Overlap between ligament and synovial fibroblast subpopulations was also apparent in the combined synovial and ligament fibroblast UMAP. UMAP, an indication of transcriptional profile similarity, showed an overlap of regions between L.F1 and S.F1 cluster, between the L.F2, L.F4, S.F2 and S.F3 clusters, and between the L.F3, L.F5 and S.F4 clusters (Figure 4.23B).

Besides similarities between the fibroblasts, comparison analysis of the two tissues revealed differentially expressed ligament subpopulation-specific markers. This included *Cytl1* and *Spp1* which were not expressed in any synovial fibroblast cluster (Figure 4.23C). *Cytl1* is a chondrogenesis marker [344] and *Spp1* is a mineralisation and osteogenic regulator [345], and both were upregulated and downregulated in the L.F5 cartilage-like subpopulation (Figure 4.23C). Hence, these ‘ligament specific markers’ are only specific to a unique subpopulation of ligament fibroblasts and are not whole tissue specific. Whole tissue specific markers could not be identified. This is yet another example of the importance of fibroblast heterogeneity over tissue specificity and highlights the overlap between ligament and synovial fibroblasts. This is also further evidence that L.F5 subpopulation plays a unique role in the ligament, a role not found in the neighbouring synovial fibroblasts.

4.4.4 Current literature

A cellular atlas of knee joint ligaments does not currently exist. However, as previously mentioned, two recent publications identified cell populations in mouse Achilles tendon [236] and

in pooled human tendons [235]. In the murine Achilles tendon, only two tendon fibroblast subpopulations were identified [236], demonstrating less fibroblast heterogeneity when one tendon was sequenced. Murine Achilles tendon fibroblast subpopulation 1 (TF1) had high expression of *Spp1* [236], the previous identified ligament subpopulation specific marker (Figure 4.23C), which is evidence that Spp1 is not ligament tissue specific. Furthermore, *Acan* was also highly expressed in the Achilles TF1 subpopulation, as well as *Scx* and *Mkx* [236]. In our ligament samples, these markers were found in two different subpopulations (L.F5 and L.F3). These could be differences in transcriptional profiles between tendons and ligaments or, more likely, differences in specific tissues (Achilles vs pooled knee ligaments) and their function. This research highlights the importance of mapping individual tissues, allowing for a better understanding of fibroblast heterogeneity and the roles of subpopulations. Future research should focus on mapping individual ligaments and microanatomical sites (enthesis, midbody).

Pooled human tendons (from the knee, ankle, and foot), also revealed high fibroblast heterogeneity similar to our results, including five tendon fibroblast subpopulations [235]. However, this study used cellular indexing of transcriptomes and epitopes by sequencing, also known as CITE-seq analysis [235] which combines scRNA-seq with a panel of surface epitopes which can achieve more detailed cellular identification [346]. In the pooled human tendon samples, a small fibroblast subpopulation also had cartilage-associated markers including *Comp*, *Pcolce2* and *Cilp*, however there was no expression of *Col2a1* which was attributed to the lack of cells from the tendon-bone enthesis [235]. It is possible that *Col2a1* and *Acan*-expressing fibroblasts is a difference between murine and human tendons-ligaments. However, both studies showed a cartilage-like fibroblast subpopulation which could have important disease applications and needs to be properly characterised.

Recent transcriptomics of the human knee synovial cell populations using scRNA-seq found two distinct synovial fibroblast subpopulations with similar markers from those in our murine synovial fibroblasts but distinct clustering (labelled Fibro 1, Fibro 2a-b) [249]. In Fibro 1, genes differentially expressed included *Mmp3*, *Thbs4* and *Cd55* [249]. In our murine synovial fibroblasts these markers were expressed in different clusters, mainly *Mmp3* in S.F1 (Figure 4.17), *Thbs4* in S.F4 (Figure 4.20) and *Cd55* in S.F2 and S.F3 (not shown here). Additionally, *Thy1* (CD90) was a prominent differentially expressed marker in the human synovial Fibro 2 subpopulation [249], however this marker was present in all the murine synovial fibroblasts (not shown here). Differences in these markers between human and murine synovial fibroblasts could highlight important species-specific differences.

A separate scRNA-seq analysis of diseased human knee joint synovial tissue revealed four distinct fibroblast subpopulations (F1-F4), each with specific differentially expressed markers: *Cd34* (F1), *Hla-dra* (F2), *Dkk3* (F3) and *Cd55* (F4) [237]. In our murine synovial fibroblasts, both *Cd34* and *Cd55* were present in the S.F2 and S.F3 clusters (not shown here), *Dkk3* was present in the S.F4 cluster (not shown here), and *Hla-dra* was not present. These two studies [237, 249] on human synovial fibroblasts highlight potential species-specific differences but differences in markers could also be due to different methodologies (cell isolation, sample preparation, single-cell library creation). These findings confirm that cellular heterogeneity in synovial fibroblasts remains poorly understood.

4.4.5 Limitations of the study

This study is limited by several tissue and analytical factors. The first general limitation is the samples and murine tissue used, which only gives a snapshot of one age, strain, and gender of 10-week-old C57BL/6J male mice. Additionally, there were limitations in tissue size and sample preparation. As previously mentioned, the small size of murine tissue could be a cause for potential cross-contamination of our sample, especially considering that the synovial membrane directly borders the collateral ligaments (Figure 4.B-C). Furthermore, pooling ligament and synovial samples together might give rise to more heterogeneity. This finding is particularly true for the ligament fibroblasts which had a greater number of subpopulations compared to the synovial fibroblasts. Different types of knee joint ligaments (extracapsular/intracapsular), which were pooled together, could be host to diverse fibroblast subpopulations. However, sample tissue pooling was necessary in large part to ensure recovery of enough cells for scRNA-seq analysis.

Methodologies for scRNA-seq are still evolving, however sample preparation and downstream analysis are the main determinant factors [247]. Sample preparation has been shown to limit the quality of RNA reads and the method for normalisation during downstream analysis has been shown to dominate pipeline analysis performance [247]. Our sample preparation ensured the highest quality cells, however during cell isolation optimization we could only measure cell viability and not RNA library quality. Cellular bias based on the cell isolation technique is also an important factor to consider with scRNA-seq. This is particularly important with less cellular and matrix-rich tissue such as ligaments, where enzymatic digestion could result in bias towards smaller or more robust cells which are easier to isolate. To account for this, the cell isolation protocol also included mincing of the ligament sample, to allow the release of cells from all areas

of the tissue. However, sequencing results for the ligament-derived cells included an initial 5,574 cells, which were filtered due to low UMI count or mitochondrial genes into the final 2,165 cells which were analysed. It is possible that in this filtering step we are only analysed the most 'robust' cells unaffected by the enzymatic isolation. In addition, enzymatic isolation has also been shown to introduce a transcriptional bias due to the cellular stress-response [347]. Despite these limitations enzymatic digestion has been extensively used for tendon cell isolation for RNA-seq [235, 236, 251, 348, 349]. One possible way to prevent such bias is the use of single-nucleus sequencing, another isolation technique that requires snap freezing tissue, dissection of tissue and a detergent buffer for the release of nuclei [350]. Studies comparing single-cell vs single-nucleus RNA-seq in tumors have found similar cell populations with slight varying proportions of cells [350]. This would suggest that enzymatic digestion is still able to capture nearly all cell types and the high-resolution capacity of single-cell sequencing ensures that all cell types are represented.

In terms of transcriptomics, 10X Genomics single-cell 3' assay also includes some limitations since it only capture polyadenylated transcripts, found in most eukaryotic messenger RNA (mRNA) [351] and some long noncoding RNAs and precursor pri-miRNAs [352] but does not capture the whole transcriptome. While this is a limitation, polyadenylated transcripts are sufficient for the purposes of this study to determine fibroblast subpopulations. RNA stability is another important potential limitation. In this regard, polyadenylated tails in eukaryotic mRNA offer some protection from mRNA decay by acting as stabilisers [353]. However, mRNA decay can still occur and time of processing is particularly important for RNA quality of tendon tissue [354]. For this reason, our protocol aimed to shorten the time necessary for enzymatic digestion and cell isolation. Generally, mRNA most likely to decay first includes mRNA that code for transcriptional factors which have shorter half-lives (< 2h) while protein encoding mRNAs have longer half-lives [355]. This is an important limitation to consider, which could limit the number of transcriptional factors important to properly characterise cluster function and pathway analysis.

Data analysis for differentially expressed markers and for predicted enriched canonical pathway and upstream regulators is also limited based on methodology and software used. Pathway analysis is limited by the IPA software which allocates genes to pathways curated from literature which will only highlight known and studied pathways and upstream regulators. Further research is needed to better understand fibroblast signalling pathways, particularly in the knee joint. Despite these limitations, our findings provide a preliminary atlas of ligament and synovial fibroblast subpopulations and their markers.

4.5 Conclusion

Through scRNA-seq analysis, we identified distinct ligament and synovial-derived cell clusters and categorised ligament and synovial fibroblast subpopulations based on their transcriptional profiles. In the murine ligament, nine distinct cell types were found including five ligament fibroblast subpopulations with distinct markers and associated functions (Figure 4.7). Ligament fibroblast subpopulations included L.F1 with mineralisation-related markers, L.F2 with inflammatory-related markers, LF3 with tendon-related markers, L.F4 with sensory-related markers and L.F5 with cartilage-related markers (Section 4.4.1). The L.F5 subpopulation was of particular interest due to the presence of cartilage (*Acan*) and OA associated markers (Figure 4.12). Presence of an ACAN-expressing fibroblast subpopulation in the mid-ligament region of the PCL was confirmed with an *Acan*-Cre-tdTomato reporter line (Figure 4.22). This data indicates five ligament fibroblast subpopulations each with unique markers and likely roles during homeostasis and disease progression that remain to be explored.

Murine synovial fibroblasts had less numerous subpopulations but similar differentially expressed markers to the ligament fibroblasts. Synovial fibroblast subpopulations included S.F1 with regulatory-related markers similar to those of L.F1, S.F2 with neuronal-related markers, S.F3 an intermediary subpopulation, and S.F4 with tendon-related markers similar to those of L.F3 (Section 4.4.2). Many synovial and ligament fibroblast differentially expressed markers overlapped (Section 4.4.3), highlighting fibroblast similarities between neighbouring tissues of the joint organ.

Overall, the identification of these ligament and synovium fibroblast markers provides a strong foundation to explore ligament and synovial fibroblast heterogeneity and spatial identity of each subpopulation. This also provides a baseline to compare joint organ fibroblast subpopulations in healthy and diseased murine tissue to further explore disease pathways and potential biomarkers and therapeutic targets.

Chapter 5:
General Discussion and Future Directions

5.1 General Discussion

Ligaments are important biological structures in the knee joint, crucial to the function of the musculoskeletal system. Damage to the ligament is a common musculoskeletal injury primarily due to ageing and or trauma [21], and though healing potential can vary, the ACL is considered to have a low healing potential [37] resulting in pain, immobility and the development of degenerative joint diseases such as OA [112]. The link between ligament trauma and OA development has long been established. However, ligaments might play a larger role than originally thought in OA development, and several findings have shown that ligament degeneration occurs before cartilage degeneration without initial trauma in human [207] and animal knee joints [121]. The biological and mechanical role that ligaments play for normal knee joint homeostasis is not well understood, even more so during OA development.

The aim of this project was to characterise and identify markers and mechanical properties in healthy and OA ligaments. Ligament pathology is often ignored when exploring OA, and this research would allow for an overview of healthy ligament biology and of ligament changes during OA pathology which could potentially uncover clues of the involved cells and OA pathways in the knee joint organ [6].

In this study, murine post-traumatic and spontaneous OA models were chosen to explore OA pathology in the early and late stages of disease progression. Despite differences in gait and weight distribution, the murine knee joint ligaments have a similar function and anatomy to the human knee joint [13]. Furthermore murine spontaneous OA models offer many similarities to human OA disease pathology, including with spontaneous OA models such as the STR/ort mice [118]. In addition, the post-traumatic OA non-invasive mechanical loading murine model allowed us to explore early stages of ligament injury and post-traumatic OA with all ligaments intact [153]. It was hypothesised that in both the post-traumatic and spontaneous OA models we would see changes in the ligament matrix, cellular markers and viscoelastic properties that coincided with disease progression.

Our results confirmed changes during OA in the ACL ECM (Section 2.3-2.6) and viscoelastic properties (Section 3.3). In the post-traumatic and spontaneous OA murine models, the ACL ECM changes in the early stages of OA included proteoglycan and COL2 deposition in the mid-ligament region and at the tibial enthesis, as well as evidence of thicker collagen birefringence in the tibial enthesis (Section 2.5 and 2.6). These ECM changes corresponded with decreased viscoelastic strain rate sensitivity in both murine OA ACLs, as well as decreased mechanical stiffness (tangent

modulus) and an increase in viscoelastic stress-relaxation in the post-traumatic OA ACL (Section 3.3). ECM and cellular changes indicate that ligament structure was compromised during early stages of OA, opening the possibility that ligaments could play an active role in OA progression. This active role of ligaments needs further investigation. Viscoelastic changes in the OA ligaments further confirmed that ligament function and ECM viscoelasticity were affected and could likewise contribute to ligament and whole joint OA pathology.

5.2 Extracellular matrix (ECM) changes in OA ligaments

Changes in the OA ligament cellular morphology and ECM confirm the past work of Hasegawa et al. [129, 207], Quasnichka et al. [121], and Anderson-MacKenzie et al. [114]. Hasegawa et al. showed that ACL degeneration can precede cartilage changes in OA in humans, and that ACL degeneration corresponded with chondroid metaplasia, with SOX9, RUNX2 and COL2 expression [129]. Our results in Chapter 2 confirmed these findings, but also showed that chondroid metaplasia occurred in the early stages of OA before ligament degeneration, particularly at the ACL-tibial enthesis. Furthermore, we showed that these changes cell markers and ECM occur not only in the spontaneous OA models [114, 121] (Section 2.3.1 and 2.3.4), but also in the post-traumatic OA model where ECM changes also included COL2 deposition and ASPN expression (Figure 2.22) in the mid-ligament region. Expression of ASPN expression in the same area of chondroid metaplasia was also seen in the STR/ort ACL (Figure 2.4), indicating a potential role of ASPN in OA ligaments. Overall, our results confirm previous findings seen in human OA also occur in murine OA at early stages of disease progression. In addition, our results indicate that both post-traumatic and spontaneous OA follow similar pathways of chondroid-like cells, therefore understanding the driving force of chondroid metaplasia, by chondrogenesis or endochondral ossification is important to understand both OA models.

5.2.1 Proteoglycans

As mentioned previously, proteoglycan composition in the ligament ECM is often overlooked but is particularly important for ligament fibre formation [29] and for water retention and viscoelastic properties [2, 122]. Deficiencies in decorin and biglycan have been shown to affect strain rate sensitivity and viscoelastic behaviour [69, 79]. Robinson et al. theorised that an increase in proteoglycan content (particularly GAGs) would increase strain rate sensitivity [69]. However,

this is the opposite of our findings, which found that strain rate sensitivity in OA ligaments decreased despite proteoglycan deposition seen with Toluidine blue staining (Section 2.3.1-4). This could indicate that individual proteoglycans (such as decorin or biglycan) or other ECM component, are responsible for strain rate sensitivity. It remains unclear how proteoglycans impede strain rate sensitivity and other viscoelastic properties and could provide further insights into the link between mechanics and cell response. Our study did not evaluate decorin or biglycan or quantify GAG content in OA ligaments, a limitation in this research which needs to be addressed.

The only specific proteoglycan expression analysed in this study was ASPN, an SLRP lacking GAG chains necessary for water retention [193]. As previous mentioned, we identified ASPN as a potential marker of OA in the ACLs of post-traumatic (Section 2.3.3) and spontaneous OA murine models (Section 2.3.1). ASPN has been previously found in healthy ligament and tendons, usually surrounding fibroblasts [171]. Though the role of ASPN in the ligament remains unknown, it has been associated with a regulatory role in mineralisation [194] and its association with OA is not new. ASPN is upregulated in OA cartilage and involved in the TGF-β signalling pathway [356]. Our results showed ASPN colocalization in areas with changes in rounded cell morphology and COL2 deposition (Section 2.3.1 and 2.3.3). This is further evidence that ASPN plays a regulatory role in OA, particularly in ligaments and needs to be further explored.

As previously mentioned, proteoglycan content has been shown to increase in the synovial fluid after trauma [108] and in the ACL before ligament rupture [125]. Therefore, proteoglycan deposition in OA is not a new concept and could allow for more water content and viscous behaviour, potentially as a protective effect from trauma or OA. The role of proteoglycans deposition in OA is still not well understood including the pathways that activate proteoglycan deposition and could be an important biomarker for disease progression. Our research theorised that rounded-cell morphology associated with COL2 deposition could be responsible for proteoglycan deposition. Potential proteoglycans of interest include ASPN and also ACAN, which was expressed in the L.F5 subpopulation (Figure 4.12), and is another proteoglycan previously associated with OA [177].

5.2.2 Collagen type II (COL2)

Similarly the role of COL2 on ligament biology and mechanical properties remains relatively unknown. Collagen composition is essential for ligament stiffness and function [69], and is

considered the basic building block of ligament and tendon fibres [69]. Meanwhile, COL2 deposition in tendons and ligaments has been associated with the fibrocartilaginous region and adaptation to compressive load [30, 357] as well as with disease and ageing [358], including in human OA ligaments [129] and guinea pig OA ligaments [121]. Our findings confirmed these results on COL2 deposition associated with OA disease progression, but also showed that this was not limited only to ligaments (ACL and MCL), but also to the fibrous region of the menisci (Section 2.3.1-4), reinforcing the idea that this is a whole joint pathology.

COL2 could be involved in ligament ECM biomechanical properties and potentially OA progression. As previously mentioned, COL2 stiffness [232] could potentially account for the decrease in ligament stiffness seen in the post-traumatic OA ACLs (Figure 3.26). Furthermore, COL2 deposition was also seen in the mid-ligament region of 12-week-old CD1 spontaneous OA ACLs (Figure 2.33) and more importantly, COL2 deposition in 12-week-old mice preceded cartilage lesions (Figure 2.28). Therefore, if COL2 deposition affects ligament viscoelastic properties and biomechanical pathways, it could be an early trigger for spontaneous OA progression. Interestingly, COL2 denaturation is seen in early OA in articular cartilage as well as synthesis of damaged COL2 molecules [359]. It is possible, that the same pathways are initiating COL2 synthesis in the ligaments and menisci.

Overall, COL2 deposition occurred in both the spontaneous and post-traumatic OA ligaments including at early stages of OA progression in both the ligament enthesis and mid-body regions associated to areas with rounded chondroid-like cells. Understanding COL2 synthesis in the ligament could provide further insights in OA pathology.

5.2.3 Other collagens

Other collagens could also affect ligament mechanical properties in OA. Collagen type III is another component of the healthy ligament ECM [2] which is upregulated in areas of ligament injury resulting in lower mechanical stiffness [357]. Moreover collagen V mutations also account for a decrease in ligament stiffness maximum load and resulted in secondary OA progression [141]. Collagen type I, III and V expression were not directly explored in this study. However, polarised PR staining demonstrated an increase in red collagen birefringence indicative of thicker collagen organisation [167] in the enthesis and epiligament layers of both the post-traumatic (Section 2.5) and spontaneous OA ACLs (Section 2.6). These changes in collagen organisation did not result in stiffer mechanical properties of the ACL as could be expected from thicker

collagen fibres (Section 3.3). Despite this, past studies have shown that collagens are important in ligament mechanics, therefore evaluating the full collagen blueprint in the healthy and diseased ligaments is necessary to determine the role of collagens in ligament mechanics and in OA.

5.2.4 Mineralisation

Other OA pathologies seen in OA ligaments included evidence of mineralisation. Mineralisation was found mainly in the MCL and the outer menisci regions in the late stages of OA development in all murine OA models except the post-traumatic non-invasive loading model (Section 2.3-2.6). Changes in the medial compartment during OA have been attributed to an increase in weight bearing forces [174]. Unfortunately, our study did not measure the mechanical properties of the MCL, however this is in line with past studies which found an increase in MCL stiffness in OA patients [140]. This could indicate that the MCL could also play an active role in OA progression, and deserves further consideration.

Mineralisation of the joint space was quantified with μCT, a new but powerful methodology to quantify OA progression [165]. Mineralisation of joint space was quantified in the novel CD1 spontaneous OA murine OA model and mineralisation increased from 12 to the 24-week-old knee joints (Figure 2.29). This mineralisation did not result in stiffer tangent modulus of the ACL between these two age groups (Figure 3.19), likely explained by the fact that increased mineralisation occurred mainly in the medial compartment (consisting of the medial menisci and MCLs) (Figure 2.29). Changes of cell morphology, SOX9 and RUNX2 expression, collagen birefringence and COL2 and proteoglycan deposition was always found in areas surrounding mineralisation (Section 2.3-2.6), therefore it is possible that these changes are associated, potentially through endochondral ossification pathways. More evidence is needed to confirm what is driving this increase in mineralisation, which likely have a major impact in knee stiffness and pain often associated with OA [6].

Overall, we can conclude that in the early stages of OA ligament ECM is severely affected and in the later stages of OA this resulted in mineralisation in OA models particularly in the MCL.

5.3 Viscoelastic changes in OA ligaments

In this study, mechanical testing of the ACL provided further evidence of ECM changes during OA. It is also important to note that differences in the strain rate sensitivity were found in the normalised tangent modulus-stress curves at higher strain rates (1%/s vs 10%/s) of both the spontaneous and post-traumatic OA models (Figure 3.21 and Figure 3.28). Changes at higher strain rates could be more physiologically relevant, strain rates of normal tendon function in horses exceeded 200%/s [360]. Normal strain rates in mouse tendons and ligaments have not been described. At higher strain rates, collagen fibril strain has been found to be more prevalent than global tissue strain, and this has been speculated to be due to less time for water content to dissipate and allow for viscous behaviour of non-collagenous ECM components [361]. Since strain rate sensitivity was lacking at higher strain rates of the OA ligaments, it is possible that collagen content could be responsible for this mechanical change.

It is also worth mentioning that in our mechanical analysis no differences between healthy and OA ligaments were found in some viscoelastic properties including stress-strain curves and hysteresis (including hysteresis strain rate sensitivity) (Section 3.3.5-6). These results could be attributed to high standard deviation particularly in the stress-strain curves within our ACL samples discussed in Chapter 3 and could also be due to our testing methodology with varied from past studies on murine ligaments [114, 141, 148]. Similar to strain rate sensitivity, hysteresis is also believed to be regulated by proteoglycan content [73]. However, our results found no differences in hysteresis despite proteoglycan deposition in all OA ACLs. Furthermore, it is unclear why strain rate sensitivity was compromised in stress-strain curves but not in hysteresis strain rate sensitivity. This could in part be due to error in our mechanical analysis which resulted in negative hysteresis at higher strain rates (discussed in Section 3.4.3). These findings however also agree with several studies that showed that GAG depletion did not affect MCL viscoelastic behaviour (including hysteresis) [77] as well as canine ACL viscoelastic behaviour [61]. Therefore, it is possible that different ECM components are affecting hysteresis other than proteoglycans. The mechanical role of proteoglycans is currently under debate and could be tissue specific, as has been shown with collagen type V [204].

Mechanical testing of our murine OA ACLs did not find differences in the material strength as measured by in the ultimate load to failure in both murine OA models (Section 3.3.5-6). This does not concur with past studies on OA ligaments which found a decrease in ultimate load [114]. We theorised that this could be due to different OA models used and different timepoints in OA

progression. Our findings could suggest that viscoelastic properties are more prominent than material properties in these stages of OA and could be a useful diagnosis tool to measure OA progression. This also highlights the importance of understanding the underlying ECM components affecting viscoelastic behaviour, which can further elucidate OA pathology.

The driving force of these ACL ECM compositional changes is likely due to the ligamentocytes. Hagesawa et al. postulated that the rounded chondrocyte-like cell types contribute to COL2 deposition and abnormal ECM production [129], and therefore could consequently be driving changes in the ligament viscoelastic properties. Our findings confirmed the co-localisation of rounded-cell morphology with SOX9 and RUNX2 expression and COL2 and proteoglycan deposition (Section 2.3.1-4). This cartilage-like population has been previously seen in healthy and high-rupture risk canine ACLs [20, 122]. COL2 deposition was also seen in the 12-week-old CD1 ACLs (Figure 2.33), which could be a result of these chondrocyte-like fibroblasts similar to those seen in canine ligaments with a high-rupture risk [122]. These chondrocyte-like cells could be an important fibroblast subpopulation driving OA ECM changes and consequently viscoelastic properties.

Overall, ligament viscoelastic properties, particularly normalised strain rate sensitivity at high strain rates, were affected in both the spontaneous and post-traumatic OA ACLs at the early stages of OA. This is evidence that ligament function is an important OA factor regardless of aetiology. The ECM changes mentioned previously, proteoglycan and COL2 deposition could be responsible for these viscoelastic properties.

5.4 Ligament fibroblast subpopulations

To understand these activated cellular pathways, a better understanding of the innate ligamentocytes during healthy ligament homeostasis is necessary. This includes identifying fibroblast subpopulations and their roles beyond ECM production. Fibroblasts roles have been shown to range from ECM production [2] to sensory [310], and even regulating differentiation [362]. However, fibroblasts heterogeneity [239], raises the question that not all fibroblasts are equal, and roles could be fibroblast-specific. To understand this, it is necessary to look at the single-cell level, including the spatial organisation and the encompassing ECM, which could also affect fibroblast phenotype.

To address this, our final goal was to categorise ligament fibroblast markers and subpopulations, the beginning of a ligament cellular atlas, which is fundamental to identify future biomarkers. It was hypothesised that distinct ligament fibroblast subpopulations could be identified using scRNA-seq. ScRNA-seq successfully identified nine distinct cell types including five ligament fibroblast subpopulations (L.F1-5) (Section 4.3.2). Interestingly, know tendon-ligament markers were mainly concentrated in one fibroblast subpopulation (L.F3) and markers included *Scx*, *Tnmd*, *Mkx* and *Fmod* (Figure 4.10). This would indicate that these markers are not as widespread in ligaments as previously thought and is similar to the findings in murine tendons [47]. Many of the other fibroblast subpopulations (L.F1-2, and L.F4) had a range of markers with relatively unknown functions within ligaments.

The scRNA-seq approach used for this study was novel for murine ligaments, though it has previously been used to identify cell populations for mouse [236] and human tendon [235] and synovium [249]. Our results demonstrated many similarities in fibroblast heterogeneity between murine ligament and synovium tissue including subpopulations and markers (Section 4.3.5). This matches the similar pathological changes seen in the OA menisci and ligaments of all the murine OA models (Section 2.3-2.6), and could imply that connective tissues in the knee joint share similar fibroblast subpopulations, further evidence of the knee joint organ [6]. Fibroblast heterogeneity has revealed the true cellular complexity within these matrix-rich connective tissues, uncovering new markers and roles in healthy and subsequently in diseased tissue.

Overall, we were able to identify distinct ligament fibroblast subpopulations with diverse markers which indicate diverse functions for each subpopulation.

5.4.1 The L.F5 subpopulation

Ligament fibroblasts also included a cartilage-like subpopulation (L.F5) that had a high expression of cartilage-associated markers (*Acan*, *Col2a1* and *Sox9*) (Figure 4.12). While this is not novel, SOX9 and COL2 expression are present in the fibrocartilaginous insertion sites [318] and have been found in the mid-ligament region of canine ACLs [20, 122]. Our results, via a transgenic *Acan*-reporter mouse line, confirmed that ACAN expressing cells were found in the mid-ligament section of healthy murine ligaments (Section 4.3.4). Our scRNA-seq analysis not only confirms *Acan*-fibroblasts but indicates the presence of an entire cartilage-like fibroblast subpopulation with multiple cartilage-associated markers throughout the healthy ligament. These

findings question the definition of cartilage-specific markers, introduces a new dimension to fibroblast heterogeneity and potentially a new role to ligament fibroblasts.

The L.F5 markers were remarkably similar to the markers expressed in the rounded-cell phenotype ligamentocytes seen in the post-traumatic and spontaneous OA ligaments (*Sox9* and *Col2a1*) (Figure 4.12). It is possible that the L.F5 fibroblast subpopulation are the cells undergoing the rounded morphological change and are activated during OA resulting in SOX9 and COL2 translation and expression. Understanding the underlying pathways of this native L.F5 subpopulation is of particular importance for future therapeutic targets of OA. For example, SOX9 has been shown to promote healing in the bone-tendon-junction [363], therefore activation of this gene could simply be a protective or healing effect. How this L.F5 ligamentocyte subpopulation contributes to healthy ligament homeostasis and to OA progression and interacts with other fibroblast subpopulations remains to be seen. Understanding this subpopulation, as well as the other relatively unknown subpopulations could reveal additional roles of the ligament fibroblasts in knee joint health.

5.5 Future Directions

Future research should continue to characterise the material and viscoelastic properties of all knee joint ligaments. This will allow for the creation of a comprehensive knee and ligament 3D model. Modelling the knee joint with all ligaments could give insights of whole knee mechanics and differences between healthy and diseased knee joints [364], which can be used to diagnose OA progression and ligament mechanical properties in patients without invasive procedures. In addition, finite element 3D modelling of the OA knee joint could predict areas of mechanical stress which trigger mechanotransduction pathways. This modelling has already been shown to be effective in articular cartilage [364].

There is also an emerging field of biomechanics focusing on revealing which aspects of the ligament ECM control specific mechanical properties [365]. This includes determining the role that proteoglycans play in ligament mechanics and can be revealed by characterising all proteoglycan content and other important matrix components (i.e. elastin) in healthy and OA ligaments. This would allow us to determine which ECM components are affecting strain rate sensitivity and give a better understanding of ECM biomarkers of OA progression. Furthermore, how the viscous ECM affects the biomechanical response of native ligament fibroblasts is a vital next step to finally expose elusive mechanotransduction pathways [224]. To do this, we must first

identify and characterise which cells in the ligament matrix can sense the ECM. In this study, scRNA-seq analysis potentially identified a sensory-related fibroblast subpopulation (L.F4). Confirming the role of this subpopulation could be key to determine if ligaments play an active role in OA pathology. Healthy sensory cells can be compared with those of less stiff or diseased ligaments to discover which factors govern the sensory switch between the two states.

In the future, scRNA-seq could also be used in conjunction with machine learning to reveal OA progression and predict regulatory networks and signalling pathways in diseased ligaments [366]. Currently, scRNA-seq has predicted upstream regulators of synoviocytes and chondrocytes from OA tissue and revealed molecular crosstalk networks between the two tissues [367]. For a better understanding of these outcomes, *in situ* hybridization or spatial transcriptomics can also be used to analyse which regions of the ligaments are affected during OA progression, thus creating a detailed molecular map of cells and their surrounding ECM [368]. These techniques could allow for more in depth analysis of specific regions of interest, as has been done recently on inflammatory regions of synovial tissue from rheumatoid arthritis patients to analyse the immune response [369].

Since the aetiology of OA is complex and multifactorial [6], transcriptomics will only provide one layer of information about disease progression. For a more complete understanding of knee joint organ OA, a multi-omics data approach will most likely be necessary to understand the epigenome, proteome and metabolome mechanisms of disease [370]. Integrative analysis of multiple omics data could be used for a multimodal definition of cellular identity which improves cell type characterisation and function [371] and could allow for identification of more biologically relevant biomarkers.

2.6 Conclusions

The work detailed in this thesis demonstrated markers present in the ligament tissues in the early and late stages of post-traumatic (DMM and non-invasive loading) and spontaneous (STR/ort and CD1) murine OA models. This study confirmed changes in the ACL and MCL matrix including toluidine blue staining indicative of proteoglycan deposition, red collagen birefringence indicative of thicker collagen fibres and COL2 deposition occurring at the insertion sites and in some cases in the mid-ligament region. Furthermore, we also confirmed changes in the fibroblast cell phenotype including rounded-cell morphology with SOX9 and RUNX2 expression, as well as an increase in ASPN SLRP expression. Changes in ACL ECM composition associated with changes

of the ligament viscoelastic properties, particularly normalised tangent modulus-stress strain rate sensitivity which was reduced in both the murine spontaneous (CD1) and post-traumatic (non-invasive loading) OA ACLs. Furthermore, post-traumatic OA also resulted in decreased viscoelastic stiffness and stress-relaxation, highlighting the important role of the ECM on viscoelastic properties. These findings confirm that OA pathological changes do affect ligament function (and potentially vice-versa). This study was also the first to use scRNA-seq to identify cell population in murine knee joint ligaments. Nine distinct cell types and five ligament fibroblasts subpopulations (L.F1-5) were successfully identified. Characterisation of these ligament fibroblast subpopulations and their role will be instrumental to discover ligament-related pathways and ligament fibroblast contribution to OA pathology.

References

1. Flandry, F. and G. Hommel, *Normal anatomy and biomechanics of the knee.* Sports Med Arthrosc Rev, 2011. **19**(2): p. 82-92.
2. Frank, C.B., *Ligament structure, physiology and function.* J Musculoskelet Neuronal Interact, 2004. **4**(2): p. 199-201.
3. Messner, K. and J. Gao, *The menisci of the knee joint. Anatomical and functional characteristics, and a rationale for clinical treatment.* J Anat, 1998. **193 (Pt 2)**: p. 161-78.
4. Schulze-Tanzil, G., *Intraarticular Ligament Degeneration Is Interrelated with Cartilage and Bone Destruction in Osteoarthritis.* Cells, 2019. **8**(9).
5. Smith, M.D., *The normal synovium.* Open Rheumatol J, 2011. **5**: p. 100-6.
6. Loeser, R.F., et al., *Osteoarthritis: A Disease of the Joint as an Organ.* Arthritis and Rheumatism, 2012. **64**(6): p. 1697-1707.
7. Arnoczky, S.P., *Anatomy of the anterior cruciate ligament.* Clinical Orthopaedics and Related Research, 1983. **No. 172**: p. 19-25.
8. Caplan, N. and D.F. Kader, *Ligamentous Restraints to Anterior-Posterior Drawer in the Human Knee: A Biomechanical Study*, in *Classic Papers in Orthopaedics*, P.A. Banaszkiewicz and D.F. Kader, Editors. 2014, Springer London: London. p. 141-143.
9. Dargel, J., et al., *Biomechanics of the anterior cruciate ligament and implications for surgical reconstruction.* Strategies in Trauma and Limb Reconstruction, 2007. **2**(1): p. 1-12.
10. Voos, J.E., et al., *Posterior Cruciate Ligament:Anatomy, Biomechanics, and Outcomes.* The American Journal of Sports Medicine, 2012. **40**(1): p. 222-231.
11. Wymenga, A.B., et al., *Surgical anatomy of the medial collateral ligament and the posteromedial capsule of the knee.* Knee Surgery, Sports Traumatology, Arthroscopy, 2006. **14**(3): p. 229-234.
12. Meister, B.R., et al., *Anatomy and kinematics of the lateral collateral ligament of the knee.* American Journal of Sports Medicine, 2000. **28**(6): p. 869-878.
13. Carballo, C.B., et al., *Biomechanics and Microstructural Analysis of the Mouse Knee and Ligaments.* J Knee Surg, 2018. **31**(6): p. 520-527.
14. Lakes, E.H. and K.D. Allen, *Gait analysis methods for rodent models of arthritic disorders: reviews and recommendations.* Osteoarthritis and cartilage, 2016. **24**(11): p. 1837-1849.
15. Woo, S.L., et al., *Tensile properties of the human femur-anterior cruciate ligament-tibia complex. The effects of specimen age and orientation.* Am J Sports Med, 1991. **19**(3): p. 217-25.
16. de Rooster, H., T. de Bruin, and H. van Bree, *Morphologic and functional features of the canine cruciate ligaments.* Vet Surg, 2006. **35**(8): p. 769-80.
17. Glasson, S.S., et al., *The OARSI histopathology initiative - recommendations for histological assessments of osteoarthritis in the mouse.* Osteoarthritis Cartilage, 2010. **18 Suppl 3**: p. S17-23.
18. Staines, K.A., et al., *The STR/ort mouse model of spontaneous osteoarthritis – an update.* Osteoarthritis and Cartilage, 2017. **25**(6): p. 802-808.
19. Birch, H.L., C.T. Thorpe, and A.P. Rumian, *Specialisation of extracellular matrix for function in tendons and ligaments.* Muscles, Ligaments and Tendons Journal, 2013. **3**(1): p. 12-22.
20. Kharaz, Y.A., et al., *Variations in internal structure, composition and protein distribution between intra- and extra-articular knee ligaments and tendons.* Journal of anatomy, 2018. **232**(6): p. 943-955.
21. Lane, J.G. and D. Amiel, *Ligament Histology, Composition, Anatomy, Injury, and Healing Mechanisms*, in *Bio-orthopaedics: A New Approach*, A. Gobbi, et al., Editors. 2017, Springer Berlin Heidelberg: Berlin, Heidelberg. p. 291-312.
22. Woo, S.L.Y., et al., *Biomechanics of knee ligaments: injury, healing, and repair.* Journal of Biomechanics. **39**(1): p. 1-20.
23. *Tendon and Ligament*, in *Tissue Mechanics*, S.C. Cowin and S.B. Doty, Editors. 2007, Springer New York: New York, NY. p. 559-594.
24. Bland, Y.S. and D.E. Ashhurst, *Changes in the distribution of fibrillar collagens in the collateral and cruciate ligaments of the rabbit knee joint during fetal and postnatal development.* The Histochemical Journal, 1996. **28**(5): p. 325-334.
25. Amiel, D., et al., *Tendons and ligaments: a morphological and biochemical comparison.* J Orthop Res, 1984. **1**(3): p. 257-65.

26. Wan, C., et al., *A Quantitative Study of the Relationship between the Distribution of Different Types of Collagen and the Mechanical Behavior of Rabbit Medial Collateral Ligaments.* PLOS ONE, 2014. **9**(7): p. e103363.
27. Amiel, D., et al., *The phenomenon of "ligamentization": anterior cruciate ligament reconstruction with autogenous patellar tendon.* J Orthop Res, 1986. **4**(2): p. 162-72.
28. Henninger, H.B., et al., *Elastin governs the mechanical response of medial collateral ligament under shear and transverse tensile loading.* Acta Biomaterialia, 2015. **25**: p. 304-312.
29. Yoon, J.H. and J. Halper, *Tendon proteoglycans: biochemistry and function.* J Musculoskelet Neuronal Interact, 2005. **5**(1): p. 22-34.
30. Benjamin, M. and J.R. Ralphs, *Fibrocartilage in tendons and ligaments — an adaptation to compressive load.* Journal of Anatomy, 1998. **193**(Pt 4): p. 481-494.
31. Smith, K.D., et al., *Elastin content is high in the canine cruciate ligament and is associated with degeneration.* Vet J, 2014. **199**(1): p. 169-74.
32. Johnson, D.H. and R.A. Pedowitz, *Practical Orthopaedic Sports Medicine and Arthroscopy*. 2007: Lippincott Williams & Wilkins.
33. Stamenov, N., et al., *The Epiligament: Structure, Postnatal Development and Role in Ligament Healing.* Cureus, 2019. **11**(6): p. e4836.
34. Kastelic, J., A. Galeski, and E. Baer, *The Multicomposite Structure of Tendon.* Connective Tissue Research, 1978. **6**(1): p. 11-23.
35. Scapinelli, R., *Vascular anatomy of the human cruciate ligaments and surrounding structures.* Clinical Anatomy, 1997. **10**(3): p. 151-162.
36. Fenwick, S.A., B.L. Hazleman, and G.P. Riley, *The vasculature and its role in the damaged and healing tendon.* Arthritis research, 2002. **4**(4): p. 252-260.
37. Bray, R.C., C.A. Leonard, and P.T. Salo, *Vascular physiology and long-term healing of partial ligament tears.* Journal of Orthopaedic Research, 2002. **20**(5): p. 984-989.
38. Haus, J. and Z. Halata, *Innervation of the anterior cruciate ligament.* Int Orthop, 1990. **14**(3): p. 293-6.
39. Krogsgaard, M.R., P. Dyhre-Poulsen, and T. Fischer-Rasmussen, *Cruciate ligament reflexes.* J Electromyogr Kinesiol, 2002. **12**(3): p. 177-82.
40. Han, Y.H., B. Li, and Y. Wen, *Distribution, quantity and gene expression of mechanoreceptors in ligaments and tendons of knee joint in rabbits.* Journal of Molecular Histology, 2020. **51**(3): p. 233-240.
41. Katonis, P., et al., *Mechanoreceptors of the Posterior Cruciate Ligament.* Journal of International Medical Research, 2008. **36**(3): p. 387-393.
42. Alberts B, J.A., Lewis J, *Fibroblasts and Their Transformations: The Connective-Tissue Cell Family*, in *Molecular Biology of the Cell. 4th edition*. 2002, Garland Science: New York.
43. Benjamin, M. and J.R. Ralphs, *The cell and developmental biology of tendons and ligaments*, in *International Review of Cytology*. 2000, Academic Press. p. 85-130.
44. Chi, S.S., et al., *Gap junctions of the medial collateral ligament: structure, distribution, associations and function.* Journal of Anatomy, 2005. **207**(2): p. 145-154.
45. Schwartz, A.G., et al., *Mineral Distributions at the Developing Tendon Enthesis.* PLOS ONE, 2012. **7**(11): p. e48630.
46. Lee, K.J., et al., *Ligament-Derived Stem Cells: Identification, Characterisation, and Therapeutic Application.* Stem cells international, 2017. **2017**: p. 1919845-1919845.
47. Disser, N.P., et al., *Widespread diversity in the transcriptomes of functionally divergent limb tendons.* Journal of Physiology, 2020. **598**(8): p. 1537-1550.
48. Anderson, D.M., et al., *Mohawk is a novel homeobox gene expressed in the developing mouse embryo.* Dev Dyn, 2006. **235**(3): p. 792-801.
49. Sugimoto, Y., et al., *Scx+/Sox9+ progenitors contribute to the establishment of the junction between cartilage and tendon/ligament.* Development, 2013. **140**(11): p. 2280-8.
50. Alberton, P., et al., *Conversion of Human Bone Marrow-Derived Mesenchymal Stem Cells into Tendon Progenitor Cells by Ectopic Expression of Scleraxis.* Stem Cells and Development, 2011. **21**(6): p. 846-858.
51. Murchison, N.D., et al., *Regulation of tendon differentiation by scleraxis distinguishes force-transmitting tendons from muscle-anchoring tendons.* Development, 2007. **134**(14): p. 2697-708.

52. Ito, Y., et al., *The Mohawk homeobox gene is a critical regulator of tendon differentiation.* Proceedings of the National Academy of Sciences of the United States of America, 2010. **107**(23): p. 10538-10542.
53. Liu, H., et al., *Mohawk promotes the tenogenesis of mesenchymal stem cells through activation of the TGFbeta signaling pathway.* Stem Cells, 2015. **33**(2): p. 443-55.
54. Chang, S.C., et al., *Cartilage-derived morphogenetic proteins. New members of the transforming growth factor-beta superfamily predominantly expressed in long bones during human embryonic development.* J Biol Chem, 1994. **269**(45): p. 28227-34.
55. Shwartz, Y., et al., *Joint Development Involves a Continuous Influx of Gdf5-Positive Cells.* Cell Reports, 2016. **15**(12): p. 2577-2587.
56. Harada, M., et al., *Developmental failure of the intra-articular ligaments in mice with absence of growth differentiation factor 5.* Osteoarthritis and Cartilage, 2007. **15**(4): p. 468-474.
57. Guerquin, M.J., et al., *Transcription factor EGR1 directs tendon differentiation and promotes tendon repair.* J Clin Invest, 2013. **123**(8): p. 3564-76.
58. Keller, T.C., et al., *Growth/differentiation factor-5 modulates the synthesis and expression of extracellular matrix and cell-adhesion-related molecules of rat Achilles tendon fibroblasts.* Connect Tissue Res, 2011. **52**(4): p. 353-64.
59. Woo, S.L., *Mechanical properties of tendons and ligaments. I. Quasi-static and nonlinear viscoelastic properties.* Biorheology, 1982. **19**(3): p. 385-96.
60. Franchi, M., et al., *Collagen structure of tendon relates to function.* ScientificWorldJournal, 2007. **7**: p. 404-20.
61. Hama Rashid, R.A., *Viscoelastic behaviour of the canine cranial cruciate ligament complex*. 2017, University of Liverpool.
62. Zitnay, J.L. and J.A. Weiss, *Load transfer, damage, and failure in ligaments and tendons.* Journal of Orthopaedic Research, 2018. **36**(12): p. 3093-3104.
63. Kelc, R., et al., *The Physiology of Sports Injuries and Repair Processes*. 2013. 43-86.
64. Fung, Y.-C., *Bioviscoelastic Solids*, in *Biomechanics: Mechanical Properties of Living Tissues*, Y.-C. Fung, Editor. 1993, Springer New York: New York, NY. p. 242-320.
65. Provenzano, P., et al., *Nonlinear ligament viscoelasticity.* Ann Biomed Eng, 2001. **29**(10): p. 908-14.
66. Schatzmann, L., P. Brunner, and H.U. Stäubli, *Effect of cyclic preconditioning on the tensile properties of human quadriceps tendons and patellar ligaments.* Knee Surgery, Sports Traumatology, Arthroscopy, 1998. **6**(SUPPL. 1): p. S56-S61.
67. Bonner, T.J., et al., *Strain-rate sensitivity of the lateral collateral ligament of the knee.* Journal of the Mechanical Behavior of Biomedical Materials, 2015. **41**: p. 261-270.
68. Fratzl, P., et al., *Fibrillar Structure and Mechanical Properties of Collagen.* Journal of Structural Biology, 1998. **122**(1): p. 119-122.
69. Robinson, P.S., et al., *Strain-rate sensitive mechanical properties of tendon fascicles from mice with genetically engineered alterations in collagen and decorin.* J Biomech Eng, 2004. **126**(2): p. 252-7.
70. Thornton, G.M., N.G. Shrive, and C.B. Frank, *Altering ligament water content affects ligament pre-stress and creep behaviour.* Journal of Orthopaedic Research, 2001. **19**(5): p. 845-851.
71. Miller, K.S., et al., *Effect of preconditioning and stress relaxation on local collagen fiber re-alignment: inhomogeneous properties of rat supraspinatus tendon.* J Biomech Eng, 2012. **134**(3): p. 031007.
72. Hingorani, R.V., et al., *Nonlinear Viscoelasticity in Rabbit Medial Collateral Ligament.* Annals of Biomedical Engineering, 2004. **32**(2): p. 306-312.
73. Elliott, D.M., et al., *Effect of altered matrix proteins on quasilinear viscoelastic properties in transgenic mouse tail tendons.* Ann Biomed Eng, 2003. **31**(5): p. 599-605.
74. Lujan, T.J., et al., *Contribution of glycosaminoglycans to viscoelastic tensile behavior of human ligament.* J Appl Physiol (1985), 2009. **106**(2): p. 423-31.
75. Thornton, G.M., N.G. Shrive, and C.B. Frank, *Ligament creep recruits fibres at low stresses and can lead to modulus-reducing fibre damage at higher creep stresses: a study in rabbit medial collateral ligament model.* J Orthop Res, 2002. **20**(5): p. 967-74.
76. Yahia, L.H. and G. Drouin, *Study of the hysteresis phenomenon in canine anterior cruciate ligaments.* Journal of Biomedical Engineering, 1990. **12**(1): p. 57-62.

77. Lujan, T.J., et al., *Effect of dermatan sulfate glycosaminoglycans on the quasi-static material properties of the human medial collateral ligament.* Journal of Orthopaedic Research, 2007. **25**(7): p. 894-903.
78. Woo, S.L.Y., et al., *Effects of postmortem storage by freezing on ligament tensile behavior.* Journal of Biomechanics, 1986. **19**(5): p. 399-404.
79. Dourte, L.M., et al., *Influence of Decorin on the Mechanical, Compositional, and Structural Properties of the Mouse Patellar Tendon.* Journal of Biomechanical Engineering, 2012. **134**(3): p. 031005-031005-8.
80. Robinson, K.A., et al., *Decorin and biglycan are necessary for maintaining collagen fibril structure, fiber realignment, and mechanical properties of mature tendons.* Matrix Biol, 2017. **64**: p. 81-93.
81. Temenoff, J.S. and A.G. Mikos, *Review: tissue engineering for regeneration of articular cartilage.* Biomaterials, 2000. **21**: p. 431 - 440.
82. Woolf, A.D. and B. Pfleger, *Burden of major musculoskeletal conditions.* Bull World Health Organ, 2003. **81**(9): p. 646-56.
83. Yu, D., et al., *Annual consultation incidence of osteoarthritis estimated from population-based health care data in England.* Rheumatology (United Kingdom), 2015. **54**(11): p. 2051-2060.
84. Heidari, B., *Knee osteoarthritis prevalence, risk factors, pathogenesis and features: Part I.* Caspian Journal of Internal Medicine, 2011. **2**(2): p. 205-212.
85. Alshami, A.M., *Knee osteoarthritis related pain: a narrative review of diagnosis and treatment.* International Journal of Health Sciences, 2014. **8**(1): p. 85-104.
86. Sandell, L.J. and T. Aigner, *Articular cartilage and changes in Arthritis: Cell biology of osteoarthritis.* Arthritis Research & Therapy, 2001. **3**(2): p. 1-7.
87. Hamerman, D., *The biology of osteoarthritis.* N Engl J Med, 1989. **320**(20): p. 1322-30.
88. Loeser, R.F., J.A. Collins, and B.O. Diekman, *Ageing and the pathogenesis of osteoarthritis.* Nat Rev Rheumatol, 2016. **12**(7): p. 412-420.
89. Lories, R.J. and F.P. Luyten, *Osteoarthritis, a disease bridging development and regeneration.* Bonekey Rep, 2012. **1**: p. 136.
90. van der Kraan, P.M. and W.B. van den Berg, *Osteophytes: relevance and biology.* Osteoarthritis Cartilage, 2007. **15**(3): p. 237-44.
91. Mathiessen, A. and P.G. Conaghan, *Synovitis in osteoarthritis: current understanding with therapeutic implications.* Arthritis Research & Therapy, 2017. **19**: p. 18.
92. Sellam, J. and F. Berenbaum, *The role of synovitis in pathophysiology and clinical symptoms of osteoarthritis.* Nat Rev Rheumatol, 2010. **6**(11): p. 625-35.
93. Englund, M., A. Guermazi, and S.L. Lohmander, *The role of the meniscus in knee osteoarthritis: a cause or consequence?* Radiol Clin North Am, 2009. **47**(4): p. 703-12.
94. Li, G., et al., *Subchondral bone in osteoarthritis: insight into risk factors and microstructural changes.* Arthritis Research & Therapy, 2013. **15**(6): p. 223.
95. Blalock, D., et al., *Joint Instability and Osteoarthritis.* Clinical Medicine Insights. Arthritis and Musculoskeletal Disorders, 2015. **8**: p. 15-23.
96. Wluka, A.E., C.B. Lombard, and F.M. Cicuttini, *Tackling obesity in knee osteoarthritis.* Nature Reviews Rheumatology, 2013. **9**(4): p. 225-235.
97. Moses, B., J. Orchard, and J. Orchard, *Systematic Review: Annual Incidence of ACL Injury and Surgery in Various Populations.* Research in Sports Medicine, 2012. **20**(3-4): p. 157-179.
98. Arendt, E.A., J. Agel, and R. Dick, *Anterior cruciate ligament injury patterns among collegiate men and women.* Journal of athletic training, 1999. **34**(2): p. 86-92.
99. Lohmander, L.S., et al., *The long-term consequence of anterior cruciate ligament and meniscus injuries: osteoarthritis.* Am J Sports Med, 2007. **35**(10): p. 1756-69.
100. Lohmander, L.S., et al., *High prevalence of knee osteoarthritis, pain, and functional limitations in female soccer players twelve years after anterior cruciate ligament injury.* Arthritis Rheum, 2004. **50**(10): p. 3145-52.
101. Hill, C.L., et al., *Cruciate ligament integrity in osteoarthritis of the knee.* Arthritis & Rheumatism, 2005. **52**(3): p. 794-799.
102. Kuyinu, E.L., et al., *Animal models of osteoarthritis: classification, update, and measurement of outcomes.* Journal of Orthopaedic Surgery and Research, 2016. **11**: p. 19.
103. Pond, M.J. and J.R. Campbell, *The canine stifle joint I. Rupture of the anterior cruciate ligament.* Journal of Small Animal Practice, 1972. **13**(1): p. 1-10.

104. Pond, M.J. and G. Nuki, *Experimentally-induced osteoarthritis in the dog.* Ann Rheum Dis, 1973. **32**(4): p. 387-8.
105. Kamekura, S., et al., *Osteoarthritis development in novel experimental mouse models induced by knee joint instability.* Osteoarthritis Cartilage, 2005. **13**(7): p. 632-41.
106. Fang, H. and F. Beier, *Mouse models of osteoarthritis: modelling risk factors and assessing outcomes.* Nat Rev Rheumatol, 2014. **10**(7): p. 413-421.
107. Glasson, S.S., T.J. Blanchet, and E.A. Morris, *The surgical destabilization of the medial meniscus (DMM) model of osteoarthritis in the 129/SvEv mouse.* Osteoarthritis and Cartilage, 2007. **15**(9): p. 1061-1069.
108. Lohmander, L.S., et al., *Increased levels of proteoglycan fragments in knee joint fluid after injury.* Arthritis Rheum, 1989. **32**(11): p. 1434-42.
109. Haslauer, C.M., et al., *Loss of extracellular matrix from articular cartilage is mediated by the synovium and ligament after anterior cruciate ligament injury.* Osteoarthritis and Cartilage, 2013. **21**(12): p. 1950-1957.
110. Wright, R.W., et al., *Medial collateral ligament healing in macrophage metalloelastase (MMP-12)-deficient mice.* Journal of Orthopaedic Research, 2006. **24**(11): p. 2106-2113.
111. Plaas, A.H., et al., *Proteoglycan metabolism during repair of the ruptured medial collateral ligament in skeletally mature rabbits.* Arch Biochem Biophys, 2000. **374**(1): p. 35-41.
112. R.A. Hauser, E.E.D., H.J. Phillips, A.C. Newlin, R.E. Moore, B.A. Woldin, *Ligament Injury and Healing: A Review of Current Clinical Diagnostics and Therapeutics.* The Open Rehabilitation Journal 2013. **8**: p. 1-20.
113. J., G.S., et al., *Inflammatory and degenerative phases resulting from anterior cruciate rupture in a non-invasive murine model of post-traumatic osteoarthritis.* Journal of Orthopaedic Research. **0**(0).
114. Anderson-MacKenzie, J.M., M.E. Billingham, and A.J. Bailey, *Collagen Remodeling in the Anterior Cruciate Ligament Associated with Developing Spontaneous Murine Osteoarthritis.* Biochemical and Biophysical Research Communications, 1999. **258**(3): p. 763-767.
115. Chinzei, N., et al., *Molecular influence of anterior cruciate ligament tear remnants on chondrocytes: a biologic connection between injury and osteoarthritis.* Osteoarthritis Cartilage, 2018. **26**(4): p. 588-599.
116. Quasnichka, H.L., et al., *Cruciate ligament laxity and femoral intercondylar notch narrowing in early-stage knee osteoarthritis.* Arthritis & Rheumatism, 2005. **52**(10): p. 3100-3109.
117. Mason, R.M., et al., *The STR/ort mouse and its use as a model of osteoarthritis.* Osteoarthritis Cartilage, 2001. **9**(2): p. 85-91.
118. Mason, R.M., et al., *The STR/ort mouse and its use as a model of osteoarthritis.* Osteoarthritis and Cartilage, 2001. **9**(2): p. 85-91.
119. Jimenez, P.A., et al., *Spontaneous osteoarthritis in Dunkin Hartley guinea pigs: histologic, radiologic, and biochemical changes.* Lab Anim Sci, 1997. **47**(6): p. 598-601.
120. Tessier, J.J., et al., *Characterisation of the guinea pig model of osteoarthritis by in vivo three-dimensional magnetic resonance imaging.* Osteoarthritis and Cartilage, 2003. **11**(12): p. 845-853.
121. Quasnichka, H.L., J.M. Anderson-MacKenzie, and A.J. Bailey, *Subchondral bone and ligament changes precede cartilage degradation in guinea pig osteoarthritis.* Biorheology, 2006. **43**(3,4): p. 389-97.
122. Comerford, E.J., et al., *Investigation of the composition, turnover, and thermal properties of ruptured cranial cruciate ligaments of dogs.* Am J Vet Res, 2004. **65**(8): p. 1136-41.
123. Tirgari, M. and L.C. Vaughan, *Arthritis of the canine stifle joint.* Vet Rec, 1975. **96**(18): p. 394-9.
124. Comerford, E.J., et al., *Ultrastructural Differences in Cranial Cruciate Ligaments from Dogs of Two Breeds with a Differing Predisposition to Ligament Degeneration and Rupture.* Journal of Comparative Pathology, 2006. **134**(1): p. 8-16.
125. Comerford, E.J., et al., *Distal femoral intercondylar notch dimensions and their relationship to composition and metabolism of the canine anterior cruciate ligament.* Osteoarthritis Cartilage, 2006. **14**(3): p. 273-8.
126. Hasegawa, A., et al., *Anterior cruciate ligament changes in the human knee joint in aging and osteoarthritis.* Arthritis & Rheumatism, 2012. **64**(3): p. 696-704.
127. Aggarwal, A.K., A. Goel, and B.D. Radotra, *Predictors of Posterior Cruciate Ligament Degeneration in Osteoarthritic Knees.* Journal of Orthopaedic Surgery, 2013. **21**(1): p. 15-18.

128. Mullaji, A.B., et al., *Cruciate Ligaments in Arthritic Knees: A Histologic Study With Radiologic Correlation.* The Journal of Arthroplasty, 2008. **23**(4): p. 567-572.
129. Hasegawa, A., et al., *Cellular and extracellular matrix changes in anterior cruciate ligaments during human knee aging and osteoarthritis.* Arthritis Research & Therapy, 2013. **15**(1): p. R29.
130. Nakahara, H., et al., *Transcription Factor Mohawk and the Pathogenesis of Human Anterior Cruciate Ligament Degradation.* Arthritis & Rheumatism, 2013. **65**(8): p. 2081-2089.
131. Kumagai, K., et al., *The extent of degeneration of cruciate ligament is associated with chondrogenic differentiation in patients with osteoarthritis of the knee.* Osteoarthritis and Cartilage, 2012. **20**(11): p. 1258-1267.
132. Ruschke, K., et al., *Bone morphogenetic protein 2/SMAD signalling in human ligamentocytes of degenerated and aged anterior cruciate ligaments.* Osteoarthritis and Cartilage, 2016. **24**(10): p. 1816-1825.
133. Witoński, D. and M. Wągrowska-Danilewicz, *Distribution of substance-P nerve fibers in intact and ruptured human anterior cruciate ligament: a semi-quantitative immunohistochemical assessment.* Knee Surgery, Sports Traumatology, Arthroscopy, 2004. **12**(5): p. 497-502.
134. Nelissen, R.G.H.H. and P.C.W. Hogendoorn, *Retain or sacrifice the posterior cruciate ligament in total knee arthroplasty? A histopathological study of the cruciate ligament in osteoarthritic and rheumatoid disease.* Journal of Clinical Pathology, 2001. **54**(5): p. 381-384.
135. Martins, G.C., G. Camanho, and M.I. Rodrigues, *Immunohistochemical analysis of the neural structures of the posterior cruciate ligament in osteoarthritis patients submitted to total knee arthroplasty: an analysis of thirty-four cases.* Clinics, 2015. **70**(2): p. 81-86.
136. Ikeuchi, M., et al., *Nociceptive sensory innervation of the posterior cruciate ligament in osteoarthritic knees.* Archives of Orthopaedic and Trauma Surgery, 2012. **132**(6): p. 891-895.
137. Comerford, E.J., et al., *Metabolism and composition of the canine anterior cruciate ligament relate to differences in knee joint mechanics and predisposition to ligament rupture.* J Orthop Res, 2005. **23**(1): p. 61-6.
138. Hagena, F.-W., et al., *The cruciate ligaments in knee replacement.* International Orthopaedics, 1989. **13**(1): p. 13-16.
139. Creaby, M.W., et al., *Varus–valgus laxity and passive stiffness in medial knee osteoarthritis.* Arthritis Care & Research, 2010. **62**(9): p. 1237-1243.
140. Fishkin, Z., et al., *Changes in human knee ligament stiffness secondary to osteoarthritis.* Journal of Orthopaedic Research, 2002. **20**(2): p. 204-207.
141. Sun, M., et al., *Targeted Deletion of Collagen V in Tendons and Ligaments Results in a Classic Ehlers-Danlos Syndrome Joint Phenotype.* The American Journal of Pathology, 2015. **185**(5): p. 1436-1447.
142. Ameye, L., et al., *Abnormal collagen fibrils in tendons of biglycan/fibromodulin-deficient mice lead to gait impairment, ectopic ossification, and osteoarthritis.* FASEB Journal, 2002. **16**(7): p. 673-680.
143. Gill, M.R., Å. Oldberg, and F.P. Reinholt, *Fibromodulin-null murine knee joints display increased incidences of osteoarthritis and alterations in tissue biochemistry.* Osteoarthritis and Cartilage, 2002. **10**(10): p. 751-757.
144. Roddy, K.A. and C.A. Boulter, *Targeted mutation of NOV/CCN3 in mice disrupts joint homeostasis and causes osteoarthritis-like disease.* Osteoarthritis and Cartilage, 2015. **23**(4): p. 607-615.
145. Louis, E., et al., *Nitric oxide and metalloproteinases in canine articular ligaments: A comparison between the cranial cruciate, the medial genual collateral and the femoral head ligament.* The Veterinary Journal, 2006. **172**(3): p. 466-472.
146. Roman-Blas, J.A., et al., *Osteoarthritis associated with estrogen deficiency.* Arthritis Research & Therapy, 2009. **11**(5): p. 241-241.
147. Liu, S.H., et al., *Primary immunolocalization of estrogen and progesterone target cells in the human anterior cruciate ligament.* Journal of Orthopaedic Research, 1996. **14**(4): p. 526-533.
148. Warden, S.J., et al., *Knee ligament mechanical properties are not influenced by estrogen or its receptors.* American Journal of Physiology - Endocrinology And Metabolism, 2006. **290**(5): p. E1034-E1040.
149. Strickland, S.M., et al., *Lack of hormonal influences on mechanical properties of sheep knee ligaments.* Am J Sports Med, 2003. **31**(2): p. 210-5.

150. Murrell, G.A., D. Jang, and R.J. Williams, *Nitric oxide activates metalloprotease enzymes in articular cartilage.* Biochem Biophys Res Commun, 1995. **206**(1): p. 15-21.
151. Hsu, C.C., et al., *The protective role of nitric oxide-dependent innate immunosuppression in the early stage of cartilage damage in rats: Role of nitric oxide in cartilage damage.* Bone & Joint Research, 2017. **6**(4): p. 253-258.
152. Walton, M., *Degenerative joint disease in the mouse knee; histological observations.* J Pathol, 1977. **123**(2): p. 109-22.
153. Poulet, B., et al., *Characterizing a novel and adjustable noninvasive murine joint loading model.* Arthritis Rheum, 2011. **63**(1): p. 137-47.
154. Ratneswaran, A., et al., *Strain-dependent differences in age-associated osteoarthritis pathogenesis.* Osteoarthritis and Cartilage, 2017. **25**: p. S88-S89.
155. Walton, M. and M.W. Elves, *Bone thickening in osteoarthrosis. Observations of an osteoarthrosis-prone strain of mouse.* Acta Orthop Scand, 1979. **50**(5): p. 501-6.
156. Brewster, M., et al., *Ro 32-3555, an orally active collagenase selective inhibitor, prevents structural damage in the STR/ORT mouse model of osteoarthritis.* Arthritis Rheum, 1998. **41**(9): p. 1639-44.
157. Blaney Davidson, E.N., et al., *Expression of transforming growth factor-beta (TGFbeta) and the TGFbeta signalling molecule SMAD-2P in spontaneous and instability-induced osteoarthritis: role in cartilage degradation, chondrogenesis and osteophyte formation.* Ann Rheum Dis, 2006. **65**(11): p. 1414-21.
158. Poulet, B., et al., *Time-series transcriptional profiling yields new perspectives on susceptibility to osteoarthritis.* Arthritis Rheum, 2012. **64**(10): p. 3256-66.
159. Poulet, B., et al., *Spontaneous osteoarthritis in Str/ort mice is unlikely due to greater vulnerability to mechanical trauma.* Osteoarthritis Cartilage, 2013. **21**(5): p. 756-63.
160. Walton, M., *Degenerative joint disease in the mouse knee; radiological and morphological observations.* J Pathol, 1977b. **123**(2): p. 97-107.
161. Christiansen, B.A., et al., *Non-invasive mouse models of post-traumatic osteoarthritis.* Osteoarthritis and Cartilage, 2015. **23**(10): p. 1627-1638.
162. Glasson, S.S., T.J. Blanchet, and E.A. Morris, *The surgical destabilization of the medial meniscus (DMM) model of osteoarthritis in the 129/SvEv mouse.* Osteoarthritis Cartilage, 2007. **15**(9): p. 1061-9.
163. McNulty, M.A., et al., *Histopathology of naturally occurring and surgically induced osteoarthritis in mice.* Osteoarthritis Cartilage, 2012. **20**(8): p. 949-56.
164. Keenan, C.M., et al., *Post-traumatic osteoarthritis development is not modified by postnatal chondrocyte deletion of <em>Ccn2</em&gt.* Disease Models & Mechanisms, 2020. **13**(7): p. dmm044719.
165. Ramos-Mucci, L., et al., *Meniscal and ligament modifications in spontaneous and post-traumatic mouse models of osteoarthritis.* Arthritis Research & Therapy, 2020. **22**(1): p. 171.
166. Borges, L.F., et al., *Picrosirius-polarization staining method as an efficient histopathological tool for collagenolysis detection in vesical prolapse lesions.* Micron, 2007. **38**(6): p. 580-3.
167. Junqueira, L.C.U., G. Bignolas, and R.R. Brentani, *Picrosirius staining plus polarization microscopy, a specific method for collagen detection in tissue sections.* The Histochemical Journal, 1979. **11**(4): p. 447-455.
168. Hasegawa, A., et al., *Anterior cruciate ligament changes in the human knee joint in aging and osteoarthritis.* Arthritis Rheum, 2012. **64**(3): p. 696-704.
169. Levy, Y.D., et al., *Histopathological changes in the human posterior cruciate ligament during aging and osteoarthritis: correlations with anterior cruciate ligament and cartilage changes.* Ann Rheum Dis, 2013. **72**(2): p. 271-7.
170. Kizawa, H., et al., *An aspartic acid repeat polymorphism in asporin inhibits chondrogenesis and increases susceptibility to osteoarthritis.* Nature Genetics, 2005. **37**(2): p. 138-144.
171. Kharaz, Y.A., et al., *Proteomic differences between native and tissue-engineered tendon and ligament.* Proteomics, 2016. **16**(10): p. 1547-1556.
172. Andrews, K., et al., *Review: Medial collateral ligament injuries.* Journal of orthopaedics, 2017. **14**(4): p. 550-554.
173. Kwok, J., et al., *Histopathological analyses of murine menisci: implications for joint aging and osteoarthritis.* Osteoarthritis and cartilage, 2016. **24**(4): p. 709-718.

174. Kumar, D., K.T. Manal, and K.S. Rudolph, *Knee joint loading during gait in healthy controls and individuals with knee osteoarthritis.* Osteoarthritis and cartilage, 2013. **21**(2): p. 298-305.
175. Schmitz, N., et al., *Basic methods in histopathology of joint tissues.* Osteoarthritis and Cartilage, 2010. **18**: p. S113-S116.
176. Aigner, T., et al., *SOX9 expression does not correlate with type II collagen expression in adult articular chondrocytes.* Matrix Biol, 2003. **22**(4): p. 363-72.
177. Chambers, M.G., et al., *Expression of collagen and aggrecan genes in normal and osteoarthritic murine knee joints.* Osteoarthritis Cartilage, 2002. **10**(1): p. 51-61.
178. Christiansen, B.A., et al., *Musculoskeletal changes following non-invasive knee injury using a novel mouse model of post-traumatic osteoarthritis.* Osteoarthritis and Cartilage, 2012. **20**(7): p. 773-782.
179. Sim, J.A., et al., *The risk of concomitant injuries of the contralateral side in valgus injured knee by lateral bumper impact – "Windswept injury mechanism".* Injury, 2020. **51**(8): p. 1863-1866.
180. Collins, C., et al., *Chondro-osseous metaplasia, bone density and patellar cartilage proteoglycan content in the osteoarthritis of STR/ORT mice.* Osteoarthritis Cartilage, 1994. **2**(2): p. 111-8.
181. Englund, M., et al., *Risk factors for medial meniscal pathology on knee MRI in older US adults: a multicentre prospective cohort study.* Ann Rheum Dis, 2011. **70**(10): p. 1733-9.
182. Raustol, O.A., et al., *The meniscal ossicle revisited: etiology and an arthroscopic technique for treatment.* Arthroscopy, 2006. **22**(6): p. 687 e1-3.
183. Sun, Y., et al., *Calcium deposition in osteoarthritic meniscus and meniscal cell culture.* Arthritis Res Ther, 2010. **12**(2): p. R56.
184. Pauli, C., et al., *Macroscopic and histopathologic analysis of human knee menisci in aging and osteoarthritis.* Osteoarthritis Cartilage, 2011. **19**(9): p. 1132-41.
185. Sugita, D., et al., *Indian hedgehog signaling promotes chondrocyte differentiation in enchondral ossification in human cervical ossification of the posterior longitudinal ligament.* Spine (Phila Pa 1976), 2013. **38**(22): p. E1388-96.
186. Uchida, K., et al., *Ossification process involving the human thoracic ligamentum flavum: role of transcription factors.* Arthritis Res Ther, 2011. **13**(5): p. R144.
187. Young, R.D., et al., *Type II collagen deposition in cruciate ligament precedes osteoarthritis in the guinea pig knee.* Osteoarthritis Cartilage, 2002. **10**(5): p. 420-8.
188. Lefebvre, V., et al., *SOX9 is a potent activator of the chondrocyte-specific enhancer of the pro alpha1(II) collagen gene.* Mol Cell Biol, 1997. **17**(4): p. 2336-46.
189. Sekiya, I., et al., *SOX9 enhances aggrecan gene promoter/enhancer activity and is up-regulated by retinoic acid in a cartilage-derived cell line, TC6.* J Biol Chem, 2000. **275**(15): p. 10738-44.
190. Maes, C. and H.M. Kronenberg, *Chapter 60 - Bone Development and Remodeling*, in *Endocrinology: Adult and Pediatric (Seventh Edition)*, J.L. Jameson, et al., Editors. 2016, W.B. Saunders: Philadelphia. p. 1038-1062.e8.
191. Chen, H., et al., *Runx2 Regulates Endochondral Ossification Through Control of Chondrocyte Proliferation and Differentiation.* Journal of Bone and Mineral Research, 2014. **29**(12): p. 2653-2665.
192. Gruber, H.E., et al., *Asporin, a susceptibility gene in osteoarthritis, is expressed at higher levels in the more degenerate human intervertebral disc.* Arthritis research & therapy, 2009. **11**(2): p. R47-R47.
193. Maccarana, M., et al., *Asporin-deficient mice have tougher skin and altered skin glycosaminoglycan content and structure.* PLOS ONE, 2017. **12**(8): p. e0184028.
194. Yamada, S., et al., *PLAP-1/asporin, a novel negative regulator of periodontal ligament mineralization.* J Biol Chem, 2007. **282**(32): p. 23070-80.
195. Park, J.O., et al., *Inflammatory cytokines induce fibrosis and ossification of human ligamentum flavum cells.* J Spinal Disord Tech, 2013. **26**(1): p. E6-12.
196. Kong, Q., et al., *COL6A1 polymorphisms associated with ossification of the ligamentum flavum and ossification of the posterior longitudinal ligament.* Spine (Phila Pa 1976), 2007. **32**(25): p. 2834-8.
197. Liu, Y., et al., *RUNX2 polymorphisms associated with OPLL and OLF in the Han population.* Clin Orthop Relat Res, 2010. **468**(12): p. 3333-41.
198. Alexopoulos, L.G., et al., *Developmental and osteoarthritic changes in Col6a1-knockout mice: biomechanics of type VI collagen in the cartilage pericellular matrix.* Arthritis Rheum, 2009. **60**(3): p. 771-9.

199. Kamekura, S., et al., *Contribution of runt-related transcription factor 2 to the pathogenesis of osteoarthritis in mice after induction of knee joint instability.* Arthritis Rheum, 2006. **54**(8): p. 2462-70.
200. Hou, X.F., et al., *Recombinant human bone morphogenetic protein-2-induced ossification of the ligamentum flavum in rats and the associated global modification of histone H3.* J Neurosurg Spine, 2014. **21**(3): p. 334-41.
201. Hayashi, K., et al., *Expression and localization of bone morphogenetic proteins (BMPs) and BMP receptors in ossification of the ligamentum flavum.* Bone, 1997. **21**(1): p. 23-30.
202. Pest, M.A., et al., *Disturbed cartilage and joint homeostasis resulting from a loss of mitogen-inducible gene 6 in a mouse model of joint dysfunction.* Arthritis Rheumatol, 2014. **66**(10): p. 2816-27.
203. Wang, J.H.C., *Mechanobiology of tendon.* Journal of Biomechanics, 2006. **39**(9): p. 1563-1582.
204. Connizzo, B.K., et al., *Regulatory role of collagen V in establishing mechanical properties of tendons and ligaments is tissue dependent.* Journal of Orthopaedic Research, 2015. **33**(6): p. 882-888.
205. Connizzo, B.K., et al., *Effect of age and proteoglycan deficiency on collagen fiber re-alignment and mechanical properties in mouse supraspinatus tendon.* Journal of biomechanical engineering, 2013. **135**(2): p. 021019-021019.
206. Zeni Jr, J.A. and J.S. Higginson, *Dynamic knee joint stiffness in subjects with a progressive increase in severity of knee osteoarthritis.* Clinical Biomechanics, 2009. **24**(4): p. 366-371.
207. Hasegawa, A., et al., *Anterior cruciate ligament changes in the human knee joint in aging and osteoarthritis.* Arthritis Rheum, 2012. **64**.
208. Dupont, W.D. and W.D. Plummer, Jr., *Power and sample size calculations for studies involving linear regression.* Control Clin Trials, 1998. **19**(6): p. 589-601.
209. Moon, D.K., et al., *The effects of refreezing on the viscoelastic and tensile properties of ligaments.* J Biomech, 2006. **39**(6): p. 1153-7.
210. Wang, H., et al., *Measurement of normal patellar ligament and anterior cruciate ligament by MRI and data analysis.* Exp Ther Med, 2013. **5**(3): p. 917-921.
211. Das Neves Borges, P., et al., *Rapid, automated imaging of mouse articular cartilage by microCT for early detection of osteoarthritis and finite element modelling of joint mechanics.* Osteoarthritis and cartilage, 2014. **22**(10): p. 1419-1428.
212. Fung, Y.C., *Elasticity of soft tissues in simple elongation.* American Journal of Physiology-Legacy Content, 1967. **213**(6): p. 1532-1544.
213. Kwan, M.K., T.H. Lin, and S.L. Woo, *On the viscoelastic properties of the anteromedial bundle of the anterior cruciate ligament.* J Biomech, 1993. **26**(4-5): p. 447-52.
214. Geraghty, B., et al., *Age-related variations in the biomechanical properties of human sclera.* Journal of the Mechanical Behavior of Biomedical Materials, 2012. **16**: p. 181-191.
215. Gillis, C., et al., *Effect of maturation and aging on material and ultrasonographic properties of equine superficial digital flexor tendon.* Am J Vet Res, 1995. **56**(10): p. 1345-50.
216. Oza, A.L., R. Vanderby, and R.S. Lakes, *Creep and Relaxation in Ligament: Theory, Methods and Experiment*, in *Mechanics of Biological Tissue*, G.A. Holzapfel and R.W. Ogden, Editors. 2006, Springer Berlin Heidelberg: Berlin, Heidelberg. p. 379-397.
217. Peltonen, J., et al., *Viscoelastic properties of the Achilles tendon in vivo.* SpringerPlus, 2013. **2**(1): p. 212-212.
218. Zelik, K.E. and J.R. Franz, *It's positive to be negative: Achilles tendon work loops during human locomotion.* PLOS ONE, 2017. **12**(7): p. e0179976.
219. Lam, T.C., C.B. Frank, and N.G. Shrive, *Changes in the cyclic and static relaxations of the rabbit medial collateral ligament complex during maturation.* J Biomech, 1993. **26**(1): p. 9-17.
220. Vogel, H.G., *Age dependence of mechanical properties of rat tail tendons (hysteresis experiments).* Aktuelle Gerontol, 1983. **13**(1): p. 22-7.
221. Shadwick, R.E., *Elastic energy storage in tendons: mechanical differences related to function and age.* J Appl Physiol (1985), 1990. **68**(3): p. 1033-40.
222. Waugh, C.M., et al., *Age-related changes in mechanical properties of the Achilles tendon.* Journal of anatomy, 2012. **220**(2): p. 144-155.
223. Somerville, J.M., et al., *Growth of C57BL/6 mice and the material and mechanical properties of cortical bone from the tibia.* Calcif Tissue Int, 2004. **74**(5): p. 469-75.

224. Humphrey, J.D., E.R. Dufresne, and M.A. Schwartz, *Mechanotransduction and extracellular matrix homeostasis.* Nature reviews. Molecular cell biology, 2014. **15**(12): p. 802-812.
225. Screen, H.R., et al., *Cyclic tensile strain upregulates collagen synthesis in isolated tendon fascicles.* Biochem Biophys Res Commun, 2005. **336**(2): p. 424-9.
226. Lavagnino, M., et al., *Effect of amplitude and frequency of cyclic tensile strain on the inhibition of MMP-1 mRNA expression in tendon cells: an in vitro study.* Connect Tissue Res, 2003. **44**(3-4): p. 181-7.
227. Cantini, M., et al., *The Plot Thickens: The Emerging Role of Matrix Viscosity in Cell Mechanotransduction.* Advanced Healthcare Materials, 2020. **9**(8): p. 1901259.
228. Jansen, K.A., et al., *A guide to mechanobiology: Where biology and physics meet.* Biochimica et Biophysica Acta (BBA) - Molecular Cell Research, 2015. **1853**(11, Part B): p. 3043-3052.
229. Legerlotz, K., G.P. Riley, and H.R.C. Screen, *GAG depletion increases the stress-relaxation response of tendon fascicles, but does not influence recovery.* Acta biomaterialia, 2013. **9**(6): p. 6860-6866.
230. Darnell, M., et al., *Substrate Stress-Relaxation Regulates Scaffold Remodeling and Bone Formation In Vivo.* Advanced healthcare materials, 2017. **6**(1): p. 10.1002/adhm.201601185.
231. Kershaw-Young, C.M., et al., *The effect of glycosaminoglycan enzymes and proteases on the viscosity of alpaca seminal plasma and sperm function.* Anim Reprod Sci, 2013. **138**(3-4): p. 261-7.
232. Luo, Z.P., et al., *Single molecule mechanical properties of type II collagen and hyaluronan measured by optical tweezers.* Biorheology, 2004. **41**(3-4): p. 247-54.
233. Walker, P., H.C. Amstutz, and M. Rubinfeld, *Canine tendon studies. II. Biomechanical evaluation of normal and regrown canine tendons.* J Biomed Mater Res, 1976. **10**(1): p. 61-76.
234. E, L., et al., *Large amplitude oscillatory shear properties of human skin.* Journal of the Mechanical Behavior of Biomedical Materials, 2013. **28**: p. 462-470.
235. Kendal, A.R., et al., *Multi-omic single cell analysis resolves novel stromal cell populations in healthy and diseased human tendon.* Scientific Reports, 2020. **10**(1): p. 13939.
236. De Micheli, A.J., et al., *Single-cell transcriptomic analysis identifies extensive heterogeneity in the cellular composition of mouse Achilles tendons.* American Journal of Physiology-Cell Physiology, 2020. **319**(5): p. C885-C894.
237. Zhang, F., et al., *Defining inflammatory cell states in rheumatoid arthritis joint synovial tissues by integrating single-cell transcriptomics and mass cytometry.* 2019. **20**(7): p. 928-942.
238. Cochain, C., et al., *Single-Cell RNA-Seq Reveals the Transcriptional Landscape and Heterogeneity of Aortic Macrophages in Murine Atherosclerosis.* Circulation Research, 2018. **122**(12): p. 1661-1674.
239. Huang, S., *Non-genetic heterogeneity of cells in development: more than just noise.* Development, 2009. **136**(23): p. 3853-62.
240. Subramanian, A. and T.F. Schilling, *Tendon development and musculoskeletal assembly: emerging roles for the extracellular matrix.* Development (Cambridge, England), 2015. **142**(24): p. 4191-4204.
241. Wang, I.E., et al., *Role of osteoblast-fibroblast interactions in the formation of the ligament-to-bone interface.* J Orthop Res, 2007. **25**(12): p. 1609-20.
242. Matsumoto, T., et al., *Isolation and characterization of human anterior cruciate ligament-derived vascular stem cells.* Stem cells and development, 2012. **21**(6): p. 859-872.
243. Shukunami, C., et al., *Scleraxis positively regulates the expression of tenomodulin, a differentiation marker of tenocytes.* Dev Biol, 2006. **298**.
244. Kurowska-Stolarska, M. and S. Alivernini, *Synovial tissue macrophages: friend or foe?* RMD Open, 2017. **3**(2): p. e000527.
245. Ospelt, C., *Synovial fibroblasts in 2017.* RMD open, 2017. **3**(2): p. e000471-e000471.
246. Abuwarwar, M.H., K. Knoblich, and A.L. Fletcher, *A pathogenic hierarchy for synovial fibroblasts in rheumatoid arthritis.* Annals of translational medicine, 2018. **6**(Suppl 1): p. S75-S75.
247. Hwang, B., J.H. Lee, and D. Bang, *Single-cell RNA sequencing technologies and bioinformatics pipelines.* Experimental & Molecular Medicine, 2018. **50**(8): p. 96.
248. Wu, A.R., et al., *Quantitative assessment of single-cell RNA-sequencing methods.* Nature Methods, 2014. **11**(1): p. 41-46.
249. Stephenson, W., et al., *Single-cell RNA-seq of rheumatoid arthritis synovial tissue using low-cost microfluidic instrumentation.* Nature Communications, 2018. **9**(1): p. 791.

250. Swanson, J.B., et al., *A single-cell transcriptional atlas identifies extensive heterogeneity in the cellular composition of tendons.* bioRxiv, 2019: p. 801266.
251. Tan, G.-K., et al., *Tgfβ signaling is critical for maintenance of the tendon cell fate.* eLife, 2020. **9**: p. e52695.
252. Paolillo, C., E. Londin, and P. Fortina, *Single-Cell Genomics.* Clinical Chemistry, 2019. **65**(8): p. 972-985.
253. Butler, A., et al., *Integrating single-cell transcriptomic data across different conditions, technologies, and species.* Nature Biotechnology, 2018. **36**(5): p. 411-420.
254. Krämer, A., et al., *Causal analysis approaches in Ingenuity Pathway Analysis.* Bioinformatics, 2014. **30**(4): p. 523-530.
255. Taylor, S.E., et al., *Gene expression markers of tendon fibroblasts in normal and diseased tissue compared to monolayer and three dimensional culture systems.* BMC musculoskeletal disorders, 2009. **10**: p. 27-27.
256. Lertkiatmongkol, P., et al., *Endothelial functions of platelet/endothelial cell adhesion molecule-1 (CD31).* Current opinion in hematology, 2016. **23**(3): p. 253-259.
257. Schechter, A.N., *Hemoglobin research and the origins of molecular medicine.* Blood, 2008. **112**(10): p. 3927-3938.
258. Dawes, R., et al., *Combinations of CD45 isoforms are crucial for immune function and disease.* Journal of immunology (Baltimore, Md. : 1950), 2006. **176**(6): p. 3417-3425.
259. Simmons, D.L., et al., *Monocyte antigen CD14 is a phospholipid anchored membrane protein*. Blood, 1989. **73**(1): p. 284-289.
260. Liu, Z., et al., *Specific marker expression and cell state of Schwann cells during culture in vitro.* PLoS One, 2015. **10**(4): p. e0123278.
261. Zammit, P.S., et al., *Pax7 and myogenic progression in skeletal muscle satellite cells.* Journal of Cell Science, 2006. **119**(9): p. 1824.
262. Duperray, A., et al., *Biosynthesis and assembly of platelet GPIIb-IIIa in human megakaryocytes: evidence that assembly between pro-GPIIb and GPIIIa is a prerequisite for expression of the complex on the cell surface.* Blood, 1989. **74**(5): p. 1603-1611.
263. Carlsson, L., et al., *Myotilin: a prominent marker of myofibrillar remodelling.* Neuromuscul Disord, 2007. **17**(1): p. 61-8.
264. Soneson, C. and M.D. Robinson, *Bias, robustness and scalability in single-cell differential expression analysis.* Nature Methods, 2018. **15**(4): p. 255-261.
265. Han, Y. and V. Lefebvre, *L-Sox5 and Sox6 drive expression of the aggrecan gene in cartilage by securing binding of Sox9 to a far-upstream enhancer.* Mol Cell Biol, 2008. **28**(16): p. 4999-5013.
266. Cascio, L.L., et al., *Generation of a mouse line harboring a bi-transgene expressing luciferase and tamoxifen-activatable creERT2 recombinase in cartilage.* genesis, 2014. **52**(2): p. 110-119.
267. Kanakis, I., et al., *Cartilage-Specific CreCre Recombinase TransgenesTransgenes/Alleles in the Mouse*, in *Chondrocytes: Methods and Protocols*, T.M. Haqqi and V. Lefebvre, Editors. 2021, Springer US: New York, NY. p. 23-38.
268. Sugden, C.J., et al., *Laminin N-terminus α31 expression during development in an inducible-transgenic mouse model is lethal and causes a multitude of tissue-specific defects.* bioRxiv, 2020: p. 2020.07.26.221663.
269. Bradley, L.M., et al., *Matrix Metalloprotease 9 Mediates Neutrophil Migration into the Airways in Response to Influenza Virus-Induced Toll-Like Receptor Signaling.* PLOS Pathogens, 2012. **8**(4): p. e1002641.
270. Lin, M., et al., *Matrix metalloproteinase-8 facilitates neutrophil migration through the corneal stromal matrix by collagen degradation and production of the chemotactic peptide Pro-Gly-Pro.* The American journal of pathology, 2008. **173**(1): p. 144-153.
271. Puig-Kröger, A., et al., *Folate Receptor β Is Expressed by Tumor-Associated Macrophages and Constitutes a Marker for M2 Anti-inflammatory/Regulatory Macrophages.* Cancer Research, 2009. **69**(24): p. 9395-9403.
272. Murray, Peter J., et al., *Macrophage Activation and Polarization: Nomenclature and Experimental Guidelines.* Immunity, 2014. **41**(2): p. 339-340.
273. Mouton, A.J., et al., *Mapping macrophage polarization over the myocardial infarction time continuum.* Basic research in cardiology, 2018. **113**(4): p. 26-26.

274. Boniakowski, A.E., et al., *Murine macrophage chemokine receptor CCR2 plays a crucial role in macrophage recruitment and regulated inflammation in wound healing.* European journal of immunology, 2018. **48**(9): p. 1445-1455.
275. Spilsbury, K., et al., *Isolation of a novel macrophage-specific gene by differential cDNA analysis.* Blood, 1995. **85**(6): p. 1620-9.
276. Gao, L., et al., *PLD4 promotes M1 macrophages to perform antitumor effects in colon cancer cells.* Oncol Rep, 2017. **37**(1): p. 408-416.
277. Ishibashi, T., et al., *Identification of MS4A3 as a reliable marker for early myeloid differentiation in human hematopoiesis.* Biochemical and Biophysical Research Communications, 2018. **495**(3): p. 2338-2343.
278. Lee, R.D., et al., *Single-cell analysis of developing B cells reveals dynamic gene expression networks that govern B cell development and transformation.* bioRxiv, 2020: p. 2020.06.30.178301.
279. Nawroth, R., et al., *VE-PTP and VE-cadherin ectodomains interact to facilitate regulation of phosphorylation and cell contacts.* The EMBO journal, 2002. **21**(18): p. 4885-4895.
280. Mustonen, T. and K. Alitalo, *Endothelial receptor tyrosine kinases involved in angiogenesis.* Journal of Cell Biology, 1995. **129**(4): p. 895-898.
281. Rogelj, B., et al., *The X11/Mint family of adaptor proteins.* Brain Research Reviews, 2006. **52**(2): p. 305-315.
282. Kitabgi, P. and P. Freychet, *Effects of neurotensin on isolated intestinal smooth muscles.* Eur J Pharmacol, 1978. **50**(4): p. 349-57.
283. Kuang, S.-Q., et al., *Rare, Nonsynonymous Variant in the Smooth Muscle-Specific Isoform of Myosin Heavy Chain, MYH11, R247C, Alters Force Generation in the Aorta and Phenotype of Smooth Muscle Cells.* Circulation Research, 2012. **110**(11): p. 1411-1422.
284. Krishnakumar, R., et al., *FOXD3 Regulates Pluripotent Stem Cell Potential by Simultaneously Initiating and Repressing Enhancer Activity.* Cell stem cell, 2016. **18**(1): p. 104-117.
285. Britsch, S., et al., *The transcription factor Sox10 is a key regulator of peripheral glial development.* Genes & Development, 2001. **15**(1): p. 66-78.
286. Patel, J., et al., *RGS1 regulates myeloid cell accumulation in atherosclerosis and aortic aneurysm rupture through altered chemokine signalling.* Nature Communications, 2015. **6**(1): p. 6614.
287. Choi, M., et al., *Targeted delivery of Chil3/Chil4 siRNA to alveolar macrophages using ternary complexes composed of HMG and oligoarginine micelles.* Nanoscale, 2020. **12**(2): p. 933-943.
288. Li, J., et al., *VSIG4 inhibits proinflammatory macrophage activation by reprogramming mitochondrial pyruvate metabolism.* Nature Communications, 2017. **8**(1): p. 1322.
289. Pirillo, A., G.D. Norata, and A.L. Catapano, *LOX-1, OxLDL, and Atherosclerosis.* Mediators of Inflammation, 2013. **2013**: p. 152786.
290. Meyaard, L., et al., *LAIR-1, a Novel Inhibitory Receptor Expressed on Human Mononuclear Leukocytes.* Immunity, 1997. **7**(2): p. 283-290.
291. Wu, R., et al., *ACOD1 in immunometabolism and disease.* Cellular & Molecular Immunology, 2020. **17**(8): p. 822-833.
292. Nagaev, I., et al., *Human resistin is a systemic immune-derived proinflammatory cytokine targeting both leukocytes and adipocytes.* PLoS One, 2006. **1**(1): p. e31.
293. Choi, H.-D., et al., *Analysis of gene expression during mineralization of cultured human periodontal ligament cells.* Journal of periodontal & implant science, 2011. **41**(1): p. 30-43.
294. Gopinathan, G., et al., *The Wnt Antagonist SFRP1: A Key Regulator of Periodontal Mineral Homeostasis.* Stem Cells Dev, 2019. **28**(15): p. 1004-1014.
295. Liu, C.-F., et al., *A Role for Hedgehog Signaling in the Differentiation of the Insertion Site of the Patellar Tendon in the Mouse.* PLOS ONE, 2013. **8**(6): p. e65411.
296. Havis, E., et al., *Transcriptomic analysis of mouse limb tendon cells during development.* Development, 2014. **141**(19): p. 3683-3696.
297. Capurro, M.I., et al., *Glypican-3 inhibits Hedgehog signaling during development by competing with patched for Hedgehog binding.* Dev Cell, 2008. **14**(5): p. 700-11.
298. Nassari, S., et al., *The chemokines CXCL12 and CXCL14 differentially regulate connective tissue markers during limb development.* Scientific reports, 2017. **7**(1): p. 17279-17279.
299. Kim, K., et al., *MafB negatively regulates RANKL-mediated osteoclast differentiation.* Blood, 2007. **109**(8): p. 3253-9.

300. Hazell, G.G.J., et al., *PI16 is a shear stress and inflammation-regulated inhibitor of MMP2.* Scientific Reports, 2016. **6**(1): p. 39553.
301. Zhao, Y.Y., Y.Q. Lin, and Y.O. Xu, *Functional Identification of Allograft Inflammatory Factor 1-Like Gene in Luning Chicken.* Anim Biotechnol, 2018. **29**(3): p. 234-240.
302. Shimizu, K., et al., *IL-1 receptor type 2 suppresses collagen-induced arthritis by inhibiting IL-1 signal on macrophages.* J Immunol, 2015. **194**(7): p. 3156-68.
303. McClellan, A., et al., *A novel mechanism for the protection of embryonic stem cell derived tenocytes from inflammatory cytokine interleukin 1 beta.* Scientific Reports, 2019. **9**(1): p. 2755.
304. Davie, E.W., K. Fujikawa, and W. Kisiel, *The coagulation cascade: initiation, maintenance, and regulation.* Biochemistry, 1991. **30**(43): p. 10363-10370.
305. Hu, F., et al., *Toll-like receptors expressed by synovial fibroblasts perpetuate Th1 and th17 cell responses in rheumatoid arthritis.* PloS one, 2014. **9**(6): p. e100266-e100266.
306. Subramanian, A. and T.F. Schilling, *Thrombospondin-4 controls matrix assembly during development and repair of myotendinous junctions.* eLife, 2014. **3**: p. e02372.
307. Ezura, Y., et al., *Differential expression of lumican and fibromodulin regulate collagen fibrillogenesis in developing mouse tendons.* Journal of Cell Biology, 2000. **151**(4): p. 779-787.
308. Rees, S.G., et al., *Immunolocalisation and expression of keratocan in tendon.* Osteoarthritis and Cartilage, 2009. **17**(2): p. 276-279.
309. Lorda-Diez, C.I., et al., *Ligand- and Stage-Dependent Divergent Functions of BMP Signaling in the Differentiation of Embryonic Skeletogenic Progenitors In Vitro.* Journal of Bone and Mineral Research, 2014. **29**(3): p. 735-748.
310. Blanchard, J.W., et al., *Selective conversion of fibroblasts into peripheral sensory neurons.* Nature neuroscience, 2015. **18**(1): p. 25-35.
311. Puelles, E., et al., *Otx2 regulates the extent, identity and fate of neuronal progenitor domains in the ventral midbrain.* Development, 2004. **131**(9): p. 2037-2048.
312. Abudureyimu, S., et al., *Essential Role of Linx/Islr2 in the Development of the Forebrain Anterior Commissure.* Scientific Reports, 2018. **8**(1): p. 7292.
313. Hecht, I., et al., *ILDR2 Is a Novel B7-like Protein That Negatively Regulates T Cell Responses.* Journal of immunology (Baltimore, Md. : 1950), 2018. **200**(6): p. 2025-2037.
314. Vogel, B.E. and E.M. Hedgecock, *Hemicentin, a conserved extracellular member of the immunoglobulin superfamily, organizes epithelial and other cell attachments into oriented line-shaped junctions.* Development, 2001. **128**(6): p. 883-894.
315. Pilipow, K., et al., *IL15 and T-cell Stemness in T-cell–Based Cancer Immunotherapy.* Cancer Research, 2015. **75**(24): p. 5187.
316. Bourane, S., et al., *Low-threshold mechanoreceptor subtypes selectively express MafA and are specified by Ret signaling.* Neuron, 2009. **64**(6): p. 857-70.
317. Lin, L., et al., *Sox11 regulates survival and axonal growth of embryonic sensory neurons.* Developmental Dynamics, 2011. **240**(1): p. 52-64.
318. Thomopoulos, S., G.M. Genin, and L.M. Galatz, *The development and morphogenesis of the tendon-to-bone insertion - what development can teach us about healing.* Journal of musculoskeletal & neuronal interactions, 2010. **10**(1): p. 35-45.
319. Archambault, J.M., et al., *Rat supraspinatus tendon expresses cartilage markers with overuse.* J Orthop Res, 2007. **25**(5): p. 617-24.
320. Green, J.D., et al., *Multifaceted signaling regulators of chondrogenesis: Implications in cartilage regeneration and tissue engineering.* Genes & diseases, 2015. **2**(4): p. 307-327.
321. Kubota, E., et al., *Interleukin 1β and stromelysin (MMP3) activity of synovial fluid as possible markers of osteoarthritis in the temporomandibular joint.* Journal of Oral and Maxillofacial Surgery, 1997. **55**(1): p. 20-27.
322. Balakrishnan, L., et al., *Poteomic analysis of human osteoarthritis synovial fluid.* Clinical Proteomics, 2014. **11**(1).
323. Tanaka, Y., et al., *Six-transmembrane epithelial antigen of prostate4 (STEAP4) is a tumor necrosis factor alpha-induced protein that regulates IL-6, IL-8, and cell proliferation in synovium from patients with rheumatoid arthritis.* Modern Rheumatology, 2012. **22**(1): p. 128-136.
324. Cagnard, N., et al., *Interleukin-32, CCL2, PF4F1 and GFD10 are the only cytokine/chemokine genes differentially expressed by in vitro cultured rheumatoid and osteoarthritis fibroblast-like synoviocytes.* Eur Cytokine Netw, 2005. **16**(4): p. 289-92.

325. Xu, D.H., et al., *The role of IL-11 in immunity and cancer.* Cancer Letters, 2016. **373**(2): p. 156-163.
326. Korshunova, I., et al., *Characterization of BASP1-mediated neurite outgrowth.* Journal of Neuroscience Research, 2008. **86**(10): p. 2201-2213.
327. Majumdar, D. and M.O. Bevensee, *Na-coupled bicarbonate transporters of the solute carrier 4 family in the nervous system: function, localization, and relevance to neurologic function.* Neuroscience, 2010. **171**(4): p. 951-72.
328. Wang, X., et al., *A time-course microarray data analysis reveals consistent dysregulated genes and upstream microRNAs in autoantibody-mediated arthritis.* Journal of Orthopaedic Surgery and Research, 2017. **12**(1).
329. Li, X., et al., *CHST1 and CHST2 sulfotransferase expression by vascular endothelial cells regulates shear-resistant leukocyte rolling via L-selectin.* Journal of Leukocyte Biology, 2001. **69**(4): p. 565-574.
330. Knoepfler, P.S., P.F. Cheng, and R.N. Eisenman, *N-myc is essential during neurogenesis for the rapid expansion of progenitor cell populations and the inhibition of neuronal differentiation.* Genes & Development, 2002. **16**(20): p. 2699-2712.
331. Roivainen, A., et al., *Expression of the myc-family proto-oncogenes and related genes max and mad in synovial tissue.* Scand J Rheumatol, 1999. **28**(5): p. 314-8.
332. Hammaker, D., D.L. Boyle, and G.S. Firestein, *Synoviocyte innate immune responses: TANK-binding kinase-1 as a potential therapeutic target in rheumatoid arthritis.* Rheumatology (Oxford), 2012. **51**(4): p. 610-8.
333. Chamberlain, N.D., et al., *Ligation of TLR7 by rheumatoid arthritis synovial fluid single strand RNA induces transcription of TNFα in monocytes.* Annals of the Rheumatic Diseases, 2013. **72**(3): p. 418-426.
334. Lin, M.J. and S.J. Lee, *Stathmin-like 4 is critical for the maintenance of neural progenitor cells in dorsal midbrain of zebrafish larvae.* Scientific Reports, 2016. **6**.
335. Fernandez, H.L., et al., *Calcitonin receptor-like receptor expression in rat skeletal muscle fibers.* Brain Research, 2011. **1371**: p. 1-6.
336. Yoshida, M., et al., *Expression analysis of three isoforms of hyaluronan synthase and hyaluronidase in the synovium of knees in osteoarthritis and rheumatoid arthritis by quantitative real-time reverse transcriptase polymerase chain reaction.* Arthritis research & therapy, 2004. **6**(6): p. R514-520.
337. Karouzakis, E., et al., *Epigenome analysis reveals TBX5 as a novel transcription factor involved in the activation of rheumatoid arthritis synovial fibroblasts.* Journal of Immunology, 2014. **193**(10): p. 4945-4951.
338. Inoue, J., et al., *The expression of LIM-homeobox genes, Lhx1 and Lhx5, in the forebrain is essential for neural retina differentiation.* Dev Growth Differ, 2013. **55**(7): p. 668-75.
339. Ishibe, T., et al., *Neuronal Differentiation of Synovial Sarcoma and Its Therapeutic Application.* Clinical Orthopaedics and Related Research, 2008. **466**(9): p. 2147-2155.
340. Wenstrup, R.J., et al., *Regulation of collagen fibril nucleation and initial fibril assembly involves coordinate interactions with collagens V and XI in developing tendon.* J Biol Chem, 2011. **286**(23): p. 20455-65.
341. Ma, C.H., et al., *Genes relevant with osteoarthritis by comparison gene expression profiles of synovial membrane of osteoarthritis patients at different stages.* Eur Rev Med Pharmacol Sci, 2014. **18**(3): p. 431-9.
342. Okamoto, K., et al., *Effect of interleukin-1beta and dehydroepiandrosterone on the expression of lumican and fibromodulin in fibroblast-like synovial cells of the human temporomandibular joint.* European Journal of Histochemistry, 2015. **59**(1).
343. Mitani, G., et al., *Potential utility of cell sheets derived from the anterior cruciate ligament and synovium fabricated in temperature-responsive culture dishes.* Journal of Biomedical Materials Research - Part A, 2014. **102**(9): p. 2927-2933.
344. Ai, Z., W. Jing, and L. Fang, *Cytokine-Like Protein 1(Cytl1): A Potential Molecular Mediator in Embryo Implantation.* PloS one, 2016. **11**(1): p. e0147424-e0147424.
345. Li, L., et al., *Hypoxia regulates the proliferation and osteogenic differentiation of human periodontal ligament cells under cyclic tensile stress via mitogen-activated protein kinase pathways.* J Periodontol, 2014. **85**(3): p. 498-508.
346. Stoeckius, M., et al., *Simultaneous epitope and transcriptome measurement in single cells.* Nature methods, 2017. **14**(9): p. 865-868.

347. Mattei, D., et al., *Enzymatic Dissociation Induces Transcriptional and Proteotype Bias in Brain Cell Populations.* Int J Mol Sci, 2020. **21**(21).
348. Harvey, T., S. Flamenco, and C.-M. Fan, *A Tppp3+Pdgfra+ tendon stem cell population contributes to regeneration and reveals a shared role for PDGF signalling in regeneration and fibrosis.* Nature Cell Biology, 2019. **21**(12): p. 1490-1503.
349. Liu, H., et al., *Whole transcriptome expression profiling of mouse limb tendon development by using RNA-seq.* Journal of Orthopaedic Research, 2015. **33**(6): p. 840-848.
350. Slyper, M., et al., *A single-cell and single-nucleus RNA-Seq toolbox for fresh and frozen human tumors.* Nature Medicine, 2020. **26**(5): p. 792-802.
351. Tian, B. and J.L. Manley, *Alternative polyadenylation of mRNA precursors.* Nature Reviews Molecular Cell Biology, 2017. **18**(1): p. 18-30.
352. Sun, Q., Q. Hao, and K.V. Prasanth, *Nuclear Long Noncoding RNAs: Key Regulators of Gene Expression.* Trends in genetics : TIG, 2018. **34**(2): p. 142-157.
353. Dreyfus, M. and P. Régnier, *The Poly(A) Tail of mRNAs: Bodyguard in Eukaryotes, Scavenger in Bacteria.* Cell, 2002. **111**(5): p. 611-613.
354. Grinstein, M., et al., *A robust method for RNA extraction and purification from a single adult mouse tendon.* PeerJ, 2018. **6**: p. e4664.
355. Yang, E., et al., *Decay rates of human mRNAs: correlation with functional characteristics and sequence attributes.* Genome research, 2003. **13**(8): p. 1863-1872.
356. Xu, L., et al., *Asporin and osteoarthritis.* Osteoarthritis Cartilage, 2015. **23**(6): p. 933-9.
357. Buckley, M.R., et al., *Distributions of types I, II and III collagen by region in the human supraspinatus tendon.* Connective tissue research, 2013. **54**(6): p. 374-379.
358. Benjamin, M., R.N. Tyers, and J.R. Ralphs, *Age-related changes in tendon fibrocartilage.* Journal of anatomy, 1991. **179**: p. 127-136.
359. Poole, A.R., et al., *Type II collagen degradation and its regulation in articular cartilage in osteoarthritis.* Annals of the Rheumatic Diseases, 2002. **61**(suppl 2): p. ii78.
360. Herrick, W.C., H.B. Kingsbury, and D.Y. Lou, *A study of the normal range of strain, strain rate, and stiffness of tendon.* J Biomed Mater Res, 1978. **12**(6): p. 877-94.
361. Clemmer, J., et al., *A mechanistic study for strain rate sensitivity of rabbit patellar tendon.* Journal of biomechanics, 2010. **43**(14): p. 2785-2791.
362. Sokos, D., V. Everts, and T.J. de Vries, *Role of periodontal ligament fibroblasts in osteoclastogenesis: a review.* Journal of Periodontal Research, 2015. **50**(2): p. 152-159.
363. Zhu, Z., et al., *Effects of Sox9 gene therapy on the healing of bone-tendon junction: An experimental study.* Indian journal of orthopaedics, 2014. **48**(1): p. 88-95.
364. Kazemi, M., Y. Dabiri, and L.P. Li, *Recent Advances in Computational Mechanics of the Human Knee Joint.* Computational and Mathematical Methods in Medicine, 2013. **2013**: p. 718423.
365. Amis, A.A., *The Biomechanics of Ligaments*, in *Biomechanics and Biomaterials in Orthopedics*, D.G. Poitout, Editor. 2004, Springer London: London. p. 550-563.
366. Chen, G., B. Ning, and T. Shi, *Single-Cell RNA-Seq Technologies and Related Computational Data Analysis.* Frontiers in Genetics, 2019. **10**(317).
367. Chou, C.-H., et al., *Synovial cell cross-talk with cartilage plays a major role in the pathogenesis of osteoarthritis.* Scientific Reports, 2020. **10**(1): p. 10868.
368. Burgess, D.J., *Spatial transcriptomics coming of age.* Nature Reviews Genetics, 2019. **20**(6): p. 317-317.
369. Carlberg, K., et al., *Exploring inflammatory signatures in arthritic joint biopsies with Spatial Transcriptomics.* Scientific Reports, 2019. **9**(1): p. 18975.
370. Hasin, Y., M. Seldin, and A. Lusis, *Multi-omics approaches to disease.* Genome Biology, 2017. **18**(1): p. 83.
371. Hao, Y., et al., *Integrated analysis of multimodal single-cell data.* bioRxiv, 2020: p. 2020.10.12.335331.

Publications

Ramos-Mucci, L., Javaheri, B., van ‘t Hof, R., Bou-Gharios, G., Pitsillides, A.A., Comerford, E., & Poulet, B. Meniscal and ligament modifications in spontaneous and post-traumatic mouse models of osteoarthritis. *Arthritis Res Ther*. **22**, 171 (2020).

Keenan, C.M., Ramos-Mucci, L., Kanakis, I., Milner, P.I., Leask, A., Abraham, D., Bou-Gharios, G., Poulet, B. Post-traumatic osteoarthritis development is not modified by postnatal chondrocyte deletion of Ccn2. *Disease Models & Mechanisms*. **13** (2020).

Kanakis, I., Alhashmi, M., Liu, K., Keenan, C., Ramos Mucci, L., Poulet, B., Bou-Gharios, G. Cartilage-Specific Cre Recombinase Transgenes/Alleles in the Mouse. In: Haqqi T.M., Lefebvre V. (eds) Chondrocytes. Methods in Molecular Biology, vol 2245. Humana, New York, NY. (2021).

Appendix

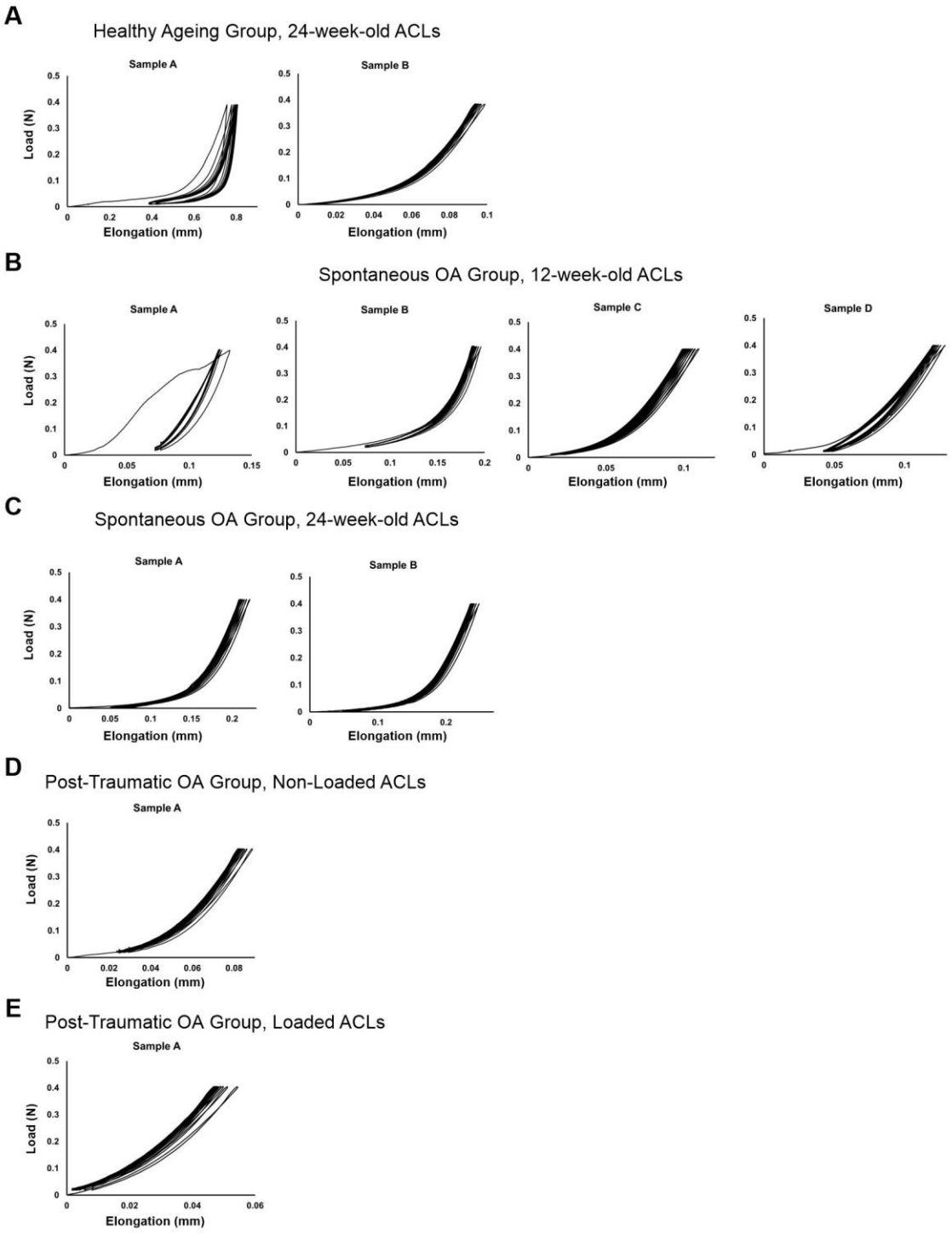

Sup Fig 1 Load-elongation curves of the first ten preconditioning cycles from each murine group of all samples discarded from analysis. Samples were removed from the healthy ageing group 24-week-old ACLs (A), spontaneous OA 12 (B) and 24-week-old (C) ACLs, and the post-traumatic non loaded (D) and loaded (E) ACLs. Samples removed from analysis had a greater than 5% increase in elongation during preconditioning. This increase in elongation is due to slipping of the sample from the polymethyl methacrylate fixation.

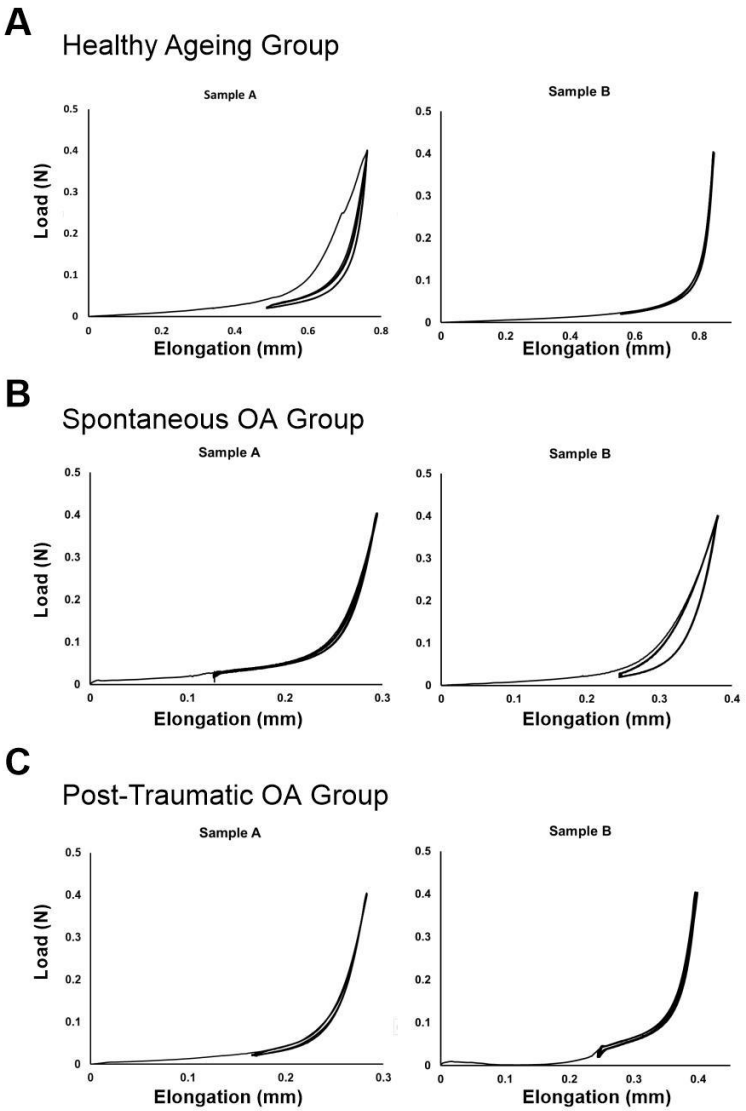

Sup Fig 2 Representative load-elongation curves during preconditioning from each murine group. Groups included the Healthy ageing group (A), spontaneous OA group (B) and post-traumatic OA group (C). These samples showed minimal changes in elongation during preconditioning and were further examined for stress-strain and mechanical analysis.

```
> library(Seurat)
> library(ggplot2)


#Synovial data file was created from matrices provided by 10X Genomics
S2.raw <- Read10X(data.dir="S2_10000ec/outs/…")

#Use Vlnplot to see raw data features and mitochondrial gene percentage
> VlnPlot(S2.raw, features = c("nFeature_RNA", "nCount_RNA", "percent.mt"), n
col = 3)

> #Filter cells, keep cells with <10% mit and >200 and <3000 features.
> S2.flt4.norm <- subset(S2.raw, subset = nFeature_RNA > 200 & nFeature_RNA <
3000 & percent.mt < 10)
> View(S2.flt4.norm)
```

```
> VlnPlot(S2.flt4.norm, features = c("nFeature_RNA", "nCount_RNA", "percent.
mt"), ncol = 3)
> FeatureScatter(S2.flt4.norm, feature1 = "nCount_RNA", feature2 = "percent.
mt")
> #Now normalize data
> S2.flt4.norm <- NormalizeData(S2.flt4.norm, normalization.method = "LogNor
malize", scale.factor = 10000)
> #Now, identify highly variable features
> S2.flt4.norm <- FindVariableFeatures(S2.flt4.norm, selection.method = "vst
", nfeatures = 3000)
> # Identify the 10 most highly variable genes
> top10 <- head(VariableFeatures(S2.flt4.norm), 10)
> # Plot variable features with and without labels
> plot1 <- VariableFeaturePlot(S2.flt4.norm)
> plot2 <- LabelPoints(plot = plot1, points = top10, repel = TRUE)
> #Now scale the data
> all.genes <- rownames(S2.flt4.norm)
> S2.flt4.norm <- ScaleData(S2.flt4.norm, features = all.genes)
> #Next run PCA
> S2.flt4.norm <- RunPCA(S2.flt4.norm, features = VariableFeatures(object = S
2.flt4.norm))
> #Examine and visualize PCA results a few different ways
> print(S2.flt4.norm[["pca"]], dims = 1:10, nfeatures = 5)
> VizDimLoadings(S2.flt4.norm, dims = 1:10, reduction = "pca")
> DimHeatmap(S2.flt4.norm, dims = 1:15, cells = 500, balanced = TRUE)
> #Determining dimensionality
> S2.flt4.norm <- JackStraw(S2.flt4.norm, num.replicate = 100)
> S2.flt4.norm <- ScoreJackStraw(S2.flt4.norm, dims = 1:20)
> JackStrawPlot(S2.flt4.norm, dims = 1:20)
> #Significant dims chosen were dims 1 to 20
> #Cluster cells
> S2.flt4.norm <- FindNeighbors(S2.flt4.norm, dims = 1:20)
> S2.flt4.norm <- FindClusters(S2.flt4.norm, resolution = 0.5)
> #Run UMAP to visualize clusters
> S2.flt4.norm <- RunUMAP(S2.flt4.norm, dims = 1:20)
> DimPlot(S2.flt4.norm, reduction = "umap")

> #Find markers of each cluster
> cluster0.markers <- FindMarkers(S2.flt4.norm, ident.1 = 0, min.pct = 0.25)
> write.csv(cluster0.markers, file = "S2flt4norm_cluster0.csv")
> #Repeat with all clusters

> #With markers of each cluster we can identify each cluster
> #Now we can change cluster labels
> new.cluster.ids <- c("Syn fibroblasts 1", "Syn fibroblasts 2", "Immune cel
ls 1", "Syn fibroblasts 3", "Syn fibroblasts 4", "Immune cells 2", "Immune c
ells 3", "Red blood cells", "Endothelial cells", "Immune cells 4", "Immune c
ells 5")
> names(new.cluster.ids) <- levels(S2.flt4.norm)
> S2.flt4.norm <- RenameIdents(S2.flt4.norm, new.cluster.ids)
> DimPlot(S2.flt4.norm, reduction = "umap", label = TRUE, pt.size = 0.5)

> #For each cluster, we can visualize expression using Dotplot, Heatmap, Vln
plot, and others, see examples below
> DotPlot(object, features = c(“marker name”))
> DoHeatmap(object, features = c(“marker name”))
> FeaturePlot(object, features = c(“marker name”))
> VlnPlot(object, features = c(“marker name”))
> RidgePlot(object, features = c(“marker name”))

> #Make a fibroblast subset
> S2.flt4.Norm.fib <- subset(S2.flt4.norm, idents = c("Syn fibroblasts 1", "
Syn fibroblasts 2", "Syn fibroblasts 3", "Syn fibroblasts 4"))
> #Rename clusters as S.F1 to S.F4
> new.cluster.ids <- c("S.F1", "S.F2", "S.F3", "S.F4")
> names(new.cluster.ids) <- levels(S2.flt4.Norm.fib)
> S2.flt4.Norm.fib <- RenameIdents(S2.flt4.Norm.fib, new.cluster.ids)
> DimPlot(S2.flt4.Norm.fib, reduction = "umap", label = TRUE, pt.size = 0.5)
> #Now can do FindMarkers again this time with the Fib subset, same as above
, see above code for FindMarkers
```

```
> #Can visualize expression with plots same as above, see DotPlot, DoHeatmap
, FeaturePlot, VlnPlot, RidgePlot


> #Find markers between multiple clusters (ex all fibroblasts vs all other c
lusters)
> FibClusters.markers <- FindMarkers(S2.flt4.Norm, ident.1 = c("Syn fibrobla
sts 1", "Syn fibroblasts 2", "Syn fibroblasts 3", "Syn fibroblasts 4"), iden
t.2 = c("Immune cells 1", "Immune cells 2", "Immune cells 3", "Red blood cel
ls", "Endothelial cells", "Immune cells 4", "Immune cells 5"), min.pct = 0.2
5)
> write.csv(SynFibClusters.markers, file = "S2FibClustersMarkers.csv")
```

Sup Fig 3 Rscript used for single-cell RNA-seq downstream analysis. The standard Seurat workflow was followed (https://satijalab.org/seurat/v3.1/pbmc3k_tutorial.html) and adapted according to our data and markers. The same workflow was use for the ligament sample, except for changes in the initial filtering of cells, see methods (Section 4.2.5) for the parameters used.